Ab initio and Density Functional Theory Study of the Monsanto Catalytic Cycle

Tim Robert Griffin

January 9, 1997

Department of Chemistry

University of Sheffield

Submitted for the degree of
Doctor of Philosophy

Ab initio and Density Functional Theory Study of the Monsanto Catalytic Cycle

Tim R. Griffin

Abstract

The results of an effective core potential *ab initio* and Density Functional Theory (DFT) quantum mechanical study of the rhodium- and iodide-catalysed Monsanto acetic acid cycle are presented. The geometries and energetics of the intermediates and transition states have been determined for the key steps of the cycle. The potential influence of variables such as solvent and ligands, and the controlling electronic structure features have been examined. Theoretical data for the analogous iridium system are also reported. The lowest energy transition state determined at the restricted Hartree-Fock (RHF) level for the oxidative addition of CH_3I to *cis*-$[M(CO)_2I_2]^-$ (M=Rh, Ir) is a "linear" structure, involving classical S_N2 backside attack by the transition metal. Secondary α-Deuterium kinetic isotope effects calculated for this mechanism are in excellent agreement with experiment. Both electron correlation and an electrostatic medium have a significant influence on the nucleophilic substitution reaction energetics. Second-order Møller-Plesset theory (MP2) calculations, with the effect of solvent included, using the self-consistent reaction field (SCRF) model, predict activation barriers in good agreement with experiment. The overall oxidative addition process is found to be exothermic at the MP2 level for both metal systems, but more so for iridium. The transition state and intrinsic reaction co-ordinate (IRC) calculated for migratory insertion in $[CH_3M(CO)_2I_3]^-$ (M=Rh, Ir), indicate that the reaction proceeds via a concerted movement of CH_3 and CO groups toward each other. In the rhodium system this reaction is predicted to take place with a low activation barrier and lead to exothermic formation of a five co-ordinate acyl complex in agreement with experiment. By contrast, migratory insertion in the iridium system has a high barrier and is endothermic. Analyses suggest that the difference in reactivity of rhodium and iridium complexes can be correlated to the greater strength of metal–carbon bonds for the heavier transition metal. DFT calculations of the strongly bound ground state complexes yield geometrical structures and carbonyl vibrational frequencies which are comparable, or superior, to those obtained at the RHF and MP2 levels in the same Gaussian basis. However, calculations of the transition states and reaction co-ordinates have not been successful. It is proposed that the currently used functionals are not suitable for the calculation of transition states when weak interactions become important.

Acknowledgements

I am eternally grateful for the expertise, support, advice and patience of Dr Dave Cook, my supervisor during the last three and a bit years. A special thanks must go to Dr Tony Haynes, who has educated me in the finer arts of inorganic chemistry and always been there to answer my questions. Thanks also to Dr George Morris, my CASE supervisor from BP chemicals (Hull) for useful discussions and defending the relevance of my work to sceptical industrialists. Drs Grayson, Pickup and Whitehead deserve a mention for academic help, and the latter for also being unspeakably cheeky to an employee of the chemical industry.

The Jackson room will always hold fond memories for me, a sanctuary of comedy stories and scandal. For this I must thank the boss man Dr Jackson, who only evicted me on one or two occasions, and his minions past and present. In particular, Lowri D (for slaps, many visits to the S&G and being there at a rather difficult time), Simon McG (for his ridiculous behaviour), Lorraine (for hotel, the voice and Barry woes), Dr Gill (the most sensitive man I have ever met – I did not call you stupid), Dr Galindo and Aris (I hope to learn from your fantastically cool attitude on life) and Dr Richy Sear (one day your past will be valuable to me). I would also like to thank Squilts, Michael Odeneye, Ian Maxfield, the Zoids (now defunct) and the rest of G floor. Denise, thankyou for brightening my afternoons, and sometimes mornings even.

I am obliged to thank Miss Lesley Harrison.

A special tribute must go to the friends from home, who have supported me in times of particular woe, shared with me the most fantastic times and I hope will remain themselves for many years to come; Lee, Paul, Rich, Mr and Mrs Moles, Andrew and people past.

Thanks go to the SERC and BP Chemicals (Hull) for funding.

Finally, and most importantly, I send my love and gratitude to my family for being there and not losing faith in me, even when I had none; Dr Jon and Joanne, Jo and Gareth, Doris and Sophy, Mum and Dad: thankyou.

Contents

Chapter 1

Introduction

This first chapter sets out the preliminary material necessary for a basic understanding of the Monsanto acetic acid process. The rudimentary concepts of homogeneous catalysis and a brief account of the background to rhodium and iridium catalysed methanol carbonylation is presented. The results from a number of mechanistic studies that have been carried out in this area are reviewed, focusing on the nature of the active catalytic species and the important reaction steps that have been proposed to participate in the catalytic cycles. The remainder of the introduction discusses the current capabilities of theoretical computational methods as applied to problems in organometallic chemistry.

1.1 Catalysis

A catalyst is a substance that increases the rate of a chemical reaction but is not itself consumed. The reaction is facilitated by providing pathways with lower Gibbs free energies of activation which avoid the slow rate-determining step of the un-catalysed process. If alternative routes exist, a catalyst can enhance product selectivity by accelerating just one of the competing reaction sequences. Since a catalyst works by lowering activation barriers its action is purely kinetic. Thus, reactions that are thermodynamically unfavourable cannot be made favourable in this way.

Catalytic agents are numerous and diverse in application, ranging from the natural action of enzymes in biological systems, to the large-scale production of bulk organic chemicals by metal catalysis. Approximately 70% of all chemicals produced commercially have involved catalysis at some point during their manufacture [1].

Catalysts are classified as *heterogeneous* if they are present in a different phase to the reagents and *homogeneous* if they are present in the same phase. Processes

employing the former typically involve the combination of gaseous reactants over a solid or supported metal surface. The latter usually means that the catalyst is a transition metal complex which is soluble in the liquid reaction mixture. Of the two, heterogeneous catalysis has had the greater economic impact, although homogeneous technology does offer some key practical advantages. Homogeneous systems allow relatively mild reaction conditions and are often highly selective toward the formation of a desired product. This type of catalysis is also generally of greater academic interest since the action of the catalyst can be studied at the molecular level directly, or by observation of model reactions using conventional analytical chemistry techniques. Their major disadvantage is in the separation of the catalyst from the reaction mixture. One of the most important examples of a process homogeneously catalysed by a metal complex in solution is the Monsanto synthesis of acetic acid from methanol which is the subject of this thesis.

1.1.1 Principles of Homogeneous Catalysis

Homogeneous catalysts operate within a cycle. The *catalytic cycle* comprises a sequence of stoichiometric reactions forming a closed loop that is repeated each time a reactant molecule is converted into a product molecule. The overall rate of reaction for the whole process is dependent on the slowest step of the cycle which is therefore rate determining.

The role of the active catalyst is to provide a centre on which chemical reactions can take place. Transition metal species have several characteristics which make them ideally suited for this purpose:

- they have a range of oxidation states and co-ordination environments which they can adopt allowing a variety of redox and substitution reactions to occur;
- they can activate relatively inert molecules, such as carbon monoxide, by co-ordination;
- they can be electronically and sterically 'tuned' by the effect of different ligands to alter their reactivity.

The catalysis of molecular transformations generally requires facile co-ordination of reactants to metal ions and equally facile loss of products from the co-ordination sphere. Both processes must occur with low activation barriers, so highly labile metal complexes are required. These labile complexes are co-ordinatively unsaturated in the sense that they contain an open co-ordination site or have a ligand that is only weakly co-ordinated. Square planar 16-electron complexes are co-ordinatively unsaturated and are commonly employed to catalyse the reactions

of organic molecules. Good examples of these include Rh(I) complexes such as the olefin hydrogenation catalyst, $[RhCl(PPh_3)_3]$ [2] (the "Wilkinson" catalyst), and the species believed to be the active catalyst in the Monsanto catalytic cycle, $[Rh(CO)_2I_2]^-$.

The *trans* effect and *trans* influence of co-ordinated ligands are important concepts in organometallic chemistry [3, 4]. The *trans* effect was first studied in ligand replacement reactions of square planar platinum complexes. From these studies a number of ligands have been arranged in a series with respect to their ability to facilitate substitution in the site *trans* to themselves. The approximate order of increasing *trans* effect in square planar complexes is: CO, CN^-, C_2H_4 > PR_3, H^- > CH_3^- > $C_6H_5^-$, NO_2^-, I^-, SCN^- > Br^-, Cl^- > py, NH_3, OH^-, H_2O. It should be noted that the *trans* effect is purely a kinetic phenomenon.

Of greater importance to the present study is the influence that a ligand has on the strength of the metal ligand bond *trans* to itself. *Trans* influence is a thermodynamic property of the ground state complex and can be evaluated from bond lengths. The more a bond is lengthened by the presence of a given *trans* ligand the greater the *trans* influence of that ligand is said to be. The approximate order of increasing *trans* influence in square planar complexes is: H^- > PR_3 > SCN^- > CH_3^-, CO, CN^-, I^- > Br^- > Cl^- > NH_3 > OH^-. At one time the origin and mechanism of this phenomenon was the subject of some debate [3]. The widely accepted view now though, is that the lengthening of metal–ligand bonds is caused by a disproportionate sharing of metal bonding orbitals. The ligand with the greatest *trans* influence will generally have a greater overlap with the metal orbitals and thus strengthen its bond at the expense of the bond to the ligand in the *trans* position.

The ligand series given above for the *trans* effect and *trans* influence are derived from investigations of square planar platinum(II) complexes. It is not completely clear to what extent these series apply to octahedral complexes. However, correlations with the *trans* influence series above have been observed in studies of the effect of *trans* ligands on the metal–halide and metal–hydride stretching frequencies in six co-ordinate iridium(III) complexes [5]-[8].

There are many different types of chemical reaction that take place in homogeneous catalytic cycles. Those of relevance to the present study are discussed briefly below.

Ligand Co-ordination

Addition or loss of carbon monoxide, to or from a metal centre, is an obligatory step in many homogeneous transition metal catalysed processes. Formally CO contains a triple bond: one σ and two mutually perpendicular π bonds. There is a lone pair of electrons on each atom housed in an *sp* hybrid orbital. The highest

occupied molecular orbital (HOMO) is the non-bonding sp σ orbital on carbon. The lowest unoccupied molecular orbital (LUMO) is the doubly degenerate pair of antibonding π^* orbitals, with mainly carbon $2p$ orbital character. It is this combination of frontier orbitals which allows CO to complex with transition metals and in particular be able to stabilize low oxidation states. The binding mechanism is usually explained in terms of the traditional Dewar-Chatt-Duncanson model [9, 10], Figure 1.1. This involves σ donation from the HOMO localised on carbon into vacant metal orbitals, with concomitant back-donation from occupied metal d orbitals into the vacant CO π^* orbitals. The coupling of the two bonding modes allows a synergism which can strengthen the M–CO bond; σ donation increases the electropositive nature of the CO ligand and it therefore becomes more susceptible to receiving electron density from the metal by back-donation. In this way the CO ligand is said to act as a π acid. Back-donation into CO π^* orbitals weakens the C–O bond, which results in a bond lengthening and a lowering of the stretching frequency relative to the unbound molecule.

The interaction with a transition metal modifies the reactivity of the CO molecule, in particular making it more reactive towards nucleophiles. A special case of this occurs when the nucleophile is also a co-ordinated ligand such as a hydride or an alkyl group. Intramolecular nucleophilic attack, termed migratory insertion, is an important reaction in many homogeneous processes utilising carbon monoxide.

Oxidative Addition

Transition metal complexes can act as nucleophiles, providing they are relatively electron rich and have a vacant site (or potentially vacant site). *Oxidative additions* of organic substrates to transition metal complexes are important elementary processes in catalytic applications of organic synthesis [11]. An oxidative addition is characterized by the transition-metal increasing its co-ordination number and formal oxidation state by two units, Figure 1.2a. The reverse process, termed *reductive elimination* (Figure 1.2b), is also important, producing an organic compound by the coupling of two ligands. Reductive elimination is often the final step of a catalytic cycle, yielding the desired organic product.

The most extensively studied oxidative addition reactions are those of transition metals with d^8 (e.g. Fe^0, Ru^0, Rh^I, Ir^I) or d^{10} (e.g. Ni^0, Pd^0, Pt^0) electronic configurations. The archetypal example of an organometallic nucleophile that undergoes oxidative addition is Vaska's complex, *trans*-$[Ir(CO)Cl(PPh_3)_2]$ [12, 13]. This square planar d^8 species reacts with a variety of substrates including H_2 and CH_4, polar molecules such as CH_3I, and multiply-bonded substrates such as O_2.

The oxidative addition of alkyl halides to transition metal centres has been studied extensively [14]-[24]. The majority of the experimental observations are consistent

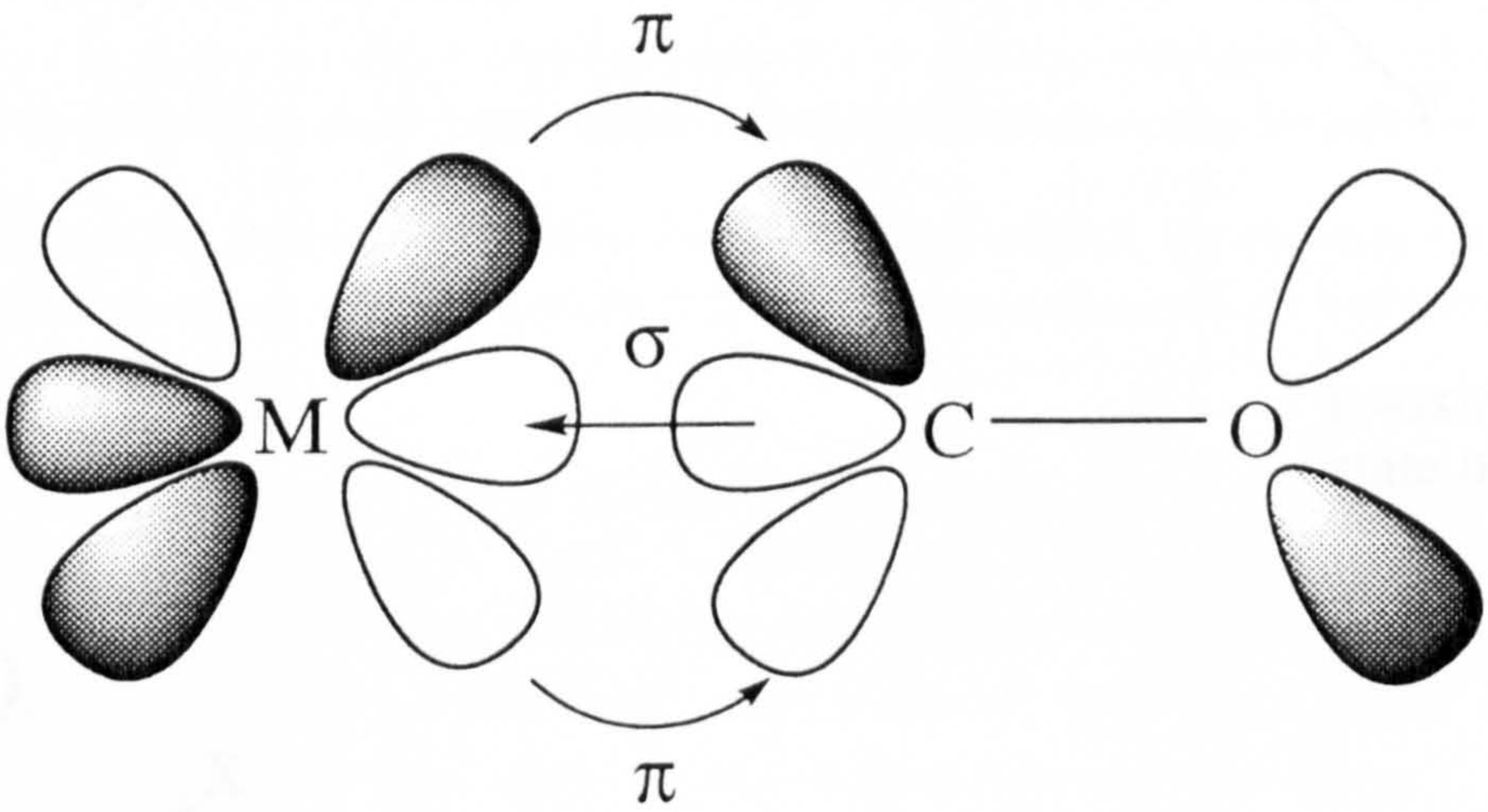

Figure 1.1: The interaction of metal and carbon monoxide orbitals in a transition metal carbonyl complex.

(a)

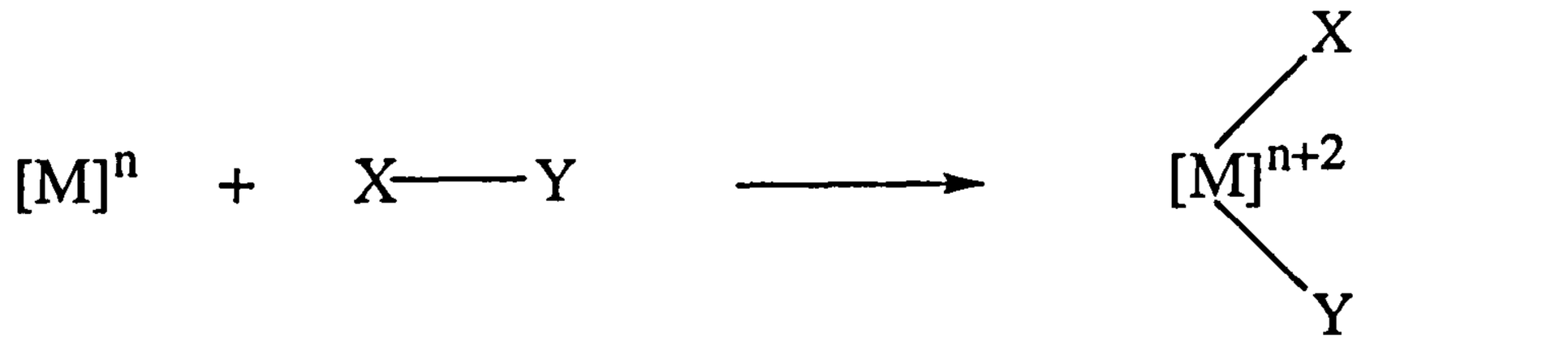

(b)

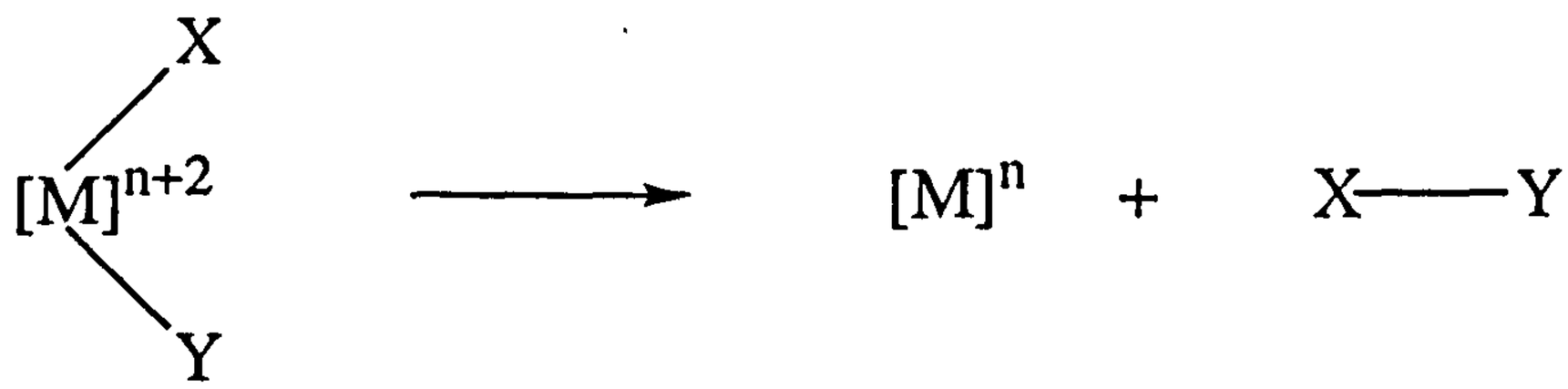

Figure 1.2: (a) Oxidative addition; (b) reductive elimination.

with an S_N2 mechanism, although alternative mechanisms such as concerted addition of the carbon-halide bond to the metal centre have been proposed. Other systems show behaviour consistent with the formation of radicals.

Several factors have been found to affect the ease of oxidative addition. In particular, it is widely believed that the reactivity of metal complexes toward organic substrates increases with the electron donating ability of the ligands [13].

Migratory Insertion

An insertion reaction is an intramolecular process in which a ligand 'inserts' itself into the mutually *cis* metal–ligand bond of one of its neighbours, Figure 1.3a. The process is more correctly termed a *migratory insertion* since ligand Y usually migrates onto ligand X rather than inserting itself directly into the M–X bond.

Carbonyl insertion processes into M–R bonds (R=H,alkyl) are key steps in many homogeneous catalytic transformations [11]. Early studies focused on the migratory insertion reaction:

$$[CH_3Mn(CO)_5] \; + \; L \; \rightarrow \; [(CH_3CO)Mn(CO)_4L], \qquad (1.1)$$

where it was established by isotopic labelling that the entering ligand occupied the position previously taken up by the alkyl, *cis* to the newly formed acyl group [25]. Thus, the reaction is an alkyl migration rather than a carbonyl insertion. The results of theoretical studies have also supported an alkyl migration mechanism in this system [26]-[28].

Kinetic studies have identified two limiting mechanisms for the migratory insertion of carbon monoxide. The first (Figure 1.3b) is a two-step mechanism where the initial product is a co-ordinatively unsaturated acyl intermediate but this rapidly takes up an external ligand to complete the co-ordination sphere of the complex [29]. The rate of this reaction can sometimes be accelerated if the solvent can act as a co-ordinating ligand [30]. In a *solvent assisted migratory insertion*, Figure 1.3c, the solvent is proposed to act as a nucleophile to form a solvated acyl intermediate, followed by rapid displacement of the solvent molecule by the incoming ligand.

The second mechanism which has been proposed is a one-step concerted process, where the ligand L attacks the metal centre with simultaneous migration of the alkyl group [31], Figure 1.3d. The actual mechanism that is observed is dependent upon the nature of the solvent and the external ligand. The present study will concentrate on the former mechanism involving the formation of a five co-ordinate intermediate.

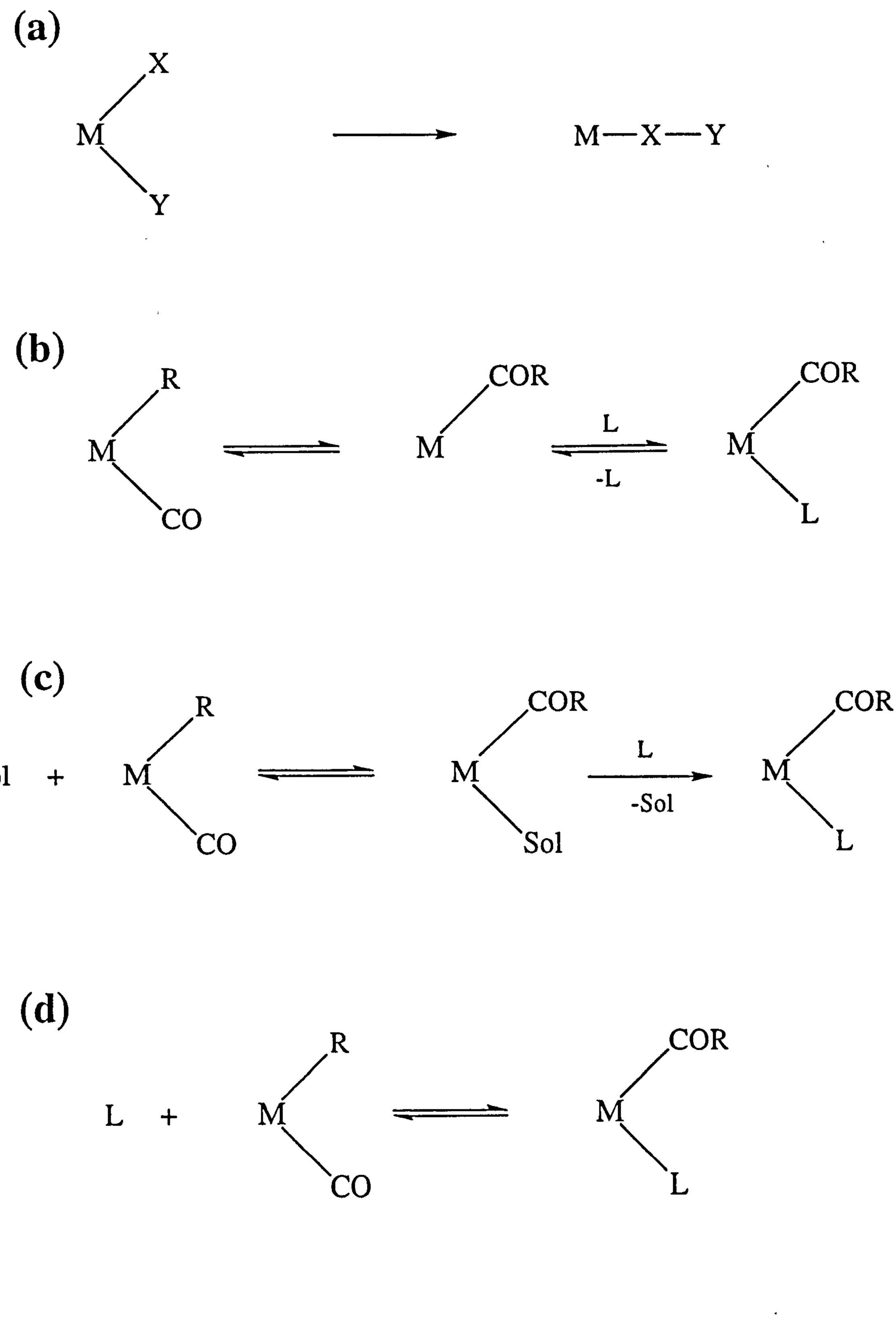

Figure 1.3: Mechanisms of migratory insertion: (a) general insertion reaction; (b) two-step migratory insertion of carbon monoxide; (c) solvent assisted migratory insertion; (d) one-step concerted migratory insertion of carbon monoxide.

1.2 Industrial Acetic Acid Production

The annual world production of acetic acid is presently greater than five million tonnes [32]. Acetyl compounds are essential intermediates in the chemical industry, used in the manufacture of paints, solvents, textiles, adhesives and pharmaceuticals. The most important commercial derivative accounting for *ca.* 50% of the world production of acetic acid is vinyl acetate which is used as a monomer or co-monomer in a variety of polymers.

The majority (*ca.* 60%) of the world manufacturing capacity for acetic acid is now based on the rhodium catalysed carbonylation of methanol. This technology has also been successfully extended to the manufacture of acetic anhydride [32]-[33] although most of the industrial capacity is still based on the dehydration of acetic acid.

1.2.1 History of Acetic Acid Manufacture

Acetic acid has been produced in relatively large quantities for more than 100 years. The oldest method for synthesizing acetic acid is by aerobic bacterial action on dilute aqueous ethanol which produces vinegar. Fermentation processes were used to produce many other organic chemicals in the early days of the chemical industry. The first major synthetic process to appear was the hydrolysis of acetylene to acetaldehyde catalysed by the mercuric ion, followed by oxidation of the acetaldehyde to acetic acid. This process dominated production for more than 40 years until the late 1950's when two new processes were developed. Celanese in the United States and British Petroleum (BP) in Europe introduced short chain-naptha oxidation using manganese or cobalt salts as the catalysts in a free radical process. The second new process, developed by Wacker Chemie, used a palladium-copper catalyst to convert ethene to acetaldehyde which was then oxidised to acetic acid using known technology.

In 1965 BASF reported a high pressure process for the carbonylation of methanol to acetic acid using an iodide-promoted cobalt catalyst [34, 35]. Despite severe operating conditions (210 °C and 700 atmospheres of CO) and poor selectivities (70% based on methanol), the process was developed commercially and practised on a large scale for a number of years.

In 1968 Paulik and Roth of the Monsanto Company announced the discovery of a low pressure methanol carbonylation using an iodide-promoted rhodium or iridium catalyst [36]. The process was developed further, culminating in the opening of a commercial plant based on the rhodium-iodide catalyst in 1970. In 1986 Monsanto sold the technology to British Petroleum who now operate acetic acid plants worldwide.

1.3 The Rhodium Catalysed Carbonylation of Methanol

The rhodium based process has several major advantages over the older cobalt technology. Operating conditions are considerably milder giving substantial savings in construction and running costs; temperatures of 150–200°C and 30–60 atmospheres carbon monoxide are typical. The rhodium process also gives significantly higher selectivities; > 99% based on methanol, > 85% based on carbon monoxide. Higher selectivity leads to easier purification making further savings. One problem associated with the modern catalytic process is that rhodium is a rare and expensive metal. However, the major disadvantage of any of these carbonylation processes is that the reaction medium is very corrosive, requiring the use of high cost materials for plant construction. Despite these difficulties, the majority of new facilities are based on this technology.

In addition to its immense industrial importance, the rhodium process has in recent years also attracted a considerable amount of academic interest. The actual reaction conditions necessary to catalyse the formation of acetic acid are far milder than the conditions employed commercially would imply. In fact, the complete cycle can be realized at room temperature and just 1 atmosphere of carbon monoxide. This allows the study of the component reactions under ambient conditions.

1.3.1 The Active Catalyst $[Rh(CO)_2I_2]^-$

It is a feature of rhodium-iodide catalysed carbonylation reactions that a wide range of soluble rhodium sources often achieve identical catalytic results. For example, rhodium(III) halides and rhodium(I) phosphine complexes yield very similar reaction rates after an initial induction period. This observation suggested that a common species was being formed under reaction conditions. Kinetic and spectroscopic studies have shown that the carbonylation of rhodium(III) halides in alcoholic [37] and aqueous media [38] leads to the formation of dicarbonyldihalorhodate(I) anions:

$$RhX_3 + 3CO + H_2O \rightarrow [Rh(CO)_2X_2]^- + H^+ + CO_2 + HX. \quad (1.2)$$

In situ high pressure infra red spectroscopy has verified that this anion is also the predominant rhodium species generated in the reaction mixture under catalytic conditions [40]. The rhodium(I) complex $[Rh(CO)_2I_2]^-$ is therefore considered to be the catalytically active species.

1.3.2 Mechanistic Studies of Rhodium Catalysed Carbonylation of Methanol

Mechanistic studies by Forster [39]-[41] and others [42]-[47] have led to the formulation of the catalytic cycle illustrated in Figure 1.4.

An interesting feature of the carbonylation reaction is that its rate is independent of methanol, acetic acid or carbon monoxide pressure over a wide range of concentrations but shows a first order dependence on both rhodium and the iodide promoter. Only the catalyst and neither the reactants or products therefore appear in the rate equation:

$$-\frac{d[CH_3OH]}{dt} = k[Rh][I]. \tag{1.3}$$

Critical to effective catalysis is the *in situ* formation of methyl iodide; this is the most important role of the iodide promoter. Reaction conditions are set to maximize the formation of hydrogen iodide which reacts with methanol to form the methyl iodide:

$$CH_3OH + HI \rightarrow CH_3I + H_2O. \tag{1.4}$$

Methyl iodide is far more susceptible to nucleophilic attack by an electron-rich metal species than methanol, and is known to react with many low-valent transition metal complexes under mild conditions [52, 53].

The first step of the catalytic cycle is oxidative addition of methyl iodide to the four co-ordinate rhodium(I) centre producing the six co-ordinate rhodium(III) complex $[CH_3Rh(CO)_2I_3]^-$. On the basis of the observed kinetic dependencies on rhodium and iodide concentrations, and the prevalence of $[Rh(CO)_2I_2]^-$ in catalyst solutions, the oxidative addition reaction has been proposed to be the rate determining step of the catalytic cycle. This is supported by the fact that activation parameters measured for the oxidative addition step [54, 15] are similar to those reported for the whole catalytic carbonylation process [39].

Direct observation of the rhodium alkyl complex resulting from oxidative addition has only recently been accomplished. Haynes *et al.* spectroscopically detected $[CH_3Rh(CO)_2I_3]^-$ during the reaction of $[Rh(CO)_2I_2]^-$ with neat methyl iodide [15]. Infra-red data indicated the alkyl intermediate to be present to the extent of *ca.* 1% of $[Rh(CO)_2I_2]^-$ under steady state conditions. The results of analysis by FTIR and low-temperature ^{13}C NMR techniques are consistent with the *fac-cis-* geometry of $[CH_3Rh(CO)_2I_3]^-$, as shown in the catalytic cycle of Figure 1.4. The structure is analogous to that of the isolable iridium complex $[CH_3Ir(CO)_2I_3]^-$ which exhibits a similar infra red spectrum indicative of this stereochemistry. X-ray determinations of the crystal structures for the re-

lated compounds $[(^nC_6H_{13})Ir(CO)_2I_3]^-$ [55] and $[CH_3Ir(CO)_2Cl_3]^-$ [56] have also revealed a preference for the *fac-cis-* geometry.

Following oxidative addition, intramolecular migratory insertion of CO yields the unsaturated rhodium acyl complex $[(COCH_3)Rh(CO)I_3]^-$. In the previous studies of the reaction of $[Rh(CO)_2I_2]^-$ with CH_3I, the only product observed was the 16-electron rhodium acyl species. A rhodium alkyl species was not observed, suggesting that migratory insertion is very rapid in this system. However, there is one other feasible explanation for this behaviour. Haynes *et al.* examined the possibility of a facile reductive elimination of CH_3I from $[CH_3Rh(CO)_2I_3]^-$, leading to a rapid pre-equilibrium step preceding a rate determining migratory insertion [15]. Both facile migratory insertion or facile reductive elimination could lead to the observed small steady-state concentration of the alkyl intermediate. On the basis of kinetic measurements it was concluded that the high reactivity of $[CH_3Rh(CO)_2I_3]^-$ was primarily due to rapid migratory insertion and that reductive elimination of CH_3I was relatively insignificant. This work provided the first quantitative measurement of the rate of the crucial C–C bond forming step in the rhodium cycle. The rate of migratory insertion observed in this system is at least an order of magnitude greater than previously reported for other unactivated metals in low polarity solvents [30, 57]. The extremely labile nature of $[CH_3Rh(CO)_2I_3]^-$ is a key factor in contributing to the high selectivity of the rhodium catalysed process.

The five co-ordinate acyl product of migratory insertion, $[(COCH_3)Rh(CO)I_3]^-$, has been isolated as its trimethylphenylammonium salt [48]. An X-ray determination showed it to be dimeric in the solid state with assymetric Rh–I–Rh bridges [58]. Co-ordination of CO to the acyl intermediate generates the octahedral 18-electron complex $[(CH_3CO)Rh(CO)_2I_3]^-$. The final step of the cycle is reductive elimination of acetyl iodide to regenerate the catalytically active species $[Rh(CO)_2I_2]^-$. The acetyl iodide is then rapidly hydrolysed to form acetic acid and regenerate HI, the co-catalyst:

$$CH_3COI + H_2O \rightarrow CH_3COOH + HI. \qquad (1.5)$$

1.3.3 Potential Side Reactions

For practical reasons associated with catalyst stability, methanol carbonylation has generally been operated in the presence of significant quantities of water. Under these conditions the rhodium catalysed water gas-shift reaction [59, 60] converts

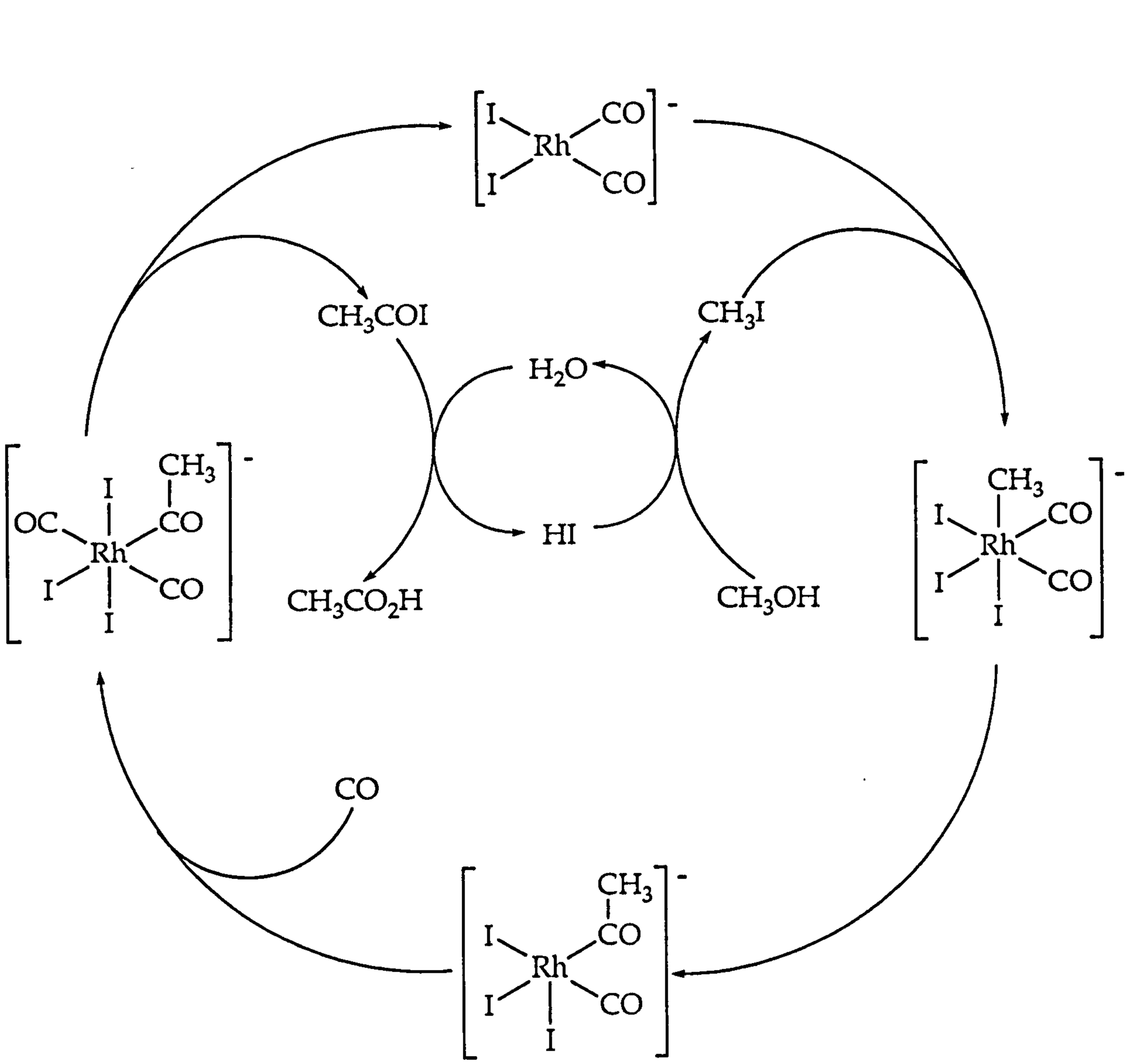

Figure 1.4: The catalytic cycle proposed for the rhodium and iodide catalysed carbonylation of methanol to acetic acid.

water and carbon monoxide to hydrogen and carbon dioxide:

$$CO + H_2O \rightleftharpoons CO_2 + H_2. \quad (1.6)$$

A mechanism has been proposed involving a redox cycle at rhodium:

$$[Rh^{I}(CO)_2I_2]^- + 2HI \rightarrow [Rh^{III}(CO)_2I_4]^- + H_2 \quad (1.7)$$

$$[Rh^{III}(CO)_2I_4]^- + H_2O + CO \rightarrow [Rh^{I}(CO)_2I_2]^- + CO_2 + 2HI. \quad (1.8)$$

In the first step $[Rh(CO)_2I_2]^-$ is oxidised by HI to generate *trans*-$[Rh(CO)_2I_4]^-$ and hydrogen. This is followed by reduction of the tetraiodide by CO and H_2O to give CO_2 and regenerate $[Rh(CO)_2I_2]^-$ and HI. Under conditions where HI exists in large quantities, the water gas-shift reaction is a potential competing reaction to methanol carbonylation. However, only small quantities of water gas shift products are ever observed. The equilibrium constant for reaction (1.4) strongly favours methyl iodide over hydrogen iodide, and the water gas-shift reaction is therefore not expected to be a significant competitor.

Other complexes related to the species known to play a direct role in the catalysis can be observed under certain conditions. For example, the *cis* isomer of $[Rh(CO)_2I_4]^-$ can be formed by oxidative addition of I_2 to $[Rh(CO)_2I_2]^-$ but only the more stable *trans* isomer has ever been observed in working catalyst solutions [49]. Another rhodium(III) species, $[Rh(CO)I_5]^{2-}$, is also well characterized. This complex is related to $[Rh(CO)_2I_4]^-$ through displacement of carbon monoxide by iodide:

$$[Rh(CO)_2I_4]^- + I^- \rightleftharpoons [Rh(CO)I_5]^{2-} + CO. \quad (1.9)$$

The equilibrium is readily established and the different species can be quantified as a function of carbon monoxide partial pressure and iodide concentration [50].

The main liquid by-product of the carbonylation process is propanoic acid, originating from the formation of ethyl iodide in the reaction vessel. Methane formation is generally not a problem in this system since the extremely short lifetime of any $Rh-CH_3$ species prevents elimination of CH_4 to any significant extent.

1.3.4 Postulated Species

Experimental studies have provided strong evidence for the existence of all the rhodium complexes discussed thus far, and indicated their significance to the overall catalytic process. Some of the complexes are stable, well characterized and can be quantified under process conditions. Others, like $[CH_3Rh(CO)_2I_3]^-$ for example, can only be detected under carefully chosen reaction conditions but not from the working process itself. Further work has indicated the existence of other species which may be involved in the cycle but have never been observed under

any conditions.

One such molecule that has received a great deal of attention is the tri-iodide species $[Rh(CO)_2I_3]^{2-}$. Early studies on the rhodium acetyl process suggested that addition of certain iodide salts promoted carbonylation rates and stabilized the catalyst system. These factors could allow the process to operate at significantly lower water concentrations leading to substantial cost reductions involved in separation of the acid product. Many groups were active in this area, in particular at Celanese [42, 61]. It has been shown that some iodide salts can react with methyl acetate[1] to form methyl iodide and the corresponding acetate salts which themselves might be effective promoters. However, an explanation favoured by the Celanese group was that iodide ions could co-ordinate with $[Rh(CO)_2I_2]^-$ to form a five co-ordinate complex, $[Rh(CO)_2I_3]^{2-}$, which would facilitate a more rapid oxidative addition with methyl iodide. The explanation for this is based upon the concept that additional electron density enhances the nucleophilicity of the metal centre. The presence of a negative charge on rhodium does appear to significantly enhance the nucleophilicity relative to neutral rhodium(I) species [51]. Hickey and Maitlis noted similar promotional effects when $\{Ph_4As^+\}\{X^-\}$ (X=Cl, I) salts were added to rhodium catalyst solutions [62]. The formation of a highly nucleophilic dianion was also proposed by these workers to explain the kinetics they observed. However, no firm spectroscopic evidence has ever been found for the presence of $[Rh(CO)_2I_3]^{2-}$, even under the most favourable reaction conditions [61].

1.4 The Iridium Catalysed Carbonylation of Methanol

Iridium complexes in conjunction with iodide promoters are also excellent alcohol carbonylation catalysts. Similar behaviour to rhodium for an iridium-iodide catalytic system was noted by Paulik and Roth in their original report of the low pressure carbonylation process [36]. Mechanistic investigations of the iridium catalysed process have been reported by Brodski *et al.* [63], Matsumoto *et al.* [64, 65], Forster [66] and by Pearson *et al.* [67, 68]. From these investigations it is clear that the iridium system resembles the rhodium system as far as the fundamental steps are concerned, though in the former case a rather more complex dependence on the reaction conditions is observed; the nature of the solvent, water concentration, iodide concentration and carbon monoxide pressure all make a significant contribution in determining which catalytic species and reaction sequences predominate.

In the early studies of the iridium system there was some debate regarding the

[1] Under process conditions methanol fed to the reactor is often largely present through the thermodynamically favourable and kinetically facile esterification as methyl acetate.

nature of the rate determining step and the predominant catalytic species. Matsumoto *et al.* [64] studied the process in the temperature range 125 to 175°C at moderate to high concentrations of iodide ($[CH_3I]/[Ir]>20$) and carbon monoxide pressures greater than 15 atmospheres. Under these conditions they concluded that the rate was first order in iridium concentration but independent of both methyl iodide concentration and carbon monoxide pressure. At lower iodide concentration or lower carbon monoxide pressure a first order dependence on methanol was observed. The different dependencies for rhodium and iridium catalysts led to the conclusion that the rate determining steps for the two systems must be different. Electrophilic attack of an iridium acyl species on methanol was proposed as the rate determining step. However, the evidence for this was based on the speculative proposal that the predominant form of iridium in the reaction medium was an iridium acyl complex.

Forster [66] conducted a detailed study of the iridium catalysed carbonylation of methanol which led to rather different conclusions to those of Matsumoto. Two catalytic cycles were proposed to be operating, depending on the reaction conditions that were invoked: the "neutral" cycle involving only neutral carbonyl iodide species; the "anionic" cycle involving anionic iridium species. The principal factor controlling the choice of the cycle is the ionic iodide concentration. In the present study we concentrate on the anionic cycle which generally predominates under regimes of moderate to high levels of ionic iodide. A catalytic cycle for the anionic process as proposed by Forster is illustrated in Figure 1.5. The scheme was elucidated from kinetic observations, *in situ* spectroscopic measurements and by studies of the observable intermediates. A competitive water gas-shift reaction was also reported as in the case of the rhodium system, but this is described elsewhere [36]. Comparison of the catalytic cycles for rhodium and iridium in Figures 1.4 and 1.5, reveals that the component reactions are very similar. The main difference is in the relative reaction rates of the corresponding steps. Furthermore, the iridium cycle explicitly involves the participation of ionic iodide.

Oxidative addition of methyl iodide to the iridium(I) nucleophile $[Ir(CO)_2I_2]^-$ is rapid. High pressure infra red studies showed that the main species present in the iridium system was the iridium(III) complex $[CH_3Ir(CO)_2I_3]^-$. Carbonylation rates were found to increase with increasing carbon monoxide pressure but decrease with increasing levels of ionic iodide. From these observations Forster proposed that the rate determining step of the anionic cycle was migratory insertion in $[CH_3Ir(CO)_2I_3]^-$, after initial replacement of an iodide ligand by carbon monoxide [66]. Supporting evidence for this proposal is that $[CH_3Ir(CO)_2I_3]^-$ can be converted into $[(CH_3CO)Ir(CO)_2I_3]^-$ when a pressure of carbon monoxide is applied at 80–100°C but no acyl species is observed in the absence of carbon monoxide. Moreover, the addition of large excesses of iodide can prevent this transformation from occurring, irrespective of the carbon monoxide pressure. Dissociative sub-

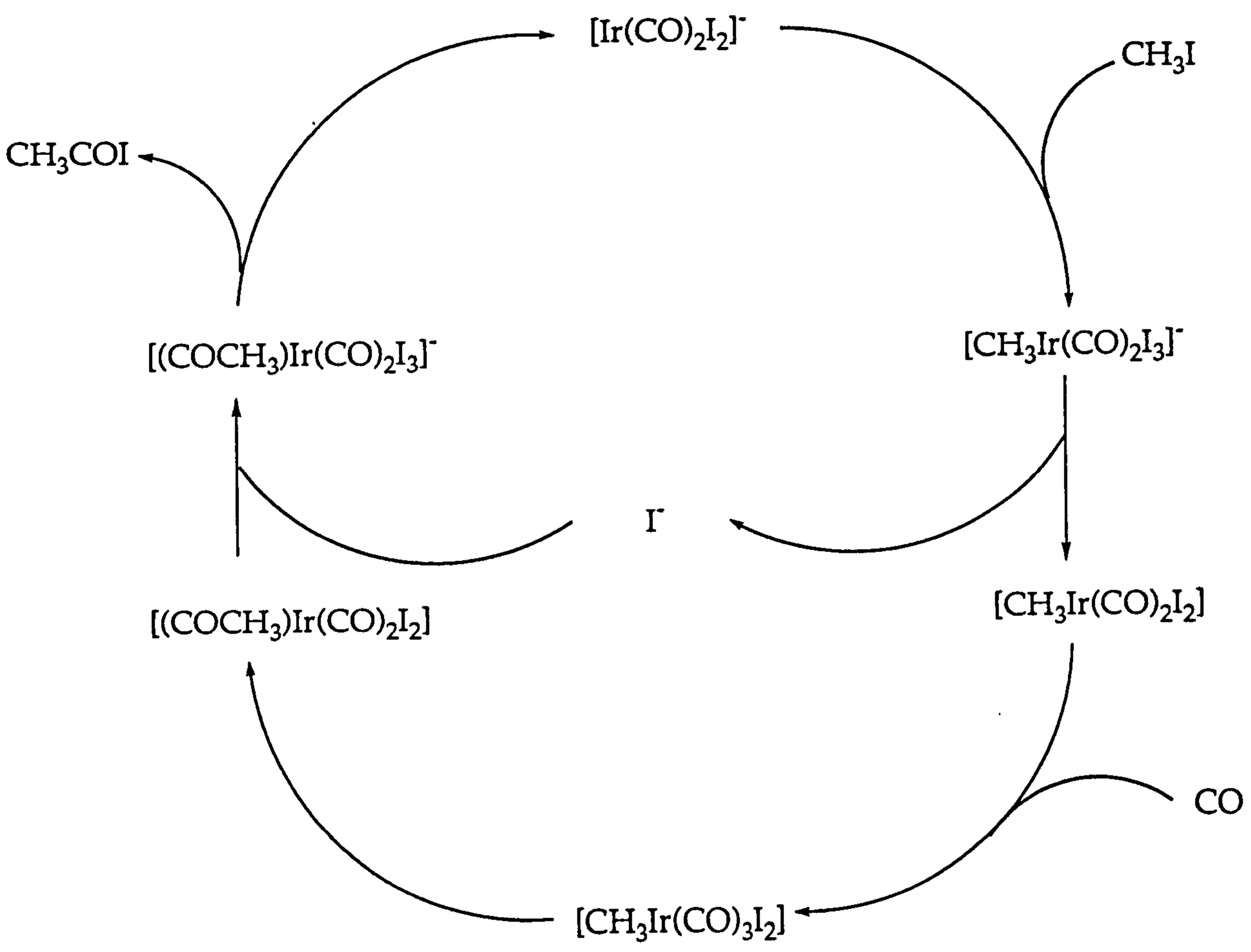

Figure 1.5: The "anionic" catalytic cycle for the iridium and iodide catalysed carbonylation of methanol to acetic acid.

stitution of an iodide ligand in $[CH_3Ir(CO)_2I_3]^-$ to form the neutral tricarbonyl $[CH_3Ir(CO)_3I_2]$ was expected to contribute significantly to the rate determining step. $[CH_3Ir(CO)_3I_2]$ has never been observed, either in working catalyst solutions or in model reactions, leading to the suggestion that once formed migratory insertion in this complex is fast. These observations are in marked contrast to the rhodium system, where rate determining oxidative addition is followed by rapid migratory insertion, even in the absence of carbon monoxide pressure. The differences in the rates of the individual steps catalysed by rhodium and iridium species can probably be related to the greater strength of iridium–carbon bonds [55].

The most recent mechanistic investigation of iridium catalysed carbonylation has been carried out by Pearson *et al.* [67, 68]. In general, the observations from this study are consistent with the schemes proposed by Forster. However, carbonylation of $[CH_3Ir(CO)_2I_3]^-$ to form the acyl complex $[(CH_3CO)Ir(CO)_2I_3]^-$ was observed to proceed by two different mechanisms. In neat chlorobenzene, kinetic studies and stereochemical analysis of the products suggested that migratory insertion was occurring directly in the anion $[CH_3Ir(CO)_2I_3]^-$, and also in the neutral species $[CH_3Ir(CO)_3I_2]$ after initial dissociation of an iodide ligand in the way Forster described. On addition of iodide to the reaction mixture, the stereochemistry of the products suggested that the iodide dissociation pathway had been suppressed and that migratory insertion in the anion was the only mechanism operating.

An interesting effect on iridium migratory insertion was observed upon the addition of small quantities of methanol. The reaction was dramatically accelerated giving activation parameters which were quite different from those measured in neat chlorobenzene. Similar effects were noted upon the addition of the Lewis acid SnI_2.

1.5 Computational Chemistry

This introductory chapter has given a description of the chemistry involved in the rhodium and iridium catalysed carbonylations of methanol. Mechanistic studies of model reactions using a variety of analytical techniques supported by information obtained from direct observation of the working process, have yielded a fairly good understanding of the catalytic system. The efficiency of the working process has benefited greatly from these studies and there is a continuing programme of experimental research in this area. As in many homogeneous processes though, the presence of certain unobservable species does not allow for a full understanding through experimental studies alone.

Quantum mechanical techniques offer an alternative approach to the investigation of catalytic processes. In the last decade *ab initio* Molecular Orbital (MO) methods

and Density Functional Theory (DFT) have been successfully introduced for the study of elementary steps of catalytic cycles [69]. It is the aim of the present study to use these methods to develop a deeper understanding of the rhodium and iridium catalysed processes for methanol carbonylation. Although not quite making the impact that some of the reported successes would suggest they deserve, future studies into the viability of potential catalytic systems may be carried out initially by theoretical methods, without the need for invoking expensive experimental conditions. Certainly, it is the hope of every theoretician in this area that their work might lead to the suggestion of new experiments to perform. Some of the capabilities of modern theoretical methods and their advantages and limitations in practical use are discussed below.

In a theoretical approach, the properties of all relevant species can be studied, including the normally inaccessible transition states and reactive intermediates. Molecular structures can be optimized and in the case of equilibrium complexes compared directly with experiment, for example with an X-ray crystal structure if this is available. The harmonic vibrational frequencies of the optimized structures can be evaluated and likewise compared to the measured spectroscopic data. In this way, theory can aid experiment in the characterization of molecular species.

The optimization of transition state structures can provide an insight into the complex molecular interactions that take place in chemical reactions. Moreover, if one can locate the transition state it is usually straightforward to compute a reaction pathway from which the mechanism of a given reaction step can be inferred. The calculated energies of the reactant molecules and of the transition state give an estimate of the activation energy for a chemical reaction. From a knowledge of the stationary points and the reaction pathways that link them, a general picture of the potential energy surface for a chemical process can be constructed. The effect of variables, such as the choice of central metal atom or the type of ligands employed, can be tested once the key features of the potential energy surface have been characterized. The existence and potential significance of hypothetical molecules which have never been observed in catalyst solutions can be investigated by theoretical methods.

The processor time that is required to perform a given calculation is the crucial limiting factor in any theoretical investigation. Without this constraint, many of the chemical problems would already have been solved quite precisely by theoretical methods. The greater the number of atoms or molecules that have to be computed, the greater is the time required for the calculation. *Ab initio* and DFT calculations scale at least with the third power of the system size. Hence, at the present time only relatively small molecular systems may be investigated. Practical calculations on systems involving transition metals and other heavy atoms have only become commonplace since the advent of the Effective Core Potential (ECP). In the ECP or pseudopotential approximation, the system size is dra-

matically reduced by replacing the chemically uninteresting core electrons by an effective potential which mimics the shielding effect of the core shells and provides an effective field in which the valence electrons move. This approach is particularly attractive for the computation of third-row transition elements since the ECP may be adapted to include some relativistic corrections.

The results of theoretical calculations are not always guaranteed to be accurate or to coincide with experimental observations. In the simplest of approaches, calculations are performed on hypothetical motionless molecules *in vacuo* – conditions that are only likely to be encountered in outer space at zero Kelvin. It is an encouraging fact though, that laboratory conditions used to conduct mechanistic studies are also rather different from the reaction conditions employed in the working industrial process. The modelling of limited (electrostatic) solvent effects is possible through the use of continuum models in reaction field theory. More advanced theories, which give an improved treatment of the solvent-solute boundary have still not found widespread application. Discrete representations of solvent, in which solvent molecules participate directly in the reaction mechanism, by for example co-ordination to an active site or through hydrogen bonding interactions, are difficult to implement because in general a large number of solvent molecules have to be explicitly treated. The size of system that can be considered also usually precludes the calculation of absolute reaction rates.

In spite of their limitations, chemical calculations have obvious advantages over bench research. A single calculation can give a remarkable amount of information in comparison to what chemists might expect from similar research using experimental techniques. If a calculation predicts behaviour that is not observed experimentally, it may be an indication that entropy or solvent effects are controlling the reaction or that another mechanism is operative.

The majority of the results presented in this thesis are derived from *ab initio* calculations[2] for which there is a vast amount of experience in their use at hand. The Hartree-Fock (HF) or Self-Consistent Field (SCF) method is the simplest such *ab initio* technique. A mean-field approach to electron repulsion is employed to obtain a unique set of optimal molecular orbitals. An attractive feature of the method is that it offers a readily interpretable orbital picture of the electronic structure of a molecule. For quantitative results in studies of organometallic systems however, it is usually necessary to go beyond the Hartree-Fock approximation and include *electron correlation.*

The application of theory to organometallic systems has proven to be a rather

[2]In this work we define *ab initio* methods as those that do not require experimental information and are based on a conventional Molecular Orbital approach; for example, we use this term in reference to the HF and MP2 methods. Density Functional Theory is considered separate to this formalism since experimental parameters are generally used in the construction of the exchange-correlation functional, and the density is the basic variable (see Chapter 2).

more difficult exercise than in, for example, the area of organic chemistry where theory has provided a wealth of excellent quantitative information. The bonding in organometallic species is much 'softer' and there are a considerably greater number of electrons to deal with. The electronic energy levels of transition metal complexes are generally very close together which can render even a qualitative treatment of reaction energetics rather difficult to perform. The so called 'near-degeneracy' effect continues to be one of the greatest problems in the description of the electronic structure and reactivity of transition metal species. Correlated methods such as multi-reference or perturbation techniques which make some allowance for individual electron-electron interactions are required to give an adequate description of these systems. There is however, an additional expense associated with the use of such methods and they also lack the simple orbital picture provided by the HF approach. Therefore the understanding may come from a HF calculation whereas the higher accuracy for the quantitative data is achieved using a correlation treatment without trying to interpret this improvement too closely.

A secondary aim of this project was to assess the performance of modern Density Functional Theory (DFT) in comparison to the conventional *ab initio* techniques with respect to computations of the Monsanto catalytic cycle. In the DFT formalism the energy is sought as a (formally unknown but existing) *functional* of the electron density. Progress in the development of this methodology depends primarily on finding sufficiently accurate approximations to the exchange–correlation potentials of atoms and molecules in the form of analytical expressions for the density functionals. A variety of functionals are now available to choose from, ranging from the local approximation which utilises the results for a uniform electron gas to more sophisticated schemes which attempt to account for inhomogenity by applying gradient corrections to the electron density. The popularity of approximate DFT stems largely from its computational expedience which should make it amenable to large molecular systems at a reduced cost to the processor times required for correlated *ab initio* calculations. Preliminary indications are that this method can provide estimates for the properties of strongly bound ground state molecules which are in very good agreement with experiment. Calculations of the organometallic species and the reactions involved in homogeneously catalysed processes should provide a rigorous testing ground for the appraisal of modern density functionals and of the DFT formalism in general.

This work presents the results of *ab initio* and DFT calculations on the rhodium and iridium species and reactions of key significance to the Monsanto acetic acid synthesis. A brief guide to the presentation of this thesis is as follows. Chapter 2 reviews the formal theory behind the *ab initio* and DFT methodologies. A description of the ECP approach to molecular computations involving heavy atoms is also given. The methods employed for optimizing and characterizing molecules and reaction pathways are discussed in Chapter 3, along with various other computa-

tional details that require a mention. Chapter 4 presents the results of calculations performed on the small molecules and equilibrium complexes known to play a role in the catalytic cycle. The emphasis in this chapter is on the accuracy of the different techniques in determining the ground state properties of the transition metal complexes, such as the geometrical structure and carbonyl ligand vibrational frequencies. Chapters 5 and 6 present the results of principal importance to this work, namely the results of calculations carried out on the oxidative addition and migratory insertion steps of the catalytic cycles. The final chapter summarizes the main results obtained and presents the concluding remarks.

Chapter 2

Theoretical Background

This chapter presents a review of the theoretical concepts behind the widely employed quantum chemistry methods, *ab initio* molecular orbital theory and density functional theory. The effective core potential approximation which facilitates the calculation of the electronic structure of heavy atoms is also discussed.

2.1 Ab initio Molecular Orbital Theory

2.1.1 The Schrödinger Equation

The structure and properties of a stationary molecular system comprising of M nuclei and N electrons can be determined in principle by solution of the non-relativistic time-independent Schrödinger equation [70]:

$$\hat{H}\Psi(\mathbf{x}_1, \mathbf{x}_2, \ldots, \mathbf{x}_N; \mathbf{y}_1, \mathbf{y}_2, \ldots, \mathbf{y}_M) = E\Psi(\mathbf{x}_1, \mathbf{x}_2, \ldots, \mathbf{x}_N; \mathbf{y}_1, \mathbf{y}_2, \ldots, \mathbf{y}_M). \quad (2.1)$$

$\mathbf{x}_i$ is shorthand notation representing the space-spin co-ordinates of electron i (x_i, y_i, z_i, s_i) and $\mathbf{y}_A$ represents the space-spin co-ordinates of nucleus A. $\hat{H}$ is called the Hamiltonian operator or simply the "Hamiltonian". Equation (2.1) is a differential eigenvalue equation which can only be solved exactly for very simple systems, namely atoms or molecules which have only one electron. Application of the Schrödinger equation to larger systems of interest therefore depends upon the introduction of approximations. E is the total energy of the system, the so-called eigenvalue of equation (2.1) and Ψ is the required function, the wavefunction, which will be defined later.

In atomic units[1][71] the Hamiltonian for a system comprising of N electrons and

[1]Atomic units are employed throughout this chapter: the length unit is the Bohr radius

M nuclei in the absence of any perturbing fields is defined by

$$\begin{aligned}\hat{H} &= -\sum_{i=1}^{N}\frac{1}{2}\nabla_i^2 - \sum_{A=1}^{M}\frac{1}{2M_A}\nabla_A^2 - \sum_{i=1}^{N}\sum_{A=1}^{M}\frac{Z_A}{r_{iA}}, \\ &+ \sum_{i=1}^{N}\sum_{j>i}^{N}\frac{1}{r_{ij}} + \sum_{A=1}^{M}\sum_{B>A}^{M}\frac{Z_A Z_B}{R_{AB}}. \end{aligned} \tag{2.2}$$

M_A is the ratio of the mass of the nucleus A to the mass of an electron, Z_A is the atomic number of nucleus A and the Laplacian operators ∇_i^2 and ∇_A^2 involve differentiation with respect to the i^{th} electron and A^{th} nucleus, respectively. The first two terms in the molecular Hamiltonian, are the operators for the kinetic energy of the electrons and nuclei, respectively; the third term represents attraction between the electrons and nuclei; the last two terms define the inter-electron and inter-nuclear repulsions, respectively.

The first of several approximations in seeking a solution to the Schrödinger equation, is to separate nuclear and electronic motions. The Born-Oppenheimer or "clamped nuclei" approximation [72] is based upon the fact that nuclei are very much heavier than electrons (for first row atoms, $m_N \simeq 10,000 m_e$). The mass difference means that we can assume electrons adjust their positions with respect to the nuclei almost instantaneously which allows the problem to be reformulated in terms of a static nuclear system without introducing any significant error. Within this approximation, the kinetic energy of the nuclei can be ignored and the inter-nuclear repulsion treated as a constant. An *electronic* Hamiltonian for electrons moving in a field due to fixed nuclei can therefore be constructed as

$$\hat{H}_{elec} = \sum_{i=1}^{N}\hat{h}(i) + \sum_{j>i}^{N}\hat{g}(i,j) + V_{nuc}, \tag{2.3}$$

where $\hat{h}(i)$ is the one-electron Hamiltonian incorporating both kinetic and potential energy terms which operate on the co-ordinates of electron i:

$$\hat{h}(i) = -\frac{1}{2}\nabla_i^2 - \sum_{A=1}^{M}\frac{Z_A}{r_{iA}}, \tag{2.4}$$

and $\hat{g}(i,j)$ is the two-electron component of the Hamiltonian representing the coulombic repulsion between electrons i and j:

$$\hat{g}(i,j) = \frac{1}{r_{ij}}. \tag{2.5}$$

The final term in equation (2.3), V_{nuc}, is the constant inter-nuclear repulsion.

---

a_0(=0.5292 Å), the charge unit is the charge of the electron, e, and the mass unit is the mass of the electron, m_e.

Using this non-relativistic Born-Oppenheimer Hamiltonian, the time-independent Schrödinger equation (2.1) can be simplified to

$$\hat{H}_{elec}\Psi_{elec}(\mathbf{x}_1, \mathbf{x}_2, \ldots, \mathbf{x}_N) = E_{elec}\Psi_{elec}(\mathbf{x}_1, \mathbf{x}_2, \ldots, \mathbf{x}_N), \tag{2.6}$$

where the nuclear co-ordinates have now been omitted from the definition of the wavefunction. The electronic energy E_{elec} is the energy of the N electrons moving in the field due to the fixed nuclei. It depends explicitly on the electronic co-ordinates but only parametrically on the nuclear co-ordinates, as does the electronic wavefunction. The total energy of the system is the sum of the electronic energy and the constant nuclear repulsion which can be added on completion of the electronic problem:

$$E_{tot} = E_{elec} + \sum_{A=1}^{M} \sum_{B>A}^{M} \frac{Z_A Z_B}{R_{AB}}. \tag{2.7}$$

The potential energy surface for a molecular system can be interpolated from a series of calculations of the electronic structure, each corresponding to a different set of fixed nuclear co-ordinates. From now on we drop the subscript "elec" and concentrate solely on the electronic problem.

2.1.2 The Orbital Model

Having applied the Born-Oppenheimer approximation we can proceed to model the system of interest, that is attempt to describe the details of the electron distribution. These are contained in the *molecular electronic wavefunction* Ψ, which is defined with the interpretation that

$$|\ \Psi(\mathbf{x}_1, \mathbf{x}_2, \ldots, \mathbf{x}_N)\ |^2\ d\mathbf{x}_1 d\mathbf{x}_2 \ldots d\mathbf{x}_N \tag{2.8}$$

is the probability of simultaneously finding electrons 1, 2,..., N occupying volume elements $d\mathbf{x}_1$, $d\mathbf{x}_2$,..., $d\mathbf{x}_N$. The function $|\ \Psi(\mathbf{x}_1, \mathbf{x}_2, \ldots, \mathbf{x}_N)\ |^2$ is therefore the probability density for the electron distribution in a $4N$-dimensional space. All knowledge of the properties of the N-electron system are contained within the molecular electronic wavefunction.

We wish to find approximate solutions to the Schrödinger equation for systems comprising of more than one electron. The usual approach is to introduce "model" approximations which consist of making simplifying assumptions about the nature of the physical system under investigation. Mathematically, this means restricting the form of any function with which to approximate the molecular wavefunction. The simplest model is to assume that each electron has its own independent distribution which is generated by its motion in the field of the static nuclei. By neglecting the two-electron repulsion terms in equation (2.3), the Hamiltonian for

a system of N non-interacting electrons can be written

$$\hat{H}' = \sum_{i=1}^{N} \hat{h}(i). \tag{2.9}$$

This yields the modified, independent particle, Schrödinger equation:

$$\hat{H}\Psi = \left(\sum_{i=1}^{N} \hat{h}(i)\right) \Psi = E\Psi. \tag{2.10}$$

The operator $\hat{h}(i)$ has a set of eigenfunctions which are solutions to a set of one-electron equations:

$$\hat{h}(i)\chi_j(\mathbf{x}_i) = \varepsilon_j \chi_j(\mathbf{x}_i) \tag{2.11}$$

Each χ_i is a one-electron wavefunction or more commonly, is referred to as an *orbital.* It is easy to verify by direct substitution into equation (2.10) that the required eigenfunctions and eigenvalues of the N electron problem are

$$\Psi_{HP}(\mathbf{x}_1, \mathbf{x}_2, \ldots, \mathbf{x}_N) = \chi_i(\mathbf{x}_1)\chi_j(\mathbf{x}_2)\ldots\chi_k(\mathbf{x}_N), \tag{2.12}$$

and

$$E = \varepsilon_i + \varepsilon_j + \ldots + \varepsilon_k. \tag{2.13}$$

Thus, the independent particle model leads to a many-electron wavefunction which is simply the product of the orbitals describing each electron and a total energy which is just the sum of the orbital energies. The many-electron wavefunction obtained in this way is called a *Hartree-product.* Approximation methods which assign individual electrons to one-electron functions, which are themselves solutions to some effective one-electron Schrödinger equation, constitute an orbital model for the description of molecular electronic structure. However, the simple Hartree-product is not a valid wavefunction. For the model to be complete, the wavefunction must adhere to certain conditions such that approximate solutions obtained from the Schrödinger equation are physically acceptable.

An important requirement is the need for the wavefunction to satisfy the Pauli antisymmetry principle [73], which states that the model function must be anti-symmetric with respect to the interchange of the co-ordinates of any two electrons:

$$\Psi(\mathbf{x}_1, \ldots, \mathbf{x}_i, \mathbf{x}_j, \ldots, \mathbf{x}_N) = -\Psi(\mathbf{x}_1, \ldots, \mathbf{x}_j, \mathbf{x}_i, \ldots, \mathbf{x}_N). \tag{2.14}$$

Since electrons are 'indistinguishable' the probability density $|\ \Psi\ |^2$ defined in equation (2.8), does not change either its sign or value when any number of the electrons interchange their co-ordinates. Two further properties of any particular solution Ψ_n, are usually either satisfied or enforced. The wavefunction must generate a distribution such that the N electrons are wholly contained within the $4N$-dimensional space. This can be ensured by insisting that the wavefunction is

normalized:

$$\int \Psi_n^* \Psi_n d\tau = 1. \tag{2.15}$$

Secondly, the wavefunction must be orthogonal to all other solutions of the associated Schrödinger equation:

$$\int \Psi_n^* \Psi_m d\tau = 0. \tag{2.16}$$

The integration is carried out in each case over all space where $d\tau$ is the shorthand notation for a volume element incorporating integration over all space-spin coordinates.

Imposition of the Pauli antisymmetry principle can be realized by writing, instead of a simple product, an antisymmetrised product. Many-electron wavefunctions can be expressed in terms of linear combinations of antisymmetrised products of molecular orbitals. These are conveniently represented mathematically by Slater determinants [74, 75]. For example, the wavefunction for an N-electron system may be approximated as a single determinant:

$$\Psi(\mathbf{x}_1, \mathbf{x}_2, \ldots, \mathbf{x}_N) = \frac{1}{\sqrt{N!}} \begin{vmatrix} \chi_i(\mathbf{x}_1) & \chi_j(\mathbf{x}_1) & \cdots & \chi_k(\mathbf{x}_1) \\ \chi_i(\mathbf{x}_2) & \chi_j(\mathbf{x}_2) & \cdots & \chi_k(\mathbf{x}_2) \\ \vdots & \vdots & \cdots & \vdots \\ \chi_i(\mathbf{x}_N) & \chi_j(\mathbf{x}_N) & \cdots & \chi_k(\mathbf{x}_N) \end{vmatrix} \tag{2.17}$$

where the first term is the normalization factor and the $\chi_i(\mathbf{x})$ are spin orbitals defined by:

$$\chi_i(\mathbf{x}) = \psi(\mathbf{r})\alpha(s) \qquad or \qquad \chi_i(\mathbf{x}) = \psi(\mathbf{r})\beta(s). \tag{2.18}$$

A spin orbital is the wavefunction of a single electron which describes both its spatial distribution and its spin. The spin factors are added to the definition of an orbital to differentiate between electrons having spin angular momenta of $+\frac{1}{2}$ (α) and $-\frac{1}{2}$ (β). Given a set of K spatial orbitals $\{\psi_i | i = 1, 2, \ldots, K\}$, one can thus form a set of $2K$ spin orbitals $\{\chi_i | i = 1, 2, \ldots, 2K\}$ as

$$\chi_{2i-1}(\mathbf{x}) = \psi_i(\mathbf{r})\alpha(s) \tag{2.19}$$

$$\chi_{2i}(\mathbf{x}) = \psi_i(\mathbf{r})\beta(s). \tag{2.20}$$

In general, the many-electron wavefunction will be expressed as a linear combination of determinants which represent different configurations of the spin orbitals:

$$\Psi = \sum_i D_i \Psi_i = D_0\Psi_0 + D_1\Psi_1 + D_2\Psi_2 + \ldots, \tag{2.21}$$

where the Ψ_i functions are the determinants and the D_i are coefficients which define the contribution of state i to the overall wavefunction.

The requirement for the wavefunction to be anti-symmetric is accounted for by the determinant representation, since the interchange of any two rows or columns will result in the desired sign change. Moreover, the wavefunction vanishes if any two columns in the determinant are the same. Thus, the antisymmetry requirement immediately leads to the statement of the Pauli exclusion principle, namely that more than one electron cannot occupy the same spin orbital.

2.1.3 The Variation Principle

Having specified the model orbital approximation for the many electron wavefunction, the problem is now reduced to finding a set of optimum spin orbitals χ_i or a set of optimum expansion coefficients D_i. Central to modern computational techniques for executing this task is the variation principle which is described below.

In practice, approximate solutions are sought to

$$\hat{H}\Psi_0 = E_0\Psi_0, \tag{2.22}$$

where we have dropped the space-spin co-ordinates for brevity and use the zero subscript to denote ground state solutions for the energy and wavefunction. Multiplying the above equation from the left hand side by Ψ_0^* and integrating leads to an expression for the exact ground state energy:

$$E_0[\Psi_0] = \frac{\int \Psi_0^* \hat{H} \Psi_0 d\tau}{\int \Psi_0^* \Psi_0 d\tau}. \tag{2.23}$$

The square brackets denote that Ψ_0 determines E_0; we say that the energy is a *functional* of the wavefunction. If Ψ_0 is now replaced by any approximate function $\tilde{\Psi}$, such as that provided by a Slater determinant, then *the value of the approximate energy $\tilde{E}$ is an upper bound to the exact ground state energy*:

$$\tilde{E}[\tilde{\Psi}] = \frac{\int \tilde{\Psi}^* \hat{H} \tilde{\Psi} d\tau}{\int \tilde{\Psi}^* \tilde{\Psi} d\tau} \geq E_0. \tag{2.24}$$

The equality holds only when $\tilde{\Psi}$ is identical to Ψ_0.

This important result suggests a practical procedure for the optimization of any trial molecular wavefunction, and in particular, the orbital model wavefunction, equation (2.21), introduced in the previous section. The approximate model wavefunction $\tilde{\Psi}$ is substituted into the variational expression (2.24) and adjusted until a minimum is found in the energy. It is important to note that the values of the adjustable parameters at the minimum define the best possible wavefunction of that particular functional form. This means that the variation principle can only yield, at best, a molecular electronic distribution which is consistent with the limitations of the model wavefunction employed.

For normalized functions the energy expression is reduced to just the numerator of equation (2.23). This can be written more compactly in Dirac bra-ket notation [76] as

$$E_0 = \langle \Psi_0 | \hat{H} | \Psi_0 \rangle, \tag{2.25}$$

and is called the *expectation value* of the energy.

2.1.4 The Hartree-Fock Approximation

As stated previously, analytical solutions to the time-independent Schrödinger equation (2.1) are only possible for systems comprising of a single electron. The problem for N-electron systems is complicated primarily by the repulsion term $\frac{1}{r_{ij}}$ in the Hamiltonian (2.3), which mixes the co-ordinates of electrons i and j and results in the Schrödinger equation becoming a $3N$-dimensional non-separable differential equation. The Hartree-Fock approximation, which is equivalent to the molecular orbital approximation is central to quantum calculations [77, 78]. The approximation is also the starting point for more accurate *ab initio* techniques which include the effects of electron correlation. The essence of the Hartree-Fock approximation is to replace the complicated many-electron problem by a one-electron problem, in which the electron-electron repulsion is treated in an *average* way. In this section we summarize the main results obtained in a derivation of the Hartree-Fock equations.

The Hartree-Fock approximation is a special case of the general orbital model in which the many-electron wavefunction is approximated as a *single determinant of spin orbitals.* A determinantal wavefunction equivalent to that in equation (2.17) can be written in abbreviated form including just its diagonal elements:

$$|\Psi_{HF}\rangle = |\chi_1 \chi_2 \cdots \chi_i \cdots \chi_j \cdots \chi_N\rangle \tag{2.26}$$

The principle aim is to determine the optimum set of spin orbitals which give the best possible approximation to the exact N-electron wavefunction within the constraints of the model. Given that the spin orbitals are orthonormal:

$$\int \chi_i^*(\mathbf{x}_1)\chi_j(\mathbf{x}_1)d\mathbf{x}_1 = \delta_{ij} = \begin{cases} 1 & \text{if } i = j \\ 0 & \text{otherwise} \end{cases} \tag{2.27}$$

the determinant wavefunction (2.26) can be substituted into the variational expression (2.24) to give the energy expectation value:

$$\begin{aligned} E_{HF} &= \langle \Psi_{HF} | \hat{H} | \Psi_{HF} \rangle \\ &= \sum_i^N h_{ii} + \frac{1}{2} \sum_{ij}^N J_{ij} - K_{ij}, \end{aligned} \tag{2.28}$$

The terms in summations may be written more fully as:

$$h_{ii} = \int \chi_i^*(\mathbf{x}_1)\hat{h}\chi_i(\mathbf{x}_1)d\mathbf{x}_1, \tag{2.29}$$

$$J_{ij} = \int\int \chi_i^*(\mathbf{x}_1)\chi_j^*(\mathbf{x}_2)\frac{1}{r_{12}}\chi_i(\mathbf{x}_1)\chi_j(\mathbf{x}_2)d\mathbf{x}_1 d\mathbf{x}_2, \tag{2.30}$$

$$K_{ij} = \int\int \chi_i^*(\mathbf{x}_1)\chi_j^*(\mathbf{x}_2)\frac{1}{r_{12}}\chi_j(\mathbf{x}_1)\chi_i(\mathbf{x}_2)d\mathbf{x}_1 d\mathbf{x}_2. \tag{2.31}$$

The terms given by equation (2.29), are the one-electron energies; the kinetic energy and nuclear attraction energy of an electron occupying orbital χ_i. The first of the two-electron terms J_{ij}, is called the *coulomb* term, representing the classical electrostatic repulsion energy between the charge distributions of electrons in orbitals χ_i and χ_j. The *exchange* integrals, K_{ij}, do not have a convenient classical interpretation but arise naturally as a consequence of imposing the antisymmetry principle. The two-electron terms have the important property:

$$J_{ii} = K_{ii} \tag{2.32}$$

which can be interpreted as an exact cancellation of the "self-repulsion"; the diagonal J_{ii} terms represent the spurious situation of an electron in an orbital χ_i interacting with itself. The equality is the reason why the double summation in equation (2.28) can include the $i = j$ terms. The self-interaction of electrons which is dealt with so neatly and exactly in Hartree-Fock theory is an important problem in Density Functional Theory (section 2.2.4).

Associated with the interpretation of the two-electron integrals (2.30) and (2.31), it is convenient to introduce the corresponding (one-electron) coulomb and exchange operators. They are defined by their effect when operating on a spin orbital $\chi_i(1)$:

$$\hat{J}_j(1)\chi_i(1) = \left[\int \chi_j^*(2)\frac{1}{r_{12}}\chi_j(2)d\mathbf{x}_2\right]\chi_i(1), \tag{2.33}$$

$$\hat{K}_j(1)\chi_i(1) = \left[\int \chi_j^*(2)\frac{1}{r_{12}}\chi_i(2)d\mathbf{x}_2\right]\chi_j(1). \tag{2.34}$$

The coulomb operator represents the average local potential at $\mathbf{x}_1$ arising from an electron (2) in χ_j. Operating with $\hat{K}_j(1)$ on $\chi_i(1)$ involves an "exchange" of electron (1) and electron (2). Unlike the coulomb operator, the exchange operator is said to be non-local since the result of operating on $\chi_i(1)$ depends on the value of χ_i throughout all spaces, not just at some point $\mathbf{x}_1$ as is evident from the integrand in equation (2.34).

To derive the Hartree-Fock equations we must minimize the energy expression (2.28) with respect to the component spin orbitals, that is, we wish to find the determinant which satisfies the stationary principle:

$$\delta E_{HF}[\chi] = 0. \tag{2.35}$$

It is necessary to restate equation (2.35) in a way that ensures that the spin orbitals remain orthonormal throughout the minimization procedure. This can be achieved by Lagranges's method of undetermined multipliers. Minimization of $E_{HF}[\chi]$ subject to the orthonormalization constraint (2.27) is equivalent to making stationary without constraint the quantity

$$E[\chi] - \sum_{ij}^{N} \varepsilon_{ji}((\chi_i|\chi_j)) - \delta_{ij}). \tag{2.36}$$

The new stationary principle incorporating the orthogonality constraints can therefore be written

$$\delta \left\{ E_{HF}[\chi] - \sum_{ij}^{N} \varepsilon_{ji}\langle\chi_i|\chi_j\rangle \right\}, \tag{2.37}$$

where the ε_{ji} are a set of Lagrange multipliers. This follows directly from equation (2.36) since the variation in a constant (δ_{ij}) is zero. By performing the appropriate expansion for the Hartree-Fock energy (2.28) and using the definitions of the Coulomb and Exchange operators given in equations (2.33) and (2.34), it can be shown that the stationary principle leads to the following expression for the spin orbitals

$$\hat{f}(1)\chi_i(1) = \sum_{j}^{N} \varepsilon_{ji}\chi_j(1). \tag{2.38}$$

$\hat{f}(1)$ is an effective one-electron operator called the Fock operator:

$$\hat{f}(1) = \hat{h}(1) + \sum_{j}^{N} \hat{J}_j(1) - \hat{K}_j(1) \tag{2.39}$$

$$= \hat{h}(1) + \hat{v}^{HF}(1) \tag{2.40}$$

$$\tag{2.41}$$

The first term is the usual core Hamiltonian incorporating the effects of the kinetic energy and nuclear attraction. The second term is called the effective Hartree-Fock potential $\hat{v}^{HF}(1)$, defined such that the effects of the two-electron repulsion contributions generated by operators of the form $\hat{g}(i,j)$ in the full Hamiltonian are treated in an average manner. More concisely, $\hat{v}^{HF}(1)$ is the average potential experienced by electron (1) due to the presence of all the other electrons.

An important property of the determinant wavefunction is that a unitary transformation of the set of occupied orbitals χ to another set of orbitals χ' leaves the wavefunction unchanged, except possibly by an inconsequential phase factor. In addition, it can be shown that the sum of the coulomb and exchange operators are also invariant to such a transformation. The matrix of Lagrange multipliers ε is Hermitian and it is always possible to find a unitary matrix which diagonalizes it.

That is to say, if we let

$$\chi_i' = \sum_j \chi_j U_{ji}, \tag{2.42}$$

where $\mathbf{U}$ is a unitary matrix ($\mathbf{U}^\dagger\mathbf{U} = \mathbf{1}$) which diagonalizes ε:

$$\varepsilon' = \mathbf{U}^\dagger \varepsilon \mathbf{U}, \tag{2.43}$$

then equation (2.38) becomes:

$$\hat{f}(1)\chi_i'(1) = \varepsilon_{ii}'\chi_i'(1). \tag{2.44}$$

The unique set of spin orbitals (χ') which satisfy these equations are known as the canonical Hartree-Fock orbitals. Dropping the primes, the canonical Hartree-Fock equations can be written in their standard eigenvalue form:

$$\hat{f}(1)\chi_i(\mathbf{x}_1) = \varepsilon_i\chi_i(\mathbf{x}_1). \tag{2.45}$$

The Fock operator has a functional dependence on the spin orbitals through the coulomb and exchange operators. The Hartree-Fock equations are therefore a set of coupled nonlinear equations and will need to be solved by iterative procedures.

In principle, there are an infinite number of solutions to the canonical Hartree-Fock equations. Multiplying equation (2.45) by χ_i^* and integrating, one obtains the formula for the orbital energies. In particular the energies for the occupied orbitals are given by

$$\varepsilon_i = h_{ii} + \sum_j^N J_{ij} - K_{ij} \qquad i = 1, 2, \ldots, N \tag{2.46}$$

with an equivalent expression defining the unoccupied, or virtual orbitals except that there are an infinite number of them. The sum of the ε_i for each of the N electrons in the ground state is:

$$\sum_i^N \varepsilon_i = \sum_i^N h_{ii} + \sum_{ij}^N J_{ij} - K_{ij}. \tag{2.47}$$

Comparing this equation with the Hartree-Fock ground state energy given by (2.28), it is evident that

$$E_{HF} \neq \sum_i^N \varepsilon_i. \tag{2.48}$$

Thus the sum of the occupied orbital energies is not equal to the total ground state energy. A physical interpretation for the Hartree-Fock orbital energies was provided by Koopmans [79]. Stated simply, the orbital energies provide a means of estimating ionization energies and electron affinities. The theorem assumes that no reorganization on ionization or attachment takes place and the lowest

energy single-determinantal description for the ion is the determinant built from the canonical Hartree-Fock orbitals. One then finds (approximately) that

$$\mathrm{IE} = -\varepsilon_c, \tag{2.49}$$

where IE represents the ionization energy associated with removing an electron from the spin orbital χ_c. Similarly, the electron affinity for adding an electron to a virtual spin orbital χ_r is

$$\mathrm{EA} = -\varepsilon_r. \tag{2.50}$$

The frozen orbital approximation tends to produce ionization potentials which are too positive and electron affinities which are too negative. In addition to this, removal and attachment processes are both correlated phenomena and it is necessary to go beyond the Hartree-Fock level in order to produce further corrections to the results obtained by Koopmans' theorem.

The major part of this thesis is concerned with the calculation of molecular systems which have even numbers of electrons in closed-shell configurations. The electronic structure for closed-shell systems can be calculated by the restricted Hartree-Fock method (RHF) which assigns each pair of electrons to a spatial orbital ψ_i, and the spin dependence does not enter into the mathematics explicitly. In essence this restricts our discussion to closed-shell ground states. It can be shown that the ground state energy for a determinant of $N/2$ doubly occupied spatial orbitals is given by

$$E_{RHF} = 2\sum_{i}^{\frac{N}{2}} h_{ii} + \sum_{ij}^{\frac{N}{2}} 2J_{ij} - K_{ij}, \tag{2.51}$$

where the spatial integrals are defined in an analogous way to those given by equations (2.29) to (2.31), except, of course, the χ_i are replaced by ψ_i and the spin dependence in the electron co-ordinates is omitted. The RHF equations are simply:

$$\hat{f}(1)\psi_i(\mathbf{r}_1) = \varepsilon_i\psi_i(\mathbf{r}_1). \tag{2.52}$$

When the number of electrons is odd, or the system is in an unpaired excited-state configuration, the standard Hartree-Fock scheme employed is the unrestricted Hartree-Fock method (UHF) [80].

2.1.5 The Roothaan-Hall Equations

Most molecules have complex shapes and symmetries, and it is not possible to write down a simple functional form for the molecular orbitals. The only way to calculate molecular orbitals in quantum theory is to expand them in terms of a set of known functions. The usual approach is to expand the molecular orbitals in terms of atomic orbitals (or approximations to them) of the constituent atoms.

This approximation is commonly known as the Linear Combination of Atomic Orbitals to form Molecular Orbitals method or simply as the LCAO method. Each molecular orbital is expanded in terms of a finite set of *basis functions* $\{\phi_\mu\}$:

$$\psi_i = \sum_{\mu=1}^{K} C_{\mu i}\phi_\mu \qquad i = 1, 2, \ldots, K \tag{2.53}$$

The two most common sets of functions employed for this expansion are Gaussian-type functions (GTFs):

$$\phi_\mu(\mathbf{r}) = x^l y^m z^n e^{-\alpha_\mu r^2} \tag{2.54}$$

and Slater-type orbitals (STOs):

$$\phi_\mu(\mathbf{r}) = x^l y^m z^n e^{-\zeta_\mu r} \tag{2.55}$$

where l, m and n are integers and r is a radial distance. The variables α and ζ are the orbital exponents which determine the diffuseness or size of the basis function; a low exponent indicates a large diffuse orbital and a high exponent indicates a compact orbital close to the nucleus. GTFs are usually the preferred choice of *primitive functions* as they are more convenient to deal with mathematically. They have the important advantage that all integrals in the computations can be separated into analytically solvable forms without recourse to numerical integration. In practice though, the basis functions used to expand the molecular orbitals are a set of STOs, which themselves have been expanded in terms of a set of GTFs:

$$\phi_\mu(\zeta) = \sum_j D_{\mu j}\eta_j(\alpha_j) \tag{2.56}$$

Basis functions constructed in this way are called contracted Gaussians. Using the LCAO formalism the desirable functional form of Slater orbitals is retained, whilst exploiting the computational expedience of Gaussians.

By performing an LCAO expansion of the type (2.53) for the spatial orbitals, it can be shown that the integro-differential equation (2.52) is transformed to a set of algebraic equations which are solvable by standard matrix techniques. Using this approximation, the solution of the Schrödinger equation is reduced to the problem of optimizing the molecular orbitals through variation of the expansion coefficients $C_{\mu i}$. The algebraic equations necessary to do this were derived independently for the closed-shell wavefunction by Roothaan [81] and Hall [82]. The Roothaan-Hall equations for the molecular orbital expansion coefficients are

$$\sum_{\nu=1}^{K} F_{\mu\nu}C_{\nu i} = \varepsilon_i \sum_{\nu=1}^{K} S_{\mu\nu}C_{\nu i} \qquad i = 1, 2, \ldots, K \tag{2.57}$$

where K is the total number of basis functions used in the expansion. The equa-

tions can be written more compactly in their equivalent matrix form:

$$\mathbf{FC} = \mathbf{SC}\varepsilon. \tag{2.58}$$

Here, ε is a diagonal matrix of the orbital energies ε_i. $\mathbf{C}$ is a $K \times K$ square matrix of the expansion coefficients $C_{\mu i}$, the optimum values of which we wish to obtain. The overlap matrix $\mathbf{S}$, is a $K \times K$ Hermitian matrix with elements given by

$$S_{\mu\nu} = \int \phi_\mu^*(1)\phi_\nu(1)d\mathbf{r}_1. \tag{2.59}$$

The Fock matrix $\mathbf{F}$, is a $K \times K$ Hermitian matrix representing the fock operator $\hat{f}$ in the basis $\{\phi_\mu\}$. Its elements are defined as follows:

$$\begin{aligned} F_{\mu\nu} &= \int \phi_\mu^*(1)\hat{f}(1)\phi_\nu(1)d\mathbf{r}_1, \\ F_{\mu\nu} &= H_{\mu\nu}^{core} + \sum_{\lambda\sigma}^{K} P_{\lambda\sigma}[(\mu\nu \mid \lambda\sigma) - \frac{1}{2}(\mu\lambda \mid \nu\sigma)]. \end{aligned} \tag{2.60}$$

The matrix elements $H_{\mu\nu}^{core}$ represent the energy of a single electron in the field of the bare nuclei:

$$H_{\mu\nu}^{core} = \int \phi_\mu^* \hat{h}(1)\phi_\nu d\mathbf{r}_1, \tag{2.61}$$

where the core operator $\hat{h}(1)$ contains the one-electron kinetic energy and nuclear attraction terms as defined in equation (2.4).

The $P_{\lambda\sigma}$ terms are elements of the density matrix or the charge-density bond-order matrix $\mathbf{P}$, which for a closed-shell system are defined by

$$P_{\lambda\sigma} = 2\sum_{i}^{\frac{N}{2}} C_{\lambda i}C_{\sigma i}^*. \tag{2.62}$$

In matrix notation this is

$$\mathbf{P} = 2\mathbf{C}\mathbf{C}^\dagger. \tag{2.63}$$

The total charge density of the system is simply the sum of the individual probability distribution functions for each electron:

$$\rho(\mathbf{r}) = 2\sum_{i}^{\frac{N}{2}} \psi_i^*(\mathbf{r})\psi_i(\mathbf{r}), \tag{2.64}$$

which integrated yields the total number of electrons:

$$\int \rho(\mathbf{r})d\mathbf{r} = 2\sum_{i}^{\frac{N}{2}} \int |\psi_i(\mathbf{r})|^2 = 2\sum_{i}^{\frac{N}{2}} 1 = N. \tag{2.65}$$

Substituting the molecular orbital expansion into equation (2.64) for the ψ_i we

obtain the relationship between the charge density and the density matrix:

$$\rho(\mathbf{r}) = \sum_{\lambda\sigma} P_{\lambda\sigma}\phi_\lambda(\mathbf{r})\phi^*_\sigma(\mathbf{r}) \tag{2.66}$$

Thus, the density matrix **P** specifies completely the charge density of the system in terms of the known basis functions.

The quantities $(\mu\nu \mid \lambda\sigma)$ appearing in the summation of (2.60) denote two-electron repulsion integrals:

$$(\mu\nu \mid \lambda\sigma) = \int\int \phi^*_\mu(1)\phi_\nu(1)\frac{1}{r_{12}}\phi^*_\lambda(2)\phi_\sigma(2)d\mathbf{r}_1 d\mathbf{r}_2 \tag{2.67}$$

Because of their large number, the evaluation and manipulation of these two-electron integrals is the major difficulty in a Hartree-Fock calculation.

The overlap matrix is included in the Roothaan-Hall equations since the basis functions, although assumed to be normalized and linearly independent, are not in general orthogonal to each other. If the overlap matrix can in some way be eliminated from equation (2.58), then the orbital coefficients and eigenvalues could be obtained by just diagonalizing the Fock matrix. The most efficient procedure for orthogonalizing the basis is to obtain a transformation matrix **X**, which generates a new coefficient matrix **C′**:

$$\mathbf{C}' = \mathbf{X}^{-1}\mathbf{C} \qquad \mathbf{C} = \mathbf{X}\mathbf{C}' \tag{2.68}$$

and has the property whereby

$$\mathbf{X}^\dagger\mathbf{S}\mathbf{X} = 1. \tag{2.69}$$

This can be accomplished, for example, by setting $\mathbf{X}=\mathbf{S}^{-1/2}$. Substituting $\mathbf{C}=\mathbf{X}\mathbf{C}'$ into equation (2.58) and multiplying from the left by $\mathbf{X}^\dagger$ gives

$$(\mathbf{X}^\dagger\mathbf{F}\mathbf{X})\mathbf{C}' = (\mathbf{X}^\dagger\mathbf{S}\mathbf{X})\mathbf{C}'\varepsilon. \tag{2.70}$$

If we define a new Fock matrix **F′** by

$$\mathbf{F}' = \mathbf{X}^\dagger\mathbf{F}\mathbf{X}, \tag{2.71}$$

and use equation (2.69) then

$$\mathbf{F}'\mathbf{C}' = \mathbf{C}'\varepsilon. \tag{2.72}$$

These are the transformed Roothaan-Hall matrix equations, which can be solved for **C′** by diagonalizing **F′**, providing of course that **F** is known. Given **C′**, then **C** can be obtained from (2.68).

2.1.6 The Self-Consistent Field Method

Having established the final algebraic form of the equations which can yield the orbital coefficients, the problem left outstanding is how to solve them for the optimum orbital coefficients. The Fock matrix depends on the density matrix, or equivalently on the expansion coefficients:

$$\mathbf{F} = \mathbf{F(P)} \qquad \mathbf{F} = \mathbf{F(C)} \tag{2.73}$$

The Roothaan-Hall equations are therefore non-linear and their solution is necessarily an iterative process. The procedure employed to do this is called the *Self-Consistent Field* (SCF) method. At convergence, the energy is at a minimum and the orbitals regenerate a field, which in turn produces a set of orbitals which are insignificantly changed. At this point the orbitals are said to be self-consistent and are accepted as a solution to the problem.

A general SCF procedure is as follows:

(i) Specify a molecular system and a basis set $\{\phi_\mu\}$.

(ii) Evaluate the integrals, $S_{\mu\nu}$ (2.59), $H_{\mu\nu}^{core}$ (2.61) and $(\mu\nu \mid \lambda\sigma)$ (2.67).

(iii) Diagonalize the overlap matrix **S** and obtain a transformation matrix **X**.

(iv) Guess the density matrix **P**.

(v) Assemble the Fock matrix **F** from the elements of $\mathbf{H}^{core}$, **P** and the two-electron integrals $(\mu\nu|\lambda\sigma)$ according to equation (2.60).

(vi) Calculate the transformed Fock matrix $\mathbf{F}' = \mathbf{X}^\dagger\mathbf{F}\mathbf{X}$.

(vii) Diagonalize $\mathbf{F}'$ to obtain $\mathbf{C}'$ and ϵ.

(viii) Calculate $\mathbf{C}=\mathbf{X}\mathbf{C}'$.

(ix) Construct a new density matrix **P** from **C** using equation (2.62).

(x) Determine whether the SCF procedure has converged. For example, is the new density matrix the same as the previous density matrix to within a specified criterion? If the procedure has not converged the next iteration is performed by returning to step (v) and recalculating the Fock matrix from the new density.

Once the convergence criteria are met, the resultant solutions, represented by **C**, **P**, **F**, etc., are used to calculate expectation values and other quantities of interest. For example, substituting the basis set expansion (2.53) into equation (2.51) leads

to the expression:

$$E_{RHF} = \sum_{\mu\nu} P_{\mu\nu} H^{core}_{\mu\nu} + \frac{1}{2} \sum_{\mu\nu\lambda\sigma} P_{\mu\nu} P_{\lambda\sigma} [(\mu\nu|\lambda\sigma) - \frac{1}{2}(\mu\lambda|\nu\sigma)] \quad (2.74)$$

$$= \frac{1}{2} \sum_{\mu\nu} P_{\mu\nu} (H^{core}_{\mu\nu} + F_{\mu\nu}), \quad (2.75)$$

which provides a convenient means of calculating the energy at any stage during the SCF procedure.

Within the framework of the Hartree-Fock approximation, each electron "sees" all the other electrons as an average distribution. Instantaneous inter-electron repulsion, or *electron correlation*, is not accounted for in the single determinant model. Neglecting electron correlation has in many cases proven to be a reasonable approximation. The ground states of most organic molecules, for example, receive an adequate description by this treatment. Nevertheless, it should be recognised that exact wavefunctions cannot generally be expressed as single determinants and there are a number of frequently quoted examples to illustrate this point. Of relevance to the present study is the failure of the HF scheme to yield quantitative results for transition metals, which require a correlated description of near-degenerate energy levels, and for transition states, which require a correlated description of partially broken bonds. Thus, in this work, where we examine transition metal–transition states some correction for correlation will necessarily be required.

In molecular orbital theory there is a general hierarchy of techniques which increase in complexity toward the exact solution of the Schrödinger equation. Any *ab initio* method which goes beyond the HF approximation in attempting to treat electron repulsion in a more exact way is known as a *post-HF method.* These methods are primarily concerned with obtaining the correlation energy. This is defined as the difference between the exact non-relativistic energy of the system and the Hartree-Fock energy obtained in the limit that the basis set approaches completeness:

$$E_{corr} = E_{exact} - E_{HF} \quad (2.76)$$

In the following sections, we briefly outline two such methods that address this problem.

2.1.7 Configuration Interaction

The logical and most straightforward improvement to the Hartree-Fock procedure is to include more than one N-electron function in the description of the molecular wavefunction. Recall that the many-electron wavefunction can be expanded as a

linear combination of Slater determinants:

$$\Psi = \sum_i D_i \Psi_i = D_0\Psi_0 + D_1\Psi_1 + D_2\Psi_2 + \ldots, \tag{2.77}$$

A full expansion including all possible determinantal configurations yields a total wavefunction which is exact within the limits of a finite basis. This approach is called full configuration interaction (CI) but is rarely applied in practice due to the enormous number of configurations which must be computed. Given a set of K basis functions, the number of unique determinantal configurations that can be generated is $(2K!)/[N!(2K-N)!]$, which is clearly beyond the capabilities of modern computer systems for all but the simplest molecules.

A more common approach is to truncate the expansion to include only certain configurations. For example, CISD [83] includes only singly- and doubly-excited configurations which are constructed from a reference ground state HF wavefunction:

$$\Psi_{CISD} = D_0\Psi_0 + \sum_{ra} D_a^r \Psi_a^r + \sum_{b>a,s>r} D_{ab}^{rs}\Psi_{ab}^{rs}. \tag{2.78}$$

Here, Ψ_a^r denotes excitation of an electron in the reference wavefunction Ψ_0, from an occupied to a virtual spin orbital, $\chi_a \rightarrow \chi_r$. Similarly, the second term Ψ_{ab}^{rs}, represents a configuration incorporating simultaneous excitation of two electrons in the reference wavefunction. The full wavefunction is constructed from several of these determinants and their relative contributions are determined by solving for the coefficients using a variational procedure. Note that singly excited determinants do not contribute directly to the correlation energy because the matrix elements $\langle\Psi_0|\hat{H}|\Psi_a^r\rangle$ are all equal to zero. This important result is referred to as Brillouin's theorem [84].

A related method, which has found widespread use in the calculation of transition metals, is the multi-configurational SCF method (MCSCF) [85]. In this approach a subset of configurations of the full expansion (2.77) are used, selecting those deemed to be of chemical importance:

$$\Psi_{MCSCF} = \sum_i^m D_i \Psi_i. \tag{2.79}$$

For example, in the case of transition metals one would include those states which contribute most to the near-degeneracy. This method differs from conventional CI, principally in that both the expansion coefficients (D_i) and the orbitals contained in the Ψ_i are optimized.

Truncated CI methods provide a rigorous variational treatment of molecular electronic structure. There are, however, a number of drawbacks associated with their use. Firstly they are still rather costly on computer resources. Secondly, and perhaps of greater importance in certain applications, is that they are not *size-*

consistent. That is, the energies calculated by these schemes do not vary linearly with the number of particles (n) in the limit $n \rightarrow \infty$. For example, in the special case of a supermolecule formed from n closed-shell non-interacting monomers, a size-consistent scheme yields a supermolecule energy which is just n times the monomer energy. If this condition is not satisfied, then clearly the calculated relative energies of interacting molecules may also be in error. This discrepancy can be partly resolved by applying a numerical correction to the energy, such as that provided by Davidson for the CISD energy [86]:

$$\Delta E_{Davidson} = (1 - D_0^2) E_{CISD}, \tag{2.80}$$

where E_{CISD} is the correlation energy at the CISD level and D_0 is the coefficient of the Hartree-Fock function in the CISD expansion. However, this is still a rather crude approximation and a more reliable approach to the calculation of relative reaction energies, for example, is to employ a fully size-consistent method such as a coupled-pair or perturbation theory. Pair theories [87, 88] express the total correlation energy as a sum of interaction energies between electron pairs. Some of the highest quality *ab initio* results obtained have been derived from calculations based on this methodology. However, these methods are prohibitively expensive for large systems such as those involving transition metal complexes. In this work we use Møller-Plesset theory [89] which is an example of a perturbational approach to the calculation of correlation energies.

2.1.8 Møller-Plesset Perturbation Theory

Møller-Plesset calculations add higher excitations to the Hartree-Fock wavefunction as a non-variational correction, drawing upon the technique known as many-body perturbation theory.

The starting point in perturbation theory, are the known ground- ($i = 0$) and excited-state ($i \geq 1$) solutions corresponding to a well-defined unperturbed Hamiltonian, $\hat{H}_0$, defined by:

$$\hat{H}_0 \Psi_i^{(0)} = E_i^{(0)} \Psi_i^{(0)}. \tag{2.81}$$

In practice though, approximate solutions, incorporating say the effects of electron correlation, are sought to some general Schrödinger equation:

$$\hat{H} \Phi_i = \mathcal{E}_i \Phi_i. \tag{2.82}$$

where the $\mathcal{E}_i$ and Φ_i are the exact (but unknown) eigenvalues and eigenfunctions of a general N-electron system. Perturbation theory assumes a generalised Hamiltonian which can be divided into two parts: a zeroth-order part, $\hat{H}_0$, which has known eigenfunctions and eigenvalues defined by equation (2.81), and a perturba-

tion, $\hat{V}$, into which all the additional effects not accounted for by the zeroth-order component are absorbed. The generalised Hamiltonian may be written as

$$\hat{H} = \hat{H}_0 + \lambda\hat{V}, \tag{2.83}$$

where λ is a dimensionless ordering parameter included for mathematical reasons. The central assumption of Rayleigh-Schrödinger perturbation theory [90] is that if the perturbation $\hat{V}$ is small in comparison to $\hat{H}_0$, then the exact energy and wavefunction can be expanded as a power series in the parameter λ according to:

$$\Phi_i = \Psi_i^{(0)} + \lambda\Psi_i^{(1)} + \lambda^2\Psi_i^{(2)} + \ldots \tag{2.84}$$

$$\mathcal{E}_i = E_i^{(0)} + \lambda E_i^{(1)} + \lambda^2 E_i^{(2)} + \ldots \tag{2.85}$$

The terms $\Psi_i^{(n)}$ and $E_i^{(n)}$ are called the nth-order corrections to the wavefunction and energy, respectively. By substituting (2.84) and (2.85) into the general Schrödinger equation (2.82) and equating like powers of λ, expressions for the unknown corrections can be obtained in terms of the known zeroth-order solutions. Assuming that the $\Psi_i^{(0)}$ are orthonormal, the leading terms in the energy expansion (for the ground state) are given by

$$E_0^{(0)} = \langle\Psi_0^{(0)} \mid \hat{H}_0 \mid \Psi_0^{(0)}\rangle, \tag{2.86}$$

$$E_0^{(1)} = \langle\Psi_0^{(0)} \mid \hat{V} \mid \Psi_0^{(0)}\rangle, \tag{2.87}$$

$$E_0^{(2)} = \sum_{k=1}^{\infty} \frac{|\langle\Psi_0^{(0)} \mid \hat{V} \mid \Psi_k^{(0)}\rangle|^2}{E_0^{(0)} - E_k^{(0)}}. \tag{2.88}$$

Practical correlation methods may now be considered by identifying suitable choices for the zeroth and perturbed systems.

In Møller-Plesset theory, the zeroth-order Hamiltonian $\hat{H}_0$ is taken to be the sum of one-electron Fock operators:

$$\hat{H}_0 = \sum \hat{f}(i) = \sum_i \left[\hat{h}(i) + \hat{v}^{HF}(i)\right]. \tag{2.89}$$

It follows that the zeroth-order wavefunction is a single determinant of spin orbitals and the corresponding energy is simply the sum of the Hartree-Fock orbital energies:

$$E_0^{(0)} = \sum_i \varepsilon_i. \tag{2.90}$$

The perturbation is given by the difference between the full Hamiltonian and the Hartree-Fock Hamiltonian:

$$\begin{aligned} \hat{V} &= \hat{H} - \hat{H}_0, \\ &= \sum_{i<j}^{N} r_{ij}^{-1} - \sum_i v^{HF}(i), \end{aligned} \tag{2.91}$$

that is, the difference between the exact two-electron repulsion and the average one-electron Hartree-Fock repulsion. The first-order energy correction can now be evaluated by substituting the above expression for $\hat{V}$ into equation (2.87):

$$\begin{aligned} E_0^{(1)} &= \langle \Psi_0^{(0)} \mid \hat{H} \mid \Psi_0^{(0)} \rangle - \langle \Psi_0^{(0)} \mid \hat{H}_0 \mid \Psi_0^{(0)} \rangle, \\ &= E_{HF} - \sum_i \varepsilon_i. \end{aligned} \tag{2.92}$$

Rearranging and using (2.90) leads to the important result that the Hartree-Fock energy is the sum of the zeroth and first-order energies:

$$E_{HF} = E^{(0)} + E^{(1)}. \tag{2.93}$$

Thus the first non-zero correction to the Hartree-Fock energy occurs in the second order of perturbation theory.

The general expression for the second-order energy (2.88) involves a sum of integrals over zeroth-order excited state wavefunctions. The problem that remains is deciding which states to include in this summation. States which include single excitations are all zero:

$$\begin{aligned} \langle \Psi_0^{(0)} | \hat{V} | \Psi_a^r \rangle &= \langle \Psi_0^{(0)} | \hat{H} - \hat{H}_0 | \Psi_a^r \rangle \\ &= \langle \Psi_0^{(0)} | \hat{H} | \Psi_a^r \rangle - f_{ar} = 0. \end{aligned} \tag{2.94}$$

The first term vanishes because of Brillouin's theorem and the second because the spin orbitals are eigenfunctions of the Fock operator. In addition, determinants with triple and higher substitutions do not mix with the HF reference state because of the two-electron nature of the perturbation. This only leaves double excitations Ψ_{ab}^{rs}, and the second-order energy correction is given by:

$$\begin{aligned} E_0^{(2)} &= \sum_{a<b} \sum_{r<s} \frac{| \langle \Psi_0^{(0)} \mid \sum_{i<j} r_{ij}^{-1} \mid \Psi_{ab}^{rs} \rangle |^2}{\varepsilon_a + \varepsilon_b - \varepsilon_r - \varepsilon_s} \\ &= \sum_{a<b} \sum_{r<s} \frac{| \langle ab||rs \rangle |^2}{\varepsilon_a + \varepsilon_b - \varepsilon_r - \varepsilon_s}. \end{aligned} \tag{2.95}$$

The quantity $\langle ab||rs \rangle$ is a two-electron integral over spin orbitals, defined by

$$\langle ab||rs \rangle = \int \int \chi_a^*(1)\chi_b^*(2) \left(\frac{1}{r_{12}}\right) [\chi_r(1)\chi_s(2) - \chi_s(1)\chi_r(2)] \, dx_1 dx_2. \tag{2.96}$$

Expressions for contributions to the correlation energy from higher terms can also be derived but in the present study we generally only consider energies calculated up to the second-order of Møller-Plesset perturbation theory, which is referred to as MP2. Equation (2.95) for the MP2 energy probably represents the simplest approximate expression for the correlation energy. The major computational task involved, is a transformation of two-electron integrals over basis functions, equa-

tion (2.67), into the corresponsing integrals over the Hartree-Fock spin orbitals. Energies calculated at the MP2 level are size-consistent, as are all higher-order Møller-Plesset expansions; in this respect, the perturbation expressions are more satisfactory than the CISD method for determining correlation energies. However, unlike truncated CI, perturbation theory results are not variational and the total electronic energy obtained using them can be lower than the true energy.

2.2 Density Functional Theory

Density functional theory (DFT) is a relatively old theory, dating back to the early work of Thomas [91], Fermi [92, 93], Dirac [94], and Wigner [95] in the 1920's and 1930's. Molecular calculations based on this methodology did not, however, emerge before the late 1960's and have only recently found widespread appeal through a number of innovative implementations which parallel the familiar concepts of *ab initio* computational techniques. There is increasing evidence that modern DFT offers a promising alternative to the conventional *ab initio* approach. It includes electron correlation in a form that does not lead to the excessive computational requirements of post-HF methods. More importantly, perhaps, is the fact that molecular properties derived from DFT methods, such as equilibrium geometries, vibrational frequencies and atomisation energies, often attain accuracies comparable to or even better than those from *ab initio* methods [96]-[99].

Revived interest in methods which seek to express the energy of an electronic system in terms of the density has largely been due to the ground-breaking work of Hohenberg, Kohn and Sham. In 1964, Hohenberg and Kohn [100] provided the formal proof that the ground state energy of an electronic system is uniquely defined by its density. This was closely followed by the introduction of a set of one-electron Hartree-Fock-like equations by Kohn and Sham [101], from which the exact electron density and thus the exact electronic energy could in principle be obtained. The Kohn-Sham equations have served as a starting point for new approximations, and the majority of modern DFT implementations are now based on this formalism.

2.2.1 The Hohenberg Kohn Theorem

Following Hohenberg and Kohn, consider an N-electron system moving in an external potential, $v(\mathbf{r})$, provided by a set of M nuclei. The electronic Hamiltonian can be written

$$\hat{H} = \hat{T} + \hat{V}_{ne} + \hat{V}_{ee}, \tag{2.97}$$

where $\hat{T}$ is the kinetic energy operator, $\hat{V}_{ee}$ is the inter-electron repulsion operator and $\hat{V}_{ne}$ is the electron-nucleus attraction operator. The nuclear attraction term

may be written as the sum of the external potentials acting on each electron:

$$\hat{V}_{ne} = \sum_{i=1}^{N} v(\mathbf{r}_i) = \sum_{i=1}^{N} \sum_{A=1}^{M} \frac{Z_A}{r_{iA}}. \tag{2.98}$$

Let the (non-degenerate) ground state solution of the associated Schrödinger equation be Ψ:

$$\hat{H}\Psi = E_0\Psi. \tag{2.99}$$

The electron density associated with this solution is

$$\rho(\mathbf{r}) = N \int |\Psi|^2 d\mathbf{r}_2 \ldots d\mathbf{r}_N ds_1 \ldots ds_N. \tag{2.100}$$

For any reasonable density (such as that derived from an antisymmetric wavefunction), the relationship

$$\int \rho(\mathbf{r}) d\mathbf{r} = N \tag{2.101}$$

is always satisfied.

Recall from section (2.1.3) that the ground state energy and ground state wavefunction of an electronic system are determined by minimization of the energy functional $E[\Psi]$. However, for an N-electron system, the external potential $v(\mathbf{r})$ completely fixes the Hamiltonian. The ground state energy is also therefore a functional of N and $v(\mathbf{r})$ ($E[N, v]$), and these determine all the properties for the ground state. Hohenberg and Kohn showed how Ψ, N and v could be replaced by the electron density, ρ, as the basic variable in a variational method for the calculation of electronic structure. The Hohenberg-Kohn theorem states: *The external potential $v(\mathbf{r})$ is determined, within a trivial additive constant, by the electron density $\rho(\mathbf{r})$.* Since ρ determines the number of electrons, then it follows from this theorem that ρ also determines the ground state energy and all other electronic properties of the system.

The proof of the Hohenberg-Kohn theorem is by *reductio ad absurdum*, i.e. by proving that a given assumption generates a contradiction, hence establishing the opposite of that assumption. We proceed by assuming that there exist two possible external potentials $v(\mathbf{r})$ and $v'(\mathbf{r})$ which generate the same density. The second potential $v'(\mathbf{r})$ will be associated with a different Hamiltonian:

$$\hat{H}' = \hat{T} + \hat{V}'_{ne} + \hat{V}_{ee} \tag{2.102}$$

and different solution of the associated Schrödinger equation:

$$\hat{H}'\Psi' = E'_0\Psi'. \tag{2.103}$$

By employing the variation principle and choosing Ψ' as a (normalised) trial func-

tion for the $\hat{H}$ problem, we can write

$$E_0 < \langle \Psi' | \hat{H} | \Psi' \rangle = \langle \Psi' | \hat{H}' | \Psi' \rangle + \langle \Psi' | \hat{H} - \hat{H}' | \Psi' \rangle. \tag{2.104}$$

Since the external potential is just a local multiplicative operator:

$$\langle \Psi | \hat{V} | \Psi \rangle = \int \rho(\mathbf{r}) v(\mathbf{r}) d\mathbf{r} \tag{2.105}$$

and the kinetic energy and electron repulsion terms cancel, then

$$E_0 < \langle \Psi' | \hat{H} | \Psi' \rangle = E_0' + \int \rho(\mathbf{r}) \{ v(\mathbf{r}) - v'(\mathbf{r}) \} d\mathbf{r}. \tag{2.106}$$

Similarly, taking Ψ as a trial function for the $\hat{H}'$ problem,

$$E_0' < \langle \Psi | \hat{H}' | \Psi \rangle = \langle \Psi | \hat{H} | \Psi \rangle + \langle \Psi | \hat{H}' - \hat{H} | \Psi \rangle \tag{2.107}$$

$$= E_0 - \int \rho(\mathbf{r}) \{ v(\mathbf{r}) - v'(\mathbf{r}) \} d\mathbf{r}. \tag{2.108}$$

Adding (2.106) and (2.108) we obtain

$$(E_0 + E_0') < (E_0' + E_0) \tag{2.109}$$

a contradiction, so there cannot be two different potentials v which give the same ρ for their ground states. Thus ρ uniquely determines v (to within a constant) and N (equation 2.101) and hence all the ground state properties. The ground state wavefunction and total energy are therefore functionals of the ground state density.

The energy functional can be divided into separate functionals for the kinetic energy, nuclear attraction and electron repulsion terms:

$$E_0[\rho] = T[\rho] + V[\rho] + U[\rho]. \tag{2.110}$$

Making the dependence on v explicit in the definition of the energy functional gives

$$E_v[\rho] = \int \rho(\mathbf{r}) v(\mathbf{r}) d\mathbf{r} + F_{HK}[\rho], \tag{2.111}$$

where

$$F_{HK}[\rho] = T[\rho] + U[\rho]. \tag{2.112}$$

A variation principle, analogous to that for wavefunctions, was proved which showed that E_v has a minimum for the true ground state density. It reads: *For a trial density* $\tilde{\rho}(\mathbf{r})$ *such that*

$$\tilde{\rho}(\mathbf{r}) \geq 0 \quad \textit{and} \quad \int \tilde{\rho}(\mathbf{r}) d\mathbf{r} = N, \tag{2.113}$$

then

$$E_v[\tilde{\rho}] \geq E_0. \tag{2.114}$$

To prove this theorem, note that the previous theorem assures that $\tilde{\rho}$ determines its own $\tilde{v}$, Hamiltonian $\hat{H}$ and wavefunction $\tilde{\Psi}$. Taking $\tilde{\Psi}$ as a trial function for the problem of interest having a ground state associated with the external potential v, we find:

$$\langle \tilde{\Psi} | \hat{H} | \tilde{\Psi} \rangle = \int \tilde{\rho}(\mathbf{r}) v(\mathbf{r}) d\mathbf{r} + F_{HK}[\tilde{\rho}] = E_v[\tilde{\rho}] \geq E_v[\rho]. \tag{2.115}$$

Thus the minimal property of (2.111) is established relative to all density functions $\tilde{\rho}(\mathbf{r})$ associated with some other external potential $\tilde{v}(\mathbf{r})$.

The variation principle requires that the ground state density satisfies the stationary principle

$$\delta E_v[\rho] = 0, \tag{2.116}$$

subject to the normalisation constraint of equation (2.101). We can therefore construct the function

$$\delta \left\{ E_v[\rho] - \mu \left[\int \rho(\mathbf{r}) d\mathbf{r} - N \right] \right\} = 0, \tag{2.117}$$

where μ is the Lagrange parameter. This gives the Euler-Lagrange equation

$$\mu = \frac{\partial E_v[\rho]}{\partial \rho(\mathbf{r})} = v(\mathbf{r}) + \frac{\partial F_{HK}[\rho]}{\partial \rho(\mathbf{r})} \tag{2.118}$$

which is the basic working equation of density functional theory for the ground states of atoms, molecules and solids. The quantity μ is the *chemical potential*, defined as the rate of change of energy with respect to the addition or removal of density for a given $v(\mathbf{r})$. More informally, μ measures the escaping tendency of an electron cloud. The derivatives of μ with respect to N and v also have a physical significance. These relate to the *hardness* of a chemical species $(\partial\mu/\partial N)$ and the response of the chemical potential to an external perturbation $(\partial\mu/\partial v)$. The latter forms the basis of the frontier-electron theory of reactivity in DFT [102], which through the definition of the Fukui reactivity indices, is a measure of the susceptibility of chemical sites on a substrate to attack by a given reagent.

$F_{HK}[\rho]$ is a *universal* functional of ρ, independent of the form of the external potential. This means that once an explicit form for $F_{HK}[\rho]$ has been obtained, then in principle the method can be applied to any system regardless of the particular nuclear framework. Unfortunately the explicit functional dependence of F_{HK}, and therefore, E_v on ρ is unknown. The difficulty becomes clear when we try to express the components of $F_{HK}[\rho]$ in some form relating to the electron density.

The kinetic energy functional is

$$T[\rho] = \langle \Psi | \hat{T} | \Psi \rangle = \int \Psi \left(-\frac{1}{2} \sum_{i=1}^{N} \nabla^2(\mathbf{r}_i) \right) \Psi^* d\mathbf{r}. \tag{2.119}$$

$\hat{T}$ is a non-multiplicative differential operator and there can be no way of simplifying the integrand into a form which explicitly depends on $\rho(\mathbf{r})$. The only way the kinetic energy functional can be expressed in a density-orientated form, is in terms of the one-particle density *matrix* $\rho_1(\mathbf{r}_1, \mathbf{r}_2)$:

$$T[\rho] = \int \left[-\frac{1}{2} \nabla^2(\mathbf{r}_1) \rho_1(\mathbf{r}_1, \mathbf{r}_2) \right]_{r_2 \to r_1} d\mathbf{r}_1. \tag{2.120}$$

$\hat{V}_{ee}$ is a sum of two-electron operators and the resulting functional requires the use of a two-particle density function. The total electron repulsion energy, in terms of the two-electron density matrix ρ_2 is

$$U[\rho] = \int \int \frac{1}{r_{12}} \rho_2(\mathbf{r}_1, \mathbf{r}_2) d\mathbf{r}_1 d\mathbf{r}_2. \tag{2.121}$$

(For a discussion of density matrices and their application in density functional theory see Parr and Yang [103].) Equations (2.120) and (2.121) both involve functions of six variables, representing a formidable computational task. This is obviously contrary to the original ideas of DFT and approximations must be sought which transform equation (2.111) into a form amenable to practical solutions.

Many years before Hohenberg and Kohn had even provided the formal proof that justifies DFT, approximations were being made to try to solve its fundamental equations. The early work of Thomas [91] and Fermi [93] (1927), and later Dirac [94] (1930), applied results taken from the theory of a uniform electron gas to construct explicit approximate forms for $T[\rho]$ and $V_{ee}[\rho]$. The resulting equations involved only the electron density and were trivial to solve. However, there are insurmountable difficulties in going beyond this crude level of approximation. As we shall see in the next section, Kohn and Sham used a rather more indirect approach to this problem, which has turned density functional theory into a practical tool for electronic structure calculations.

2.2.2 The Kohn-Sham Method

Kohn and Sham provided one route to a set of working equations. They first separated the 'classical' Coulomb energy in $F[\rho]$:

$$F[\rho] = J[\rho] + G[\rho] \tag{2.122}$$

$$= \frac{1}{2} \int \int \frac{\rho(\mathbf{r}) \rho(\mathbf{r}')}{|\mathbf{r} - \mathbf{r}'|} d\mathbf{r} d\mathbf{r}' + G[\rho], \tag{2.123}$$

where the new universal functional $G[\rho]$ contains the kinetic energy and the non-classical terms due to exchange and correlation. $G[\rho]$ was then further separated into two more terms:

$$G[\rho] = T_s[\rho] + E_{XC}[\rho]. \tag{2.124}$$

$T_s[\rho]$ is the kinetic energy of a system of *independent non-interacting* electrons which have the same density $\rho(\mathbf{r})$ as the 'real' system of interacting electrons. This is the principle strategy of the Kohn-Sham method; construct a non-interacting kinetic energy functional and absorb the interacting component into a more general term $E_{XC}[\rho]$ which also contains everything else that is unknown about the system. $E_{XC}[\rho]$ contains all the details of two-body exchange and dynamical correlation as well as the interacting kinetic energy component. The Euler equation (2.118) can now be written

$$\mu = v_{eff}(\mathbf{r}) + \frac{\partial T_s[\rho]}{\partial \rho(\mathbf{r})}, \tag{2.125}$$

where the Kohn-Sham *effective potential* is defined by

$$\begin{aligned} v_{eff}(\mathbf{r}) &= v(\mathbf{r}) + \frac{\partial J[\rho]}{\partial \rho(\mathbf{r})} + \frac{\partial E_{XC}[\rho]}{\partial \rho(\mathbf{r})} && (2.126) \\ &= v(\mathbf{r}) + \int \frac{\rho(\mathbf{r}')}{|\mathbf{r} - \mathbf{r}'|} d\mathbf{r}' + v_{XC}(\mathbf{r}). && (2.127) \end{aligned}$$

The *exchange-correlation potential* is defined as

$$v_{XC}(\mathbf{r}) = \frac{\partial E_{XC}[\rho]}{\partial \rho(\mathbf{r})}. \tag{2.128}$$

Equation (2.125) with the constraint (2.101) is precisely the same equation that one would obtain by applying conventional DFT to a system of non-interacting electrons moving in an external potential $v_{eff}(\mathbf{r})$. The Schrödinger equation is separable for non-interacting systems and the problem can be expressed in terms of a set of one-electron Hartree-like equations. Therefore, for a given $v_{eff}(\mathbf{r})$. one obtains the $\rho(\mathbf{r})$ that satisfies (2.125) by solving the N one-electron equations

$$\begin{aligned} \hat{h}_{KS}\chi_i(\mathbf{x}) &= \varepsilon_i \chi_i(\mathbf{x}) && (2.129) \\ \left[-\frac{1}{2}\nabla^2 + v_{eff}(\mathbf{r})\right] \chi_i(\mathbf{x}) &= \varepsilon_i \chi_i(\mathbf{x}) && (2.130) \end{aligned}$$

and by setting the density:

$$\rho(\mathbf{r}) = \sum_{i=1}^{N} \sum_{s} |\chi_i(\mathbf{r}, s)|^2. \tag{2.131}$$

Equations (2.125) to (2.131) are collectively known as the Kohn-Sham (KS) equations. They must be solved iteratively since $v_{eff}(\mathbf{r})$ depends on $\rho(\mathbf{r})$ through (2.128). One begins with a guessed $\rho(\mathbf{r})$ and constructs $v_{eff}(\mathbf{r})$ from (2.127). A new $\rho(\mathbf{r})$ is then calculated from (2.130) and (2.131. Once self-consistency is

achieved the KS total electronic energy can be determined from

$$\begin{aligned} E[\rho] &= T_s[\rho] + J[\rho] + \int v(\mathbf{r})\rho(\mathbf{r})d\mathbf{r} + E_{XC}[\rho] \\ &= \sum_{i=1}^{N}\sum_{s}\int \chi_i^*(\mathbf{r})(-\frac{1}{2}\nabla^2)\chi_i(\mathbf{r})d\mathbf{r} + \frac{1}{2}\int\int \frac{\rho(\mathbf{r})\rho(\mathbf{r}')}{|\mathbf{r}-\mathbf{r}'|}d\mathbf{r}d\mathbf{r}' \\ &\quad + \int v(\mathbf{r})\rho(\mathbf{r})d\mathbf{r} + E_{XC}[\rho]. \end{aligned} \tag{2.132}$$

Implicit in the Kohn-Sham approach is the re-introduction of a set of orbitals (χ) into the theory. For a non-interacting system of electrons there will be an exact determinantal ground state solution:

$$\Psi_{KS} = |\chi_1\chi_2\cdots\chi_i\cdots\chi_j\cdots\chi_N\rangle, \tag{2.133}$$

where the χ_i are the N lowest eigenstates of the one-electron Hamiltonian $\hat{h}_{KS}$. Through the introduction of the KS orbitals the dominant part of the kinetic energy $T_s[\rho]$ is handled *exactly*, albeit indirectly:

$$T_s[\rho] = \sum_{i=1}^{N}\langle\chi_i| - \frac{1}{2}\nabla^2|\chi_i\rangle. \tag{2.134}$$

This represents a major advance over the Thomas-Fermi type methods which use direct approximations to $T[\rho]$ but comes with the penalty of increased computation associated with the solution of N, rather than just one, equations.

In addition to the clever treatment of the kinetic energy functional, the KS determinantal wavefunction also ensures that the density is always *N-representable.* A density $\rho(\mathbf{r})$ is N-representable if it is non-negative, continuous and integrates to the number of electrons. Mathematically stated, this is:

$$\rho(\mathbf{r})\geq 0, \qquad \int |\nabla\rho(\mathbf{r}^{\frac{1}{2}})|^2 d\mathbf{r} < \infty \quad \textit{and} \quad \int \rho(\mathbf{r})d\mathbf{r} = N. \tag{2.135}$$

The variational principle (2.114) is only valid for trial densities which satisfy this condition.

The KS equations have the same form as the Hartree equations (2.11) except that they contain a more general local potential $v_{eff}(\mathbf{r})$. The computational effort to solve them should therefore be less than for the Hartree-Fock equations which contain a non-local operator in the one-electron Hamiltonian. By contrast to the Hartree-Fock model (which is approximate by definition), Kohn-Sham theory is exact and can in principle fully describe both the exchange and dynamical correlation of electron repulsion. However, the functional which incorporates these effects, $E_{XC}[\rho]$, is unknown and to proceed further, approximations have to be introduced.

One final point before moving on to a description of approximate DFT schemes concerns the electron-spin degrees of freedom. Since the effective potential does not contain electron spin, the solutions of the KS equations are doubly degenerate. That is, for each eigenvalue ε_i there are two independent solutions, $\psi_i(\mathbf{r})\alpha(s)$ and $\psi_i(\mathbf{r})\beta(s)$, which are associated with the same spatial orbital. When the molecular system has an even number of electrons arranged in a closed-shell configuration, the α-spin density is equal to the β-spin density. Thus,

$$\rho(\mathbf{r}) = 2\rho^{\alpha}(\mathbf{r}) = 2\rho^{\beta}(\mathbf{r}) = 2\sum_{i=1}^{\frac{N}{2}} |\psi_i(\mathbf{r})|^2 \tag{2.136}$$

and the spin dependence does not have to be considered explicitly. When the number of electrons is odd the total electron density can be written as

$$\rho(\mathbf{r}) = \rho^{\alpha}(\mathbf{r}) + \rho^{\beta}(\mathbf{r}), \tag{2.137}$$

where the α- and β-spin densities differ by one excess orbital. The prescription for the spatial orbitals is analogous to that of the restricted Hartree-Fock method. It should be noted though, that the restriction on spatial orbitals in the KS equations arises as a natural consequence of the theory, whereas in the RHF method the restriction is a modification to the single determinant model.

2.2.3 The Local Density Approximation

As shown in the previous section, DFT can be formulated in such a way that the energy functionals $T_s[\rho]$, $J[\rho]$ and $V_{ne}[\rho]$ are all be treated in an exact manner. An accurate treatment of the remaining effects due to exchange and correlation between the interacting electrons, and the influence of correlation on the kinetic energy, continues to be the greatest challenge in modern DFT.

The simplest approximation to $E_{XC}[\rho]$ is called the *local density approximation* (LDA), also proposed by Kohn and Sham in 1965 [101]. Following the approach adopted in the early work of Thomas [91] and Fermi [93] , the uniform electron gas formula are used to construct an approximate form for the exchange-correlation functional:

$$E_{XC}^{LDA}[\rho] = \int \rho(\mathbf{r})\varepsilon_{XC}(\rho)d\mathbf{r}, \tag{2.138}$$

where $\varepsilon_{XC}(\rho)$ is the exchange and correlation energy (including the residual kinetic energy term) per particle of an interacting homogeneous electron gas of density ρ. The corresponding exchange-correlation potential of (2.128) then becomes

$$v_{XC}^{LDA}(\mathbf{r}) = \frac{\partial E_{XC}^{LDA}}{\partial \rho(\mathbf{r})} = \varepsilon_{XC}(\rho(\mathbf{r})) + \rho(\mathbf{r})\frac{\partial \varepsilon_{XC}(\rho)}{\partial \rho}. \tag{2.139}$$

and the one-electron KS-LDA equations for the case of a closed-shell system are therefore

$$\left[-\frac{1}{2}\nabla^2 + v(\mathbf{r}) + \int \frac{\rho(\mathbf{r}')}{|\mathbf{r}-\mathbf{r}'|}d\mathbf{r}' + v_{XC}^{LDA}(\mathbf{r})\right]\psi_i(\mathbf{r}) = \varepsilon_i\psi_i(\mathbf{r}). \tag{2.140}$$

The function $\varepsilon_{XC}(\rho)$ can be divided into separate exchange and correlation contributions:

$$\varepsilon_{XC}(\rho) = \varepsilon_X(\rho) + \varepsilon_C(\rho) \tag{2.141}$$

The exchange part is given by the Dirac exchange-energy formula for a uniform electron gas [94]:

$$\varepsilon_X(\rho) = -C_X\rho(\mathbf{r})^{\frac{1}{3}}, \qquad C_X = \frac{3}{4}\left(\frac{3}{\pi}\right)^{\frac{1}{3}}. \tag{2.142}$$

The correlation energy $\varepsilon_C(\rho)$ represents a rather more complex problem but accurate values have been determined by quantum Monte Carlo simulations [104]. Vosko *et al.* have interpolated these values to provide an analytical form for $\varepsilon_C(\rho)$ [105].

Simplified version of LDA were known many years before the formal development of the KS-LDA method. Of note is the Hartree-Fock-Slater method, or $X\alpha$ method, developed by Slater in 1951 [106]. In this method, the non-local Fock operator in the one-electron Hartree-Fock equations is replaced with a simple local potential derived from the uniform electron gas model. The resulting $X\alpha$ equations are

$$\left[-\frac{1}{2}\nabla^2 + v(\mathbf{r}) + \int \frac{\rho(\mathbf{r}')}{|\mathbf{r}-\mathbf{r}'|}d\mathbf{r}' + v_{X\alpha}(\mathbf{r})\right]\psi_i(\mathbf{r}) = \varepsilon_i\psi_i(\mathbf{r}), \tag{2.143}$$

where the $X\alpha$ local potential is defined by

$$v_{X\alpha}(\mathbf{r}) = -\frac{3}{2}\alpha\left\{\frac{3}{\pi}\rho(\mathbf{r})\right\}^{\frac{1}{3}}. \tag{2.144}$$

The exchange scaling parameter α was set equal to 1 in the original prescription. If correlation is neglected in equation (2.140), and the Dirac expression is used for the exchange energy (2.142), it is trivial to show that the resulting KS-LDA equation is precisely the $X\alpha$ equation (2.143) but with $\alpha = 2/3$. This ambiguity has led to α being used as an adjustable exchange parameter in many $X\alpha$ calculations. More recent studies have shown that for atoms and molecules a value of $\alpha \sim 0.75$ is more favourable than either $\alpha = 1$ or $2/3$.

By using a local approximation, one assumes that uniform electron gas results can be applied *locally* to infinitesimal portions of a given electron distribution, each portion having $\rho(\mathbf{r})d\mathbf{r}$ electrons, and then summing over all space the individual contributions $\varepsilon_C(\rho)\rho(\mathbf{r})d\mathbf{r}$. This procedure is appropriate for systems with slowly varying densities but cannot be formally justified for inhomogeneous systems such

as atoms and molecules. Despite this apparent limitation, the LDA method and its spin-polarized generalization, the local spin density approximation (LSDA) [103], have been reported to yield good predictions for a wide range of molecular properties. On the other hand, the use of this approximation has also led to a number of notable failures:

(i) The LSDA method underestimates the magnitude of the exchange energy for atoms typically by 10–15% [107]. The magnitude of the correlation is overestimated by as much as 100–200% but the error is still smaller in absolute terms than the exchange error.

(ii) Experimentally stable ions, such as H^-, O^- and F^- are predicted to be unstable by local theories [108, 109].

(iii) LSDA total energies have incorrectly favoured the $d^{n-1}s^1$ configuration over the $d^{n-2}s^2$ configuration in $3d$ transition-metal atoms [110].

(iv) M–CO bond dissociation energies for the hexacarbonyls $M(CO)_6$ (M=Cr, Mo, W) are overestimated by the LSDA method by nearly 100% [96].

(v) The local approximation has been shown to give a poor description of weak inter- and intra-molecular interactions such as those found in systems incorporating hydrogen bonds [111], Van der Waals interactions [112] and charge-transfer interactions [113, 114].

There are two main sources of error in local DFT:

- The exact exchange-correlation potential is certainly non-local;
- Introducing direct approximations to the exchange functional results in there being a spurious self-interaction of electrons.

These are discussed in the following sections.

2.2.4 Self-Interaction Correction (SIC)

An electron in a molecule interacts with other electrons via the Coulomb potential; it does not interact with itself. In Hartree-Fock theory the electron repulsion energy of an N-electron system may be written:

$$\langle V_{ee}^{HF} \rangle = \frac{1}{2} \sum_{i,j}^{N} (J_{ij} - K_{ij}), \tag{2.145}$$

where J_{ij} and K_{ij} are the two-electron Coulomb and exchange integrals defined earlier in section (2.1.4). Recall the important equality:

$$J_{ii} = K_{ii}. \tag{2.146}$$

Hence, the self-exchange K_{ii} *exactly* cancels out the self-repulsion J_{ii} in the summation of equation (2.145) and the unphysical situation of an electron interacting with itself cannot arise in the Hartree-Fock model.

In Kohn-Sham density functional theory, the *exact* exchange-correlation functional $E_{XC}[\rho]$ exactly cancels the spurious self-Coulombic repulsion. However, LDA and related theories only achieve a partial cancellation, due to the approximations made in constructing an explicit simple form for $E_{XC}[\rho]$. In the Hydrogen atom, for example, the self-interaction is 8.5eV (820 KJmol^{-1}) and only 93% of this spurious energy is cancelled within the LSDA approximation [116]. Neglect of the residual terms due to self-interaction leads to an exchange-correlation potential which has the wrong asymptotic form [115]. The true potential should decay Coulombically like $-r^{-1}$ but the LSDA potential is found to decay rather more rapidly as e^{-r}. Many of the reported failures of approximate DFT can probably be traced to this deficiency. In particular, this would seem to be the greatest source of error for those systems involving diffuse electron distributions in the outer regions of atoms and molecules, such as in the case of negative ions and weakly interacting species.

For a given approximation to the exchange-correlation functional $\tilde{E}_{XC}$, the total LSDA electron repulsion energy is given by

$$\langle V_{ee}^{LSD} \rangle = J[\rho^{\alpha} + \rho^{\beta}] + \tilde{E}_{XC}[\rho^{\alpha}, \rho^{\beta}]. \tag{2.147}$$

The necessary requirement to exclude self-interactions can be written as

$$V_{ee}[\rho_i^{\sigma}, 0] = J[\rho_i^{\sigma}] + E_{XC}[\rho_i^{\sigma}, 0] = 0 \qquad \sigma = \alpha, \beta \tag{2.148}$$

where ρ_i^{σ} is the *single particle* density for the i^{th} orbital with spin σ, i.e. $\rho_i^{\sigma} = |\psi_i^{\sigma}|^2$.

Various methods for correcting this self-interaction have been reported [116]-[118]. The procedure proposed by Perdew and Zunger [116] involves the direct subtraction of the self-interaction error, orbital by orbital, to yield a self-interaction-corrected exchange-correlation energy:

$$E_{XC}^{SIC}[\rho^{\alpha}, \rho^{\beta}] = \tilde{E}_{XC}[\rho^{\alpha}, \rho^{\beta}] - \sum_{i\sigma} \delta_{i\sigma}, \tag{2.149}$$

where,

$$\delta_{i\sigma} = J[\rho_i^{\sigma}] + \tilde{E}_{XC}[\rho^{\alpha}, 0] \tag{2.150}$$

is the self-interaction correction for orbital ψ_i^σ. The resulting modification to the exchange-correlation potential in the KS equations is given by:

$$v_{XC}^{i\sigma,SIC}(\mathbf{r}) = \frac{\partial E_{XC}^{SIC}}{\partial \rho_i^\sigma(\mathbf{r})} = \frac{\partial E_{XC}[\rho^\alpha, \rho^\beta]}{\partial \rho_i^\sigma(\mathbf{r})} - \int \frac{\rho_i^\sigma(\mathbf{r}')}{|\mathbf{r} - \mathbf{r}'|} d\mathbf{r}' - \frac{\partial E_{XC}[\rho_i^\sigma, 0]}{\partial \rho_i^\sigma(\mathbf{r})}. \quad (2.151)$$

The SIC procedure introduces an orbital dependence into the form of the effective potential. Each spin orbital is associated with a separate operator so the equation has to be solved several times. Additional effort is also required to obtain the set of orthogonal SIC orbitals. This scheme (and SIC schemes in general) is therefore dominated by the problem of finding an optimum set of orbitals and ultimately requires a great deal more computational effort. For these reasons, current implementations of approximate DFT do not normally contain a SIC option.

The residual self-interaction is an error which should be removed as one obtains more accurate expressions for the density functionals. We briefly discuss some of the developments in the construction of new approximate functionals in the following sections.

2.2.5 Gradient-Corrected Functionals

The exact exchange-correlation potential is non-local and therefore depends on the entire electron distribution rather than just the value of ρ at a given point. A logical extension to the local approximation would be to develop a theory involving the derivatives of ρ, since these should provide a measure of the inhomogeneity of the electron density. Several different prescriptions for producing gradient-corrected functionals have been described [119]-[124]. The simplest approach is to construct a functional incorporating only the lowest-order gradient correction, i.e. one that involves only the first derivative of ρ. One of the most successful and widely implemented non-local functionals of this type is the exchange functional developed by Becke [124]:

$$E_X^{Becke}[\rho] = E_X^{LDA}[\rho] - \beta \int \rho^{4/3} \frac{x^2}{(1 + 6\beta x \sinh^{-1} x)} d\mathbf{r}, \quad (2.152)$$

where x is a dimensionless ratio given by

$$x = \frac{|\nabla \rho|}{\rho^{4/3}}. \quad (2.153)$$

The first term in equation (2.152) is the LDA exchange energy for a uniform electron gas. The second term introduces a correction for the non-uniformity through the density gradient $\nabla\rho$. The parameter β was chosen by Becke to fit the known exchange energies for the inert gas atoms. The analytical form of the Becke functional was designed specifically to correct for the poor long-range behaviour

of the density and exchange potential afforded by the local theories. It should therefore involve a smaller error due to self-interaction.

Gradient corrections can also be applied to the correlation functional describing the interaction of electrons with anti-parallel spin. An example is the LYP functional developed by Lee, Yang and Parr [125] which is often paired with the Becke functional above to give a non-local description of both exchange and correlation effects in molecular systems.

2.2.6 Hybrid Methods

There has long been interest in coupling Hartree-Fock theory with density functional theory. The motivation behind such thinking has been to formulate a method which exploits the particular strengths of each partner. If the Hartree-Fock expression for exchange is kept in place of the exchange functional, this ensures that the self-Coulomb integrals are properly cancelled by self-exchange. One can therefore include the exchange effects 'exactly' leaving only the correlation energy to be dealt with by approximate DFT. For example, one could write the exchange-correlation energy as a sum of Hartree-Fock and LDA terms:

$$E_{XC} = E_X^{HF} + E_C^{LDA}. \tag{2.154}$$

Straightforward addition of DFT correlation approximations to Hartree-Fock energies has not, however, proven successful in the description of molecular bonding [126]. The problem lies in the fact that division of E_{XC} into separate exchange and correlation components is not clearly defined for densities other than Hartree-Fock. Only exchange and correlation taken together in a unified theory has ultimate physical meaning. Although the Hartree-Fock exchange is exact in a mathematical sense, it gives a very poor representation of the exchange due to configuration mixing of near-degenerate states. Short-range dynamical correlation is well represented by the LDA functional E_C^{LDA} but it contains no allowance for near-degeneracy effects since this is primarily a correction to E_X^{HF}. Thus, molecular calculations based on equation (2.154) exhibit many of the deficiencies of the original Hartree-Fock treatment.

An alternative approach to mixing Hartree-Fock and local density functional theory which does not suffer the above defects, has been proposed by Becke [127]. Within the Kohn-Sham formalism of DFT, there exists a rigorous *ab initio* formula for the exchange-correlation energy known as the "adiabatic connection" formula [128]. This may be written as

$$E_{XC} = \int_0^1 U_{XC}^{\lambda} d\lambda, \tag{2.155}$$

where λ is the coupling strength parameter connecting adiabatically the non-interacting Kohn-Sham reference system ($\lambda = 0$) with the real fully-interacting system ($\lambda = 1$); U_{XC}^{λ} is the potential energy of exchange-correlation at intermediate coupling strength λ. Unfortunately, direct *ab initio* solutions of equation (2.155) are not possible since the analytical form of U_{XC}^{λ} is unknown. To exploit this powerful result approximations must therefore be introduced.

The simplest approximation for the λ dependence of the integrand in equation (2.155) is a linear interpolation which results in the following approximate exchange-correlation energy:

$$E_{XC} \approx \frac{1}{2}U_{XC}^{0} + \frac{1}{2}U_{XC}^{1}. \tag{2.156}$$

The non-interacting potential energy U_{XC}^{0} is precisely the pure exchange energy of a Kohn-Sham Slater determinant *with no dynamical correlation.* The second term is the contribution from the fully-interacting system incorporating both exchange and correlation effects. Becke proposed a modified equation in which the non-interacting Kohn-Sham exchange was replaced by exact Hartree-Fock exchange and the interacting exchange-correlation term was estimated by a local density approximation [127]. The Becke "Half-and-Half" hybrid scheme for the exchange-correlation energy is therefore

$$E_{XC} \approx \frac{1}{2}E_{X}^{HF} + \frac{1}{2}U_{XC}^{LDA}, \tag{2.157}$$

where

$$U_{XC}^{LDA} = \int \rho(\mathbf{r}) u_{XC}(\rho) d\mathbf{r}. \tag{2.158}$$

This last equation resembles the conventional LDA expression (2.138) but involves the potential energy of exchange-correlation rather than the total energy. The choice of exact Hartree-Fock over Kohn-Sham exchange in equation (2.157) is made because the limit $\lambda = 0$ requires that the system be completely non-interacting. Local approximations which would otherwise be employed to approximate the exchange-only component, do include some crude form of correlation between antiparallel spins; while this is desirable in the interacting system, it would clearly misrepresent the non-interacting $\lambda = 0$ limit. (For a discussion of this point see reference [129].)

Becke has also extended the half-and-half theory by relaxing the λ dependence and including gradient corrections to both the exchange and correlation functionals [129]. The following expression was proposed:

$$E_{XC} = E_{XC}^{LDA} + a_0(E_{X}^{HF} - E_{X}^{LDA}) + a_X \Delta E_X + a_C \Delta E_C, \tag{2.159}$$

where a_0, a_X and a_C are semi-empirical coefficients determined by fitting to appropriate experimental data, and ΔE_X and ΔE_C are gradient corrections for exchange and correlation. The latter terms can be provided by, for example, the Becke and

LYP corrections discussed in the last section. The purpose of the second term is to replace some of the local uniform gas exchange with exact exchange in order to properly describe the small λ limit of equation (2.155).

2.2.7 Practical Implementation of the Kohn-Sham Equations

The self-consistent version of approximate DFT necessitates the solution of the Kohn-Sham equations

$$\left[-\frac{1}{2}\nabla^2 + v(\mathbf{r}) + \int \frac{\rho(\mathbf{r}')}{|\mathbf{r}-\mathbf{r}'|}d\mathbf{r}' + \tilde{v}_{XC}(\mathbf{r})\right]\psi_i(\mathbf{r}) = \varepsilon_i\psi_i(\mathbf{r}), \tag{2.160}$$

for a potential $\tilde{v}_{XC}$ derived from an approximate analytical expression for the exchange-correlation energy:

$$\tilde{v}_{XC}(\mathbf{r}) = \frac{\partial \tilde{E}_{XC}}{\partial \rho(\mathbf{r})}. \tag{2.161}$$

Various methods for generating approximate solutions to these equations have been reported. In early applications to molecular problems, the scattered-wave method was employed [131]. This involves a spherical approximation to the Coulomb potential, the so-called "muffin-tin" approximation [132], resulting in a set of equations which can be easily solved using standard numerical techniques. While this method is extremely rapid and has provided a number of useful results for large complex systems, the use of the spherical approximation precludes the accurate calculation of total energies. A more favourable method is to expand the Kohn-Sham orbitals in terms of a set of atomic orbitals and fit the density that they define to an auxiliary set of one-centre functions. The Coulomb potential can then be evaluated in a similar way to the exchange-correlation term by an economical numerical integration scheme.

For the present study we have used the method described by Pople *et al.* [133], as implemented in the GAUSSIAN92/DFT code [134]. In this approach the Coulomb integrals are evaluated exactly over atomic Gaussian basis functions and a set of matrix equations are solved for the optimum Kohn-Sham orbitals. The orbital equations have the same form as the Roothaan-Hall equations of conventional Hartree-Fock theory (see section 2.1.5), except they contain a different Fock matrix:

$$F_{\mu\nu} = H_{\mu\nu}^{core} + J_{\mu\nu} + F_{\mu\nu}^{XC}. \tag{2.162}$$

Here the $H_{\mu\nu}^{core}$ and $J_{\mu\nu}$ are elements of the one-electron Hamiltonian matrix and Coulomb matrix, respectively. The elements of the exchange-correlation matrix are given by

$$F_{\mu\nu}^{XC} = \int \phi_\mu^*(\mathbf{r})\tilde{v}_{XC}(\mathbf{r})\phi_\nu d\mathbf{r}(\mathbf{r}), \tag{2.163}$$

where the ϕ_μ are the atomic orbital basis functions. The main difference between this implementation and other formulations of approximate DFT is that no auxiliary fitting of the Coulomb or exchange correlation potentials is performed. The Coulomb integrals are defined in an identical way to those in the Self-Consistent Hartree-Fock method and can be solved analytically for Gaussian-type functions. The exchange-correlation energy and potential are obtained from numerical quadrature of the functional and its various derivatives over a grid of integration points spanning the molecular surface. Once the Kohn-Sham matrix equations have been solved self-consistently, the total energy is obtained from

$$E = \sum_{\mu\nu} P_{\mu\nu} H_{\mu\nu}^{core} + \frac{1}{2} \sum_{\mu\nu\lambda\sigma} P_{\mu\nu} P_{\lambda\sigma} (\mu\nu|\lambda\sigma) + E_{XC}. \qquad (2.164)$$

Note again the similarity between this formula and the Hartree-Fock energy given in equation (2.75), the only difference being that the HF exchange has been replaced by E_{XC}.

The GAUSSIAN92/DFT implementation has the advantage that techniques already employed in the existing *ab initio* code can be utilised for the DFT calculations. Furthermore, since the Kohn-Sham SCF procedure described does not involve any auxiliary fitting, a direct comparison of DFT and *ab initio* results obtained with the same Gaussian basis can be made.

2.3 Pseudopotentials

2.3.1 Calculations on Heavy Atoms

The accurate prediction of molecular properties for transition metal compounds represents one of the largest challenges to quantum theory. Their electronic structure and bonding is not as well understood as the properties of organic molecules which have been dealt with comprehensively by *ab initio* techniques. The comparatively slow emergence of accurate theoretical results in this area stems largely from the lack of efficient schemes for dealing with systems incorporating large numbers of electrons. The amount of computer resources required to perform a simple *ab initio* calculation rises with at least the third power of the number of electrons to be explicitly computed (N^3). For the more sophisticated methods the dependence of the computational expenditure may be more like N^6. Calculations on heavy elements using standard *all-electron* bases therefore become impractical, arising as a natural consequence of the increasing computational cost.

In addition to the practical limitations, two further difficulties have been identified. The core states of atoms are extremely energy rich and necessarily require a larger number of basis functions than the valence states for their description. If

the core region is not saturated with a good basis, then there exists the possibility of the calculation being influenced in an unpredictable way by a "variational collapse". This is the situation where core electrons use valence basis functions to improve their description at the expense of the important valence region. A second problem, which falls in a different category, is how to account for relativistic effects. Third row transition metals in particular, are well known to require some sort of relativistic treatment in order to give an adequate description of their electronic structure. The considerable effort involved in calculations by conventional relativistic methods, such as the Dirac-Hartree-Fock method, has restricted applications to small systems incorporating only a few atoms [139, 140]. These latter facts exacerbate the computational problem; even if one has the resources to perform a full *ab initio* calculation, the results are likely to be unreliable unless an enormous basis is used for the cores and relativistic effects are explicitly accounted for. For both practical and theoretical reasons, the full calculation of all electrons in molecules containing heavy atoms is therefore ill-advised.

There is, however, a large amount of evidence to suggest that inner-shell electrons play a much less significant role than the valence electrons in chemical reactions. Core electrons are essentially insensitive to the molecular environment and act predominantly to shield the nuclei and to provide an effective field in which the valence electrons move. Modern theoretical calculations therefore tend to concentrate on the 'chemically interesting' valence shells. Early work in the 1930's by Hellmann [135, 136] and Gombas [137], suggested that the calculation of electronic structure for atoms could be reduced to the treatment of just the valence electrons. Twenty years later it was rigorously shown by Phillips and Kleinman [138] that the explicit dependence of the wavefunction on the core electrons could be removed by the introduction of an effective non-local potential into the Hamiltonian. The operator which replaces the effect of the core electrons is known as the *pseudopotential.* This idea has been developed to the extent that practical molecular orbital calculations can now be performed on any atom in the periodic table. The modern formalism is called the Effective Core Potential (ECP) approximation which in addition to circumventing the practical problems also provides a convenient method for introducing relativistic effects. The main quantitative ideas in the development of ECPs are described below.

2.3.2 The Frozen-Core Approximation

Certain model wavefunctions (for example, the Hartree-Fock wavefunction) can be written as a product of core and valence wavefunctions:

$$\Psi = \hat{A}\Phi_{core}\Phi_{val}, \tag{2.165}$$

where $\hat{A}$ is the antisymmetrizer. If we assume the core wavefunction is already known and *remains invariant during the determination of the molecular wavefunction*, the problem may be reduced to the solution of a valence-only Schrödinger equation:

$$\hat{H}_{val}\Phi_{val} = E_{val}\Phi_{val}. \tag{2.166}$$

The valence Hamiltonian is then defined by

$$\hat{H}_{val} = \sum_{i}^{n_v}\left(\hat{h}(i) + \sum_{j\neq i}\frac{1}{r_{ij}}\right) + V_{core}, \tag{2.167}$$

where the summation ranges only over the valence electrons and V_{core} is the two-electron operator representing the core-valence interactions. The assumption of a rigid core wavefunction is called the *frozen core* approximation and is the first approximation made in all practical reductions to valence-only problems. However, without further development the savings obtained in practice are limited. The interaction term V_{core} is a non-local integral operator because of the exchange terms introduced by the antisymmetrizer in equation (2.166). All of the core-valence two-electron integrals therefore still have to be evaluated. In addition to this, a variational solution of equation (2.167) requires that the valence wavefunction, Φ_{val}, be maintained orthogonal to each core orbital. This must be guaranteed to prevent collapse of the valence wavefunction into the core region which is equivalent to ensuring that the valence orbitals satisfy the Pauli exclusion principle. Much greater simplification and savings could be achieved if the core-valence orthogonality constraint and the non-local core-valence interaction term were replaced by an operator that *simulated* orthogonality rather than explicitly requiring it, whilst providing the correct core potential seen by the valence electrons.

2.3.3 The Phillips-Kleinman Pseudopotential

In 1959 Phillips and Kleinman [138] provided a sound theoretical basis for replacing the explicit core-valence orthogonality constraints by a modification of the valence Hamiltonian.

Following Phillips and Kleinman we consider the case of a single valence electron moving in the potential due to n_c core electrons. The valence eigenvalue equation is written:

$$\hat{H}_v\phi_v = (\hat{h} + V_{core})\phi_v = E_v\phi_v, \tag{2.168}$$

where ϕ_v satisfies the orthogonality constraint:

$$\langle\phi_v \mid \phi_c\rangle = 0 \qquad c = 1, 2, \ldots, n_c \tag{2.169}$$

for all core-like solutions of the same Hamiltonian:

$$\hat{H}_v \phi_c = E_c \phi_c. \tag{2.170}$$

If the total wavefunction is unchanged by linear transformations amongst the orbitals (such as for example, in the case of a single determinant wavefunction), a new valence orbital χ_v can be defined that is related to ϕ_v by Schmidt orthogonalisation against the other core orbitals:

$$\phi_v = \chi_v - \sum_{c=1}^{n_c} \langle \chi_v \mid \phi_c \rangle \phi_c. \tag{2.171}$$

This ensures that for any choice of χ_v, ϕ_v will be orthogonal to the core orbitals. Equivalently, this may be written as

$$\phi_v = (1 - \hat{P}_c)\chi_v, \tag{2.172}$$

where $\hat{P}_c$ is called the core projection operator and is defined by the requirement that it project from any function that part lying in the core space. This is expressed formally as

$$\hat{P}_c = \sum_{c=1}^{n_c} \mid \phi_c \rangle \langle \phi_c \mid . \tag{2.173}$$

Substituting (2.171) into (2.168), the valence eigenvalue equation may now be written in a more general form for the χ_v:

$$(\hat{h} + V_{core} + V^{PK})\chi_v = E_v \chi_v, \tag{2.174}$$

where

$$\begin{aligned} V^{PK} &= \sum_{c=1}^{n_v} [E_v - E_c] \mid \phi_c \rangle \langle \phi_c \mid \\ &= [E_v - E_c]\hat{P}_c. \end{aligned} \tag{2.175}$$

V^{PK} is a non-local repulsive potential called the *pseudopotential* and χ_v is the associated *pseudo-orbital.* Equation (2.175) is satisfied by any function of the form

$$\chi_v = \phi_v + \sum_{c=1}^{n_c} a_c \phi_c. \tag{2.176}$$

The pseudo-orbital is therefore arbitrary to the extent that any coefficients a_c that effectively remove the orthogonality constraint may be employed. Thus, by incorporating a non-local pseudopotential into the definition of the Hamiltonian, the explicit othogonality requirement can be removed without changing the valence eigenvalues. The problem has been transformed from the study of a function satisfying certain orthogonality constraints (ϕ_v) and an unmodified Hamiltonian ($\hat{H}$), to the study of an unconstrained function (χ_v) satisfying a modified Hamiltonian

$(\hat{H} + V^{PK})$.

The importance of the pseudopotential formalism is in the theoretical justification and mathematical basis it provides for the subsequent development of effective potentials. It does not single-handedly solve the problem of avoiding a full description of the core electrons. V^{PK} is non-local and requires the evaluation of all the two-electron integrals between the valence and core orbitals. Furthermore, the arbitrary nature of the pseudo-orbital means that V^{PK} is not unique and one must examine a large number of choices for the a_c to obtain a reasonable form for the pseudopotential. Clearly, the use of the "exact" pseudopotential results in a problem of comparable difficulty to the initial all-electron problem. In order to proceed further, methods must be devised that use a local core potential with a functional form that can be fixed according to some reasonable theoretical procedure.

Several methods for deriving pseudopotentials which circumvent the above difficulties have been proposed. In one approach, the pseudopotential and the core-valence interaction terms in the valence Hamiltonian are replaced by a *model potential* which has a predetermined functional form [141]. Model potentials contain adjustable parameters which are fit to experimental atomic data. However, such empirical schemes are only tractable for one- or two-valence electron atoms and are not extendable to the entire periodic table. A more favourable method which has superseded model potentials in modern implementations is the method of *effective core potentials.*

2.3.4 Effective Core Potentials

The term effective core potential (ECP) is usually reserved to describe those potentials that have been derived in a purely *ab initio* manner. They do not assume a parametric functional form or require experimental data for their construction. The method for generating ECPs outlined here, follows the pioneering approach taken by Kahn *et al.* [142, 143]. In this work, the ECP was derived from the solutions of atomic Hartree-Fock calculations using a specific pseudo-orbital transformation. The majority of widely used ECPs, including the successful Los Alamos potentials employed in the present study [144]-[146], are based on this prescription.

The atomic Hartree-Fock equation for a valence orbital with angular momentum l may be written:

$$\left(-\frac{1}{2}\frac{\partial^2}{\partial r^2} - \frac{Z}{r} + \frac{l(l+1)}{2r^2} + V_{core} + V_{val}\right)\phi_l = \varepsilon\phi_l, \qquad (2.177)$$

where V_{core} and V_{val} represent the coulomb and exchange potentials due the core electrons and valence electrons, respectively. The third term describing the angular component of the kinetic energy, introduces an angular momentum dependence

into the formalism which is important for reasons which shall become apparent in due course. The core interaction terms and orthogonality constraint can be approximated by introducing a *local* effective core potential V_l^{ECP}, and an associated pseudo-orbital χ_l into the valence eigenvalue equation:

$$\left(-\frac{1}{2}\frac{\partial^2}{\partial r^2} - \frac{Z_{eff}}{r} + \frac{l(l+1)}{2r^2} + V_l^{ECP} + V'_{val}\right)\chi_l = \varepsilon\chi_l. \qquad (2.178)$$

Z_{eff} is the effective nuclear charge equal to the nuclear charge minus the number of core electrons, so the shielding is included in V_l^{ECP}. The tilde on $\tilde{V}_{val}$ has been added to indicate that the valence potential is evaluated over pseudo-orbitals rather than the original valence orbitals. Inversion of equation (2.178) yields an expression for the potential in terms of the pseudo-orbital:

$$V_l^{ECP} = \varepsilon_l + \frac{Z_{eff}}{r} - \frac{l(l+1)}{2r^2} + \frac{1}{2\chi_l}\frac{\partial^2\chi_l}{\partial r^2} - \frac{\tilde{V}_{val}\chi_l}{\chi_l}. \qquad (2.179)$$

If the pseudo-orbitals can be fixed according to some well-defined procedure then this expression can be used to generate a unique potential for each valence orbital of a given angular momentum. The problem, therefore, is not to find an appropriate potential but rather, to find an appropriate way to specify the pseudo-orbitals.

The developments of the previous sections do not stipulate what form the pseudo-orbital should take other than limiting it to an admixture of core and valence orbitals, equation (2.175). However, there are some reasonable conditions that could be enforced to specify the pseudo-orbital and make the problem more tractable to practical solutions:

- The valence pseudo-orbital should have no radial nodes.

A nodeless orbital is the lowest energy solution of the atomic Hartree-Fock equation (2.177) with the corresponding local equivalent potential. Therefore to ensure that χ is the lowest energy solution of equation (2.178) we require that it also be nodeless.

- The valence pseudo-orbital should be as smooth as possible.

An important practical consideration is that the valence-only problem should be amenable to solution in a reduced basis commensurate with the reduction to the valence space. Maximum basis set economy can be achieved by constructing the valence pseudo-orbital with the minimum number of spatial undulations.

- The valence pseudo-orbital χ should resemble the original Hartree-Fock valence orbital ϕ as close as possible.

Since χ is used to represent a valence electron, it seems sensible that a core admixture should not dominate the valence contribution. In particular, the pseudo-orbital should be close to the Hartree-Fock orbital in the outer part of the valence region where intra-molecular interactions are most important.

The approach used by Kahn *et al.* was to derive a set of numerical pseudo-orbitals directly from the many-valence electron orbital solutions of the atomic Hartree-Fock equations (2.177). This is the most reliable method since the local potential defined in equation (2.179) is only exact for the pseudo-orbital that generated it. By constructing the pseudo-orbitals in this way, the potentials they define hold out the hope of being transferrable to the molecular environment. A general scheme for the generation of ECPs is outlined below:

(i) Accurate numerical valence orbitals ϕ_l are obtained by solution of the atomic Hartree-Fock equations.

(ii) Smooth, nodeless pseudo-orbitals (χ_l) are derived from the numerical Hartree-Fock orbitals (ϕ_l), in a manner such that χ_l resembles as closely as possible ϕ_l in the outer-valence region.

(iii) Numerical potentials V_l^{ECP} are derived for each l from the transformation given by equation (2.179). This is equivalent to demanding that χ_l is a solution in the field of V_l^{ECP} with the same orbital energy ε_l as the Hartree-Fock orbital ϕ_l.

Several numerical prescriptions exist for producing smooth nodeless orbitals from the all-electron orbitals. Shape-consistent schemes such as that due to Christiansen *et al.* [148] are usually employed since they generate pseudo-orbitals which display the correct behaviour in the important outer-valence region. The ECP must be represented analytically to be generally useful in molecular calculations. The most popular representation is a Gaussian expansion of the type:

$$V_l^{ECP} = \sum_i A_i \frac{e^{-\alpha_i r^2}}{r^{n_i}} \tag{2.180}$$

where the parameters A_i, α_i and n_i are optimized by fitting the numerical potential. The numerical pseudo-orbitals are also fit with Gaussian functions to obtain valence basis sets for molecular orbital calculations.

The most important property of the local effective potential is its orbital angular momentum dependence. Atomic orbitals with the same angular momentum and different principle quantum number (e.g. $1s$ and $2s$) on the same centre are not orthogonal but orbitals of different angular momentum (ns, np, nd, etc.) are already orthogonal by symmetry. For this reason it is necessary to use different effective potentials for orbitals of different angular momentum in the same atom.

A further requirement is that there be a method for deciding what type of orbital a core potential is to act on. In particular, what is the symmetry of an orbital on one centre as judged from a centre which is the source of the effective potential? This problem can be solved using projection operators. The total ECP for an atom may be written:

$$\begin{aligned} V^{ECP} &= \sum_{l=0}^{\infty} V_l^{ECP} \mid l\rangle\langle l \mid, \\ &= V_s^{ECP}\hat{P}_s + V_p^{ECP}\hat{P}_p + V_d^{ECP}\hat{P}_d + \ldots, \end{aligned} \tag{2.181}$$

where V_l^{ECP} is the core potential experienced by a valence electron in an orbital of angular momentum l. The operator $\hat{P}_l$ projects out that part of the valence structure which is l-type and then applies the potential V_l^{ECP} to it. The potentials with l-values larger than the maximum in the core are all found to be very similar because the pseudopotential effects simulating orthogonality are not present. This latter fact means that equation (2.181) may be approximated by

$$V^{ECP} = V_L^{ECP} + \sum_{l=0}^{L-1}(V_l^{ECP} - V_L^{ECP}) \mid l\rangle\langle l \mid, \tag{2.182}$$

where L is one greater than the highest value of l found in the core.

As mentioned previously, the ECP formalism provides a convenient method for incorporating relativistic effects into molecular calculations. Kahn *et al.* [143] showed how the *ab initio* procedure for deriving ECPs could be extended to include relativistic effects on the valence orbitals. The method they employed was based on an approximate scheme developed by Cowan and Griffin [149] in which the mass-velocity and Darwin terms, and an averaged one-component treatment of spin-orbit coupling are added to the non-relativistic atomic Hartree-Fock equation. Numerical solution of this equation followed by a pseudo-orbital transformation analogous to the non-relativistic case leads to a set of l-dependent potentials which incorporate the major core-valence interactions of relativistic atomic structure. Since these effects are contained in the core potentials, the valence-electron calculations are non-relativistic in character and can be carried out using conventional techniques.

Effective core potentials should provide accurate results comparable to those obtained from *ab initio* all-electron calculations and for a fraction of the computational cost. However, in spite of its attractive features, the nature of the ECP method does automatically exclude certain effects from the calculation. The most important of these is probably the failure to take into account core-valence correlation, known as *core polarization*. To overcome this problem ECPs have been proposed which explicitly treat the outermost core electrons along with the valence electrons [146]. This increases the computational effort compared to the full-core

potentials since more basis functions will be needed to describe the inner orbitals, but the overall cost is still less than for a comparable all-electron calculation.

Chapter 3

Methods

3.1 Hardware and Software

The *ab initio* and DFT calculations in this work were carried out using the GAUSSIAN92/DFT computational chemistry programs [134]. The three-dimensional images of molecular orbitals and electron densities illustrated in Figures 5.11, 5.13 and 6.12 were generated with the GAUSSIAN graphical interface implemented in SPARTAN 4.0 [152]. Note that the representation of orbitals and densities obtained from ECP calculations is not a standard option in SPARTAN and some manipulation of the various input files is necessary to force the code to accept the data for graphical display. In particular, the element symbol for each heavy atom with N *valence* electrons must be changed in the archive file (file.arc) to the symbol corresponding to that element having a *total* of N core and valence electrons. For example, rhodium which formally has 9 valence electrons ($4d^8 5s^1$) is changed to fluorine which has a total of 9 valence and core electrons ($1s^2 2s^2 sp^5$).

Both the GAUSSIAN and SPARTAN codes were run on a Silicon Graphics Indigo workstation.

3.2 Basis sets

Apart from the particular model of electronic structure to be used, the most important choice in an *ab initio* or DFT calculation is the choice of basis set. The basis set determines the flexibility that electron density has to adapt to changing molecular situations and thus, the accuracy of results obtained by any method which operates within the framework of the LCAO formalism is critically dependent on the functions used to expand the molecular orbitals. For efficient computations, the choices of model and basis set have to be balanced. It would be imprudent, for

example, to employ a sophisticated correlation treatment combined with a minimal basis set. Also the cost of a calculation must be taken into account. The amount of computer resources (processor time, memory and disk usage) that is required, rises as something like the third or fourth power of the number of basis functions for the Hartree-Fock method. For the MP2 scheme the computational expenditure is greater, rising as at least the fifth power of this number. The Gaussian implementation of DFT is expected to scale in a similar way to the Hartree-Fock method.

For the calculation of the electronic structure of heavy atoms, we have used the Los Alamos relativistic effective core potentials and associated Gaussian bases due to Hay and Wadt [144]-[146]. These have been used with occasional enhancement throughout the present study. A full list of the bases along with a description of their contraction schemes is given in Table 3.1. Abbreviated codes have been assigned, which in subsequent chapters shall be used in place of the full name.

The minimal basis (MB) which uses the lowest number of functions necessary to accommodate the electrons of a neutral atom (i.e. one spatial function for each pair of electrons), can only realistically be applied for qualitative calculations. To improve the flexibility of the basis, a split-valence or "double zeta" (DZ) contraction scheme employing two functions for each atomic orbital can be used. The LANL1DZ basis is used in this work for the majority of the geometry optimizations, frequency evaluations and for the calculation of reaction paths. The more sophisticated bases are usually reserved for correlated single-point energy calculations on the stationary points located with the standard basis.

The first step in improving a basis beyond the split-valence level is the addition of higher angular momentum functions to the basis for each atom. The purpose of *polarization functions* is to allow density to be non-uniformly displaced away from the atomic centres. This is important in the description of polar molecules and for systems which do not have highly localised bonds. Polarization functions are also essential for a good description of electron correlation. The polarization basis set that we have constructed, denoted by DZ*, augments the standard DZ basis with an extra set of *d*-type functions for the heavy atoms and *p*-type functions for hydrogen. For the description of anionic species and diffuse electron distributions, it is usually recommended that a set of *diffuse functions* be added to the basis set. These are included separately in the basis denoted as DZ+ and in combination with polarization functions in the DZ*+ basis. Anions pose a special problem since the extra electron (or electrons) is typically only weakly bound. Diffuse functions are chosen with low orbital exponents (0.01 – 0.1), such that the long-range behaviour of molecular orbitals with energies close to the ionization limit can be described. Exponents of the polarization and diffuse functions used in the present study are collected in Table 3.2.

Table 3.1: ECP Gaussian basis sets used in this work.

Basis name	Code	Description
LANL1MB	MB	Full-core minimal basis contraction scheme. Each valence orbital of the heavy atoms Rh, Ir (nd, $(n+1)s$, $(n+1)p$) and I (ns and np) are described by *one* basis function. First row atoms, C, O and H are described by the STO-3G all-electron basis.
LANL1DZ	DZ	Full-core double zeta contraction scheme. Each valence orbital of the heavy atoms Rh, Ir (nd, $(n+1)s$, $(n+1)p$) and I (ns and np) are described by *two* basis functions. First row atoms, C, O and H are described by the split-valence Dunning 9-5V all-electron basis.
LANL1DZ*	DZ*	Full-core DZ basis plus polarization. A single high angular momentum function is added to the DZ basis of each atom.
LANL1DZ+	DZ+	Full-core DZ basis plus diffuse. One diffuse function of low exponent is added to the DZ basis of each atom.
LANL1DZ*+	DZ*+	Full-core DZ basis plus polarization plus diffuse. One high angular momentum and one diffuse function of low exponent is added to the DZ basis of each atom.
LANL2DZ	DZ2	Semi-core double zeta contraction scheme. Same as DZ except the metal ns and np electrons are also treated explicitly.
LANL2DZ*	DZ2*	Semi-core DZ2 basis plus polarization. A single high angular momentum function is added to the DZ2 basis of each atom.

Table 3.2: Orbital exponents of polarization and diffuse functions used in conjunction with the LANL1DZ/LANL2DZ bases.

Atom	Polarization fn.(*)	Exponent	Diffuse fn.(+)	Exponent
Rh	d^a	1.000[b]	d	0.059[c]
Ir	d^a	1.000[b]	d	0.055[c]
I	d	0.250[d]	p	0.029[c]
C	d	0.600[e]	p	0.034[f]
O	d	1.154[e]	p	0.059[f]
H	p	1.100[g]	sp	0.036[g]

[a] We are prevented from using a set of f-type polarization functions on the transition metal atoms by lack of f-derivative software at this time.

[b] Arbitrary exponent.

[c] Diffuse function exponent generated by an even tempering procedure [153].

[d] Exponent value is intermediate between the values give by Huzinaga for I and I^- [154].

[e] Reference [154].

[f] Reference [155].

[g] Reference [134].

A non-trivial problem associated with the use of ECPs is concerned with how one defines the valence distribution. The LANL1DZ basis is full-core in the sense that it only computes electrons that are formally in the valence shell, namely the nd, $(n+1)$s and $(n+1)p$ electrons. As mentioned in the previous chapter, the neglect of core-valence correlation (core polarization), which is implicit in the frozen-core approximation, is one of the greatest limitations of the ECP method. This deficiency may become significant for the transition metals atoms to the right of the periodic table; the large correlation energy of the nd shells means that even a slight mixing of the core ns and np electrons could result in large changes to the valence correlation energy. To account for this effect, along with the contraction of the valence distribution due to core-valence correlation, various authors have proposed the use of semi-core ECPs which also include the transition metal ns and np shells in the valence space. The semi-core extension to the standard Los Alamos split-valence scheme is called the LANL2DZ basis (DZ2) [146]. This can be augmented with extra functions to construct an approximate semi-core polarization basis, denoted as DZ2*. The approach we have adopted in the present study, is simply to see which ECP and bases give the better results for geometries and energies and to use them accordingly. Unfortunately, this has given rise to a rather nonuniform treatment since the results have generally indicated that for rhodium the full-core basis gives the superior description, whereas for iridium the semi-core basis is preferred. There are sporadic indications in the literature that this type of problem has been encountered by other workers (see for example, reference [263]).

3.3 Density Functionals

With an ever increasing number of functionals becoming available and their implementation in various new DFT packages becoming more frequent, some confusion has arisen over their definition and content. Various authors refer to different functionals by different acronyms and so in any DFT study it is important to provide a clear definition of the functionals that have been employed. Five different exchange-correlation schemes were used in this work:

- Hartree-Fock-Slater HFS.
  This is the simplest DFT scheme which was introduced specifically as an approximation to the Hartree-Fock method [106]. It incorporates an exchange-only functional based on the results for a homogeneous electron gas. This method is sometimes also referred to as Local Spin Density exchange. It is important to differentiate between this method and the closely related X_α method; X_α employs an empirical coefficient of 0.7 in the exchange potential, whereas the Slater scheme uses the original theoretical coefficient of 2/3 (see

section 2.2.3).

- Local Density Approximation **LDA.**
  The LDA functional incorporates the Slater exchange functional above, plus the local correlation functional of Vosko, Wilk and Nusair (VWN) [105] which is a parameterization of exact results for the uniform electron gas. This scheme is synonymous with the SVWN method and the spin unrestricted formalism is often referred to as the Local Spin Density Approximation (LSDA or LSD).

- Becke Lee-Yang-Parr **BLYP.**
  BLYP includes both exchange and correlation with non-local terms. Becke's 1988 exchange functional [124] incorporating a gradient correction to the Slater exchange is combined with the gradient-corrected correlation functional of Lee, Yang and Parr (LYP) [125].

- Becke-Half-And-Half **BHANDH**
  This is the simplest hybrid scheme which includes 50% (exact) Hartree-Fock exchange and 50% Hartree-Fock-Slater exchange. Note that the hybrid schemes available in GAUSSIAN are not those proposed by Becke [127] but involve different mixtures of exact exchange with local and gradient-corrected exchange correlation functionals. The functional implemented in the GAUSSIAN code is

$$0.5 \times E_X^{HF} + 0.5 \times E_X^{HFS} + E_C^{LYP}. \tag{3.1}$$

- Becke-three-parameter-LYP **Becke3LYP**
  The three-parameter hybrid exchange functional also proposed by Becke [129] is combined with both local and non-local correlation terms given by the LYP and VWN functionals. The Becke3LYP functional implemented has the general form:

$$A \times E_X^{HFS} + (1-A) \times E_X^{HF} + B \times E_X^{Becke} + C \times E_C^{LYP} + (1-C) \times E_C^{VWN}, \tag{3.2}$$

  where E_X^{Becke} is the non-local exchange contribution from Becke's 1988 functional [124]. The constants A, B and C are those determined by Becke by fitting heats of formation. The VWN functional provides the excess local correlation required to balance the local exchange.

In addition to the particular choice of exchange-correlation scheme, the results of DFT calculations are also dependent on the mesh size over which numerical integration of the functional is carried out. In most cases we have employed a standard grid, which has about 3000 integration points per atom. The int=finegrid option was generally not used because this tended to make the calculation rather more expensive and also appeared to suffer from greater convergence problems.

Previous DFT studies on strongly bound ground state molecules have indicated that geometries, harmonic vibrational frequencies and energetics obtained by these methods are generally favourable compared to experiment and with those obtained by conventional *ab initio* techniques [96]-[99]. In one of these studies [99], the BLYP functional was reported to give the best overall performance out of a series of pure-DFT functionals for the structure and properties of a wide range of small molecules. Approximate DFT methods incorporating non-local corrections to the density have also been reported to provide good estimates of metal–ligand bond lengths and bond energies in transition metal complexes [96]. A recent LANL1DZ ECP investigation of the structure of *trans*-$[Rh(PH_3)_2(CO)Cl]$ and the energetics involved in the halide exchange reaction with fluoride ions found that the LDA scheme yielded the best geometry while the BLYP functional yielded the most reliable energetics [156]. Information regarding the performance of the hybrid functionals has been less well documented but preliminary indications are that these methods can provide a significant improvement for some of the difficult cases [113, 114]. Recent tests have also found the Becke3LYP combination to perform well for a wide range of systems [157]. Relatively few studies on the performance of DFT applied to transition states and reaction barriers for transition metal systems have appeared in the literature. Those that have, are generally agreed that non-local corrections are required for an adequate description. The local approximation tends to overbind interacting groups leading to barriers heights which are too low and transition structures which are in significant error compared to those obtained by correlated *ab initio* methods [158]-[162].

3.4 Optimization and Characterization of Stationary Points and Reaction Pathways

In general, the potential energy surface of an N-atom molecular system is a function of $3N-6$ degrees of freedom. For all but the simplest molecules (diatomics, for example) this is conceptually and computationally unmanageable. However, theoretical studies are usually only concerned with a small portion of this surface. Regions of importance are those that correspond to minima, representing stable or metastable conformations, regions that correspond to transition states, and those intermediate points that link reactants and transition states along a reaction pathway.

The stationary points on a potential energy surface have an energy gradient equal to zero. Mathematically, this is

$$\frac{\partial E(\mathbf{r})}{\partial r_i} = 0 \qquad i = 1, 2, \ldots, 3N-6 \tag{3.3}$$

where the $\{r_i\}$ are a set of $3N-6$ internal co-ordinates used to specify the geometry of an N-atom molecule. The condition (3.3) may equivalently be defined as the conformation for which the forces acting on each atom are equal to zero. Stationary points can be distinguished from one another by construction and diagonalization of the force constant matrix, called the Hessian, the elements of which are the second derivatives of the energy with respect to the internal co-ordinates:

$$\frac{\partial^2 E(\mathbf{r})}{\partial r_i \partial r_j}, \qquad i,j = 1,2,\ldots,3N-6. \tag{3.4}$$

If the eigenvalues of this matrix are all positive, the stationary point is a local minimum corresponding to a stable molecular conformation. An equilibrium structure corresponding to a global minimum is given by the lowest energy conformation possible for a particular isomeric species. If the eigenvalues are all negative, the energy is a local maximum, a situation of little chemical interest. The term saddle point is usually reserved to describe those stationary points with *one and only one* negative eigenvalue. These correspond to regions in which the energy is at a minimum for all but one independent direction; in this one direction, represented by a linear combination of the internal co-ordinates, it is at a maximum. If the saddle point links two minima by a reaction pathway then it is also termed a transition state. The direction corresponding to the negative eigenvalue of the Hessian along which the energy is a maximum is called the reaction co-ordinate.

Numerous efficient algorithms are available for the optimization of molecular geometries. For equilibrium structures, it is often not even essential that the initial guess supplied to the calculation be especially close to the optimum geometry; bond lengths within 0.3 Å and angles within 20° are usually sufficient. However, care should be taken in the specification of the geometrical parameters to be varied, with particular attention being paid to the degree of molecular symmetry that is imposed. Too much symmetry may prevent the structure from reaching its global minimum. The optimization algorithm employed in this work is the "BERNY" algorithm (after H. Bernhard Schlegel, who developed the the original code [163]). The BERNY method uses analytically calculated atomic forces and a guessed force constant matrix which is continually updated during the optimization, to predict the position of the minimum-energy structure. A modified version of the BERNY algorithm is also used to locate transition structures, although as shall be described subsequently, the procedure involves a number of extra steps and complete success is never guaranteed. Once a geometry has been optimized a full calculation of the force constant matrix can be performed to yield the frequencies and associated normal mode vibrations. For transition metal complexes which require a pseudopotential description of the core states, analytical second derivatives are currently not available and the frequencies have to be evaluated numerically by finite difference methods.

Transition state species are not subject to direct experimental scrutiny. Qualitative structural information may sometimes be inferred from kinetic isotope effects and activation entropies. However, the only way that the geometries of reaction transition structures may be obtained is from theory. In some circles this is still considered to be somewhat of a black-art. Part of the problem is that it is difficult to ensure movement along a surface that exactly meets the conditions of a simple saddle point. In addition, a difficulty may reside in the fact that wavefunctions for a transition state may be considerably more complex than those that describe minima. A prescription for locating transition states that we have found to be generally successful, albeit with some coaxing, is as follows:

(i) Guess the geometry of the transition state paying particular attention to the parameters that are expected to make a significant contribution to the reaction co-ordinate.

(ii) Freeze the reaction co-ordinate parameters and perform a partial minimizing optimization on the rest of the geometry. For example, optimize the bond lengths for spectator atoms and ligands which are not expected to play a major role in the reaction.

(iii) Unfreeze all of the parameters and carry out a frequency calculation. This will indicate whether the reaction co-ordinate parameters chosen correspond to an area on the potential energy surface with negative curvature. If the calculation yields a single negative frequency and the forces are all reasonably low (< 0.05) then the TS optimization has a good chance of success and the next step may be attempted. Note that two negative frequencies usually indicates that too much symmetry has been imposed which is preventing the structure from reaching a minimum in one or more of the variables. At this point it may be necessary to recast the original guess and start anew from point (i).

(iv) Providing the results of the last step were favourable, one can then move directly to trying to locate the full unconstrained TS by initiating the BERNY TS algorithm with an estimate of the force constants supplied by the previous frequency calculation. This is executed in the GAUSSIAN code by specifying opt=(ts,RCFC) on the route card. *A good estimate of the force constants is the key factor for successfully locating a TS.* By default, the algorithm will terminate if the number of negative eigenvalues of the Hessian is not equal to one, i.e. do not immediately correspond to an area of saddle point curvature. This can be overruled by specifying the TS option opt=noeigentest. Combining all of these commands, a typical route card for this step would therefore look like:

```
%chk=file.chk
```

```
# HF/LANL1DZ guess=read geom=checkpoint opt=(ts,noeigentest,RCFC),
```

where guess=read and geom=checkpoint indicate that the current density and geometry are to be read, as are the force constants, from the checkpoint file file.chk containing this information generated in step (iii). If this job fails then it may be necessary to increase the number of optimization cycles or start again from step (i) with an improved guess for the geometry.

(v) To confirm that the structure obtained from the previous calculation is indeed a true saddle point maximum it is necessary to perform one additional frequency calculation. If this yields a single imaginary frequency and the associated normal mode is consistent with the the reaction being considered, then the procedure has been successful.

Of course, the procedure outlined above does not guarantee that the TS located corresponds to the lowest energy pathway for a given reaction and it may be necessary to examine several different conformations of reacting molecules in order to determine the most favourable one.

For complete confirmation that a saddle point is a transition state for a particular reaction, methods exist for establishing the downhill reaction path connecting the saddle point with the two minima. Among them, the simplest is based on the selection of the steepest descent pathway, the so-called *intrinsic reaction co-ordinate* (IRC) [164]. This method uses the principle of least motion involving the smallest change in the nuclear positions and electronic configuration to predict the easiest reaction pathway. The intermediate points calculated along an IRC can often yield valuable information about the course of a reaction which cannot be obtained from either the reactants or transition state structures.

3.5 Solvent Effects: The SCRF Model

Quantum mechanical calculations have traditionally been carried out on static isolated molecules in *vacuo*. While such calculations can often yield very good results for the study of molecules in the gas phase, they are generally not appropriate for describing systems in solution. All of the experimental data that has been reported for the Monsanto catalytic cycle relates to the process occurring in solution. Indeed, some complex dependence on the nature of the solvent has been observed. It would therefore be desirable for the purposes of comparing results with experiment and of some theoretical interest to obtain an estimate of the solvent effects in this system.

In studying solvent effects one may follow two general strategies:

- Explicitly calculate individual solvent molecules at specific sites around the molecule under investigation.

This is the so-called discrete representation of the solvent which examines the formation of kinetically stable solvated complexes. Well known examples include hydrogen-bonded complexes and acceptor-donor complexes between the solvent and solute molecules. While giving useful information about the complex solvent interactions at the molecular level, this approach has the major disadvantage in that one usually has to consider a large number of solvent molecules and interactions in order to adequately describe both the short-range and long-range influence of the medium. This type of approach is therefore more suited to semi-empirical or molecular simulation techniques and has not found widespread application in *ab initio* work where the calculation of isolated molecules is usually computationally demanding in itself.

- Introduce a model continuum approximation for the medium to describe the static electrostatic effect of the bulk solvent on any given molecular conformation of the solute.

This is the so-called continuum representation of the solvent which relies on the fact that a microscopic chemical system can be completely separated from the macroscopic medium. This approximation is only really valid if fluctuations in the solvent take place instantaneously with the solute motion of reacting molecules. The solvent is equilibriated for each given geometry and so only plays a passive role in the chemical process. Note that although this model does not calculate specific interactions between the solvent and solute, it does partly account for them, because in an equilibriated system a significant component of a specific interaction is electrostatic in origin.

In the present study we have employed the latter continuum model as implemented in the GAUSSIAN suite of quantum chemistry programs. This is the self-consistent reaction field (SCRF) technique [165]-[168] which is a self-consistent extension of the reaction field model due to Onsager [169]. In the SCRF model, the solute is placed in a spherical cavity of radius a_0, immersed in a continuous medium of uniform dielectric constant ϵ_r, Figure 3.1. A dipole in the molecule will induce a dipole in the medium, and the resulting electric field applied to the solute by the solvent will in turn interact with the molecular dipole leading to a net stabilization. The electric field generated in this way is termed the reaction field.

Within the framework of the molecular orbital approximation, the electrostatic solvent effect may be taken as an additional term, $\hat{H}_1$, in the Hamiltonian of the isolated molecule, $\hat{H}_0$:

$$\hat{H}' = \hat{H}_0 + \hat{H}_1. \tag{3.5}$$

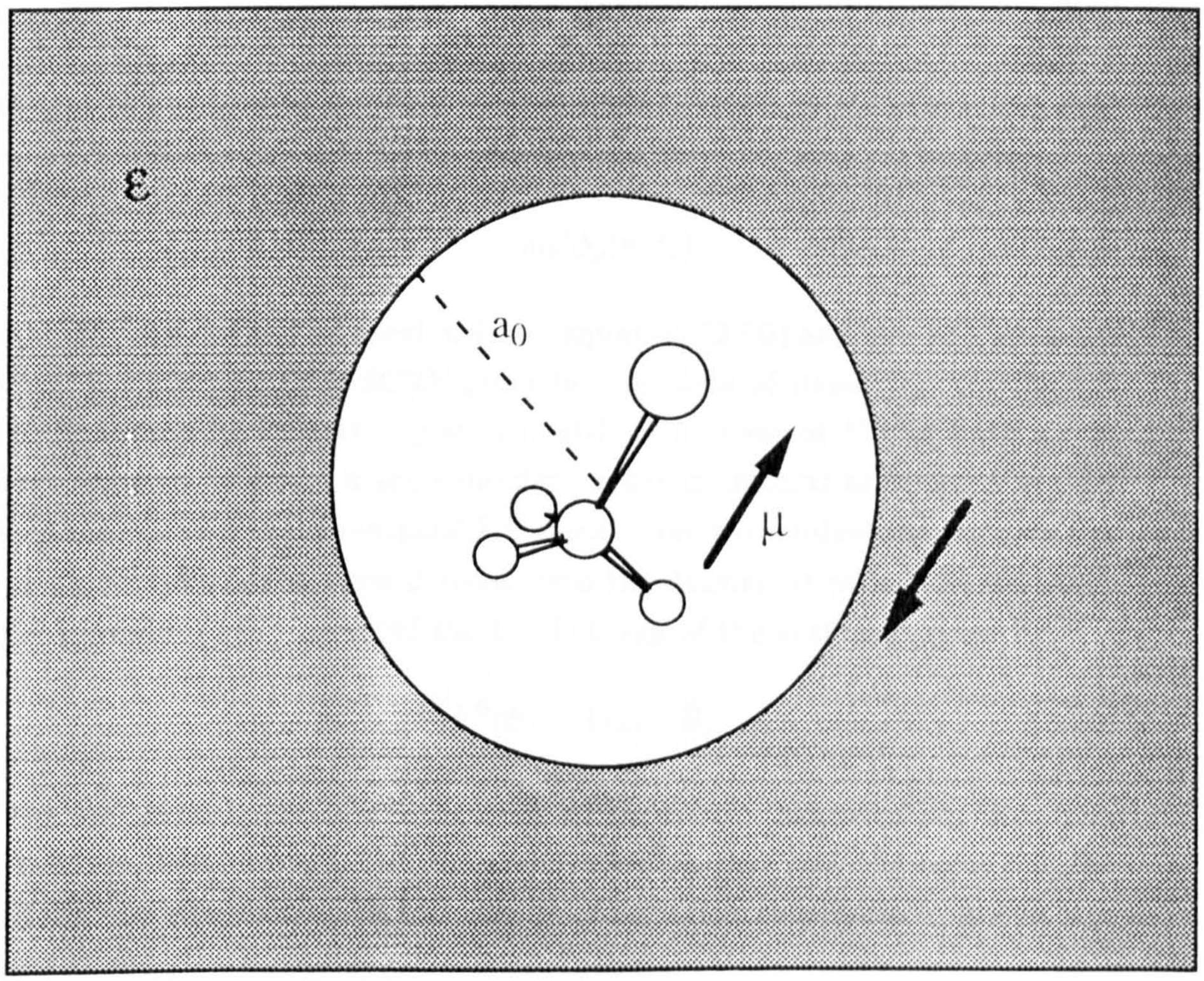

Figure 3.1: Onsager reaction field model. The solute is placed in a spherical cavity of radius a_0 surrounded by a continuous medium of uniform dielectric constant ϵ_r.

$\hat{H}_1$ is a perturbation describing the coupling between the molecular dipole operator $\hat{\mu}$, and the reaction field, $\vec{R}$:

$$\hat{H}_1 = -\hat{\mu} \cdot \vec{R}, \tag{3.6}$$

The reaction field is proportional to the molecular dipole moment $\vec{\mu}$

$$\vec{R} = -g\vec{\mu}. \tag{3.7}$$

The value of the constant g, measuring the strength of the reaction field, depends on the dielectric constant of the medium ϵ_r, and on the cavity radius, a_0 [169]:

$$g = \frac{2(\epsilon_r - 1)}{(2\epsilon_r + 1)} a_0^3. \tag{3.8}$$

For the case of a self-consistent field wavefunction, the effects of the reaction field can be incorporated as an additional one-electron term in the Fock matrix:

$$F'_{\mu\nu} = F^0_{\mu\nu} - g\vec{\mu}\langle\phi_\mu|\hat{\mu}|\phi_\nu\rangle, \tag{3.9}$$

where the $F^0_{\mu\nu}$ are defined as previously by equation (2.60) and the $\{\phi\}$ are basis functions. The Hartree-Fock SCRF procedure consists of iteratively solving the modified Roothaan-Hall matrix equations, with F' in place of F^0, for both a self-consistent reaction field and a self-consistent set of molecular orbitals. The only extra step compared to a conventional HF calculation is to update the Fock matrix with the dipole interaction term derived from the density at each SCF iteration. After the procedure has converged the total energy of the system is given by

$$E' = \langle\Psi|\hat{H}^0|\Psi\rangle - 1/2\vec{\mu} \cdot \vec{R}, \tag{3.10}$$

where the first term is the internal energy of the solute incorporating the effect of the reaction field through the perturbed wavefunction and the second is the electrostatic contribution to the free energy of solvation calculated from the self-consistent $\vec{R}$ and $\vec{\mu}$.

A self-consistent reaction field may also be applied to post-HF methods. The MP2 SCRF method implemented in GAUSSIAN is a more expensive scheme since several, rather than just one, SCF and MP2 calculations have to be carried out in order to obtain correlated energies which incorporate the effect of the reaction field exactly [165]. A generalized MP2 density is used and this requires that a macro iteration be performed; SCRF orbitals and modified Fock integrals are fed into the MP2 algorithm from which a generalized density is evaluated and a new set of modified integrals are produced to self-consistency.

The only adjustable parameter in an SCRF calculation is the cavity radius a_0. This is chosen to reflect the greatest dimension of the solute molecule under investigation, with a small correction usually being applied to account for the nearest

approach of solvent molecules. Note that under the assumption of a spherical cavity, systems having a zero dipole moment will not exhibit solvent effects in this model. This is an inherent limitation of the SCRF technique. Recent work in this area has focused on obtaining better approximations to the form of the reaction field cavity [170] and on developing theories which account for the inhomogeneity of the solvent in the vicinity of the solute molecule [171].

3.6 Population Analysis

Two different schemes have been employed for the analysis of electron densities obtained from molecular orbital calculations: (i) Mulliken analysis which assigns electron populations to atomic orbitals associated with atomic fragments; (ii) Fragment Molecular Orbital (FMO) analysis which assigns electron populations to molecular orbitals associated with molecular fragments. These methods are described below.

3.6.1 Mulliken Population Analysis

For a quantitative description of the bonding in a molecule it is desirable to allocate the electrons in some fractional manner among the constituent atoms and bonds. It may be useful, for example, to calculate the electronic charge associated with a particular atom in order that a quantitative meaning be given to such concepts as electron donating or withdrawing ability. Methods for doing this, based on a simple partitioning of the density matrix, were originally proposed by Mulliken [172].

For a single determinant wavefunction in which the orbitals are expanded in terms of a set of K basis functions $\{\phi_\mu\}$, the total electron density may be written as

$$\rho(\mathbf{r}) = \sum_{\mu}^{K}\sum_{\nu}^{K} P_{\mu\nu}\phi_\mu\phi_\nu^*, \tag{3.11}$$

where the $P_{\mu\nu}$ are elements of the density matrix defined previously. Integration of this expression leads to

$$\int \rho(\mathbf{r})d\mathbf{r} = \sum_{\mu}^{K}\sum_{\nu}^{K} P_{\mu\nu}S_{\nu\mu} = \mathrm{tr}(\mathbf{PS}) = N, \tag{3.12}$$

where the $S_{\nu\mu}$ are elements of the overlap matrix. Thus, the total electron count can be decomposed into individual terms $P_{\mu\nu}S_{\nu\mu}$, summed over the atomic basis functions. Equation (3.12) can be written as a sum of diagonal and off-diagonal

components:

$$\sum_{\mu}^{K}\sum_{\nu}^{K} P_{\mu\nu}S_{\nu\mu} = \sum_{\mu}^{K} P_{\mu\mu}S_{\mu\mu} + 2\sum_{\mu}^{K}\sum_{\nu>\mu}^{K} P_{\mu\nu}S_{\nu\mu} = N. \tag{3.13}$$

Given that the basis functions are normalized, the diagonal terms are just $P_{\mu\mu}$, and can be interpreted as the number of electrons directly associated with a particular function ϕ_μ. This is termed the net orbital population of ϕ_μ, which is assigned to that atom on which the basis function is centred. The off-diagonal components occur in pairs, $P_{\mu\nu}S_{\nu\mu}$ and $P_{\nu\mu}S_{\mu\nu}$, of equal magnitude. Their sum, $2P_{\mu\nu}S_{\nu\mu}$ is referred to as an overlap population. When both ϕ_μ and ϕ_ν reside on the same atom, it is reasonable to assign the overlap population to that atom. However, the problem remains of how to partition the remaining terms for the case when the ϕ_μ and ϕ_ν reside on different atoms. There is no unique way of partitioning the charge distribution and so any scheme which performs this task must necessarily be arbitrary.

The recipe suggested by Mulliken was simply to give each of the atomic centres half of the total overlap population, i.e. divide the last term in equation (3.13) into two equal parts and assign them accordingly. Within this scheme a gross population q_μ for each basis function can be defined according to

$$q_\mu = P_{\mu\mu} + \sum_{\mu\neq\nu} P_{\mu\nu}S_{\nu\mu}. \tag{3.14}$$

Atomic populations, q_A, and atomic charges, Q_A, follow from this definition:

$$q_A = \sum_{\mu\in A} q_\mu \qquad \textit{and} \qquad Q_A = Z_A - q_A, \tag{3.15}$$

where the summation ranges over all functions ϕ_μ on atom A and Z_A is the atomic number of A. It is also often useful to examine the total overlap population between two atoms A and B. This may be defined in a similar manner as

$$q_{AB} = \sum_{\mu\in A}\sum_{\nu\in B} 2P_{\mu\nu}S_{\nu\mu}, \tag{3.16}$$

where in this case, summation is carried out for all ϕ_μ on A and all ϕ_ν on B. Total overlap populations provide quantitative information about the binding between atoms. A large positive value for q_{AB} indicates a significant electron population in the bonding region between A and B. Conversely, a negative value implies that electrons have been displaced away from the interatomic region, indicating an antibonding interaction.

The fact that the Mulliken scheme is arbitrary, means that the populations obtained in this way can only be used as a qualitative measure of the bonding in a particular molecule. However, comparison of the electron populations for related

molecules, say along a reaction pathway, can usually yield a meaningful physical picture of bonding changes.

3.6.2 Fragment Molecular Orbital Analysis

The Mulliken partitioning scheme of electron densities only provides information about the distribution of electrons between atomic orbitals. A more suitable method for application to chemical reactions, would be to calculate the electron populations associated with interacting *molecular orbitals*. For example, in the case of an associative reaction, it is desirable to know which pair of molecular orbitals centred on different fragments contribute greatest to the bond formation. In simple reactions between organic substrates these are usually just the frontier orbitals. In reactions involving transition metal species, however, several orbitals closely matched in energy may make a significant contribution. Consequently, simple frontier arguments cannot be applied and an explicit quantitative analysis is required to identify the key orbital interactions.

In a fragment molecular orbital population analysis, the molecular orbitals of a composite system are expanded in terms of the molecular orbitals of the isolated fragments. In the simplest case of a composite molecule formed from two interacting fragments A and B, this can be realized by writing

$$\psi_i(AB) = \sum_a D_{ai}\psi_a(A) + \sum_b D_{bi}\psi_b(B). \tag{3.17}$$

To simplify the discussion we assume that both A and B are closed-shell molecules in their ground states. The expansion (3.17) can be written in matrix notation as

$$\Psi_{\mathbf{AB}} = (\Psi_{\mathbf{A}}\ \Psi_{\mathbf{B}}) \begin{pmatrix} \mathbf{D^A} \\ \mathbf{D^B} \end{pmatrix} \tag{3.18}$$

and we require the matrices of coefficients $\mathbf{D}$. Now, the canonical molecular orbitals for a composite system A–B in terms of atomic orbital basis functions can be obtained from a standard Hartree-Fock calculation. The AO coefficient matrix can be truncated to include just the occupied orbitals and partitioned such that

$$\Psi_{\mathbf{AB}} = (\Phi_{\mathbf{A}}\ \Phi_{\mathbf{B}}) \begin{pmatrix} \mathbf{C^A_{AB}} \\ \mathbf{C^B_{AB}} \end{pmatrix}. \tag{3.19}$$

The canonical MOs for the isolated fragment systems A and B can also be obtained:

$$\Psi_{\mathbf{A}} = \Phi_{\mathbf{A}}\mathbf{c_A} \qquad \textit{and} \qquad \Psi_{\mathbf{B}} = \Phi_{\mathbf{B}}\mathbf{c_B}. \tag{3.20}$$

In general, the square coefficient matrices $\mathbf{c_A}$ and $\mathbf{c_B}$ will both have a nonzero

inverse such that

$$\Phi_{\mathbf{A}} = \Psi_{\mathbf{A}} \{\mathbf{c_A}\}^{-1} \qquad \textit{and} \qquad \Phi_{\mathbf{B}} = \Psi_{\mathbf{B}} \{\mathbf{c_B}\}^{-1}. \tag{3.21}$$

Substituting these latter equations into (3.19) and rearranging gives

$$\Psi_{\mathbf{AB}} = (\Psi_{\mathbf{A}}\ \Psi_{\mathbf{B}}) \begin{pmatrix} \{\mathbf{c_A}\}^{-1}\, \mathbf{C}^{\mathbf{A}}_{\mathbf{AB}} \\ \{\mathbf{c_B}\}^{-1}\, \mathbf{C}^{\mathbf{B}}_{\mathbf{AB}} \end{pmatrix}. \tag{3.22}$$

Comparing this result to equation (3.18). we therefore obtain a simple expression for the fragment MO coefficients in terms of quantities that are readily available from calculations performed in the AO basis:

$$\mathbf{D^A} = \{\mathbf{c_A}\}^{-1}\, \mathbf{C}^{\mathbf{A}}_{\mathbf{AB}} \qquad \textit{and} \qquad \mathbf{D^B} = \{\mathbf{c_A}\}^{-1}\, \mathbf{C}^{\mathbf{B}}_{\mathbf{AB}}. \tag{3.23}$$

The density matrix can be written in terms of the MO basis as

$$\mathbf{R} = \begin{pmatrix} \mathbf{R^{AA}} & \mathbf{R^{AB}} \\ \mathbf{R^{BA}} & \mathbf{R^{BB}} \end{pmatrix}, \tag{3.24}$$

where the elements are matrices defined by:

$$\mathbf{R}^{\alpha\beta} = \mathbf{D}^{\alpha}\mathbf{D}^{\beta\dagger} \qquad \alpha,\beta = \mathbf{A},\mathbf{B}. \tag{3.25}$$

An overlap matrix over fragment MOs can be constructed in a similar way:

$$\mathbf{O} = \begin{pmatrix} \mathbf{O^{AA}} & \mathbf{O^{AB}} \\ \mathbf{O^{BA}} & \mathbf{O^{BB}} \end{pmatrix}, \tag{3.26}$$

where the elements are the partitioned blocks of the AO overlap matrix for the composite system A–B transformed to the MO basis according to:

$$\mathbf{O}^{\alpha\beta} = \mathbf{c}^{\dagger}_{\alpha}\mathbf{S_{AB}}^{\alpha\beta}\mathbf{c}_{\beta} \qquad \alpha,\beta = \mathbf{A},\mathbf{B}. \tag{3.27}$$

The elements $(\mathbf{O^{AB}})_{ab} = (\mathbf{O^{BA}})^{\dagger}_{ba}$ give the overlap populations between the molecular orbitals centred on fragment A and B, and thus, can be used to determine which molecular orbitals play a significant role in the interaction when the composite system is formed.

Fragment molecular orbital occupation numbers may now be determined by constructing the product of the density and overlap matrices and employing a suitable partitioning scheme. For a set of normalised MOs we have

$$\mathrm{tr}(\mathbf{RO} = N, \tag{3.28}$$

where N represents the total number of electrons in the combined system. Discarding the off-diagonal block matrices which are not included in the trace, this

can be expanded as

$$\mathrm{tr}(\mathbf{RO}) = \mathrm{tr}(\mathbf{R}^{\mathbf{AA}}\mathbf{O}^{\mathbf{AA}} + \mathbf{R}^{\mathbf{AB}}\mathbf{O}^{\mathbf{BA}}) + \mathrm{tr}(\mathbf{R}^{\mathbf{BB}}\mathbf{O}^{\mathbf{BB}} + \mathbf{R}^{\mathbf{BA}}\mathbf{O}^{\mathbf{AB}}). \quad (3.29)$$

Now, since

$$\mathbf{R}^{\mathbf{AB}} = \mathbf{R}^{\mathbf{BA}\dagger} \qquad \textit{and} \qquad \mathbf{O}^{\mathbf{AB}} = \mathbf{O}^{\mathbf{BA}\dagger}, \quad (3.30)$$

the trace of the matrix products mixing the orbitals of A and B are equal:

$$\mathrm{tr}(\mathbf{R}^{\mathbf{AB}}\mathbf{S}^{\mathbf{BA}}) = \mathrm{tr}(\mathbf{R}^{\mathbf{BA}}\mathbf{S}^{\mathbf{AB}}). \quad (3.31)$$

This suggests a simple recipe, analogous to the Mulliken scheme, for partitioning equation (3.29) into seperate terms representing the number of electrons associated with each fragment in the interacting system. Accordingly, we may define the following quantity as the number of electrons associated with fragment A:

$$N_A = \mathrm{tr}(\mathbf{R}^{\mathbf{AA}}\mathbf{O}^{\mathbf{AA}}) + \mathrm{tr}(\mathbf{R}^{\mathbf{AB}}\mathbf{O}^{\mathbf{BA}}), \quad (3.32)$$

with a similar expression for fragment B:

$$N_B = \mathrm{tr}(\mathbf{R}^{\mathbf{BB}}\mathbf{O}^{\mathbf{BB}}) + \mathrm{tr}(\mathbf{R}^{\mathbf{BA}}\mathbf{O}^{\mathbf{AB}}). \quad (3.33)$$

Expressions for the occupation numbers of fragment molecular orbitals follow from these definitions. The gross population of a molecular orbital Ψ_a on fragment A is

$$q_a = (\mathbf{R}^{\mathbf{AA}}\mathbf{O}^{\mathbf{AA}})_{aa} + (\mathbf{R}^{\mathbf{AB}}\mathbf{O}^{\mathbf{BA}})_{aa}, \quad (3.34)$$

and likewise, the gross population of an orbital Ψ_b on B is given by

$$q_b = (\mathbf{R}^{\mathbf{BB}}\mathbf{O}^{\mathbf{BB}})_{bb} + (\mathbf{R}^{\mathbf{BA}}\mathbf{O}^{\mathbf{AB}})_{bb}. \quad (3.35)$$

Fragment MO occupation numbers provide quantitative information about bond formation between reacting molecules. In particular, examination of these quantities should provide an indication of the number of electrons donated and accepted with regard to each MO, as well as the overall amount of charge transferred between the two reactants.

3.7 Secondary α-Deuterium Kinetic Isotope Effects

Due to the unreasonable computational demands of sophisticated models of electronic structure, a large proportion of the calculations in any study of a reactive process are inevitably carried out at a low level of theory. Simple models can usually adequately reproduce the qualitative features of molecular structure but the energetics are always potentially misleading. Hartree-Fock estimates of activation

barriers are generally too high, deviating from experiment typically by about 50 kJ mol^{-1}. Within such margins of error it is difficult to prove, for example, that a computed transition state and reaction co-ordinate represent the lowest energy pathway for a given process. A more reliable approach would be to relate the computed structures rather than the energetics to some experimentally observable property.

A sensitive test of transition state structure in nucleophilic substitution reactions of the type:

$$Y^- + CH(D)_3X \rightarrow YCH(D)_3 + X^- \qquad (3.36)$$

is the secondary α-deuterium kinetic isotope effect (KIE). This is defined as the ratio of the rate for a 'normal' hydrogenic system to the rate of an identical deuterated system:

$$KIE = \frac{k_H}{k_D}. \qquad (3.37)$$

Kinetic deuterium isotope effects can be classified as primary or secondary. Primary effects occur in reactions where the bond to deuterium is broken or formed. All other effects which can be observed with deuterated substrates are called secondary. In this work we are concerned with secondary α effects which result from isotopic substitution at the reaction centre, that is, substitution of hydrogen atoms at the α-carbon atom. The oxidative addition step of the Monsanto catalytic cycle is an example of a reaction which can be studied using secondary α-deuterium KIEs.

The magnitude of kinetic isotope effects is directly related to the isotope mass ratio and therefore hydrogen isotopes exhibit the largest effects. They arise from changes in C–H(D) bonding that take place in the transformation of reactants into the transition state. The greatest contribution to the value of the KIE comes from zero-point vibrational energy effects. This can be understood by considering the two extreme cases of an S_N2 transition state depicted in Figure 3.2. C–D groups have a larger reduced mass and therefore a smaller zero-point energy than the corresponding C–H vibrations. The change in geometry from reactants to transition state is accompanied by a change in the average energy required to excite C–H(D) vibrations. If the alkyl group is restricted in the transition state, then the energy required to excite the C–H vibrations will be higher than for C–D vibrations, Figure 3.2a. The net barrier for the deuterated substrate will therefore be lower, leading to an increase in rate relative to that for the lighter isotope. This is the so-called *inverse* isotope effect which is characterized by a KIE smaller than unity. Inverse effects are generally associated with tight transition states. When there is a tendency toward smaller force constants for C–H(D) bonds, the opposite effect occurs giving a KIE in excess of unity, Figure 3.2b. This is the so-called *normal* isotope effect which is usually indicative of a loose transition state.

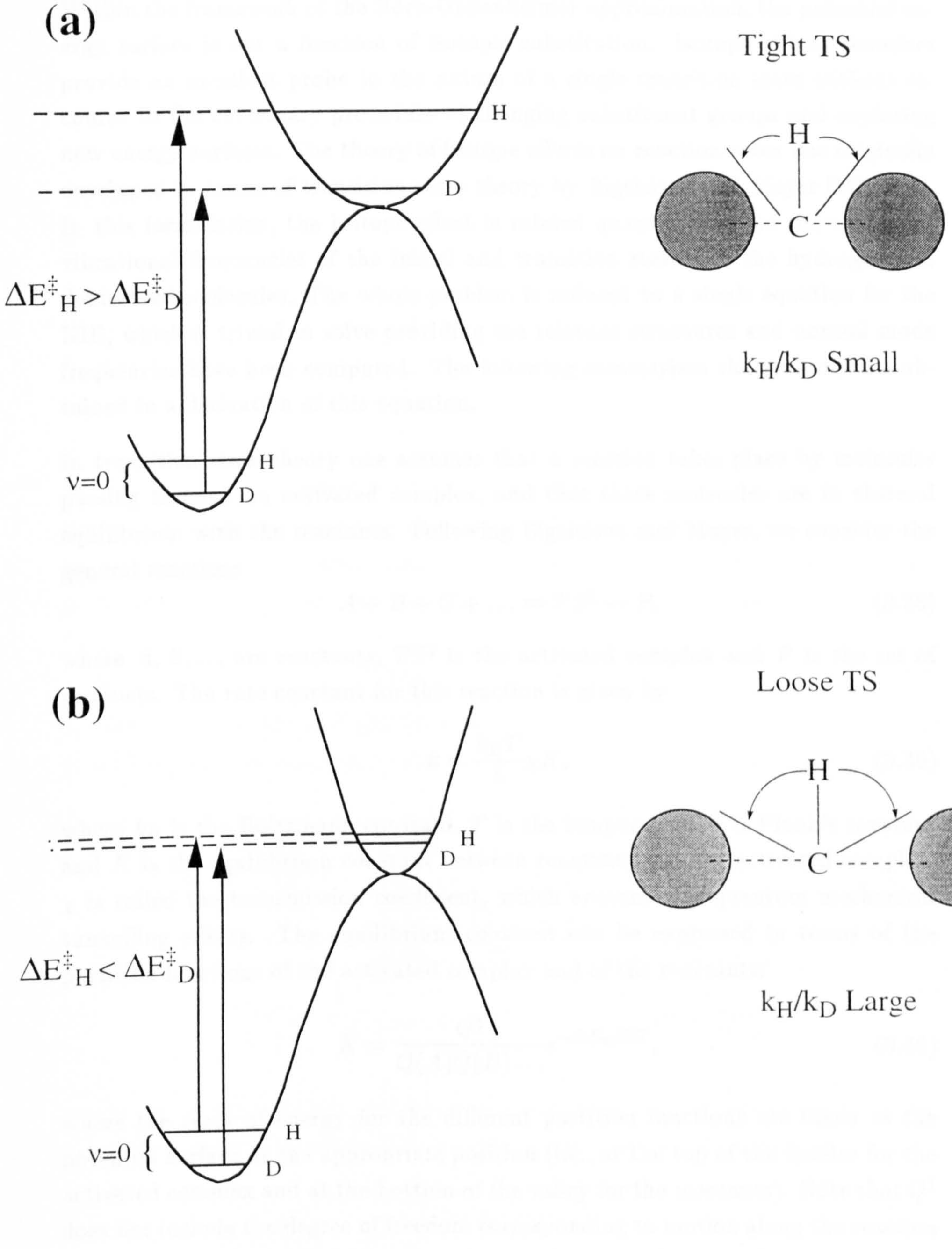

Figure 3.2: Secondary α-deuterium kinetic isotope effect; relationship between the "looseness" of an S_N2 transition state and the C–H(D) zero-point energies. A tight transition state (a) increases the difference in zero-point energies and the rate for the deuterated substrate is greater - the *inverse* effect. A loose transition state (b) results in a decrease of this difference and the rate is greater for hydrogen - the *normal* effect.

Within the framework of the Born-Oppenheimer approximation, the potential energy surface is not a function of isotopic substitution. Isotope effects therefore provide an excellent probe to the nature of a single transition state without recourse to the customary procedure of changing substituent groups and exploring new energy surfaces. The theory of isotope effects on reaction rates was originally developed in terms of transition state theory by Bigeleisen and Mayer [173, 174]. In this formulation, the isotope effect is related quantitatively to the molecular vibrational frequencies of the initial and transition states for the hydrogen and deuterated molecules. The whole problem is reduced to a single equation for the KIE, which is trivial to solve providing the relevant structures and normal mode frequencies have been computed. The following summarizes the main results obtained in a derivation of this equation.

In transition state theory one assumes that a reaction takes place by molecules passing through an activated complex, and that these molecules are in thermal equilibrium with the reactants. Following Bigeleisen and Mayer, we consider the general reaction:

$$A + B + C + \ldots \rightleftharpoons TS^{\ddagger} \rightarrow P, \tag{3.38}$$

where $A, B, \ldots$ are reactants, $TS^{\ddagger}$ is the activated complex and P is the set of products. The rate constant for this reaction is given by

$$k = \frac{k_B T}{h} \chi K, \tag{3.39}$$

where k_B is the Boltzmann constant, T is the temperature, h is Plank's constant and K is the equilibrium constant between reactants and the activated complex. χ is called the transmission coefficient, which accounts for quantum mechanical tunnelling effects. The equilibrium constant can be expressed in terms of the partition functions of the activated complex and of the reactants:

$$K = \frac{Q^{\ddagger}}{Q(A)Q(B)\ldots} e^{-\Delta E_a / RT}, \tag{3.40}$$

where the zeros of energy for the different partition functions are taken at the potential surface at the appropriate position (i.e., at the top of the barrier for the activated complex and at the bottom of the valley for the reactants). Note that $Q^{\ddagger}$ does not include the degree of freedom corresponding to motion along the reaction co-ordinate. Substituting this expression into equation (3.39) yields

$$k = \chi \frac{k_B T}{h} \frac{Q^{\ddagger}}{Q(A)Q(B)\ldots} e^{-\Delta E_a / RT}, \tag{3.41}$$

and we can write an analogous equation for the isotopically substituted system:

$$k' = \chi' \frac{k_B T}{h} \frac{Q^{\ddagger\prime}}{Q(A)'Q(B)'\ldots} e^{-\Delta E_a / RT}. \tag{3.42}$$

Next, dividing (3.41) by (3.42) and adopting the convention of subscript H for a hydrogenic system and subscript D for a deuterated system, we obtain

$$\frac{k_H}{k_D} = \frac{\chi_H}{\chi_D}\frac{Q_H^{\ddagger}}{Q_D^{\ddagger}}\frac{Q_D(A)Q_D(B)\ldots}{Q_H(A)Q_H(B)\ldots}. \tag{3.43}$$

Approximations must now be introduced to reduce the problem to a sensible computationally solvable form.

Assuming separability of the partition functions the external translational and rotational modes can be factored from each other and from the remaining $3N-6$ internal degrees of freedom:

$$Q = Q_{trans}Q_{rot}Q_{vib}. \tag{3.44}$$

For gas phase molecules other than molecular hydrogen, it is reasonable to ignore nonclassical rotations and introduce the rigid rotor approximation. In addition, we assume that the internal vibrations can be described with harmonic oscillator partition functions. Thus, an approximate partition function can be constructed from:

$$Q \approx Q_{trans}Q_{rigidrotor}Q_{harmonic}. \tag{3.45}$$

Substituting the standard statistical formulae for these partition functions [175] into (3.45) and rearranging, yields an expression for the harmonic rate ratio:

$$\begin{aligned}\frac{k_H}{k_D}\frac{s_D s_H^{\ddagger}}{s_H s_D^{\ddagger}}\frac{\chi_D}{\chi_H} &= \frac{\left(\frac{M_D}{M_H}\right)^{\frac{3}{2}}}{\left(\frac{M_D^{\ddagger}}{M_H^{\ddagger}}\right)^{\frac{3}{2}}}\frac{\left(\frac{I_{A_D}I_{B_D}I_{C_D}}{I_{A_H}I_{B_H}I_{C_H}}\right)^{\frac{1}{2}}}{\left(\frac{I_{A_D}^{\ddagger}I_{B_D}^{\ddagger}I_{C_D}^{\ddagger}}{I_{A_H}^{\ddagger}I_{B_H}^{\ddagger}I_{C_H}^{\ddagger}}\right)^{\frac{1}{2}}} \\ &\times \frac{\prod_i^{3N-6}\frac{1-e^{-u_{H_i}}}{1-e^{-u_{D_i}}}}{\prod_i^{3N-7}\frac{1-e^{-u_{H_i}^{\ddagger}}}{1-e^{-u_{D_i}^{\ddagger}}}} \times \frac{exp\left[\sum_i^{3N-6}\frac{(u_{H_i}-u_{D_i})}{2}\right]}{exp\left[\sum_i^{3N-7}\frac{(u_{H_i}^{\ddagger}-u_{D_i}^{\ddagger})}{2}\right]},\end{aligned} \tag{3.46}$$

where the M are molecular weights, and the I terms, I_A, I_B and I_C are the three principle moments of inertia. The u_i refer to the vibrational frequencies:

$$u_i = \frac{h\nu_i}{k_B T}. \tag{3.47}$$

The statistical factors s cancel from this expression if symmetry is conserved during the reaction. Tunnelling effects, represented by the χ, are only expected to make a significant contribution for reactions involving the cleavage or formation of bonds to light isotopic nuclei, for example, in proton transfer reactions which are characterized by primary isotope effects. For the purposes of the present study, we may therefore neglect both the symmetry factors and the transmission coefficients. According to the Teller-Redlich product theorem [176], one has for two isotopic

molecules:

$$\left(\frac{M_H}{M_D}\right)^{\frac{3}{2}}\left(\frac{I_{A_H}I_{B_H}I_{C_H}}{I_{A_D}I_{B_D}I_{C_D}}\right)^{\frac{1}{2}} = \prod_j^N \frac{m_{H_j}}{m_{D_j}} \prod_i^{3N-6} \frac{\nu_{H_i}}{\nu_{D_i}}. \tag{3.48}$$

A similar equation can be written for the transition state and both substituted into (3.46). Factoring out the imaginary vibration and cancelling the mass terms, leads to a solvable equation in terms of just the vibrational frequencies. This is the Bigeleisen equation which written in compact notation is

$$\frac{k_H}{k_D} = R^{\ddagger}_{imag}\left(\prod_i^{3N-7} R^{\ddagger}_i\right)\left(\prod_i^{3N-6} R^{reacts}_i\right)^{-1}, \tag{3.49}$$

where

$$R^{\ddagger}_i, R^{reacts}_i = \frac{u_{H_i}}{u_{D_i}}\frac{e^{-u_{H_i}/2}}{e^{-u_{D_i}/2}}\frac{\left(1-e^{-u_{H_i}}\right)^{-1}}{\left(1-e^{-u_{D_i}}\right)^{-1}} \qquad and \qquad R^{\ddagger}_{imag} = \frac{\nu^{\ddagger}_H}{\nu^{\ddagger}_D}. \tag{3.50}$$

The approximations employed in this derivation are not expected to lead to significant error for systems of interest to the present study. In point of fact, KIEs computed with the Bigeleisen equation should benefit from a partial cancellation of errors when the isotopic ratios are taken.

In addition to calculating absolute values for secondary α-D KIEs, it is interesting to examine the individual contributions to this value arising from changes in the vibrational modes of C–H(D) bonds during the course of the reaction. The vibrational KIE can be approximately factored into two components:

$$(k_H/k_D) \approx (k_H/k_D)_B(k_H/k_D)_S, \tag{3.51}$$

where $(k_H/k_D)_B$ is the contribution from the C_α-H(D) bending vibrations and $(k_H/k_D)_S$ is the contribution from the C_α-H(D) stretching vibrations. Analysis of the individual frequencies allow these quantities to be further partitioned into contributions from specific vibrational modes. In the present study we have used five bending vibrations (two rocking motions, one umbrella inversion and two deformations) and three stretching vibrations (a symmetric stretch and two asymmetric stretches) to partition the calculated KIEs. The set of modes considered are depicted graphically in Figure 3.3.

Recent theoretical studies of S_N2 reactions have attempted to find quantitative relationships between isotope effects and transition state structure. Wolfe *et al.* have reported correlations between the magnitude of the KIE and the 'looseness' of the TS [177]. For S_N2 reactions of the type represented by equation (3.36), the looseness parameter L_{TS} [178] is defined as

$$L_{TS} = (\%CX^{\ddagger} + \%CY^{\ddagger}), \tag{3.52}$$

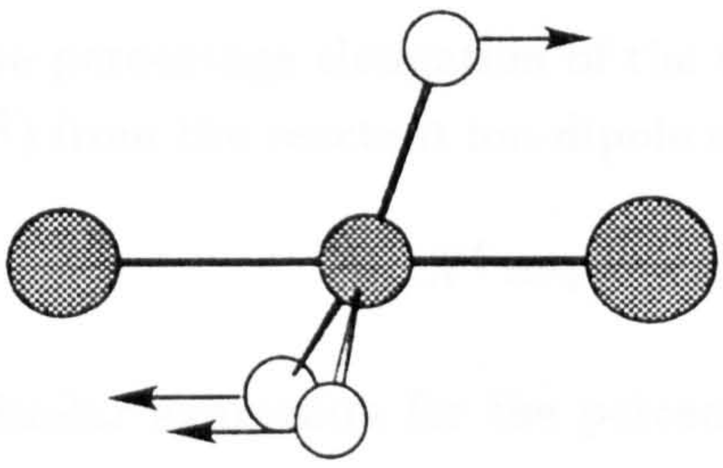

rock (2)

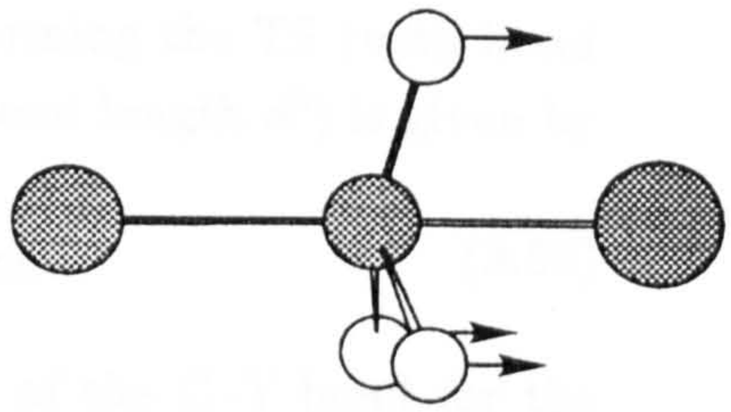

umbrella

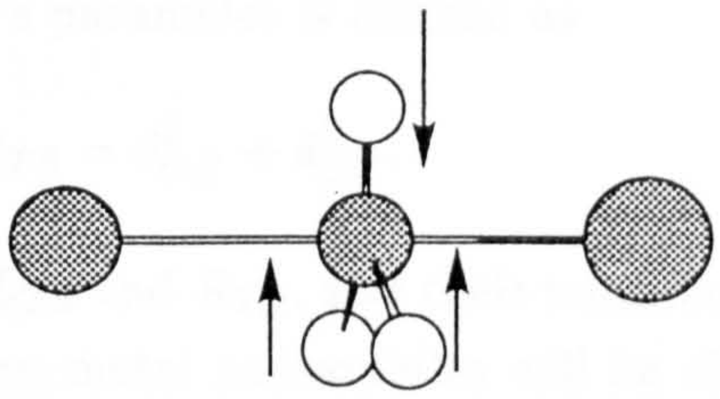

deformation (2)

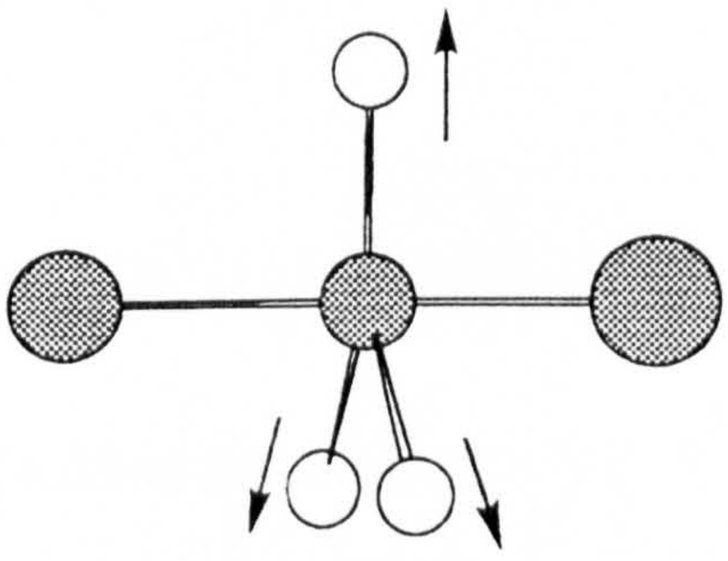

symmetric stretch

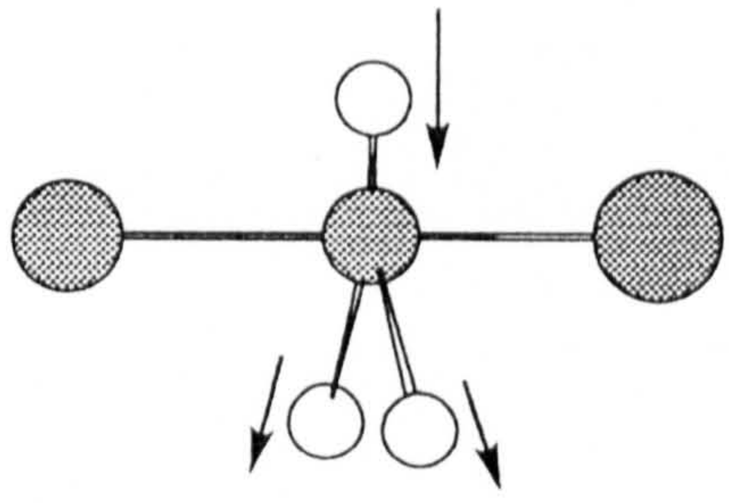

assymetric stretch (2)

Figure 3.3: Bending and stretching vibrational modes used to partition secondary α-D KIEs. The nature of the vibration is indicated by arrows superimposed on the C–H(D) bonds.

where the percentage elongation of the C–X bond on forming the TS (with bond length $d^{\ddagger}$) from the reactant ion-dipole complex (with bond length d^{0}) is given by

$$\%CX^{\ddagger} = 100 \times (d^{\ddagger}_{CX} - d^{0}_{CX})/d^{0}_{CX}, \tag{3.53}$$

with a similar expression for the percentage elongation of the C–Y bond for the reverse reaction:

$$\%CY^{\ddagger} = 100 \times (d^{\ddagger}_{CY} - d^{0}_{CY})/d^{0}_{CY}. \tag{3.54}$$

In a theoretical study of a wide range of organic S_N2 reactions, Westaway *et al.* have found a strong correlation between the magnitude of the vibrational contribution to the KIE and the sum of the nucleophile–carbon and carbon–leaving group distances [179]. Westaway's parameter is defined as

$$R_{TS} = d^{\ddagger}_{CX} + d^{\ddagger}_{CY}. \tag{3.55}$$

The values of these parameters, L_{TS} and R_{TS}, and their relationship to secondary α-D KIEs calculated for transition metal nucleophiles will be discussed in a subsequent chapter.

Chapter 4

Equilibrium Complexes and Small Molecules

This chapter presents the results of theoretical calculations performed on the small molecules and transition metal complexes known to play a role in the Monsanto catalytic cycle. Attention is paid to experimentally realizable properties such as geometrical structure, carbonyl vibrational frequencies and to the relative stabilities of different geometrical isomers. The performance of conventional *ab initio* techniques are examined and compared with the results from a representative set of currently used density functionals. The same Gaussian bases are used in each case.

4.1 Small Molecules

4.1.1 Carbon Monoxide

Table 4.1 contains the bond length, fundamental harmonic vibrational frequency and dipole moment computed for the CO molecule at various levels of theory. Several different basis sets have been used, including the near-Hartree-Fock-limit basis, 6-311++G(3*d*,3*p*), which employs a double set of diffuse functions and triple set of polarization functions. Of course, we cannot expect to use an extended basis of this size in calculations of large transition metal complexes but it is instructive to examine basis set influence for a small molecule in relation to electron correlation effects and to the choice of functional used in DFT calculations.

The calculated parameters display a significant variation over the different theoretical methods and bases employed. The RHF bond lengths are in reasonable agreement with the experimental value, in each instance predicted to within 0.02

Table 4.1: Calculated bond length, harmonic vibrational frequency and dipole moment of the CO molecule. $\Delta(R)\%$ and $\Delta(\nu)\%$ are the percentage errors in the computed bond length and vibrational frequency, respectively.
Bond lengths Å, frequencies cm^{-1}, dipole moments Debye.

Model	Basis	R_{C-O}	$\Delta(R)\%$	ν	$\Delta(\nu)\%$	μ^a
RHF	MB (10)[b]	1.146	1.60	2463	13.5	+0.124
	DZ (18)	1.138	0.89	2265	4.4	−0.478
	DZ* (28)	1.116	1.06	2426	11.9	−0.174
	6-311++G(3*d*,3*p*) (64)	1.103	2.21	2421	11.6	−0.142
MP2	MB	1.198	6.21	2009	7.4	+0.796
	DZ	1.189	5.41	1870	13.8	+0.230
	DZ*	1.154	2.30	2098	3.3	+0.394
	6-311++G(3*d*,3*p*)	1.138	0.89	2108	2.9	+0.258
MP4	DZ	1.208	7.09	1606	26.0	-[c]
	6-311++G(3*d*,3*p*)	1.146	1.51	1994	8.1	-[c]
LDA	MB	1.195	5.94	2057	5.2	+0.523
	DZ	1.170	3.72	1998	7.9	+0.122
	DZ*	1.145	1.51	2151	0.9	+0.280
	6-311++G(3*d*,3*p*)	1.127	0.09	2185	0.7	+0.225
BLYP	MB	1.169	3.63	2060	5.1	+0.468
	DZ	1.181	4.70	1921	11.5	+0.017
	DZ*	1.155	2.39	2078	4.2	+0.233
	6-311++G(3*d*,3*p*)	1.137	0.79	2112	2.7	+0.155
BHANDH	MB	1.131	0.27	2373	9.4	+0.363
	DZ	1.147	1.68	2180	0.5	−0.152
	DZ*	1.125	0.27	2334	7.6	+0.064
	6-311++G(3*d*,3*p*)	1.110	1.60	2349	8.2	+0.051
Becke3LYP	MB	1.188	5.32	2116	2.5	+0.404
	DZ	1.166	3.37	2030	6.5	−0.032
	DZ*	1.142	1.24	2185	0.7	+0.148
	6-311++G(3*d*,3*p*)	1.125	0.27	2209	1.8	+0.097
Experiment[d]		1.128		2170		+0.112

[a]Positive values indicate the polarity: $C^{\delta-}O^{\delta+}$, in agreement with experiment.
[b]Numbers in parentheses refer to the total number of basis functions.
[c]Post-SCF density not available for this method.
[d]Data from reference [180]

Å (1 to 2% error). The Hartree-Fock model has a tendency to over-bind first-row atoms and this is reflected in the calculated stretching frequencies which are in excess of the experimental value by *ca.* 100 to 300 cm^{-1}. The minimal basis (MB) results are the least accurate (13.5% error) but significant improvement is observed upon moving to the double-zeta (DZ) split valence contraction scheme (4.4% error). Adding extra polarization functions at the uncorrelated level leads to frequencies which are too high by *ca.* 250 cm^{-1}. The MP2 scheme gives rather poorer values than the RHF method with the same small basis. The inclusion of electron correlation at this level makes the C–O bond length too long and the vibrational frequency too low. Like many of the *ab initio* correlated methods, perturbation theory based schemes rely on a good description of the virtual orbitals in the original Hartree-Fock wavefunction. For multiply-bonded molecules that incorporate atoms with a large compliment of valence electrons, the virtual states will generally have a considerable antibonding character. Accordingly, an admixture of these states in the ground state Hartree-Fock wavefunction will lead to a significant bond lengthening. The correlated results for the CO molecule are therefore strongly dependent upon the quality of the basis set employed. Improvement in the MP2 parameters is observed when extra functions are added to the basis for each atom. The MP2 DZ* and 6-311++G(3*d*,3*p*) parameters for both the bond lengths and frequencies are within about 3% of the experimental values. The vibrational frequency predicted at the fourth order of Møller-Plesset perturbation theory in conjunction with the standard basis, MP4/DZ, is a substantial underestimate at 564 cm^{-1} lower than the observed fundamental. This discrepancy can be partly recovered by using the 6-311++G(3*d*,3*p*) basis which brings the frequency back to within a tolerable 10% of the measured value. Evidently, improving the quality of the *ab initio* correlated methods requires an even greater refinement to the basis set in order to obtain satisfactory geometries and vibrational frequencies.

Parameters calculated with the DFT methods also show significant variation, depending on the quality of the basis and the particular exchange-correlational functional used. The bond lengths calculated using the DZ basis are too long. The deviations from the experimental value vary from +0.019 Å for the simplest hybrid scheme, BHANDH, to +0.053 Å for the gradient-corrected BLYP functional. More favourable agreement is obtained by using one of the extended bases where the errors are generally smaller than 2%. The computed vibrational frequencies are in most cases within 10% of the experimental value. As for the bond lengths, the most accurate frequencies are generally derived from the calculations using an extended basis. The local density approximation (LDA) in conjunction with the DZ* and 6-311++G(3*d*,3*p*) bases yields frequencies with errors of 0.9% and 0.7%, respectively. Non-local corrections to the density do not improve upon these results. In fact, the sophisticated BLYP functional yields bond lengths and vibrational frequencies which overall, show the poorest agreement with experiment out of the DFT-based schemes. The Becke3LYP/DZ* method gives somewhat

better performance, predicting a frequency which is only 15 cm^{-1} higher than experiment. The BHANDH frequencies appear to follow a similar trend to those calulated using the RHF method. The most accurate value is predicted with the standard DZ basis (0.7% error); extra functions lead to a value which is too high by *ca.* 180 cm^{-1}.

The dipole moment of CO is notoriously difficult to compute accurately by theoretical methods. Although the difference in electronegativities between C and O is large, the experimental value of the dipole moment is small (0.1 D) and the negative end is on the carbon atom. The difficulty arises due to the complex distribution of the bonding and lone pair electrons. The RHF/MB calculation gives a value which, surprisingly, is in good agreement with experiment; the correct sign is predicted and the error in the magnitude is small. However, improving the quality of the calculation by moving to the DZ or either of the extended bases reverses the polarity into the incorrect direction. In general, the correlated MP2 and DFT schemes predict the correct polarity, although the computed magnitudes appear to be strongly dependent upon the quality of the basis used. The most consistent results are achieved with the extended 6-311++G(3*d*,3*p*) basis. Clearly, prediction of the correct sign and magnitude of this dipole moment at the uncorrelated RHF level using a minimal basis is purely fortuitous.

The majority of the results presented here for the CO molecule have been realized in previous work. It has long been recognised, for example, that the Hartree-Fock model gives vibrational frequencies for molecules comprising of first row-atoms which are too high. The dipole moment of the CO molecule is a celebrated example where Hartree-Fock theory completely fails to give even a qualitatively correct description. An important observation is the dependence of the correlated methods upon the quality of the basis employed. At least one set of polarization functions is required to obtain satisfactory results using the MP2, LDA, BLYP and Becke3LYP methods. An exception is the BHANDH scheme, which predicted a vibrational frequency in excellent agreement with the experimental value using the standard DZ basis. The accuracy of the DFT results for the CO molecule are in general comparable to, or better than, those obtained from the MP2 scheme with the same Gaussian basis. Similar conclusions regarding the performance of DFT methods in calculations of small molecules have been reported previously [98, 99].

4.1.2 Methyl Iodide

Table 4.2 lists the geometry and dipole moment of CH_3I computed at various levels of theory. Iodine is the first heavy atom considered that requires a pseudopotential representation of the core electrons for practical computations.

The range and size of the errors in the computed geometrical parameters are fairly

Table 4.2: Calculated geometry and dipole moment of CH_3I. $\bar{\Delta}(r)\%$ is the mean percentage deviation in the bond lengths from the experimental values, $\Delta\theta\%$ is the error in the I–C–H angle.
Bond lengths Å, angles °, dipole moments Debye.

Model	Basis	R_{C-I}	R_{C-H}	$\bar{\Delta}(R)\%$	θ_{I-C-H}	$\Delta\theta\%$	μ^a
RHF	DZ	2.181	1.075	0.64	107.39	0.07	+2.12
	DZ*	2.148	1.078	0.56	107.55	0.07	+1.97
	DZ*+	2.145	1.078	0.49	107.53	0.06	+2.08
MP2	DZ	2.193	1.097	1.93	108.23	0.71	+1.58
	DZ*	2.144	1.089	0.42	107.92	0.42	+1.70
	DZ*+	2.143	1.089	0.39	107.84	0.34	+1.80
LDA	DZ	2.165	1.099	1.37	108.06	0.55	+1.79
	DZ*	2.134	1.098	0.69	107.94	0.44	+1.74
	DZ*+	2.132	1.099	0.79	108.05	0.54	+1.78
BLYP	DZ	2.216	1.097	2.47	107.21	0.24	+1.83
	DZ*	2.184	1.096	1.68	107.30	0.16	+1.75
	DZ*+	2.181	1.097	1.65	107.37	0.09	+1.83
BHANDH	DZ	2.151	1.085	0.40	108.08	0.57	+1.88
	DZ*	2.121	1.086	0.44	108.01	0.50	+1.77
	DZ*+	2.118	1.086	0.51	108.01	0.50	+1.87
Becke3LYP	DZ	2.192	1.090	1.59	107.50	0.03	+1.86
	DZ*	2.160	1.089	0.79	107.58	0.10	+1.76
	DZ*+	2.157	1.090	0.77	107.62	0.14	+1.84
Experiment[b]		2.136	1.084		107.47		+1.62

[a]Positive values indicate the polarity: $C^{\delta+}I^{\delta-}$, in agreement with experiment.
[b]Geometry from reference [181]. Dipole moment from reference [182].

small compared to the previous results for CO. In general the RHF model yields good predictions for the geometry of CH_3I. The deviations from the experimental measurements are small for the DZ and extended bases. The errors in the bond lengths are typically 0.5% and less than 0.1% for the bond angles. Bond lengths obtained from the correlated calculations are too long with the standard DZ basis. The mean deviations from the experimental values vary from 0.40% for the BHANDH functional to 2.47% for the BLYP functional. The MP2/DZ method gives long bond lengths with a mean deviation of 1.93%. Extending the basis leads in each case to an improvement in the geometrical parameters. The MP2/DZ* bond lengths and angles are within 0.5% of experiment. The LDA/DZ* scheme predicts an excellent value for the C–I bond length (2.134 Å) but there is a clear tendency to overestimate the C–H bond length at this level. The BLYP/DZ* method still gives the poorest bond lengths (1.68% mean error) but the bond angle is predicted to within 0.2°. Both of the hybrid schemes yield geometries in good agreement with experiment when the extended basis is used. The inclusion of diffuse functions in the basis (DZ*+), which might be expected to yield a better description of the polarizable distribution for iodine, leads to slightly shorter C–I bond lengths by 0.001 to 0.003 Å.

All of the calculations predict the correct polarity for the dipole moment of CH_3I. The RHF calculations give dipole moments that are too large. This can be ascribed to the bias in this model for charge localisation on the atoms. The MP2 and DFT calculations using the DZ and DZ* bases give smaller dipole moments which compare favourably with the experimental value.

The computed geometries and dipole moments for the CH_3I molecule demonstrate the ability of the ECP approximation to generate accurate theoretical data at a fraction of the cost of all-electron calculations. The results from the LDA and hybrid DFT schemes are comparable to those obtained from the *ab initio* methods. The worst performance in geometry calculations of any of the methods is observed for the gradient-corrected BLYP functional. This scheme appears to systematically overestimate bond lengths for both CO and CH_3I even when an extended basis is employed. Similar behaviour has been observed by other workers although extensive calculations for a wide range of small molecules have indicated that the BLYP functional can give good predictions for other molecular properties [99].

4.2 Transition Metal Complexes

4.2.1 $[Rh(CO)_2I_4]^-$

Rhodium(III) tetraiodide species have been observed in side reactions of the Monsanto acetic acid process. We have calculated the structure of *trans*-$[Rh(CO)_2I_4]^-$

using the *ab initio* and DFT methods with several different basis sets. Optimized bond lengths together with the parameters obtained from an X-ray structure determination for this complex [49] are presented in Table 4.3. The structure is octahedral with D_{4h} symmetry.

Table 4.3: Calculated geometry of *trans*-$[Rh(CO)_2L_4]^-$ (D_{4h}). $\bar{\Delta}(R)\%$ is the mean deviation from the experimental structure in the calculated bond lengths. t is the processor time (hours) required to optimize the structures starting from the experimental geometry. Also included is the estimated energy change (ΔE) for the isomerisation reaction (4.1).
Bond lengths Å, energy kJmol^{-1}.

Model	Basis	R_{Rh-C}	R_{Rh-I}	R_{C-O}	$\bar{\Delta}(R)\%$	t	ΔE
RHF	DZ (86)[a]	1.970	2.741	1.130	2.1	2.3	−61.5
	DZ2 (90)	2.030	2.775	1.129	3.5	2.5	−62.7
	DZ* (131)	1.965	2.732	1.109	2.5	7.2	−46.0
	DZ+ (115)	1.968	2.738	1.129	2.0	4.5	-[b]
MP2	DZ	1.889	2.760	1.189	2.6	6.0	−24.7
	DZ2	1.923	2.780	1.189	3.4	7.5	−32.1
	DZ*	1.908	2.756	1.169	2.3	43.5	−23.9
	DZ*[c]	-	-	-	-	-	−20.0
LDA	DZ	1.895	2.706	1.172	2.1	1.5	−6.7
	DZ2	1.890	2.717	1.174	1.6	2.2	−4.9
	DZ*	1.896	2.697	1.150	0.6	11.9	+2.7
	DZ*[d]	1.898	2.697	1.150	0.6	28.5	+5.8
BLYP	DZ	1.958	2.839	1.181	4.6	1.9	−21.6
	DZ2	1.950	2.845	1.184	4.6	3.5	−21.3
	DZ*	1.958	2.826	1.157	3.7	9.3	−21.7
BHANDH	DZ	1.896	2.679	1.145	0.5	1.9	−41.4
	DZ2	1.916	2.699	1.145	1.0	3.0	−39.3
	DZ*	1.903	2.672	1.124	0.5	8.6	−31.1
Becke3LYP	DZ	1.943	2.784	1.165	3.1	2.4	−35.2
	DZ2	1.939	2.800	1.167	3.6	3.8	−29.2
	DZ*	1.946	2.774	1.142	2.4	8.1	−31.2
Experiment		1.89	2.69	1.13			

[a]Numbers in parentheses refer to the total number of basis functions.
[b]The *cis* geometry did not converge at this level.
[c]Single-point calculation carried out on the RHF/DZ geometry.
[d]Calculation performed using the *int=finegrid* option.

The calculated bond lengths agree reasonably well with the values based upon the X-ray crystal data. The RHF method predicts metal–ligand bonds which are too long. The errors are largest for the Rh–CO bonds which are overestimated by *ca.* 0.08 to 0.14 Å. This is due to the inherent deficiency of the Hartree-Fock model for describing the covalent component of M–CO bonding [183]. The

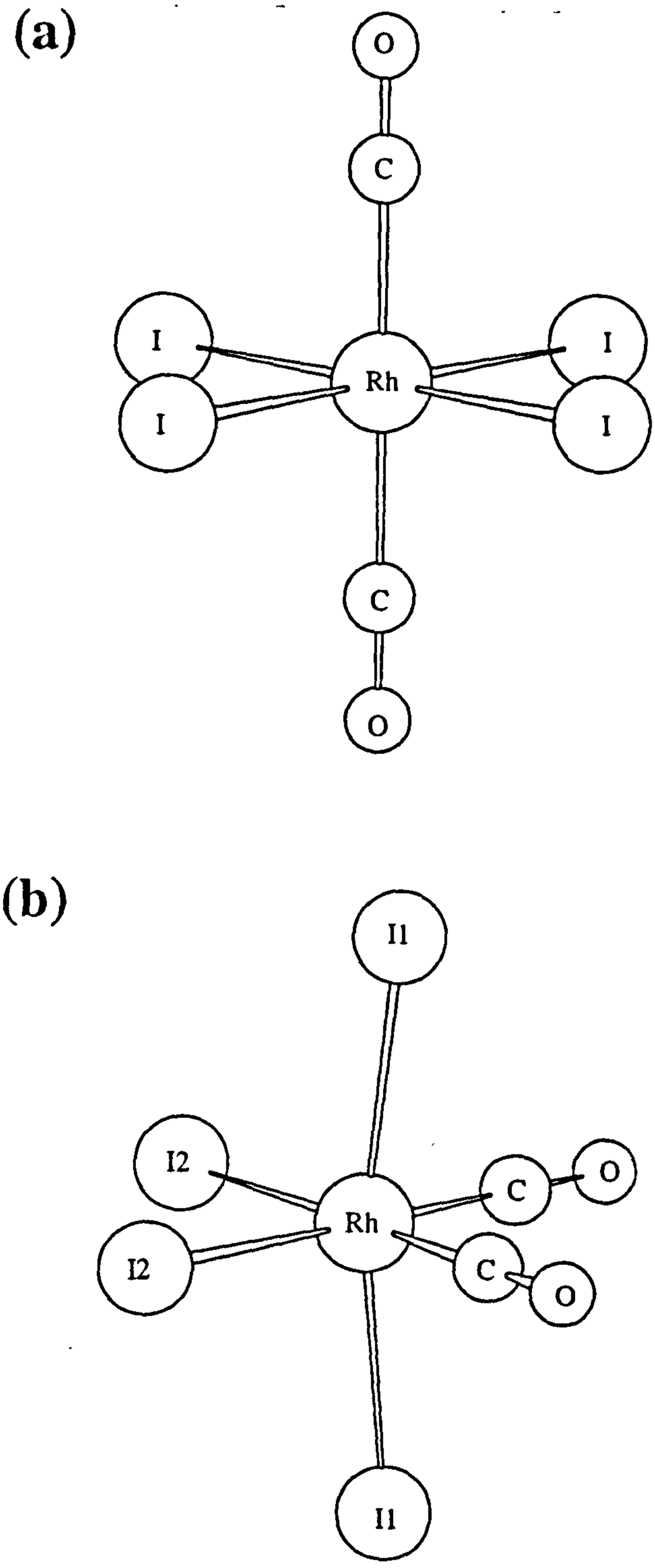

Figure 4.1: Structure of (a) *trans*-$[Rh(CO)_2I_4]^-$ (b) *cis*-$[Rh(CO)_2I_4]^-$.

Table 4.4: Calculated geometry of *cis*-$[Rh(CO)_2I_4]^-$ (C_{2v}). Atom numbers are defined in Figure 4.1. All data deduced from DZ basis calculations.
Bond lengths Å, angles °.

Model	R_{Rh-C}	R_{Rh-I1}	R_{Rh-I2}	R_{C-O}	θ_{C-Rh-C}	$\theta_{I2-Rh-I2}$	$\theta_{I1-Rh-I2}$
RHF	1.961	2.747	2.744	1.131	99.0	94.2	93.6
MP2	1.859	2.778	2.757	1.195	98.6	91.7	92.2
LDA	1.843	2.709	2.783	1.181	106.5	109.8	92.6
BLYP	1.912	2.845	2.901	1.190	104.2	108.6	93.2
BHANDH	1.871	2.683	2.696	1.148	101.9	95.1	92.7
Becke3LYP	1.915	2.802	2.791	1.170	102.3	100.1	93.3

Rh–I bonds are overestimated by *ca.* 0.03 to 0.09 Å. It is interesting to note that the semi-core ECP basis, generally considered to be the superior of the two split-valence schemes, yields the largest errors at this level. In particular, the RHF/DZ2 calculation predicts the longest Rh–CO distance (2.030 Å) of any of the methods used for geometry optimization. Inclusion of polarization functions (DZ*) at the RHF level does not result in a substantial improvement in these parameters. Diffuse functions (DZ+) cause an even smaller geometrical change but this is expected since the orbital energies calculated with the standard split-valence bases indicate that the outermost valence electrons are strongly bound (i.e. the energy of the HOMO is large and negative). In fact, apart from the dianionic species such as $[Rh(CO)I_5]^{2-}$, all of the complexes considered in the present study had stable valence electronic structures when the calculations were performed with the standard bases.

The correlated MP2 scheme yields rather better Rh–CO distances, owing to an improved description of the π back-donation. At the MP2/DZ level the Rh–CO distance is 1.889 Å, in excellent agreement with the experimental value. It has recently been demonstrated that the M–CO bond lengths of the second- and third-row transition metal hexacarbonyls $M(CO)_6$ (M=Mo, W) can be calculated with good accuracy at the MP2 level using ECPs and moderate valence basis sets [184]. The Rh–I bond length calculated with the MP2/DZ method is too long by 0.07 Å. The C–O distance is overestimated by *ca.* 0.06 Å, as was observed in calculations of the free molecule by this method. Moving to the semi-core DZ2 basis also generates larger errors than for the full-core results at the MP2 level; the predicted Rh–CO and Rh–I bond lengths are longer than the MP2/DZ estimates by 0.02 to 0.03 Å. Augmenting the standard basis with polarization functions only improves the C–O bond length.

The best overall agreement with experiment for the structure of *trans*-$[Rh(CO)_2I_4]^-$ is obtained with the local DFT functional, LDA, and the simplest hybrid func-

tional, BHANDH. The Rh–C and Rh–I bond lengths are predicted to within 0.03 Å (1 to 2% error) of the experimental values using these schemes. The C–O distances are overestimated by *ca.* 0.02 to 0.04 Å. The BLYP functional produces bond lengths which are systematically longer than other DFT values and the experimental parameters. The Rh–C and Rh–I bond lengths are overestimated by *ca.* 0.07 and 0.15 Å , respectively. These errors are larger than those obtained using the uncorrelated RHF method. The other gradient-corrected functional, Becke3LYP, also produces long Rh–C and R–I bonds (deviations of *ca.* +0.05 and +0.09 Å), although the errors are not quite as large as for the BLYP functional. It would appear that the sophisticated non-local functionals do not give good predictions for the structure of *trans*-$[Rh(CO)_2I_4]^-$. Calculations with the extended DZ* basis do not cause a marked improvement in the geometrical parameters from the standard basis values for any of the DFT methods.

A *cis* isomer of the tetraiodide is formed on addition of I_2 to $[Rh(CO)_2I_2]^-$ [50], but only the *trans* species is believed to be present in working catalyst solutions. Forster, who first reported this compound, noted that it was unique at the time since other $[M(CO)_2X_4]^-$ species, including $[Ir(CO)_2I_4]^-$, were only known as the *cis* isomer [49]. The geometrical parameters of *cis*-$[Rh(CO)_2I_4]^-$ (Figure 4.1b) calculated using the standard DZ basis are summarized in Table 4.4. The optimized structures are strained from perfect octahedral. The two iodide ligands *cis* to carbonyls increase their angles with the iodide ligands *trans* to carbonyls to minimize steric repulsion (I1–Rh–I2 ≈ 92° to 93°). Larger distortions, in some cases greater than 100° (LDA and BLYP), are observed for the I2–Rh–I2 and C–Rh–C angles between mutually *cis* iodide and carbonyl ligands in the plane. The computed Rh–CO bond lengths are shorter than the corresponding bonds in the *trans* species by *ca.* 0.01 Å (RHF) to 0.05 Å (LDA and BLYP). This can be ascribed to an increase in the M–CO π back-donative interaction when the carbonyl ligands are located *cis* to each other. The calculated Rh–I bond lengths *trans* to carbonyls are similar to the previous Rh–I bond lengths in *trans*-$[Rh(CO)_2I_4]^-$ for the *ab initio* and hybrid DFT schemes but significantly longer for the pure DFT methods. The LDA functional predicts that replacing an iodide with a carbonyl will produce an extension in the *trans* Rh–I bond of 0.08 Å. The only reported rhodium(III) crystal structure with a carbonyl *trans* to an iodide is for the dimeric acyl complex $[(COCH_3)_2Rh_2(CO)_2I_6]$ [58]. This has a Rh–CO distance of 1.860 Å and a *trans* Rh–I distance of 2.699 Å. These values compare favourably with the structures calculated using the BHANDH and MP2 schemes but suggest that the LDA functional has overestimated the *trans* influence of a carbonyl on an iodide ligand in *cis*-$[Rh(CO)_2I_4]^-$. The other trends discernible from the calculated structures of *cis*-$[Rh(CO)_2I_4]^-$ are similar to those that were observed for the *trans* complex. In particular, it can be seen that the RHF method predicts a very long Rh–C bond length (1.961 Å). Also of of note are the long Rh–C (1.912 Å) and Rh–I (2.845 and 2.901 Å) bond lengths calculated with the BLYP functional.

The energy change associated with the equilibrium:

$$cis\text{–}[Rh(CO)_2I_4]^- \quad \rightleftharpoons \quad trans\text{–}[Rh(CO)_2I_4]^- \qquad (4.1)$$

has been calculated at several different levels of theory. These are collected in the right hand column of Table 4.3. The majority of the calculations predict the *trans* isomer to be the more thermodynamically stable species, in qualitative agreement with experimental observations. The computed energy changes are largest at the RHF level, $\Delta E \approx -50$ to -60 kJ mol^{-1}. The MP2 and BLYP schemes with the extended DZ* basis predict smaller energy changes of *ca.* -20 kJ mol^{-1}. The hybrid functionals predict energy changes which are intermediate between the RHF and BLYP estimates (*ca.* -30 to -40 kJ mol^{-1}). The LDA/DZ calculation yields a small exothermic energy change (-6.7 kJ mol^{-1}) but the reaction is predicted to be mildly endothermic ($+2.7$ kJ mol^{-1}) when an extended basis is employed.

An important consideration in calculations of transition metal complexes is the relative expense of the theoretical methods employed. Table 4.3 lists the processor times required to reach geometry convergence for *trans*-$[Rh(CO)_2I_4]^-$ when the optimizations were initiated from the experimental geometry. The MP2 scheme uses about four to five times the amount of processor time that is required by the RHF and DFT methods. Comparable accuracies to the MP2 geometrical data were achieved from the LDA and BHANDH schemes with a considerable computational saving. Thus, the frequently made assertion that DFT is a cheaper alternative to conventional post-HF methods for calculating good quality correlated data holds true for this particular geometry calculation in the GAUSSIAN implementation. It should be noted however, that these calculations were performed with a modest numerical integration grid. The literature actually recommends the use of a finer grid [134] but we have found that this can lead to the calculation becoming rather more expensive. Table 4.3 contains one entry for a calculation using the LDA/DZ* scheme with the int=finegrid option. Improving the quality of the calculation in this way only had a small effect on the computed geometrical parameters and was about three times more expensive than calculations employing a standard grid.

4.2.2 $[Rh(CO)I_5]^{2-}$

Another simple rhodium(III) carbonyl iodide complex which can be observed under certain conditions is the dianionic species $[Rh(CO)I_5]^{2-}$. It is related to the tetraiodide $[Rh(CO)_2I_4]-$, through replacement of carbon monoxide by iodide:

$$[Rh(CO)_2I_4]^- \; + \; I^- \; \rightleftharpoons \; [Rh(CO)I_5]^{2-} \; + \; CO \qquad (4.2)$$

The structure of $[Rh(CO)I_5]^{2-}$ has been optimized using the *ab initio* and DFT methods with the DZ+ basis, Table 4.5. Preliminary calculations with the stan-

dard DZ basis generated species with unbound outer electrons but this was remedied by the inclusion of diffuse functions.

Table 4.5: Calculated geometry of $[Rh(CO)I_5]^{2-}$ (C_{4v}). Also included is the estimated energy change (ΔE) for reaction (4.2). Atom numbers are defined in Figure 4.2. All calculations were performed using the DZ+ basis.
Bond lengths Å, angles °, energy kJmol^{-1}.

Model	R_{Rh-C}	R_{C-O}	R_{Rh-I_1}	R_{Rh-I_2}	$\theta_{I2-Rh-C}$	ΔE^a
RHF	1.927	1.133	2.815	2.780	86.5	+286.9
MP2	1.766	1.207	2.824	2.776	88.4	+182.6
LDA	1.782	1.184	2.791	2.728	87.1	+289.9
BLYP	1.851	1.192	2.929	2.883	86.4	+263.6
BHANDH	1.809	1.153	2.755	2.699	87.4	+313.1
Becke3LYP	1.847	1.173	2.870	2.821	86.5	+287.2

[a]For $[Rh(CO)I_5]^{2-}$ geometries optimized with the DZ+ basis have been used, while for *trans*-$[Rh(CO)_2I_4]^-$ and CO single-point DZ+ calculations were carried out on the optimized DZ geometries.

Each of the calculations predict a slightly strained octahedral geometry, with the four iodides *cis* to carbonyl displaced out of the plane toward the carbonyl ligand by *ca.* 1.5 to 3.5°. The RHF model predicts a Rh–CO bond distance (1.933 Å) which is significantly longer than those given by any other method. The smallest Rh–CO bond length is given by the MP2 method, 1.767 Å. In each instance, the Rh–I bond *trans* to carbonyl is predicted to be longer than the bonds to the four iodides in the equatorial plane. The former range from 2.741 to 2.925 Å and the latter from 2.703 to 2.894 Å, the smallest and largest values given in each case by the BHANDH and BLYP functionals, respectively. The largest variation between Rh–I bond lengths is given by the LDA method which predicts that iodide *trans* to carbonyl will be longer by *ca.* 0.05 Å. One X-ray analysis of the structure of $[Rh(CO)I_5]^{2-}$ has been reported but the rhodium complex was found to be disordered in the crystal [185].

The energy change for reaction (4.2) has been estimated using the *ab initio* and DFT methods with the DZ+ basis, Table 4.5. Each of the methods predicts that the tetraiodide species is strongly favoured over the dianion. This is in qualitative agreement with experiment; modest partial pressures can displace I^- from $[Rh(CO)I_5]^{2-}$ even in the presence of high I^- concentrations. Equally, however, it should be noted that this is a sensible equilibrium whereas the large energy changes calculated by the theoretical methods imply that the dianion is an unusually unstable species. It is interesting that the MP2 scheme predicts a smaller energy change which is *ca.* 80 kJ mol^{-1} more in favour of the dianion than any other method. Further enhancement of the basis and some allowance for solvent

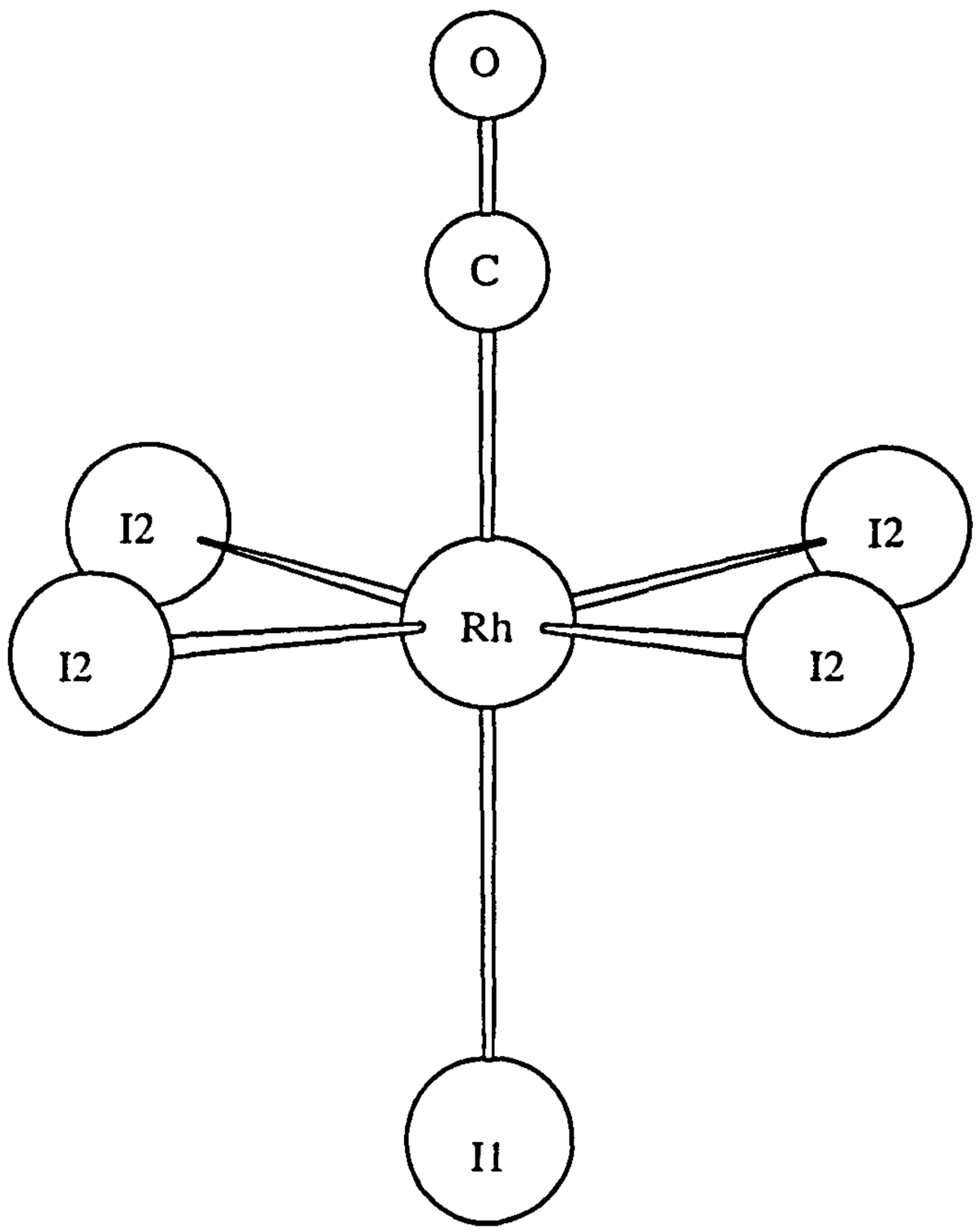

Figure 4.2: Structure of $[Rh(CO)I_5]^{2-}$.

effects may be required to fully describe this reaction.

4.2.3 $[M(CO)_2I_2]^-$ (M=Rh, Ir)

Geometrical parameters for *cis*-$[Rh(CO)_2I_2]^-$ calculated using the *ab initio* and DFT methods in conjunction with several different basis sets are presented in Table 4.6. Each of the models predicts a structure which is significantly distorted from square planar. The interligand I–Rh–I angles are greater than 90° and in general greater than the C–Rh–C angles. The departure from square planar symmetry can be attributed to steric interactions between the bulky iodide ligands. The calculations employing a minimal basis set generate the longest Rh–CO and Rh–I bond lengths. The higher quality DZ split-valence contraction scheme yields shorter bond lengths which appear to follow a trend similar to those noted in the previous results for octahedral rhodium(III) complexes. The RHF/DZ calculation gives the longest Rh–CO bond of 1.883 Å, closely followed by the BLYP/DZ and Becke3LYP/DZ calculations which yield bond lengths of 1.863 and 1.852 Å, respectively. The shortest Rh–CO bond length generated using the DZ basis is given by the MP2 scheme, 1.791 Å. This is slightly longer than the LDA and BHANDH values which are both *ca.* 1.81 Å. Variations between the computed Rh–I bond lengths also follow a trend similar to those observed for the previous rhodium iodide complexes. Calculations with the DZ basis yield Rh–I bonds ranging from 2.714 Å at the BHANDH level to 2.880 Å at the BLYP level. The RHF/DZ model gives a C–O bond length which is similar to that calculated for the unbound molecule (1.140 Å) but significant expansion (*ca.* 0.02 to 0.07 Å) is observed with the inclusion of electron correlation.

The most notable change in the calculated geometries upon moving from the full- to the semi-core ECP occurs in the Rh–CO bond distances. The RHF/DZ2 calculation yields a Rh–CO bond length (1.975 Å) which is increased from the DZ value by *ca.* 0.09 Å and in excess of values predicted by any other method by at least 0.11 Å. The value predicted by the MP2/DZ2 calculation is increased relative to the DZ value by *ca.* 0.05 Å. Rh–CO bond extension is noted for each of the density functionals, although for these schemes the DZ2 basis also causes a significant contraction in the Rh–I bond lengths. Inclusion of polarization functions in the basis (DZ*) reduces the Rh–CO distance by about 0.01 Å for all of the methods, except in the case of the MP2 calculation where the reduction is *ca.* 0.04 Å.

The geometry of the predominant catalytic species has not been determined by X-ray crystallography. Data is available, however, for the structure of the chloro-analogue, *cis*-$[Rh(CO)_2Cl_2]^-$ [186]. This complex is not significantly distorted from perfect square planar, with Rh–CO and C–O bond lengths of 1.75 and 1.17 Å, respectively. The computed parameters may also be compared to crystallographic data reported for the neutral rhodium(I) compounds, *trans*-$[Rh(CO)X(PPh_3)_2]$

(a)

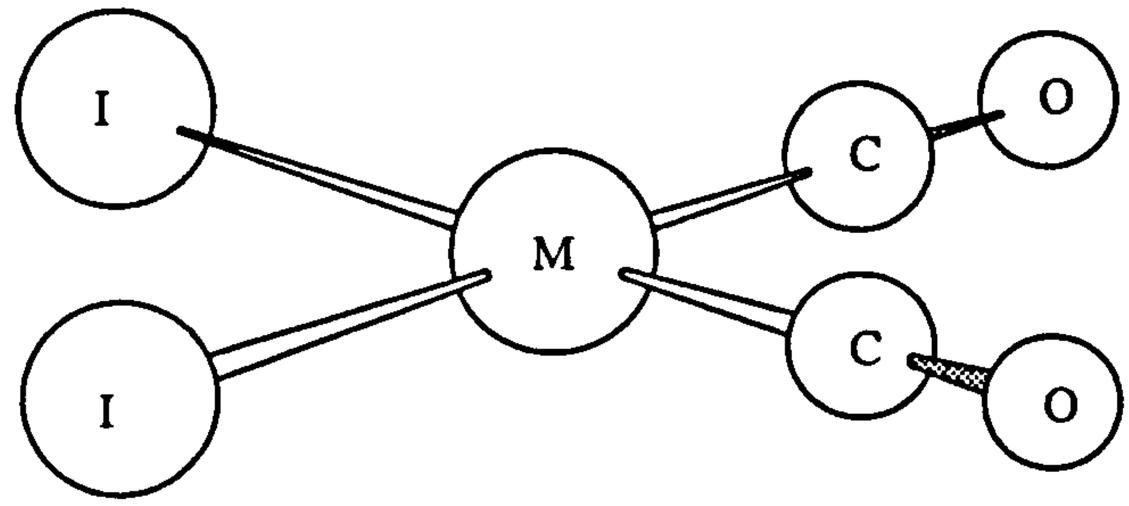

(b)

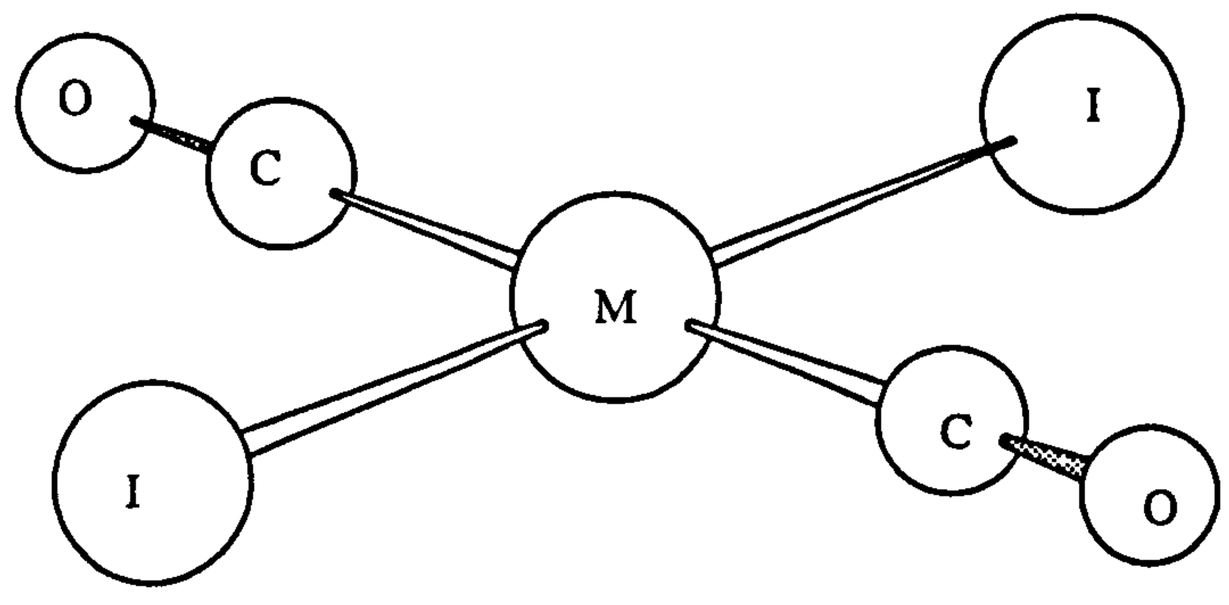

Figure 4.3: Structure of (a) *cis*-$[M(CO)_2I_2]^-$ (b) *trans*-$[M(CO)_2I_2]^-$.

(X=Cl, I) [187, 188]. The observed Rh–CO bond lengths in these complexes are very similar, 1.81 (X=I) and 1.82 Å(X=Cl). Each of the complexes above have Rh–CO bonds which are shorter than those generally found in octahedral rhodium(III) complexes, and they should therefore define a sensible range for this bond length in $[Rh(CO)_2I_2]^-$. It follows from Table 4.6 that the Rh–CO bond lengths computed by the MP2, LDA and BHANDH methods (*ca.* 1.79 to 1.81 Å, DZ basis) are in reasonable agreement with the experimental data. These schemes also generate Rh–I bond lengths (*ca.* 2.71 to 2.75 Å, DZ basis) which compare favourably with the observed value of 2.68 Åin $[Rh(CO)I(PPh_3)_2]$. As for the computed structures of *trans*-$[Rh(CO)_2I_4]^-$, the RHF and non-local DFT schemes seem to significantly overestimate both the Rh–CO and Rh–I bond lengths. Salter *et al.* have recently conducted an *ab initio* and DFT study of the structure of the model rhodium(I) Vaska complex, *trans*-$[Rh(CO)Cl(PH_3)_2]$, using the full-core Los Alamos ECP and associated LANL1DZ basis augmented with polarization functions (comparable to the DZ* basis used in this work) [156]. The LDA functional was found to give structural parameters in good agreement with the experimental geometry of *trans*-$[Rh(CO)Cl(PPh_3)_2]$, whereas the BLYP functional overestimated the Rh–CO and Rh–Cl bond lengths by 0.10 and 0.05 Å, respectively. The RHF and MP2 methods generated parameters which were in reasonable agreement with the crystal structure determination, although the latter method underestimated the expected Rh–CO bond length by 0.07 Å.

The geometry of the iridium(I) square planar complex $[Ir(CO)_2I_2]^-$ has been calculated at several levels of theory. Geometrical parameters obtained using the DZ and DZ2 bases are summarized in Table 4.7. The computed structures are distorted from perfect square planar as was observed for the rhodium complex. The Ir–CO distances computed with the full-core DZ basis are *ca.* 0.10 to 0.15 Å greater than the corresponding bond lengths predicted with the DZ basis in $[Rh(CO)_2I_2]^-$. This is a rather surprising result since comparable crystal data for rhodium and iridium carbonyl complexes generally only exhibit small M–CO bond length differences. A recent X-ray crystal structure determination of the iridium-chloro- analogue, *cis*-$[Ir(CO)_2Cl_2]^-$ [56], has revealed a Ir–CO bond length (1.81 Å) which is 0.06 Å longer than the measured Rh–CO bond length in $[Rh(CO)_2Cl_2]^-$. The Rh–CO and Ir–CO bond lengths in *trans*-$[M(CO)(OPh)(PPh_3)_2]$ are 1.801 and 1.795 Å, respectively [189, 190]. In the Vaska complexes, *trans*-$[M(CO)(Cl)(PPh_3)_2]$, the Rh–CO and Ir–CO bond lengths are 1.821 and 1.791 Å, respectively [191, 187]. Both of these latter examples for neutral metal(I) species exhibit Ir–CO bonds that are actually shorter than Rh–CO bonds. It seems therefore, that the full-core ECP and associated DZ basis is substantially overestimating Ir–CO bonds in *cis*-$[Ir(CO)_2I_2]^-$. Ir–I bonds are also extended, albeit to a lesser extent, relative to the Rh–I bonds calculated with the DZ basis. Here the bonds to the heavier metal are longer by *ca.* 0.01 to 0.05 Å.

Table 4.6: Calculated geometry of *cis*-$[Rh(CO)_2I_2]^-$ (C_{2v}).
Bond lengths Å, angles °.

Model	Basis	R_{Rh-C}	R_{Rh-I}	R_{C-O}	θ_{C-Rh-C}	θ_{I-Rh-I}
RHF	MB(37)[a]	1.992	2.982	1.148	93.9	103.1
	DZ(70)	1.883	2.807	1.143	94.0	97.9
	DZ2(74)	1.975	2.843	1.140	95.3	99.2
	DZ*(105)	1.871	2.805	1.121	92.7	98.7
	DZ*+(128)	1.871	2.802	1.120	92.6	98.3
MP2	MB	2.015	2.984	1.210	91.5	99.6
	DZ	1.791	2.738	1.211	91.4	95.2
	DZ2	1.840	2.730	1.210	92.5	94.1
	DZ*	1.750	2.734	1.177	88.3	96.6
LDA	MB	1.896	2.867	1.207	96.8	106.2
	DZ	1.811	2.748	1.188	98.3	103.3
	DZ2	1.822	2.698	1.191	96.9	95.5
	DZ*	1.801	2.737	1.164	97.1	105.4
BLYP	MB	1.963	3.002	1.217	97.1	109.2
	DZ	1.863	2.880	1.199	97.1	105.7
	DZ2	1.867	2.816	1.203	95.8	96.6
	DZ*	1.856	2.859	1.172	95.9	106.6
BHANDH	MB	1.884	2.846	1.207	96.6	105.2
	DZ	1.814	2.714	1.160	95.9	97.9
	DZ2	1.843	2.699	1.160	96.4	95.6
	DZ*	1.804	2.708	1.137	94.5	99.4
Becke3LYP	MB	1.952	2.945	1.197	96.1	105.7
	DZ	1.852	2.821	1.181	96.4	102.2
	DZ2	1.863	2.783	1.184	95.8	96.4
	DZ*	1.843	2.810	1.156	95.2	103.4

[a]Numbers in parentheses refer to the total number of basis functions.

Table 4.7: Calculated geometry of *cis*-$[Ir(CO)_2I_2]^-$ (C_{2v}).
Bond lengths Å, angles °.

Model	Basis	R_{Ir-C}	R_{Ir-I}	R_{C-O}	θ_{C-Ir-C}	θ_{I-Ir-I}
RHF	DZ	1.987	2.831	1.146	94.1	95.1
	DZ2	1.884	2.804	1.149	94.3	94.1
MP2	DZ	1.923	2.792	1.212	91.7	92.9
	DZ2	1.842	2.761	1.215	92.1	92.4
LDA	DZ	1.952	2.789	1.189	98.3	95.4
	DZ2	1.823	2.715	1.194	96.0	91.7
BLYP	DZ	2.016	2.886	1.199	97.0	96.7
	DZ2	1.856	2.818	1.207	95.3	92.8
BHANDH	DZ	1.941	2.764	1.161	96.0	93.9
	DZ2	1.829	2.712	1.166	95.3	92.2
Becke3LYP	DZ	1.995	2.846	1.181	96.4	95.7
	DZ2	1.884	2.804	1.149	94.4	94.1

By contrast to the results for rhodium species, moving to the semi-core ECP appears to significantly improve the bond lengths in the iridium complex. The Ir–CO bond lengths calculated with the DZ2 basis are reduced relative to the DZ results by *ca.* 0.1 to 0.15 Å, yielding values more in line with expectations based on experimental crystal data. The MP2, LDA and BHANDH predictions (*ca.* 1.82 to 1.84 Å) are within an acceptable range of the Ir–CO bond lengths observed in the anionic and neutral Ir(I) complexes discussed above. The Ir–I DZ2 bond lengths are reduced relative to the DZ results by *ca.* 0.03 to 0.07 Å.

Table 4.8 presents the symmetric, ν_s, and antisymmetric, ν_a, carbonyl harmonic stretching frequencies for *cis*-$[Rh(CO)_2I_2]^-$ calculated at various levels of theory. Also presented for comparison with the theoretical predictions are the measured (anharmonic) values. The RHF predictions are all substantially higher than the observed frequencies. This is expected in view of the previous results for the unbound CO molecule and the well known tendency for this model to systematically overestimate vibrational frequencies. The RHF/MB results deviate substantially from the experimental and other theoretical values (21.9 % mean error). Values calculated employing the split valence and extended bases have mean errors of 7.6 to 9.6%, in tolerable agreement with experiment. The RHF/DZ* method predicts the splitting of the vibrational modes to within 2 cm^{-1}. The minimal basis frequencies obtained from the correlated schemes are in remarkable agreement with the experimental values (0.6% to 3.8% mean errors). However, this is probably fortuitous since when one of the higher quality DZ or DZ2 bases are used, the calculations predict frequencies which are significantly too low. The MP2 and

Table 4.8: Calculated carbonyl harmonic stretching frequencies (cm^{-1}) for *cis*-$[Rh(CO)_2I_2]^-$.

Model	Basis	ν_a	ν_s	$\nu_s - \nu_a$	$\bar{\Delta}(\nu)\%$
RHF	MB	2460	2472	12	21.9
	DZ	2149	2205	56	7.6
	DZ2	2199	2234	35	9.6
	DZ*	2178	2247	69	9.3
MP2	MB	2000	2022	22	0.6
	DZ	1724	1848	124	11.8
	DZ2	1732	1836	104	11.9
LDA	MB	2035	2082	47	1.7
	DZ	1867	1941	74	5.9
	DZ2	1915	1976	61	3.9
	DZ*	1997	2067	70	0.2
BLYP	MB	1949	1983	34	2.8
	DZ	1781	1846	65	10.4
	DZ2	1810	1872	62	9.5
	DZ*	1918	1981	63	3.7
BHANDH	MB	2049	2097	48	2.5
	DZ	1868	1940	72	5.9
	DZ2	2070	2134	64	3.9
	DZ*	2184	2255	71	9.7
Becke3LYP	MB	2084	2115	31	3.8
	DZ	1880	1948	68	5.4
	DZ2	1912	1976	64	4.0
	DZ*	2033	2097	64	2.1
Experiment[a]		1988	2059	71	

[a]Experimental values for the fundamental absorption band for *cis*-$[Rh(CO)_2I_2]^-$ in CH_2Cl_2 [15].

BLYP schemes yield the largest errors of *ca.* 10 to 12%. A rather more favourable agreement is obtained from the LDA method or either of the hybrid schemes where the errors are lower than 6%. Note that the true errors are probably larger than those given in Table 4.8 because these frequencies have not been corrected for anharmonicity which would be expected to make them even lower. Polarisation functions are required in the basis set to raise the frequencies back to within an acceptable range of the observed fundamentals. The best overall agreement with experiment using the DZ* basis is obtained with the LDA functional; the deviations are *ca.* +9 cm^{-1}, and the separation of the modes is predicted to within 1 cm^{-1}. Frequencies were not calculated with the MP2/DZ* scheme owing to the unreasonable computational expense.

Harmonic vibrational frequencies for *cis*-$[Ir(CO)_2I_2]^-$ computed with the DZ and DZ2 bases are shown in Table 4.9. Frequencies estimated with the DFT schemes are in general closer to the experimental values than those obtained with the *ab initio* methods. The most accurate predictions are given by the LDA and BHANDH schemes. A slightly worrying point is the failure of the correlated methods to correctly predict the lower observed carbonyl frequencies for $[Ir(CO)_2I_2]^-$ relative to the rhodium species.

Table 4.9: Calculated carbonyl harmonic stretching frequencies (cm^{-1}) for *cis*-$[Ir(CO)_2I_2]^-$.

Model	Basis	ν_a	ν_s	$\nu_s - \nu_a$	$\bar{\Delta}(\nu)\%$
RHF	DZ	2121	2181	60	7.2
	DZ2	2111	2188	77	7.1
MP2	DZ	1741	1837	96	10.9
	DZ2	1781	1881	100	8.8
LDA	DZ	1872	1928	56	5.2
	DZ2	1925	1988	63	2.5
BLYP	DZ	1784	1835	51	9.7
	DZ2	1821	1887	66	7.6
BHANDH	DZ	2040	2104	64	3.2
	DZ2	2054	2131	77	4.3
Becke3LYP	DZ	1893	1948	55	4.3
	DZ2	2110	2188	78	7.1
Experiment[a]		1968	2046	78	

[a]Experimental values for the fundamental absorption band for *cis*-$[Ir(CO)_2I_2]^-$ in CH_2Cl_2 [15].

Geometrical parameters for *trans*-$[Rh(CO)_2I_2]^-$ computed using the standard DZ basis are listed in Table 4.10. The geometry is perfect square planar from symmetry

Table 4.10: Calculated geometry of *trans*-$[Rh(CO)_2I_2]^-$ (D_{2h}) and energy change (ΔE) for reaction (4.3). Geometrical data deduced from DZ calculations. Energies obtained from single-point calculations on these geometries using the extended DZ* basis.
Bond lengths Å, angles °, energies kJ mol^{-1}.

Model	R_{Rh-C}	R_{Rh-I}	R_{C-O}	ΔE
RHF	1.948	2.793	1.138	+20.5
MP2	1.871	2.688	1.198	−80.9
LDA	1.871	2.682	1.181	−14.0
BLYP	1.926	2.811	1.191	+3.5
BHANDH	1.873	2.671	1.153	−0.6
Becke3LYP	1.913	2.769	1.174	+8.0

considerations. The Rh–CO bond lengths are longer than those computed for *cis*-$[Rh(CO)_2I_2]^-$ by *ca.* 0.06 to 0.08 Å. The C–O bonds are shorter by *ca.* 0.005 to 0.013 Å. These geometrical changes are consistent with a reduction in the Rh–CO π back-donation which would be expected to occur when the CO ligands are competing for metal *d* electrons in *trans* positions. A weakening of the Rh–CO π interaction appears to strengthen the Rh–I bonds which become shorter relative to those computed in the *cis* isomer by *ca.* 0.02 to 0.07 Å.

Single-point calculations with the extended DZ* basis have been carried out to obtain estimates of the energy change for the isomerisation reaction:

$$trans\text{–}[Rh(CO)_2I_2]^- \rightleftharpoons cis\text{–}[Rh(CO)_2I_2]^- \qquad (4.3)$$

These are collected in the right hand column of Table 4.10. The *trans* isomer of $[Rh(CO)_2I_2]^-$ has never been observed, either in working catalyst solutions or model reactions. This experimental observation is reproduced in the MP2 calculation, which predicts that reaction (4.3) is exothermic by *ca.* 80 kJ mol^{-1}. None of the other methods, however, show such a strong preference towards the *cis* isomer. This is particularly evident in the RHF calculation which predicts that the *trans* complex is the more stable of the two isomers by *ca.* 20 kJ mol^{-1}. More surprisingly perhaps, is that the BLYP functional (which gave results in good agreement with the MP2 method for the relative stabilities of *cis*- and *trans*-$[Rh(CO)_2I_4]^-$) also predicts that *trans*-$[Rh(CO)_2I_2]^-$ is the more stable species. The energy change calculated at this level is small and endothermic. $\Delta E = +3.5$ kJ mol^{-1}. Additional calculations with the int=finegrid option only caused a further small stabilization of the *trans* isomer. It is conceivable that the MP2 scheme is overestimating the correlation energy for the *cis* isomer through an exaggerated M–CO π back-bonding interaction; this method generates the shortest Rh–CO bond and longest C–O bond in *cis*-$[Rh(CO)_2I_2]^-$, and also predicts the largest

geometrical change between the two structural isomers. On the other hand, the MP2 method did correctly predict the stability of *trans*-$[Rh(CO)_2I_4]^-$, but equally, it should be noted that M–CO π back-donation is expected to be less important in this system since the central metal is formally in a higher oxidation state. Solvent effects could be partly responsible for the observed stability of the *cis* species, although the fact that *trans*-$[Rh(CO)_2I_2]^-$ has never been observed under any conditions tends to suggest that the enthalpy change for reaction (4.3) may be exothermic even in the gas phase. The *cis* geometry is generally preferred by square planar $[M(CO)_2X_2]$ complexes but there are some exceptions to this rule. It is known, for example, that isoelectronic $[Pt(CO)_2I_2]$ exists as an equilibrium mixture of the *cis* and *trans* isomers with the *trans* isomer predominating. For the choro- analogue, $[Pt(CO)_2Cl_2]$, the *cis* isomer is more stable [192]. Clearly, the energetics of $[M(CO)_2X_2]$ complexes can be finely balanced.

4.2.4 $[CH_3M(CO)_2I_3]^-$ (M=Rh, Ir)

The structure of the key alkyl species $[CH_3M(CO)_2I_3]^-$ (M=Rh, Ir) have been optimized at the *ab initio* and DFT levels of theory using the the split-valence DZ and DZ2 bases. Calculations with the extended DZ* basis were not performed in view of the unreasonable computational requirements (147 functions). The parameters in Tables 4.11 and 4.12 refer to alkyl complexes with *facial-cis* octahedral geometry (Figure 4.4), which experiment has indicated to be the predominant stereochemical form in both metal systems [15, 55].

First we inspect the computed structural parameters of the rhodium(III) alkyl species which are summarized in Table 4.11. In each case the geometry is predicted to be distorted from perfect octahedral. The interligand angles describing the *facial* set of iodides are in general greater than 95°, as are the angles between the mutually *cis* carbonyl ligands. The methyl group appears to be tilted slightly toward the iodide ligands in the equatorial plane. The Rh–CH_3 bonds are predicted to be longer than the Rh–CO bonds. Geometry optimizations with the full-core DZ basis yield values of the former bond length ranging from 2.032 Å for the BHANDH functional to 2.138 Å at the MP2 level. The latter lie between 1.834 Å for the LDA functional to 1.936 Å at the RHF level. It is interesting that the MP2 method causes an extension of the Rh–CH_3 bond (which is predominantly σ-bonding in character) relative to the RHF value, rather than a contraction which has been observed for the M–CO bonds (σ and π character) when correlation is applied at this level. The iodide ligand *trans* to methyl has a significantly longer Rh–I bond length than the values calculated for the two iodides *trans* to carbonyl ligands. The effect, which is presumably a manifestation of the stronger *trans* influence of the methyl group, is most prominent in the structures generated by the RHF and non-local DFT schemes. For example, the BLYP/DZ method predicts that iodide

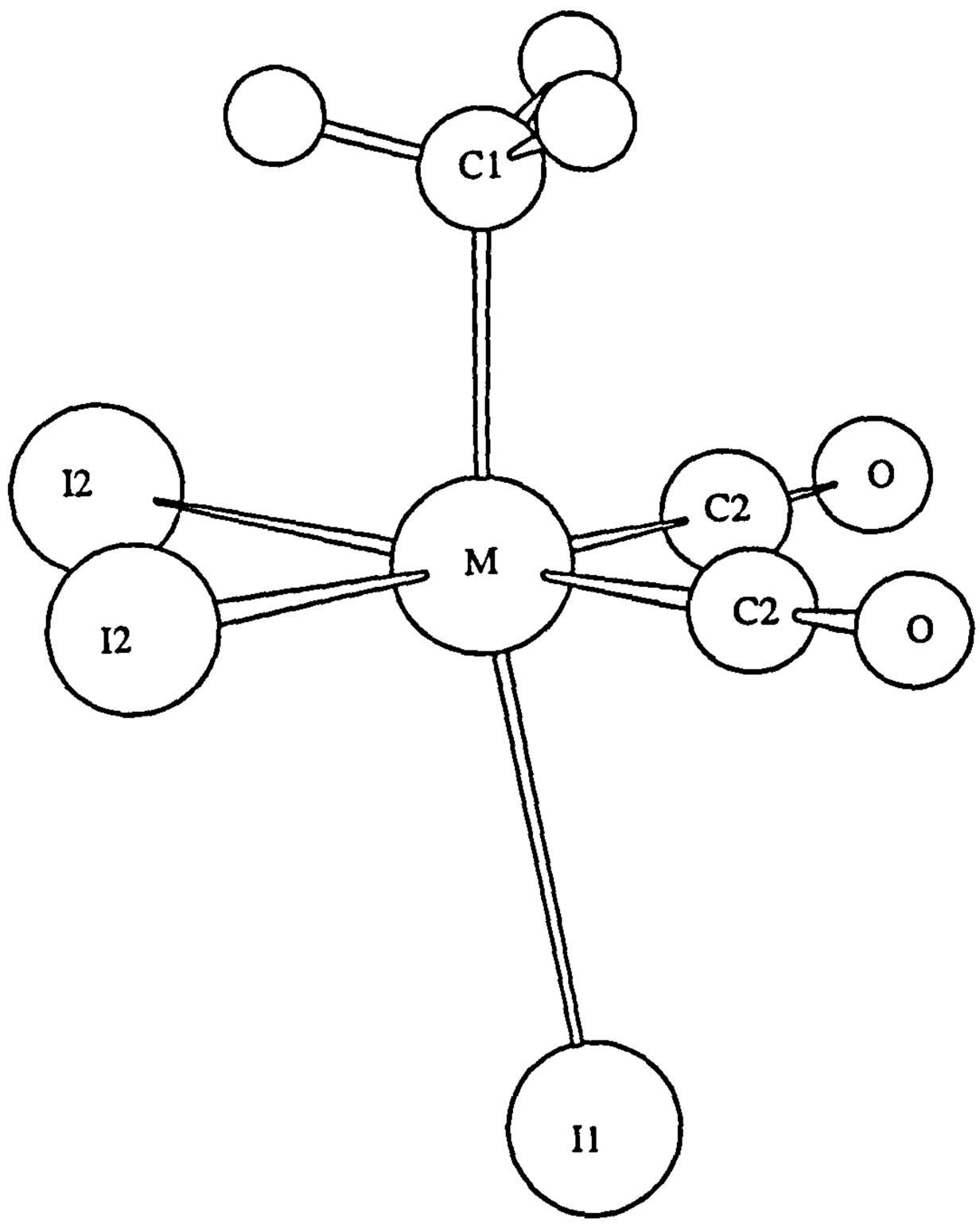

Figure 4.4: Structure of *fac-cis*-$[CH_3M(CO)_2I_3]^-$.

Table 4.11: Calculated geometry of *fac-cis*-$[CH_3Rh(CO)_2I_3]^-$ (C_s). Atom numbers defined in Figure 4.4.

		Bond Lengths (Å)				
Model	Basis	Rh-C1	Rh-C2	Rh-I1	Rh-I2	C2-O
RHF	DZ	2.050	1.936	2.942	2.770	1.133
	DZ2	2.098	2.037	3.004	2.778	1.132
MP2	DZ	2.138	1.836	2.873	2.752	1.197
	DZ2	2.207	1.889	2.873	2.746	1.197
LDA	DZ	2.047	1.834	2.886	2.773	1.183
	DZ2	2.106	1.845	2.812	2.732	1.182
BLYP	DZ	2.086	1.910	3.144	2.873	1.191
	DZ2	2.178	1.897	3.003	2.852	1.193
BHANDH	DZ	2.032	1.849	2.831	2.712	1.151
	DZ2	2.084	1.880	2.808	2.706	1.151
Becke3LYP	DZ	2.071	1.900	3.044	2.824	1.173
	DZ2	2.125	1.885	2.938	2.821	1.167

		Bond Angles (°)				
		C2-Rh-C2	I2-Rh-I2	C1-Rh-I2	C1-Rh-C2	I1-Rh-I2
RHF	DZ	97.4	96.3	88.8	89.9	98.3
	DZ2	96.9	96.2	88.7	90.7	99.9
MP2	DZ	97.5	93.5	86.5	91.5	95.3
	DZ2	98.1	91.9	86.4	91.3	95.5
LDA	DZ	102.9	105.7	87.8	93.5	98.3
	DZ2	101.0	96.0	86.1	93.6	94.1
BLYP	DZ	100.2	104.3	89.9	93.2	101.6
	DZ2	99.3	97.2	86.8	93.4	96.1
BHANDH	DZ	100.2	97.5	87.8	91.5	96.9
	DZ2	100.3	94.9	87.4	91.8	95.7
Becke3LYP	DZ	100.1	101.4	88.7	92.5	100.4
	DZ2	100.1	95.9	87.7	92.5	95.9

trans to methyl will have a longer bond length by *ca.* 0.27 Å. The MP2 method and local DFT schemes, which seem to be more reliable for calculating M–I bond lengths, yield smaller differences of *ca.* 0.12 Å.

In general, the semi-core DZ2 basis yields longer Rh–C bond lengths for both the carbonyl and methyl ligands. Experience would suggest that the shorter bond lengths predicted with the standard DZ basis are more realistic estimates of the true values. In the case of the Rh–I bonds, the semi-core basis also produces the longer values for the *ab initio* methods but significantly shorter values are observed for the DFT schemes. For example, the long Rh–I bond *trans* to methyl of 3.144 Å predicted with the BLYP/DZ scheme (which clearly must be a significant overestimate) is reduced by 0.14 Å when the DZ2 basis is employed. Smaller contractions of *ca.* 0.02 to 0.07 Å are observed for the other DFT methods.

There are no crystal structures determinations of similar anionic rhodium methyl complexes reported in the literature but there are some examples for neutral rhodium(III) species. The mutually *trans* Rh–CH_3 and Rh–I bond lengths in $[CH_3RhI[C_2(DO)(DOBF_2)]]$[1] are 2.09 and 2.81 Å, respectively [193]. A similar Rh–CH_3 bond length of 2.08 Å has been found in $[CH_3RhI_2(PPh_3)_2]$ [194]. Most of the calculations employing the full-core basis predict Rh–CH_3 bond lengths which agree reasonably well with the experimental data. A notable exception is the MP2 scheme which yields a bond length significantly in excess of the observed values and the other theoretical data.

Geometrical parameters calculated for *fac-cis*-$[CH_3Ir(CO)_2I_3]^-$ are shown in Table 4.12. The structures are also distorted, displaying similar variations in the bond angles to those observed for the rhodium alkyl species. For each theoretical method the Ir–CH_3, Ir–CO and Ir–I bond lengths are all calculated to be shorter with the semi-core DZ2 basis. Furthermore, comparing the DZ parameters for each metal, one finds that the Ir–C bonds, and to a lesser extent the Ir–I bonds, are significantly longer than the corresponding bond lengths in the rhodium complex. For example, the RHF/DZ parameters suggest that the Ir–CH_3 and Ir–CO bonds are longer than the Rh–CH_3 and Rh–CO bonds by 0.11 and 0.13 Å, respectively. A similar pattern of results was observed in the structures calculated for $[M(CO)_2I_2]^-$ by the two split-valence bases.

A recent crystal structure determination of the hexyl analogue of the iridium complex, $[n\text{-}C_6H_{13}Ir(CO)_2I_3]^-$, has shown it to have a *fac-cis* octahedral geometry [55]. The observed Ir–I bond lengths *trans* to carbonyls have a mean value of 2.705 Å. Ir–I *trans* to methyl is 2.775 Å. The mean angle between the facial set of iodides is 92.1°. The Ir–CO and Ir–C(hexyl) bond lengths are 1.90 and 2.04 Å, respectively. Another crystal structure of an iridium-iodo-carbonyl complex reported in

[1] Methyliododifluoro[3,3′-(trimethylenedinitrilo)bis(2-pentanoneoximato)]borate]rhodium(III), $Rh(CH_3)I(C_{13}H_{22}N_4O_2BF_2)$.

Table 4.12: Calculated geometry of *fac-cis*-$[CH_3Ir(CO)_2I_3]^-$ (C_s). Atom numbers defined in Figure 4.4.

		Bond Lengths (Å)				
Model	Basis	Ir-C1	Ir-C2	Ir-I1	Ir-I2	C2-O
RHF	DZ	2.166	2.066	2.951	2.803	1.133
	DZ2	2.134	1.942	2.919	2.799	1.136
MP2	DZ	2.246	1.966	2.907	2.804	1.198
	DZ2	2.200	1.869	2.865	2.787	1.202
LDA	DZ	2.184	1.990	2.937	2.791	1.180
	DZ2	2.118	1.844	2.855	2.749	1.185
BLYP	DZ	2.212	2.099	3.256	2.859	1.191
	DZ2	2.184	1.881	2.986	2.858	1.196
BHANDH	DZ	2.158	1.987	2.877	2.755	1.151
	DZ2	2.107	1.860	2.808	2.734	1.154
Becke3LYP	DZ	2.194	2.067	3.083	2.826	1.171
	DZ2	2.157	1.877	2.929	2.818	1.178

		Bond Angles (°)				
		C2-Ir-C2	I2-Ir-I2	C1-Ir-I2	C1-Ir-C2	I1-Ir-C2
RHF	DZ	97.7	94.0	87.9	90.2	96.9
	DZ2	97.9	93.8	88.1	90.7	95.5
MP2	DZ	96.7	91.7	85.3	91.7	94.3
	DZ2	96.3	91.8	85.4	92.2	93.0
LDA	DZ	101.9	94.4	85.2	95.5	96.8
	DZ2	99.2	92.4	85.4	94.6	91.8
BLYP	DZ	98.0	93.8	88.1	95.0	105.4
	DZ2	98.2	93.7	86.0	93.9	93.4
BHANDH	DZ	100.1	93.0	86.1	92.2	95.8
	DZ2	99.0	92.3	86.5	92.5	92.9
Becke3LYP	DZ	99.1	93.8	87.0	94.0	99.9
	DZ2	98.3	93.4	86.4	93.2	93.4

the literature is for the the neutral species, $[CH_3Ir(CF_3)(CO)I(PPh_3)_2]$ [195]. The Ir–I bond *trans* to methyl (2.785 Å) is slightly longer than that *trans* to the hexyl chain in $[n\text{-}C_6H_{13}Ir(CO)_2I_3]^-$. The Ir–$CH_3$ bond in the neutral complex (2.12 Å) is longer than the Ir–C(hexyl) bond by *ca.* 0.08 Å. The Ir–CO bond *trans* to the electron withdrawing CF_3 group (1.95 Å) is also longer than the corresponding bond in the hexyl species. The theoretical structures may also be compared to crystal data for the iridium chloro- analogue, *fac-cis*-$[CH_3Ir(CO)_2Cl_3]^-$ [56]. This complex has the shortest observed Ir–CO bond lengths (mean 1.874 Å) and a Ir–CH_3 bond length of 2.114 Å. The Ir–Cl bond for the chloride ligand *trans* to methyl is extended relative to those *trans* to carbonyl in the equatorial plane by *ca.* 0.12 Å.

A comparison of the theoretical data to the experimental crystal structures suggests that the LDA/DZ2 and BHANDH/DZ2 methods yield the best overall predictions for the geometry of *fac-cis*-$[CH_3Ir(CO)_2I_3]^-$. The calculated Ir–CH_3 bond lengths (2.118 and 2.107 Å) are in excellent agreement with those found in $[CH_3Ir(CF_3)(CO)I(PPh_3)_2]$ and $[CH_3Ir(CO)_2Cl_3]^-$. The Ir–I bond lengths are longer than those in $[n\text{-}C_6H_{13}Ir(CO)_2I_3]^-$, deviating by *ca.* +0.06 Å for the LDA functional and +0.03 Å for BHANDH. The Ir–CO bond lengths are slightly shorter than the measured values in the hexyl and chloro species by *ca.* 0.02 to 0.05 Å.

Table 4.13 presents theoretically predicted harmonic carbonyl vibrational frequencies for *fac-cis*-$[CH_3Rh(CO)_2I_3]^-$, together with the anharmonic values reported from a recent experimental study [15]. The calculations have been carried out with the DZ basis only. The theoretical values follow the general trend noted previously for the unbound CO molecule and also for the $[M(CO)_2I_3]^-$ complexes; frequencies calculated with the RHF method are too high, whereas the correlated schemes tend to generate frequencies which are too low. The best agreement with experiment is obtained with the BHANDH functional which yields values to within 3% of the observed fundamentals. Again it is noticeable that the sophisticated BLYP functional does not perform well compared to the other methods (mean error 11%). The experimental carbonyl vibrational frequencies for $[CH_3Rh(CO)_2I_3]^-$ are higher than those observed for $[Rh(CO)_2I_2]^-$ by *ca.* 45 and 72 cm^{-1}. This experimental observation is also reflected in the computational results, where all of the theoretical methods predict higher frequencies for the alkyl complex. The increase can be attributed to oxidation of the central metal atom which reduces the electron density available for back-donation into CO π^* orbitals.

Carbonyl stretching frequencies for *fac-cis*-$[CH_3Ir(CO)_2I_3]^-$ calculated by the RHF and DFT-based schemes with the semi-core DZ2 basis are shown in Table 4.14. In this case, good agreement with experiment is achieved by both of the hybrid DFT schemes. These functionals yield frequencies deviating from the measured values by less than 4.0 %, and predict the separation of the modes to within 2 cm^{-1}. The BHANDH frequencies are probably the most accurate since these are higher

Table 4.13: Calculated carbonyl harmonic stretching frequencies (cm^{-1}) for *fac-cis*-$[CH_3Rh(CO)_2I_3]^-$. All data deduced from DZ calculations.

Model	ν_a	ν_s	$\nu_s - \nu_a$	$\bar{\Delta}(\nu)\%$
RHF	2272	2285	13	9.5
LDA	1918	1952	34	7.1
BLYP	1841	1865	24	11.0
BHANDH	2127	2158	31	2.9
Becke3LYP	1967	1991	24	5.0
Experiment[a]	2060	2104	44	

[a]Experimental values for the fundamental absorption band for *cis*-$[CH_3Rh(CO)_2I_3]^-$ in CH_3I [15].

Table 4.14: Calculated carbonyl harmonic stretching frequencies (cm^{-1}) for *fac-cis*-$[CH_3Ir(CO)_2I_3]^-$. All data deduced from DZ2 calculations.

Model	ν_a	ν_s	$\nu_s - \nu_a$	$\bar{\Delta}(\nu)\%$
RHF	2244	2272	28	9.0
LDA	1963	2013	50	4.0
BLYP	1886	1915	29	8.6
BHANDH	2126	2177	51	3.9
Becke3LYP	1967	2019	52	3.9
Experiment[a]	2045	2098	53	

[a]Experimental values for the fundamental absorption band for *cis*-$[CH_3Ir(CO)_2I_3]^-$ in CH_2Cl_2 [15].

than the experimental values (whereas the Becke3LYP frequencies are too low) and corrections due to anharmonicity would be expected to lower them toward the observed range.

4.2.5 $[(COCH_3)M(CO)I_3]^-$ (M=Rh, Ir)

The structure of the five co-ordinate acyl intermediate $[(COCH_3)M(CO)I_3]^-$ has been optimized using the *ab initio* and DFT methods. For the rhodium species the full-core ECP and DZ basis was used, while for iridium the semi-core ECP and DZ2 basis has been employed. The particular choice of ECP for each metal is based upon their relative performances in predicting Rh–C and Ir–C bond lengths for the carbonyl and alkyl complexes discussed in the previous sections. Geometries for the acyl complex were initially set up corresponding to both square pyramidal and trigonal bipyramidal structures. However, only one stable conformation could be optimized, the calculations leading in each case to a square pyramidal structure adopting the stereochemistry shown in Figure 4.5a.

The structural parameters optimized for $[(COCH_3Rh(CO)I_3]^-$ are summarized in Table 4.15. One of the most interesting features is that the acyl ligand occupies the axial site in the square pyramid, which is a reflection of its strong *trans* influence. In fact, there are no examples of crystal structures from the literature of square pyramidal complexes exhibiting acyl ligands in basal sites. The computed Rh–$C(OCH_3)$ bond lengths range from 1.889 Å for the BHANDH functional to 1.980 Å at the MP2 level. These are shorter than the Rh–CH_3 bonds calculated for $[CH_3Rh(CO)_2I_3]^-$ by 0.12 to 0.16 Å, which may suggest a significant metal to acyl π back-donative interaction. Note though, that the Rh–$C(OCH_3)$ bond lengths are in general longer than the Rh–CO bonds in either the acyl or alkyl complexes, indicating that this interaction is smaller than for carbonyl ligands. The acyl C–O bond is aligned in the C_s plane eclipsing the basal carbonyl ligand. This conformation probably orientates the two C–O bonds such that the competition between them for metal *d* electrons is minimized. Apart from the Rh–I bond *trans* to carbonyl, which forms a large angle with the Rh–$C(OCH_3)$ bond (*ca.* 105 to 107°), the other basal ligands adopt a fairly planar arrangement around the central metal atom. The deviation from planarity for the independent iodide ligand occurs because it prefers not to be *trans* to either the carbonyl or acyl ligand. The mutually *trans* iodides are bent slightly toward the carbonyl ligand to avoid steric crowding.

An X-ray crystal structure determination of $[(COCH_3)Rh(CO)I_3]^-$ has shown it to be dimerised in the solid-state, held together through bridging iodide ligands [58]. This is shown for comparison with the theoretical geometries in Figure 4.5b. Inspecting first the bond lengths for the iodide and carbonyl ligands *cis* to acyl, we find that the BHANDH scheme again generates parameters in good accord

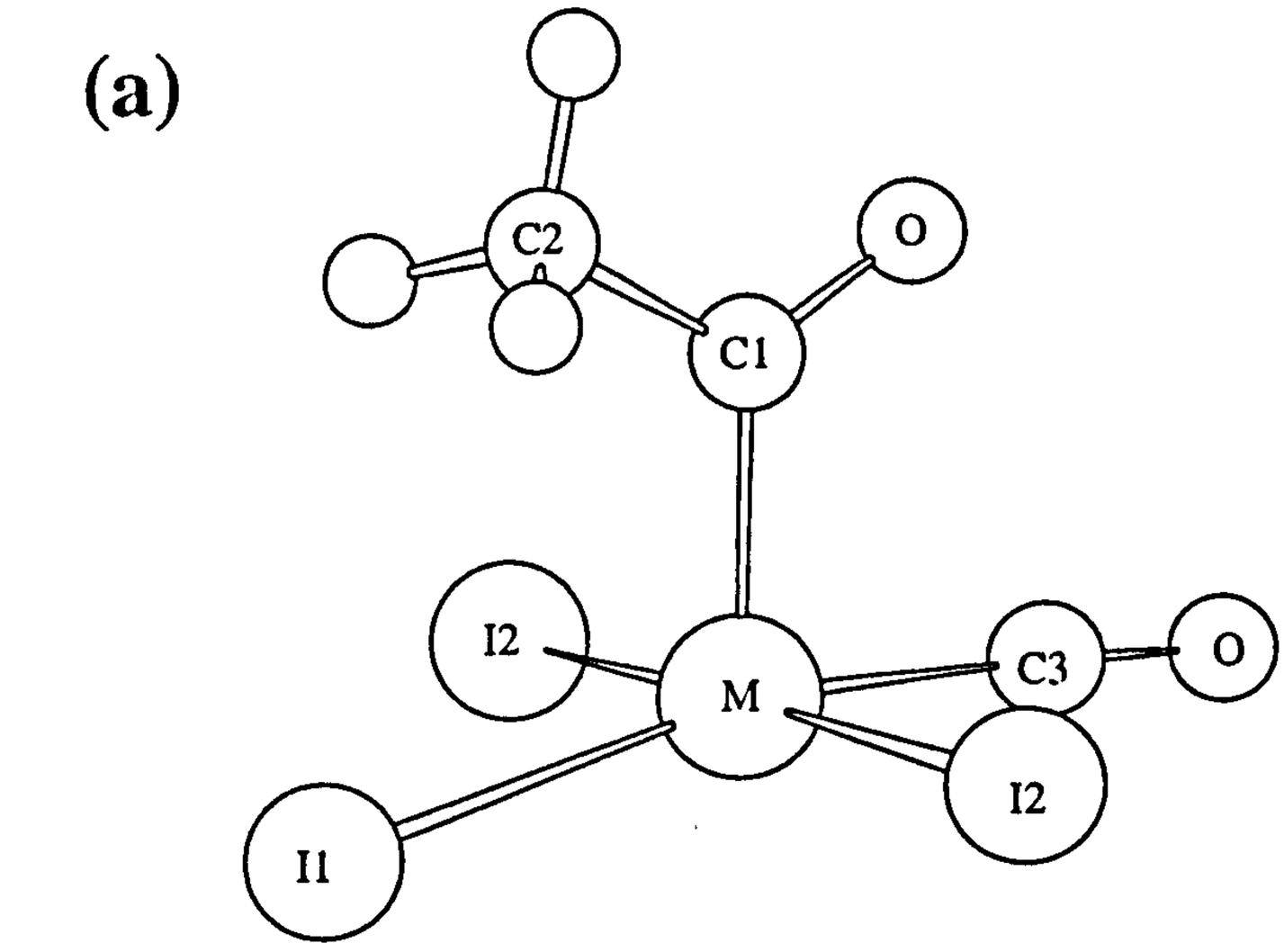

Figure 4.5: (a) Predicted structure of $[(COCH_3)M(CO)I_3]^-$; (b) Crystal structure of $[(COCH_3)_2Rh_2(CO)I_6]^{2-}$

Table 4.15: Calculated geometry of $[(COCH_3)Rh(CO)I_3]^-$ (C_s).
Atom numbers are defined in Figure 4.5. All parameters deduced from calculations using the DZ basis.

	Bond Lengths (Å)						
Model	Rh-C1	C1-C2	C1-O	Rh-C3	C3-O	Rh-I1	Rh-I2
RHF	1.930	1.515	1.217	1.965	1.131	2.768	2.722
MP2	1.980	1.557	1.240	1.788	1.205	2.765	2.725
LDA	1.898	1.495	1.227	1.830	1.180	2.749	2.687
BLYP	1.958	1.534	1.239	1.913	1.189	2.861	2.814
BHANDH	1.889	1.493	1.212	1.852	1.149	2.709	2.657
Becke3LYP	1.936	1.522	1.227	1.905	1.171	2.805	2.760

	Bond Angles (°)						
	C2-C1-O	O-C1-Rh	C1-Rh-C3	C1-Rh-I1	C1-Rh-I2	I1-Rh-I2	I2-Rh-C3
RHF	122.2	120.2	87.9	105.6	92.2	93.0	86.4
MP2	123.5	125.5	90.9	107.2	91.3	92.1	87.3
LDA	125.4	123.2	91.0	106.5	92.4	92.3	86.9
BLYP	124.3	122.0	92.5	105.6	93.3	92.8	86.0
BHANDH	124.1	122.2	88.7	106.4	91.6	92.3	87.2
Becke3LYP	124.1	121.8	91.2	106.0	92.7	92.7	86.4

Table 4.16: Calculated geometry of $[(COCH_3)Ir(CO)I_3]^-$ (C_s).
Atom numbers are defined in Figure 4.5. All parameters deduced from calculations using the DZ2 basis.

	Bond Lengths (Å)						
Model	Ir-C1	C1-C2	C1-O	Ir-C3	C3-O	Ir-I1	Ir-I2
RHF	2.021	1.515	1.223	1.954	1.134	2.779	2.763
MP2	2.056	1.558	1.247	1.830	1.211	2.770	2.753
LDA	1.979	1.509	1.237	1.826	1.188	2.722	2.707
BLYP	2.039	1.548	1.250	1.859	1.200	2.819	2.815
BHANDH	1.981	1.499	1.220	1.849	1.156	2.707	2.692
Becke3LYP	2.024	1.532	1.236	1.858	1.181	2.786	2.775
	Bond Angles (°)						
	C2-C1-O	O-C1-Ir	C1-Ir-C3	C1-Ir-I1	C1-Ir-I2	I1-Ir-I2	I2-Ir-C3
RHF	120.9	121.1	86.9	104.4	93.0	91.7	87.6
MP2	122.3	125.8	90.1	106.4	91.6	90.4	89.1
LDA	122.0	124.8	90.2	105.0	93.6	89.0	90.1
BLYP	121.2	124.4	91.2	105.7	94.0	89.6	89.2
BHANDH	122.0	123.3	88.1	105.0	92.4	90.1	89.3
Becke3LYP	121.5	124.0	90.1	105.8	93.4	89.9	89.1

with the experimental data. In particular, the Rh–CO and Rh–I bond lengths for *trans* carbonyl and iodide ligands are within 0.01 Å of the measured values in the dimer. Apart from the MP2 scheme which seems to underestimate the Rh–CO bond length by about 0.07 Å, the other theoretical methods yield bond lengths for the basal set which are generally longer than expected. The largest deviations are given by the RHF method for the Rh–CO bond (overestimated by *ca.* 0.1 Å) and the BLYP functional for the Rh–I bonds (overestimated by *ca.* 0.15 Å). The most noteworthy discrepancies between the theoretical parameters and crystal structure occur, however, in the geometry of the metal–acyl unit. Although theory correctly predicts the observed positions and co-planarity of acyl and carbonyl C–O bonds, the calculated Rh–C(OCH_3) bond lengths are all significantly shorter than the reported value. The BHANDH scheme is surprisingly in least agreement with experiment, predicting a value which is shorter than expected by 0.17 Å. The MP2 method predicts the longest and apparently most accurate value but this is still a significant underestimate of 0.08 Å. Larger deviations from the experimental data are found for the optimized acyl C–C bond distances. These appear to be systematically too large by *ca.* 0.2 Å, despite being in each case close to the ideal value for a C(sp^2)–C(sp^3) bond length (1.51 Å[196]). The calculated acyl Rh–C–O bond angles are larger than that observed for $[Rh_2(COCH_3)_2(CO)_2I_6]^{2-}$ by 9 to 12°.

Forster, who reported the dimeric crystal structure, described the co-ordination around the rhodium atoms as "approximately octahedral" and deduced from the bridging Rh–I distances that the two monomeric units were only loosely bound. However, the nature and extent of the distortion is not quantified, and it may therefore be imprudent to draw too many conclusions from this data. The structures of two related five co-ordinate rhodium(III) acyl complexes have recently been reported in the literature. The Rh–C(OCH_3) bond lengths in $[(COCH_3)RhI_2(dppm)]$ [197][2] and $[(COCH_3)RhI_2(dppp)]$ [198][3] are 2.00 and 1.98 Å, respectively. The acyl C–C bond distance and Rh–C–O bond angle are approximately the same for each complex, having values of *ca.* 1.51 Å and 125°. It is evident from Table 4.15, that the theoretical parameters resemble this data more closely than the geometrical parameters observed for $[Rh_2(COCH_3)_2(CO)_4I_2]^{2-}$. The predicted C–C bond lengths and Rh–C–O angles are in each case within 0.05 Å and 5° of the new experimental values. The Rh–C(OCH_3) bond lengths also compare more favourably but are still shorter than expected by up to 0.1 Å.

Geometrical parameters for the iridium acyl complex, $[(COCH_3)Ir(CO)I_3]$, calculated with the DZ2 basis are summarized in Table 4.16. The geometries predicted for the basal ligands are generally very similar to those computed for the rhodium acyl species. The most notable disparity is for the Ir–C(OCH_3) bond,

[2] $[(COCH_3)RhI_2(Ph_2PCH_2PPh_2)]$
[3] $[(COCH_3)RhI_2(Ph_2P(CH_2)_3PPh_2)]$

which in each instance is predicted to be longer than the corresponding bond in $[(COCH_3)Rh(CO)I_3]^-$ by *ca.* 0.09 Å. This structural difference could be interpreted as there being a weaker metal–acyl bond in the iridium complex, but the comparison may not be strictly valid since a different ECP was used for each metal system.

4.2.6 $[(COCH_3)M(CO)_2I_3]^-$ (M=Rh, Ir)

The final step of the Monsanto catalytic cycle is reductive elimination of acetyl iodide from $[(COCH_3)M(CO)_2I_3]^-$ to regenerate the active catalyst, $[M(CO)_2I_2]^-$. This reaction has not been examined in the present study but for completeness we report computed structures of the *trans* and *fac-cis* geometric isomers of the six co-ordinate acyl complexes and estimated values of their relative thermodynamic stabilities. Optimizations of the corresponding *mer-cis* complex with a carbonyl ligand *trans* to acyl failed in each case, suggesting that this isomer is unstable.

The structure of *trans*-$[(COCH_3)M(CO)_2I_3]^-$ is shown in Figure 4.6a. The geometry is a distorted octahedron with a C_s symmetry plane containing the acyl group, an iodide ligand and a pair of mutually *trans* carbonyl ligands. Selected bond lengths and angles computed with the DZ basis for the rhodium acyl species are given in Table 4.17. The largest deviation from perfect octahedral geometry occurs between the acyl group and the carbonyl ligand eclipsed by the acyl C–O bond (interligand angle CH_3OC–Rh–CO *ca.* 96 to 100°). The mutually *trans* iodide ligands are displaced upward toward the acyl group, increasing their angle with the independent iodide by 4 to 6°. The Rh–C(OCH_3) bond lengths range from 1.962 Å in the case of the BHANDH functional to 2.048 Å for the BLYP method. Lengthening of this bond relative to that in the five co-ordinate complex (*ca.* +0.08 Å) is expected to occur partly due to the *trans* influence of a co-ordinated iodide ligand but also because there are now two carbonyl ligands competing with the acyl for metal π electron density. There is a small difference between the Rh–CO bond lengths, the bond to carbonyl closest to the acyl oxygen being longer by *ca.* 0.02 to 0.04 Å. The C–O bond for this carbonyl ligand is slightly shorter, suggesting that π back-donation is less effective in this site. The terminal Rh–I bond *trans* to the acyl ligand is predicted to be significantly longer than those to the mutually *trans* pair of iodides. The magnitude of this elongation varies from +0.25 Å at the RHF level to +0.12 Å at the MP2 level. This structural feature must reflect a large *trans* influence of the acyl ligand.

The theoretical parameters may be compared to the experimental structure of $[(COCH_3)Rh(CO)(NC_5H5)I_3]^-$ [199], which is related to *trans*-$[(COCH_3)Rh(CO)_2I_3]^-$ by substitution of a carbonyl with a pyridine group. The relevant bond lengths are: 2.13 Å Rh–C(OCH_3); 1.83 Å Rh–CO; 2.66, 2.67 Å Rh–I (mutually *trans* iodides); 2.86 Å Rh–I (iodide *trans* to acyl). As in the case of the five co-ordinate species, it

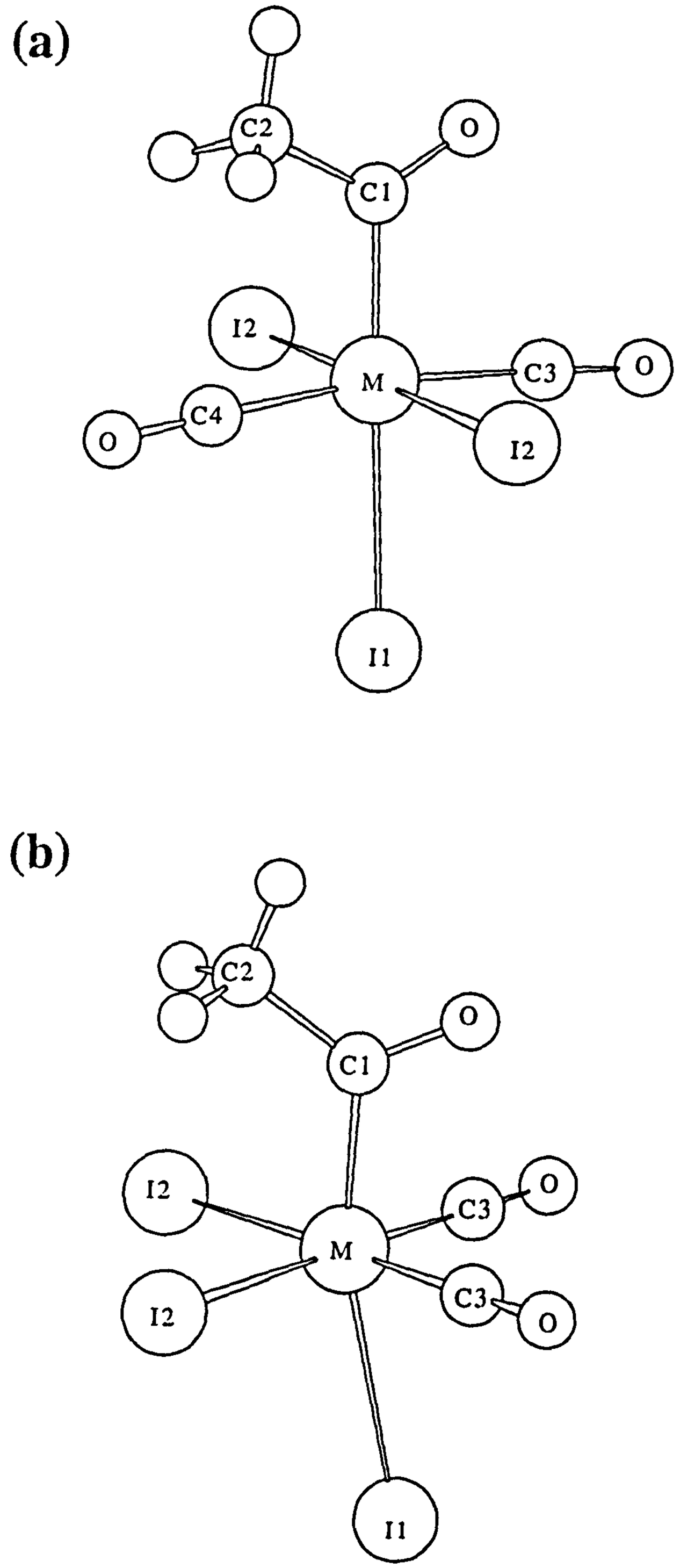

Figure 4.6: Structure of (a) *trans*-$[(COCH_3)M(CO)_2I_3]^-$ and (b) *fac-cis*-$[(COCH_3)M(CO)_2I_3]^-$.

Table 4.17: Calculated geometry of *trans*-$[(COCH_3)Rh(CO)_2I_3]^-$ (C_s).
Atom numbers are defined in Figure 4.6. All parameters deduced from calculations using the DZ basis.

	Bond Lengths (Å)				
Model	Rh-C1	C1-C2	C1-O	Rh-C3	C3-O
RHF	1.999	1.521	1.224	1.987	1.129
MP2	2.027	1.550	1.259	1.904	1.186
LDA	1.974	1.500	1.231	1.905	1.172
BLYP	2.048	1.537	1.242	1.983	1.181
BHANDH	1.962	1.500	1.220	1.908	1.143
Becke3LYP	2.022	1.526	1.232	1.966	1.164

	Rh-C4	C4-O	Rh-I1	Rh-I2
RHF	1.968	1.131	2.895	2.735
MP2	1.874	1.192	2.869	2.746
LDA	1.889	1.177	2.873	2.719
BLYP	1.946	1.186	3.065	2.867
BHANDH	1.892	1.147	2.825	2.679
Becke3LYP	1.932	1.169	2.988	2.791

	Bond Angles (°)			
	C2-C1-O	O-C1-Rh	C1-Rh-C3	C1-Rh-C4
RHF	119.8	119.3	88.9	96.2
MP2	120.1	121.9	91.5	97.1
LDA	124.0	120.6	93.3	96.6
BLYP	123.4	119.6	93.8	100.4
BHANDH	122.0	120.5	90.2	98.1
Becke3LYP	122.7	119.8	92.4	99.4

	C1-Rh-I2	I1-Rh-I2	I1-Rh-C3	I2-Rh-C4
RHF	86.1	93.9	89.0	89.3
MP2	84.6	95.4	86.6	90.1
LDA	84.2	95.8	87.4	88.5
BLYP	83.8	96.2	86.0	88.8
BHANDH	85.0	95.0	88.4	89.1
Becke3LYP	84.6	95.4	88.7	89.2

Table 4.18: Calculated geometry of *trans*-$[(COCH_3)Ir(CO)_2I_3]^-$ (C_s).
Atom numbers are defined in Figure 4.6. All parameters deduced from calculations using the DZ2 basis.

	Bond Lengths (Å)				
Model	Ir-C1	C1-C2	C1-O	Ir-C3	C3-O
RHF	2.074	1.520	1.231	1.992	1.130
MP2	2.093	1.551	1.271	1.931	1.188
LDA	2.029	1.505	1.245	1.893	1.175
BLYP	2.097	1.545	1.258	1.937	1.186
BHANDH	2.033	1.500	1.231	1.913	1.145
Becke3LYP	2.080	1.531	1.246	1.933	1.168
	Ir-C4	C4-O	Ir-I1	Ir-I2	
RHF	1.975	1.133	2.888	2.777	
MP2	1.905	1.195	2.874	2.771	
LDA	1.886	1.179	2.862	2.740	
BLYP	1.922	1.191	3.000	2.860	
BHANDH	1.899	1.150	2.814	2.714	
Becke3LYP	1.918	1.173	2.941	2.806	
	Bond Angles (°)				
	C2-C1-O	O-C1-Ir	C1-Ir-C3	C1-Ir-C4	
RHF	118.8	120.2	88.1	96.0	
MP2	119.0	122.9	89.7	96.5	
LDA	121.4	122.5	91.4	99.3	
BLYP	120.3	121.9	92.3	98.3	
BHANDH	120.1	121.8	89.0	96.4	
Becke3LYP	120.1	121.7	91.0	97.5	
	C1-Ir-I2	I1-Ir-I2	I1-Ir-C3	I2-Ir-C4	
RHF	87.3	92.8	89.2	89.5	
MP2	86.1	94.0	87.6	90.2	
LDA	86.9	93.2	85.2	88.6	
BLYP	86.9	93.2	84.6	89.4	
BHANDH	87.1	92.9	88.4	89.4	
Becke3LYP	87.1	93.0	86.2	89.5	

would appear that the theoretical methods have significantly underestimated the magnitude of the Rh–C(OCH_3) bond length. The authors who reported the crystal structure did comment however, that this bond was unusually long compared with most other rhodium acyl complexes. The steric influence of a bulky pyridine group and two iodide ligands *cis* to acyl might cause a lengthening of the Rh–C(OCH_3) bond from its ideal (electronic) value. For the other bond lengths, the MP2, LDA and BHANDH schemes are in reasonable agreement with the reported data, given the replacement of a carbonyl with pyridine. The RHF and non-local DFT schemes display their usual tendency for generating rather long Rh–CO and Rh–I bonds.

The structural parameters computed for *trans*-[($COCH_3$)Ir($CO)_2I_3$]$^-$ at several levels of theory using the DZ2 basis are summarized in Table 4.18. The interligand angles are similar to those observed for the rhodium species, as are the predicted bonds lengths to carbonyl and iodide ligands. A common feature of all the calculations is that the Ir–C(OCH_3) bond is longer than the corresponding bond in *trans*-[($COCH_3$)Rh($CO)_2I_3$]$^-$ by 0.05 to 0.07 Å. A similar structural difference was noted previously between the rhodium and iridium five co-ordinate acyl complexes but again it should be remembered that the choice of different ECPs for each metal could affect this comparison. The structure of *fac-cis*-[(CH_3CO)M($CO)_2I_3$]$^-$ is shown in Figure 4.6b. The theoretical calculations predict a geometry which exhibits a C_s plane of symmetry containing the acyl group and *trans* iodide ligand. This plane bisects the I–Ir–I and C–Ir–C bond angles of the equitorial Ir($CO)_2I_2$ unit. The acyl group is arranged such that its C–O bond lies on the same side of the molecule as the carbonyl ligands. Geometrical parameters for *facial-cis*-[(CH_3CO)Rh($CO)_2I_3$]$^-$ computed with the DZ basis are presented in Table 4.19. The structure of the rhodium complex is predicted to be substantially distorted from perfect octahedral symmetry. The interligand angles of the *facial* set of iodides are in general greater than 95°, as are the angles between the carbonyl ligands. The largest distortion however, is represented by the small angle that the iodide ligand *trans* to acyl makes with each of the carbonyl ligands. This is particularly evident in the case of the LDA and Becke3LYP functionals which predict I–Rh–CO angles of *ca.* 73°, the overall effect being a rather noticeable leaning of the iodide ligand toward the carbonyl side of the molecule. The size of the distortion appears to correlate with the predicted magnitudes of the Rh–I bond length; these are longer than the corresponding bond in *trans*-[($COCH_3$)Rh($CO)_2I_3$]$^-$ by 0.05 to 0.17 Åand longer than those to iodide ligands in the equatorial plane by 0.16 to 0.34 Å. The theoretical results suggest therefore, that the iodide ligand *trans* to acyl is quite weakly bound in *facial-cis*-[($COCH_3$)Rh($CO)_2I_3$]$^-$. The Rh–C(OCH_3) bond lengths are not markedly changed relative to those calculated for the *trans* isomer. The Rh–CO bond lengths are in general slightly shorter (*ca.* −0.02 to −0.05 Å), as would be expected for *cis* rather than *trans* π-accepting ligands.

Table 4.19: Calculated geometry of *fac-cis*-$[(COCH_3)Rh(CO)_2I_3]^-$ (C_s). Atom numbers are defined in Figure 4.6. All parameters deduced from calculations using the DZ basis.

	Bond Lengths (Å)				
Model	Rh-C1	C1-C2	C1-O	Rh-C3	C3-O
RHF	2.005	1.513	1.232	1.966	1.130
MP2	2.075	1.546	1.263	1.852	1.194
LDA	1.975	1.501	1.232	1.871	1.180
BLYP[a]	-	-	-	-	-
BHANDH	1.975	1.492	1.225	1.876	1.147
Becke3LYP	2.016	1.521	1.235	1.932	1.170

	Rh-I1	Rh-I2
RHF	2.952	2.757
MP2	2.914	2.754
LDA	3.042	2.754
BLYP	-	-
BHANDH	2.893	2.701
Becke3LYP	3.148	2.809

	Bond Angles (°)			
	C2-C1-O	O-C1-Rh	C1-Rh-C3	C1-Rh-I2
RHF	119.8	115.3	88.4	93.1
MP2	119.6	118.4	89.7	92.1
LDA	123.8	119.9	93.5	95.1
BLYP	-	-	-	-
BHANDH	121.6	117.3	90.3	93.7
Becke3LYP	122.5	117.8	92.1	94.7

	I1-Rh-I2	I2-Rh-I2	I1-Rh-C3	C3-Rh-C3
RHF	96.3	96.3	82.2	96.2
MP2	93.7	93.9	84.6	97.0
LDA	98.8	101.0	72.6	98.9
BLYP	-	-	-	-
BHANDH	95.5	96.9	80.7	98.6
Becke3LYP	100.0	100.3	73.1	98.0

[a]Geometry did not converge at this level.

Table 4.20: Calculated geometry of *fac-cis*-$[(COClH_3)Ir(CO)_2I_3]^-$ (C_s).
Atom numbers are defined in Figure 4.6. All parameters deduced from calculations using the DZ2 basis.

	Bond Lengths (Å)				
Model	Ir-C1	C1-C2	C1-O	Ir-C3	C3-O
RHF	2.092	1.512	1.236	1.964	1.132
MP2	2.151	1.543	1.271	1.883	1.197
LDA	2.086	1.497	1.245	1.856	1.180
BLYP	2.154	1.535	1.257	1.890	1.192
BHANDH	2.064	1.492	1.233	1.876	1.150
Becke3LYP	2.123	1.523	1.246	1.891	1.173

	Ir-I1	Ir-I2
RHF	2.918	2.792
MP2	2.889	2.781
LDA	2.882	2.741
BLYP	3.020	2.865
BHANDH	2.853	2.720
Becke3LYP	2.986	2.812

	Bond Angles (°)			
	C2-C1-O	O-C1-Ir	C1-Ir-C3	C1-Ir-I2
RHF	119.1	124.4	88.4	92.9
MP2	119.4	119.0	88.7	91.5
LDA	121.3	119.2	91.2	92.9
BLYP	120.7	119.0	91.5	92.5
BHANDH	120.4	118.2	89.8	92.7
Becke3LYP	120.5	118.6	90.7	92.8

	I1-Ir-I2	I2-Ir-I2	I1-Ir-C3	C3-Ir-C3
RHF	93.8	94.0	85.1	96.4
MP2	91.8	92.4	88.2	95.8
LDA	90.3	92.4	85.7	97.9
BLYP	91.3	93.9	84.9	97.6
BHANDH	91.4	92.6	86.3	97.2
Becke3LYP	92.1	93.7	84.6	97.2

The optimized parameters of *fac-cis*-$[(CH_3CO)Ir(CO)_2I_3]^-$ are shown in Table 4.20 (DZ2 basis). This structure does not display the same substantial distortions from octahedral symmetry noted for the rhodium complex. In particular, the interligand angles describing the facial set of iodides do not deviate from 90° by more than a few degrees. Also, the computed bond lengths for iodide *trans* to acyl are only slightly longer than those predicted in the *trans* isomer. A recent X-ray structure determination of the chloro- analogue, $[(CH_3CO)Ir(CO)_2Cl_3]^-$, has shown it to favour the *facial-cis* geometry in the solid-state [56]. A significant feature of the crystal structure, not realized in the theoretical calculations, is a staggered conformation for the acyl ligand. This group is orientated such that the O–C–CH_3 axis lies approximately perpendicular to the C_s plane defined by the other ligands, that is with both the oxygen and methyl lying roughly central between a carbonyl and chloride ligand. The chloro complex has mean Ir–CO bond lengths of *ca.* 1.900 Åand an observed Ir–C(OCH_3) bond length of 2.087 Å. It is interesting that the latter bond length for the acyl ligand is only slightly shorter than the Ir–CH_3 bond of 2.114 Å observed in the crystal structure of *fac-cis*-$[CH_3Ir(CO)_2Cl_3]^-$. The Ir–Cl bond for the chloride ligand *trans* to acyl is longer than those *trans* to carbonyl groups by 0.19 Å. By contrast to the results for rhodium acyl complexes, the theoretical methods generate Ir–C(OCH_3) bond lengths in satisfactory agreement with the experimental data. The values obtained with the LDA and BHANDH functionals are both within 0.02 Åof the measured bond length. The RHF method also predicts a Ir–C(OCH_3) bond length (2.092 Å) comparing favourably with this data but the Ir–CO bond is longer than expected by *ca.* 0.06 Å. The opposite behaviour is observed for the MP2 and non-local DFT schemes; these methods predict the best Ir–CO bond lengths (1.883 to 1.891 Å) but the longest and probably least accurate Ir–C(OCH_3) bonds (2.123 to 2.154 Å). All of the methods predict a significantly longer Ir–I bond *trans* to acyl, consistent with the high *trans* influence expected for acyl ligands and also with the rather long Ir–Cl bond length observed in the crystal structure of the chloro analogue.

Estimated energy changes for the interconversion of the *trans* and *fac-cis*- isomers of rhodium and iridium $[(COCH_3)M(CO)_2I_3]^-$ complexes are reported in Table 4.21. Each of the calculations on the rhodium system predict the *trans* isomer to be the more thermodynamically stable species, in qualitative agreement with experimental observations. The *fac-cis* isomer of $[(CH_3CO)Rh(CO)_2I_3]^-$ can be formed by reacting $[Rh(CO)_2I_2]^-$ with acetyl iodide but this is observed to undergo a slow isomerisation to the *trans* species. All of the methods, except for the LDA scheme, also predict the *trans* isomer to be the more stable complex in the iridium system. However, the isomerisation reaction is characterized by a significantly smaller energy change in each case, suggesting that the equilibrium will be more finely balanced. This latter result is consistent with the experimental solution behaviour of $[(COCH_3)Ir(CO)_2I_3]^-$, where it is found that in non-co-ordinating solvents both isomers can be observed [67].

Table 4.21: Estimated energy change (kJ mol^{-1}) for the isomerisation reaction: *fac-cis*-$[(COCH_3)M(CO)_2I_3]^-$ → *trans*-$[(COCH_3)M(CO)_2I_3]^-$.

Model	ΔE(Rh)[a]	ΔE(Ir)[b]
RHF	−52.1	−44.9
MP2	−38.1	−15.8
LDA	−14.7	+5.3
BLYP	−90.7[c]	−8.8
BHANDH	−39.6	−20.8
Becke3LYP	−31.0	−16.0

[a]Data deduced from DZ calculations.
[b]Data deduced from DZ2 calculations.
[c]Energy for *facial-cis* isomer determined from a single-point BLYP/DZ calculation on the optimized RHF/DZ geometry.

4.3 Conclusions

This chapter has presented the results of theoretical calculations on small molecules and equilibrium transition metal complexes that have been implicated in the Monsanto catalytic cycle. For the small molecules, CO and CH_3I, the DFT-based schemes yield molecular properties which are in general comparable to, or better than, those calculated with the conventional *ab initio* RHF and MP2 methods in the same Gaussian basis. While depending a great deal on the nature of the exchange-correlation functional, this also appears to be at least empirically true in calculations of rhodium- and iridium-iodo-carbonyl transition metal complexes.

The local density approximation, LDA, and Becke's simplest hybrid functional, BHANDH, in most cases yield very good predictions for the geometrical structures of the transition metal complexes. The bond lengths calculated by these schemes in conjunction with a split-valence basis, deviate from values based on experimental crystal data typically by less than 0.05 Å. However, in the case of the sophisticated BLYP functional, and to a lesser extent the other non-local scheme, Becke3LYP, the performance for structures is rather disappointing. For example, the BLYP functional is found to systematically overestimate the magnitude of M–I bonds by *ca.* 0.1 to 0.2 Å. Structural parameters computed with the *ab initio* methods are in reasonable agreement with experimental data. The RHF method tends to overestimate M–CO bond lengths by *ca.* 0.1 Å but these are reduced usually to within 0.05 Å of the experimental values when the MP2 scheme is employed. Inclusion of electron correlation at the MP2 level, does however, lead to M–CH_3 bonds which are somewhat longer than those predicted by the other theoretical methods and those reported from experimental determinations. The theoretically predicted M–C(OCH_3) bond lengths are in general shorter than expected. In

particular, the crystal structure data for rhodium acyl complexes suggested that all of the methods underestimate Rh–C(OCH_3) bond lengths. The following general trends for bond lengths calculated by the theoretical methods can be deduced:

- M–CO: expt < MP2 < BHANDH ~ LDA < Becke3LYP < BLYP < RHF
- M–I: expt < BHANDH < LDA < MP2 < RHF < Becke3LYP < BLYP
- M–CH_3: BHANDH < LDA < RHF < expt[4] < Becke3LYP < BLYP < MP2
- M–C(OCH_3): BHANDH < LDA < RHF < Becke3LYP < BLYP < MP2 < expt[4]
- C–O: expt < RHF < BHANDH < Becke3LYP < LDA < BLYP < MP2

Note that the positions of the experimental bond lengths in these series are only intended as an approximate guide and are likely to change depending on the central metal atom and the particular molecule considered. It should also be realized that the series above refer to calculations employing a modest split-valence quality basis. It is possible that some of the sophisticated correlated treatments (e.g. MP2, BLYP) would improve their relative standings if a more advanced basis incorporating say, several extra sets of functions was employed. Notwithstanding the likelihood of this occurring for a very large basis set, augmenting the basis with a single set of polarization functions (DZ*) was generally only found to cause significant improvement for the C–O bond lengths.

An important observation that emerges from the results of geometry calculations concerns the choice of ECP for each metal system. In the case of rhodium complexes, the full-core ECP and DZ basis, on the whole, seem to give the best results for bond lengths whereas for iridium, the semi-core ECP and DZ2 basis appear to be more accurate. This is particularly evident for the M–CO and M–CH_3 bond lengths calculated by the RHF method and the M–CH_3 bond lengths calculated by the MP2 scheme. The reason for this general tendency is not clear at this time and may require further detailed study of the actual ECPs and basis functions for the two metals.

The performance of the methods in calculating harmonic carbonyl vibrational frequencies for transition metal complexes in general parallels that for predicting C–O ligand bond distances. RHF C–O bond lengths are consistently shorter than those calculated by the other methods and the carbonyl vibrational frequencies are systematically higher than the measured anharmonic values by *ca.* 7 to 10%. The correlated schemes predict C–O bond lengths which are generally too long and frequencies which are always lower than expected. The LDA, BHANDH and

[4]Position of experimental values based on comparisons of crystal structure data with bond lengths obtained from DZ basis calculations of rhodium alkyl and acyl complexes.

Becke3LYP functionals generate frequencies in reasonable agreement with experiment (underestimated by *ca.* 5%), whereas the BLYP functional and MP2 scheme yield frequencies with much larger errors (underestimated by *ca.* 10%).

The accuracy of the methods for determining energetics is less clear since experimental enthalpy changes for the reactions considered here are not available. The results have suggested though, that many of the potential isomerisation reactions between complexes relevant to the catalysis have finely balanced equilibria. In some cases, the MP2 scheme and non-local functionals make comparable predictions for these energy changes (for example, the interconversion of *cis*- and *trans*-$[Rh(CO)_2I_4]^-$). However, there are also cases where the two schemes are in strong disagreement (for example, the interconversion of *cis*- and *trans*-$[Rh(CO)_2I_2]^-$).

Chapter 5

Oxidative Addition

This chapter reports the results of a comparative *ab initio* and DFT study of the key oxidative addition step of the Monsanto catalytic cycle:

$$[M^{I}(CO)_2I_2]^- + CH_3I \rightarrow [CH_3M^{III}(CO)_2I_3]^- \qquad M = (Rh, Ir). \qquad (5.1)$$

This reaction has been investigated theoretically with respect to its mechanistic behaviour, thermodynamics, electronic features and influence by a solvent medium. Results of calculations carried out for the reverse reductive elimination reaction are also presented.

5.1 Mechanistic Aspects of the Oxidation Addition of Alkyl Halides to Square Planar Complexes

There has been considerable debate concerning the mechanism by which alkyl halides add to square planar complexes [14]. For simple substrates such as CH_3I, most experimental observations support a stepwise addition mechanism, Figure 5.1a. The first step is nucleophilic substitution of iodide by the metal complex, expected to proceed with inversion of configuration at carbon. Subsequent co-ordination of iodide completes the addition to yield a six co-ordinate alkyl complex.

Activation parameters determined for the addition of CH_3I to $[M(CO)_2I_2]^-$ complexes (Table 5.1) are typical of those measured for S_N2 reactions. In particular, the large negative entropies of activation are an indication that these reactions pass through highly ordered transition states, consistent with an S_N2 pathway.

Chock and Halpern have studied the oxidative addition of methyl iodide to the neutral Vaska complex, *trans*-$[Ir(CO)X(PPh_3)_2]$ [53]. For X= Cl, Br and I, they reported activation parameters of $\Delta H^{\ddagger}$=23, 31, 37 kJ mol^{-1}, and $\Delta S^{\ddagger}$=−210,

(a)

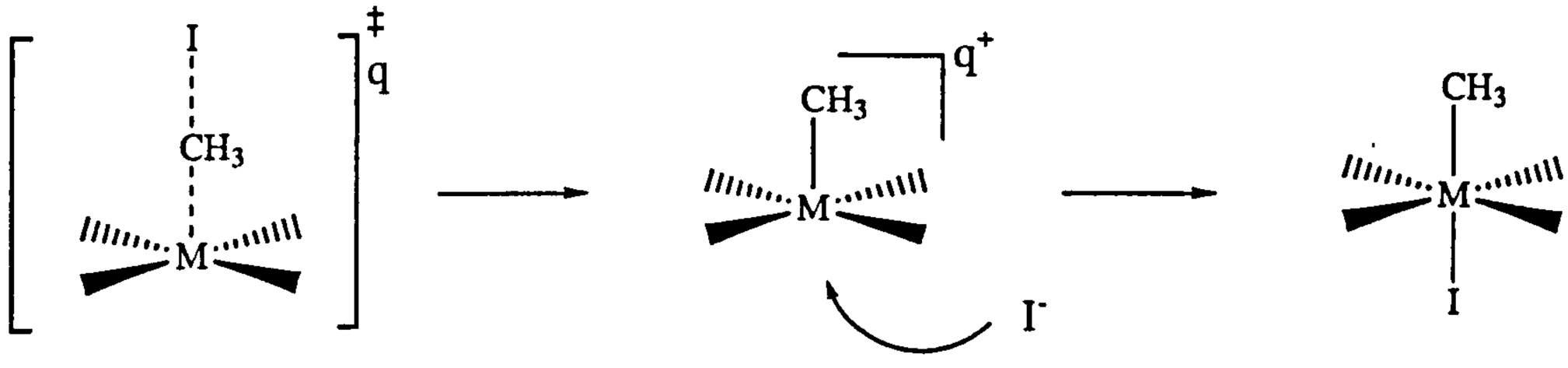

(b)

(c)

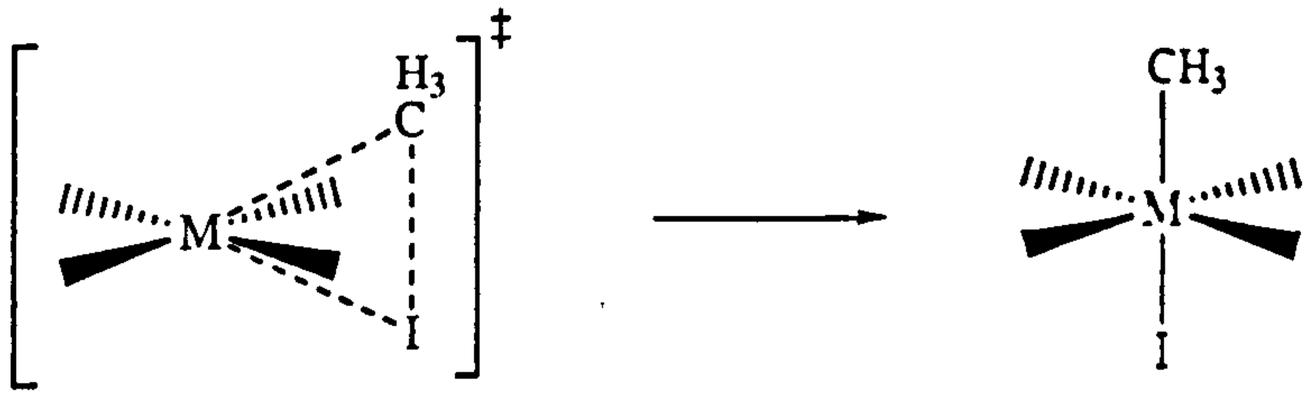

Figure 5.1: Proposed mechanisms of oxidative addition: (a) classical backside S_N2 addition, with inversion at carbon; (b) concerted *cis* addition with retention; (c) concerted *trans* addition with retention.

Table 5.1: Activation parameters for oxidative addition reactions of $[M(CO)_2I_2]^-$ with CH_3I

Conditions/solvent	$\Delta H^{\ddagger}$/kJ mol^{-1}	$\Delta S^{\ddagger}$/J mol^{-1} K^{-1}	Reference
	Rhodium Processes		
(Rh/I$^-$)[a]	63.6	−116	Forster [40]
(Rh/I$^-$)[a]	56.8	−135	Hjortkjaer [47]
Methanol	60	−120	Fulford [54]
Dichloromethane	53	−150	Fulford [54]
neat Methyl Iodide	50	−165	Haynes [15]
	Iridium Processes		
Methyl Acetate	51.9	−122	Pearson [67]
Dichloromethane	53.9	−112	Pearson [67]
Nitromethane	50.6	−126	Pearson [67]
Acetonitrile	53.2	−122	Pearson [67]

[a]Activation parameters for the catalytic carbonylation process.

−189, −176 J mol^{-1} K^{-1}. respectively. They observed a marked increase in rate on going from benzene to dimethyl formamide solvent, and suggested that their results were similar to those observed for the class of Menshutkin reactions:

$$R_3N + R'X \rightarrow R_3NR'^{+} + X^- \qquad (5.2)$$

This group of reactions exemplify the S_N2 mechanism, and are of interest since they occur between neutral species. Significant charge separation at the TS leads to a dramatic rate acceleration when polar solvents are used, which is similar to the behaviour that Chock and Halpern reported for the neutral iridium system. These observations taken together with the characteristically large activation entropies, provide strong evidence that the S_N2 mechanism is prevalent in this system.

Secondary α-deuterium kinetic isotope effect measurements (KIEs) for the reactions between alkyl halides and square planar complexes have also provided evidence supporting the S_N2 mechanism. S_N2 reactions typically exhibit inverse (< 1) or small normal (> 1) secondary deuterium kinetic isotope effects [200]. Maskill quotes measured isotope effects for various organic S_N2 reactions [201] lying in the range 0.882 to 1.179, with the majority being between 0.9 and 1.05. Stang *et al.* reported KIEs for the reaction of $[IrCl(CO)(PPh_3)_2]$ with CH_3I and $CH_3OSO_2CF_3$, in acetonitrile and toluene [16]. Reaction with CH_3I gave a KIE of 0.94–1.00±0.02 while the triflate ester gave a value of 1.13–1.17±0.02. The latter KIE is significantly larger and indicates that the TS is later and less tightly bound for this substrate. This correlates with the superior leaving ability of $CF_3SO_3^-$ compared to I^- [202]. KIEs of similar magnitude have been measured for the oxidative

addition reaction of CH_3I with $[M(CO)_2I_2]^-$ [203]. For M=Rh the measured KIE is 1.16±0.03 (25°C, neat CH_3I), while for M=Ir the value is smaller, 1.06±0.03 (25°C, CH_2Cl_2). These values are in the range expected for an S_N2 mechanism. For comparison, we note that S_N1 reactions exhibit secondary deuterium isotope effects which are generally higher than 1.20 [201].

Other arguments based on the trends observed in varying the nucleophile, the ligands, or the alkyl group have also been proposed, usually in support of these reactions proceeding via an S_N2 pathway. Hart-Davis and Graham reported relative reaction rates for [CpM(CO)L] (M=Co, Rh, Ir and L=tertiary phosphine) with CH_3I [52]. The results reflect the increasing nucleophilicity of the metal centre on descending the triad: Co, 1.0; Rh, 1.4; Ir, *ca* 8. Steric effects are not responsible for this trend since rhodium and iridium are about the same size [204]. The enhanced nucleophilicity of iridium is generally ascribed to electronic effects originating from the relativistic contraction of the valence 6*s* orbitals and expansion of the 5*d* orbitals [205].

The effect of changing the halide ligands is more complicated, because steric effects to some extent can counteract electronic effects. From an electronic point of view, iodide ligands could in principle cause a relative rate enhancement. They are less electron withdrawing than the lighter halides and so should increase the nucleophilicity by concentrating electron density at the metal centre. However, steric hindrance appears to negate this effect and reverse the predicted trend. Chock and Halpern observed that the rate for the reaction of CH_3I with $[Ir(CO)X(PPh_3)_2]$ decreased in the sequence Cl > Br > I [53].

Ellis *et al.* have studied the oxidative addition of alkyl iodides to $[M(CO)_2I_2]^-$ [18]. There was a marked reduction in reactivity with increasing chain length: Me >> Et > n-Pr. This trend in reactivity can be explained by an S_N2- type nucleophilic attack by the metal centre at the α-carbon of the alkyl halide, as it should be easier to attack the carbon of CH_3I than in the sterically congested higher alkyl groups.

Most of the evidence offered thus far has been gathered by indirect methods and cannot be accepted as conclusive proof for the S_N2 mechanism. Unequivocal proof for the S_N2 mechanism could be obtained in two ways: (i) by observing inversion of configuration at the α-carbon atom on oxidative addition; (ii) by detecting the five co-ordinate intermediate resulting from the stepwise substitution.

Labinger *et al.* reported inversion of configuration on oxidative addition of *trans*-1-bromo-2-fluorocyclohexane to *trans*-$[IrCl(CO)(PMe_3)_2]$ [17]. However, subsequent studies revealed that complete loss of stereochemistry at carbon had actually ocurred, which was interpreted as evidence for a radical-chain mechanism. Radical mechanisms for the oxidative addition of alkyl iodides to $[Ir(CO)_2I_2]^-$ have been

investigated by Ellis [206]. The results showed that for the higher alkyls, ethyl iodide and propyl iodide, radical species were present during the oxidative addition. The same reaction with methyl iodide does not, however, display complex kinetic behaviour associated with a radical mechanism and is not affected by the addition of radical scavengers. Therefore, for the purposes of this thesis we can discount a radical mechanism.

Detection of a five co-ordinate intermediate during oxidative addition involving square planar rhodium or iridium species has never been reported. There has been one report though, of a solvate of a five co-ordinate intermediate resulting from the reaction of methyl iodide with $[Pd(Me)_2(bpy)]$ in acetonitrile [19].

A concerted one-step mechanism resulting from the 'side-bonded' approach of the alkyl halide to the metal centre has also been proposed, Figure 5.1b. This pathway is expected to lead to retention of configuration at the α-carbon. Pearson and Muir studied the reaction of $[Ir(CO)ZL_2]$ (Z=Cl, I, SCN and L=PPh_3, PCH_3Ph_2) with CH_3I [20]. They found that halide ions in solution were not incorporated into the product, which indicated that all valencies were already occupied. Furthermore, there was facile addition of gaseous alkyl halides to the iridium complex, from which they inferred that the formation of ionic intermediates could be excluded. These observations strongly suggested the reactions to be proceeding by a concerted one-step addition.

Orbital symmetry constraints do not exclude a one-step *trans* mechanism for the addition of alkyl halides to square planar complexes [21], Figure 5.1c. Pearson and Muir analysed the products of the oxidative addition of CH_3I to $[Ir(CO)ZL_2]$ using far-infra red and NMR spectroscopic techniques and found that these reactions gave both *cis* and *trans* addition products[20].

5.2 Theoretical Aspects of Oxidative Addition

Three recent reviews of theoretical studies of oxidative addition to metal centres have appeared in the literature [207]-[209]. The simplest oxidative addition reaction to study from a computational point of view is the reaction of H_2 with a transition-metal complex [210]-[216]. Kitaura, Obara, and Morokuma (KOM) have investigated the addition of H_2 to $Pt(PH_3)_2$ [212]. This study reported the first theoretical determination of the transition state structure for an organotransition metal reaction. Experimentally it is found that for the oxidative addition of H_2 to $Pt(PR_3)_2$, only a *trans* product is ever observed. Seemingly contrary to this fact, the *trans* addition is symmetry forbidden, while the *cis* addition is symmetry allowed. The results of the KOM study suggested that the reaction passed through an early transition state leading directly to a *cis* product. The *cis* product was then

proposed to rapidly isomerise to the *trans* species due to a large steric repulsion between the bulky phosphine ligands. The calculations showed that the reaction was exothermic with a low activation energy, in agreement with experimental measurements of the barrier for the reverse reductive elimination. A computed kinetic isotope effect for this reaction was also consistent with experiment.

CH_4 addition to transition metal species has been extensively studied by theoretical methods [217]-[232]. Koga and Morokuma (KM) investigated the reaction of CH_4 with $[RhCl(PH_3)_2]$ as a model of C–H activation [220, 221]. KM performed full RHF optimizations on the reactant methane complex (in which two C–H bonds interact with Rh simultaneously), the three-centered transition state, and the product of the reaction $HRhCl(PH_3)_2(CH_3)$. Electron correlation effects were included by performing single-point MP2 and MP4 calculations on the RHF optimized stationary points, and on selected points along the computed RHF reaction path. The activation energy calculated at the RHF level using an extended basis set was 88 kJ mol^{-1}. This was dramatically reduced to just 12 kJ mol^{-1} at the MP2 level of theory. The exothermicity of the reaction was effectively reversed by the inclusion of correlation; the RHF model predicted the reaction to be endothermic by 53 kJ mol^{-1} relative to the isolated reactants, while at the MP2 level of theory the reaction was strongly exothermic by -119 kJ mol^{-1}. Hence, the inclusion of electron correlation led to a significant stabilization of both the transition state and the product complex relative to the reactants. This was explained in terms of the increased covalent bonding as the reaction proceeded from the reactant complex, in which there were only modest interactions between the metal and methane, to the transition state and product where covalent Rh–C and Rh–H bonds were partially or fully formed.

Several reports of theoretical studies of C–H activation by [MCp(L)] complexes have appeared in the literature. One of the earliest was a density functional theory study by Ziegler *et al.* [223] that investigated, amongst others, oxidative addition of CH_4 to rhodium and iridium cylopentadienyl complexes. For [IrCp(CO)] they estimated a modest activation barrier of 10 kJ mol^{-1} and a large exothermic reaction enthalpy of -140 kJ mol^{-1}. For M=Rh the barrier was significantly higher at 37 kJ mol^{-1} and the reaction predicted to be less exothermic by 80 kJ mol^{-1}. From their results they were also able to estimate $M–CH_3$ bond energies: 260 kJ mol^{-1} (M=Ir) and 227 kJ mol^{-1} (M=Rh). The differential was ascribed to the relativistic effect for 5*d* transition elements. Their findings are in agreement with the general experimental observation that the 5*d* species [IrCp(L)] activates C–H bonds more readily than the analogous 4*d* [RhCp(L)] complexes [224]-[226]. C–H activation by $[IrCp(PH_3)]$ has been investigated using the RHF and MP2 methods [227]. Approximate reaction profiles were constructed by systematically increasing the H–M–C angle, while relaxing the rest of the geometry at every point. The MP2 results suggested that oxidative addition for the iridium nucleophile could

proceed without a significant energy barrier.

It is widely believed that the tendency of a complex to undergo oxidative addition increases with the electron-donating ability of the ligands [11, 13]. Siegbahn and co-workers have systematically investigated the electronic structure effects of substituent ligands on the oxidative addition of methane to the second row transition metal complexes [228]-[233]. Their results for simple rhodium complexes have suggested that the addition can be facilitated by promoting the metal s^1-state, which is the main state involved in the binding of the alkyl product. It was shown that this can be achieved by employing strong covalent ligands such as hydrides. Abu Hasananyn *et al.* have studied the oxidative addition of H_2 to the model Vaska complex *trans*-[Ir(CO)X(PH_3)$_2$] for a wide range of ligands [216]. Reaction energies determined from MP2 single-point calculations suggested that increased σ-donating ability of the ligand X would favour H_2 addition, but that increased π-donating ability would strongly disfavour this addition.

There has been extensive experimental work into the addition of polar alkyl halides to transition metal complexes, but very little theoretical work in this area has appeared in the literature. To the best of our knowledge, only one significant investigation has been performed. Bickelhaupt, Ziegler and Schleyer, have carried out calculations on a model Pd and MeCl system using the Amsterdam Density Functional Code (ADF) [234]. They optimized the reactants, transition state and products corresponding to three different oxidative addition mechanisms: backside nucleophilic substitution on carbon, *cis* oxidative addition (insertion of Pd into the MeCl bond), and a radical mechanism proceeding by a single electron transfer. At the non-local level of DFT, they found the oxidative insertion mechanism to be most energetically favourable, having a small activation barrier of 7 kJ mol^{-1} relative to the separated reactants. The barrier calculated for the S_N2 mechanism was substantially higher at 124 kJ mol^{-1}. These observations were rationalized in terms of the overlap between the metal valence *d* orbitals and the LUMO on MeCl. Their calculations revealed that the LUMO of MeCl had no back-side lobe. This result differs from the conventional view where the HOMO of an approaching nucleophile can overlap with the pronounced back-side lobe of the σ^*_{CX} orbital of a substrate CH_3X, which is the onset to S_N2 substitution. With no back-side lobe present, a much more favourable overlap is achieved with say a d_{xz} orbital (rather than d_{z^2}), resulting in oxidative insertion.

5.3 Theoretical Investigation of Oxidative Addition of Methyl Iodide to $[M(CO)_2I_2]^-$ (M=Rh, Ir)

5.3.1 Transition States

Optimized geometrical parameters of transition states in the reaction of $[M(CO)_2I_2]^-$ (M=Rh, Ir) with CH_3I are summarized in Table 5.2. Geometries were initially set up corresponding to the three mechanisms displayed in Figure 5.1. Our efforts have located two markedly different Hartree-Fock transition structures: a near-linear transition state, involving classical backside S_N2 attack by the transition metal nucleophile and leading to inversion of stereochemistry at carbon (TSinv, Figure 5.2a); a significantly bent transition state, which appears to be more closely related to a concerted *cis* addition (TSret, Figure 5.2b). Both structures have a C_s symmetry plane containing the central metal atom and the Cα–I bond of the substrate. The computed energy barriers indicate that the linear transition state is strongly favoured over the bent species. All attempts to locate a transition state corresponding to the *trans* addition mechanism (Figure 5.1c) failed. The initial geometries that were guessed for this TS had extremely high energies, presumably due to unfavourable steric interactions. We have also located the corresponding MP2 and DFT saddle points, although there are some striking differences as shall be described in due course.

For comparison to the metal nucleophile results, we have also carried out optimizations of transition states and reactant complexes for the identity S_N2 reaction between I^- and CH_3I. The results of these calculations are summarized in Tables 5.3 and 5.4.

Inversion of Configuration TSinv

First we consider the geometry of the transition state displaying inversion of configuration computed for the rhodium system at the RHF/DZ level. This structure closely resembles the classical picture of the S_N2 TS, where the CH_3I substrate approaches an axial site of the complex in a linear fashion, with the iodine directed away from the metal. The geometry of the square plane is changed by a small amount relative to $[Rh(CO)_2I_2]^-$. The biggest structural difference occurs for the Rh–I bond lengths, which are shortened by *ca.* 0.07 Å. The interligand angles do not change by more than 1°. The C–H bond lengths (R_{H1} and R_{H2}) are slightly reduced from those computed for free CH_3I; an extra partial bond to Cα causes a change in the hybridization which favours a greater overlap with the hydrogen bonding *s* orbitals.

A common feature of the structures computed for TSinv is a deviation from lin-

Table 5.2: Important optimized geometrical parameters and imaginary frequencies for transition states in the reaction of *cis*-$[M(CO)_2I_2]^-$ with CH_3I. All structures have C_s symmetry. Parameters refer to those defined in Figure 5.2.
Bond distances Å, angles °, frequencies cm^{-1}.

Model	Basis	R_{Nu}	R_{LG}	R_{H1}	R_{H23}	θ	β	γ	ν_i
				Inversion of configuration TSinv(Rh)					
RHF	MB	2.162	3.182	1.081	1.086	18.8	98.9	77.0	
RHF	DZ	2.190	3.202	1.069	1.071	9.7	99.2	79.6	96*i*
RHF	DZ2	2.196	3.404	1.070	1.072	26.6	97.7	77.9	48*i*
RHF	DZ*	2.216	3.101	1.069	1.071	4.6	99.5	81.5	
RHF	DZ*+	2.276	3.063	1.069	1.071	4.4	96.0	84.9	
MP2	DZ	2.143	3.538	1.097	1.099	40.3	99.9	76.7	
MP2	DZ2	2.204	3.547	1.098	1.099	40.8	100.3	76.3	
HFS	DZ	2.107	3.669	1.138	1.122	64.5	97.6	76.5	36*i*
LDA	MB	2.126	3.442	1.107	1.105	50.2	98.5	75.8	
LDA	DZ	2.059	3.586	1.114	1.104	65.5	97.4	75.9	52*i*,38*i*
LDA	DZ*	2.050	3.549	1.117	1.102	64.9	97.6	76.2	
BLYP	DZ	2.100	3.766	1.103	1.099	71.5	98.7	77.0	73*i*,23*i*
BHANDH	DZ	2.071	3.417	1.089	1.087	41.2	98.5	75.9	49*i*
Becke3LYP	MB	2.157	3.493	1.102	1.102	46.8	98.7	75.8	
Becke3LYP	DZ	2.101	3.672	1.096	1.091	57.2	97.4	76.6	22*i*
Becke3LYP	DZ*	2.103	3.591	1.095	1.090	55.1	99.0	77.6	
				Inversion of configuration TSinv(Ir)					
RHF	DZ	2.430	2.939	1.066	1.068	2.1	96.6	85.0	303*i*
RHF	DZ2	2.380	3.036	1.068	1.069	1.9	98.0	82.8	273*i*
LDA	DZ	2.190	3.519	1.108	1.102	57.0	95.3	76.3	40*i*
Becke3LYP	DZ	2.218	3.622	1.092	1.090	50.5	96.4	75.1	24*i*
				Retention of configuration TSret(Rh)					
RHF	DZ	2.801	3.195	1.069	1.070	94.7	84.6	117.8	472*i*
LDA	DZ	2.340	2.690	1.109	1.096	92.4	94.1	118.3	290*i*
Becke3LYP	DZ	2.549	2.958	1.085	1.084	92.6	90.3	119.1	340*i*
				Retention of configuration TSret(Ir)					
RHF	DZ	2.867	3.054	1.067	1.069	94.0	86.2	123.9	525*i*
LDA	DZ	2.528	2.642	1.106	1.096	95.5	91.2	120.8	326*i*

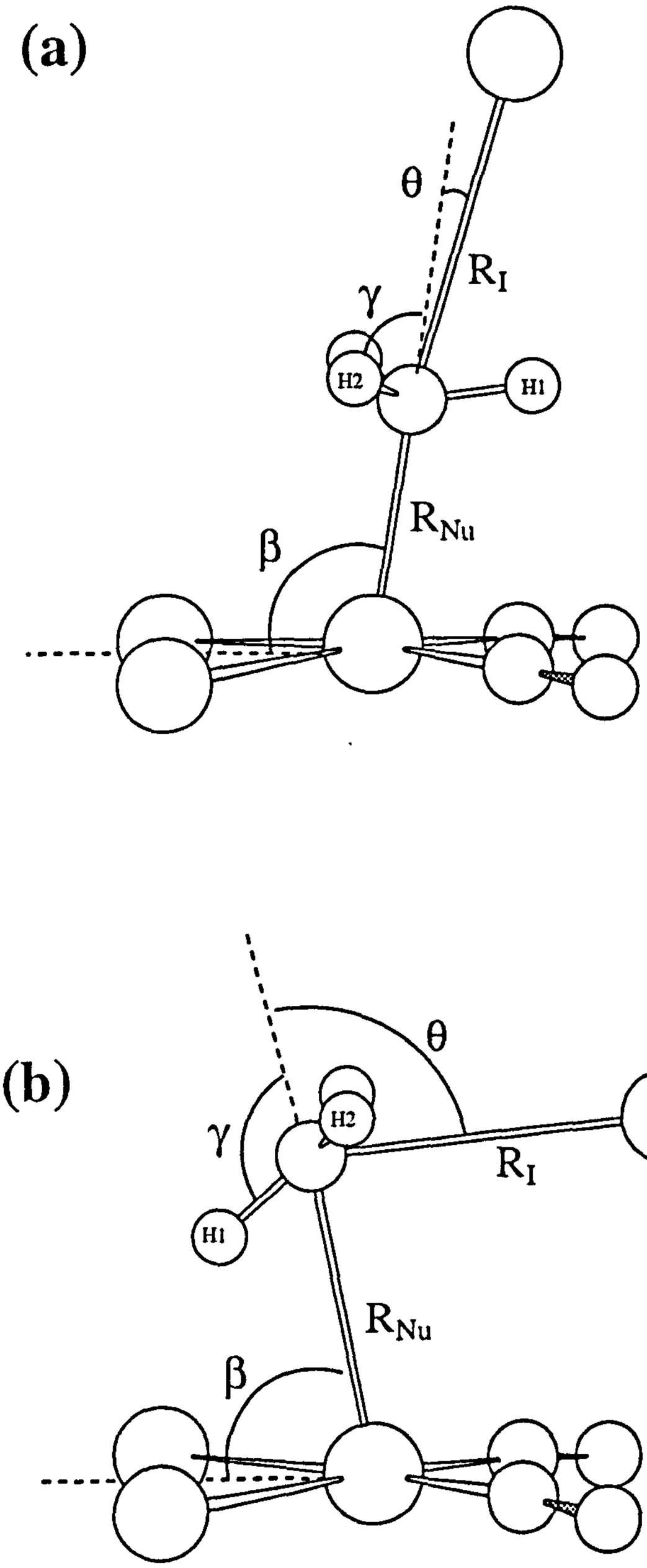

Figure 5.2: Transition states for nucleophilic attack by *cis*-$[M(CO)_2I_2]^-$ on methyl iodide: (a) inversion of configuration at carbon, TSinv; (b) retention of configuration at carbon, TSret.

Table 5.3: Optimized geometrical parameters, imaginary frequencies and activation energies for the transition state in the identity S_N2 exchange reaction between I^- and CH_3I. Parameters refer to those defined in Figure 5.3. Data deduced from DZ basis calculations.
Bond distances Å, frequencies cm^{-1}, energies kJ mol^{-1}.

Model	R_{CI}	R_{CH}	ν_i	$\Delta E^{\ddagger a}$
HF	2.788	1.065	283*i*	30.5
MP2	2.739	1.084	368*i*	35.7
LDA	2.693	1.090	230*i*	6.3
BLYP	2.815	1.087	174*i*	4.0
BHANDH	2.685	1.076	301*i*	19.9
Becke3LYP	2.772	1.080	221*i*	10.1

[a]Calculated with respect to the ion-dipole reactant complexes.

Table 5.4: Optimized geometrical parameters and complexation energies for the ion-dipole complex involved in the identity S_N2 exchange reaction between I^- and CH_3I. Parameters refer to those defined in Figure 5.3. Data deduced from DZ basis calculations.
Bond distances Å, angles ° and energies kJmol^{-1}.

Model	R_{Nu}	R_{LG}	R_{CH}	γ	ΔE_e^a
RHF	3.693	2.236	1.071	106.4	−35.5
MP2	3.623	2.231	1.093	107.9	−33.1
LDA	3.162	2.311	1.097	105.4	−69.8
BLYP	3.331	2.394	1.093	103.9	−52.9
BHANDH	3.338	2.217	1.082	107.4	−52.7
Becke3LYP	3.413	2.300	1.086	105.7	−45.3

[a]Calculated with respect to the separated reactants.

(a)

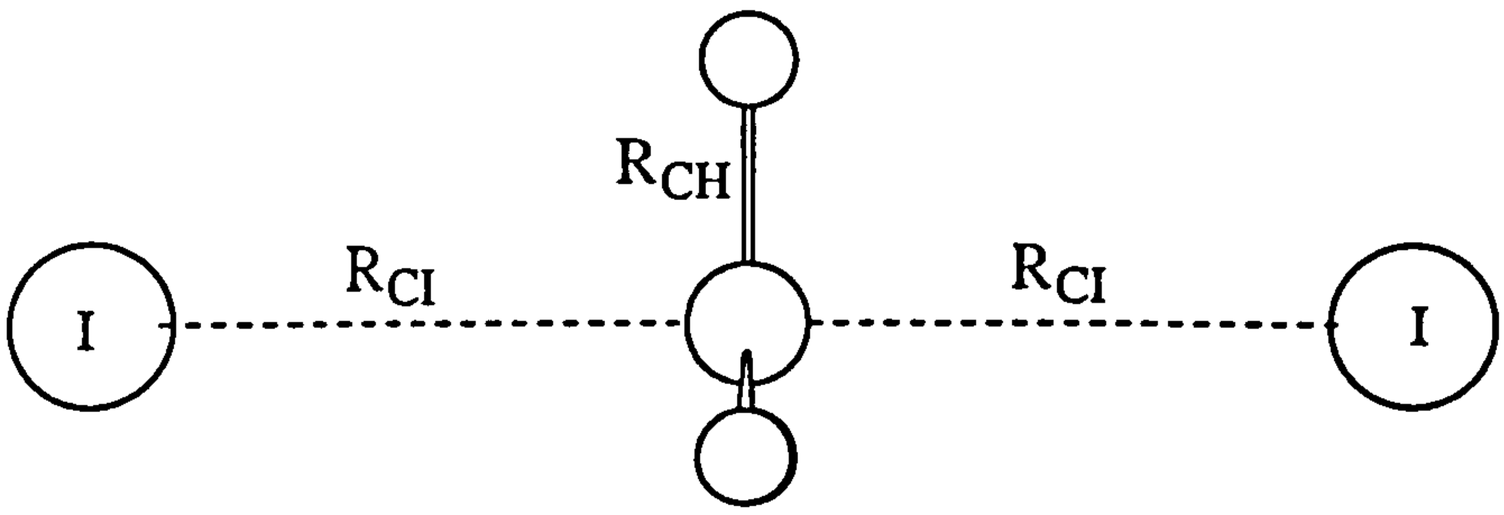

(b)

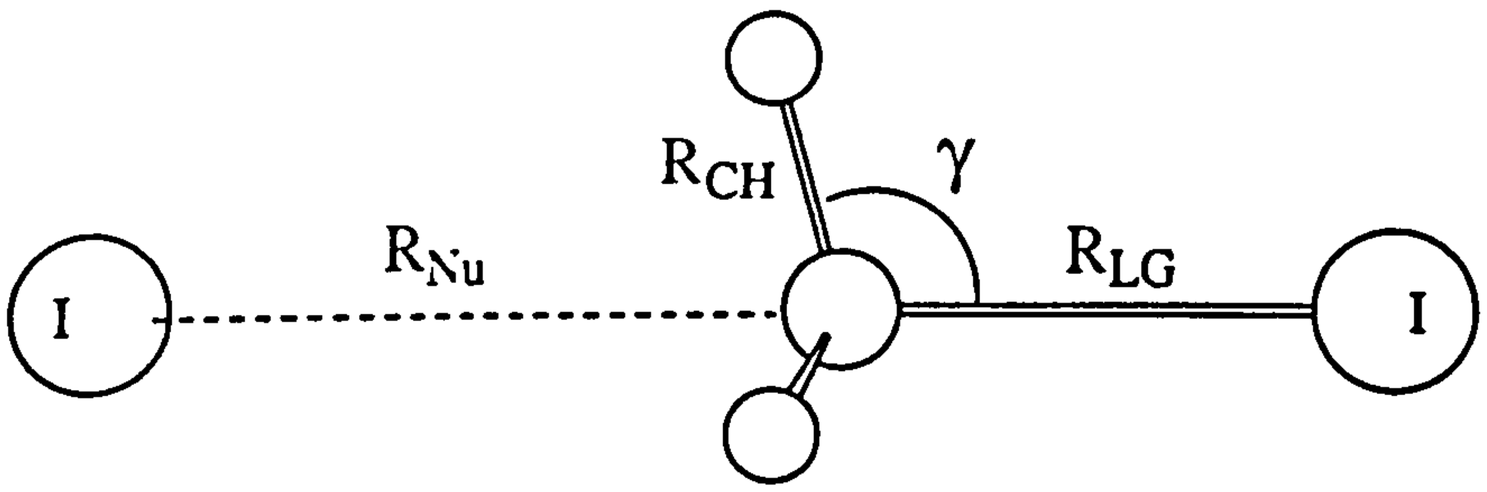

Figure 5.3: Transition state (a) and reactant ion-dipole complex (b) for the identity S_N2 reaction between I^- and CH_3I.

earity in the M–Cα–I geometry. For the rhodium RHF/DZ TS, this is quite a minor distortion, $\theta = 9.7°$. The angle that the forming Cα–Rh bond makes with the square plane (β) is also slightly greater than 90°, indicating a leaning of the substrate away from the bulky iodide ligands. The Cα–I bond ($R_{LG} = 3.202$ Å) is elongated relative to free CH_3I by nearly 50%. This is significantly longer than those reported for transition states in other nucleophilic substitutions on CH_3I. Shaik *et al.* have carried out optimizations on S_N2 transition states at the RHF level using a Los Alamos ECP [235]. For the reaction of CH_3I with the nucleophiles NH_3, Cl^-, Br^-, and I^-, they found leaving group distances of 2.86, 2.55, 2.68 and 2.79 Å, respectively. The latter value for the identity reaction is consistent with the parameters computed using the LANL1DZ basis shown in Table 5.3. The Rh–Cα distance (R_{Nu}) in TSinv(Rh) is only 0.14 Å longer than the corresponding bond length in the final product of oxidative addition $[CH_3Rh(CO)_2I_3]^-$. γ is the compliment of the Rh–Cα–H2 bond angle which describes the extent of C–H inversion in the TS. The RHF/DZ calculation predicts a value ($\gamma \approx 80°$) which is *ca.* 10° larger than this angle in the final alkyl product, indicating that inversion is about three-quarters complete in the TS. These observations suggest that TSinv(Rh) is a late product-like species.

Inclusion of a polarization function in the basis set for each atom (DZ*), leads to a more linear and slightly earlier TS. There is a reduced angular distortion, $\theta = 4.6$, and R_{Nu} is slightly increased to 2.176 Å. The partial Cα–I bond is 0.1 Å less advanced toward rupture. Adding an extra set of diffuse functions (DZ*+), generates a structure which is even earlier. For the RHF model, moving up the scale from the primitive MB basis through to the DZ*+ basis, it follows from Table 5.2 and the preceding discussion that the structures become more linear and earlier with each set of extra functions.

The DZ2 basis generates a structure with a significantly longer leaving group distance (R_{LG}=3.40) and this allows the iodide to tilt further away from the linear axis ($\theta = 26.6°$). Results of RHF geometry optimizations of rhodium ground state complexes (chapter 4) have generally indicated though, a superior performance from the conventional DZ basis. The semi-core ECP may be more appropriate for the calculations of iridium transition states.

MP2 optimization of TSinv(Rh) with either the full or semi-core ECP and associated split-valence basis, leads to a structure with a rather more distorted Rh–Cα–I geometry ($\theta \approx 40°$). Furthermore, there is a marked increase in the leaving group distance of 0.34 Å, and a shortening of R_{Nu} by 0.05 Å, relative to the RHF/DZ predictions. Thus, a small perturbation in the electronic structure of this system leads to a quite different geometry, the changes corresponding to a somewhat later TS. Clearly, this transition state is extremely sensitive to electron correlation.

In order to accurately describe electron correlation effects it is imperative to use a

good quality polarization basis set [236]-[238]. Unfortunately it is not possible to optimize the TS for this system at the MP2 level using a uniformly enhanced basis set, owing to the unreasonable computational cost. We have however, performed a less expensive calculation in which only the Rh atom of the nucleophile, and the Cα and I atoms of the substrate were augmented with extra basis functions. It should be stressed that this procedure is only intended to give a qualitative indication of the correlation effect. Quantitative data should not be inferred since like atoms have been assigned different bases, which could result in a spurious dipole moment, for example. However, Cα and I in the substrate are in a different environment to the C(O) and I ligands, which should minimize adverse affects arising from this scheme. One polarization function and one diffuse function, were added to the basis set for each of these atoms [1], with the remaining atoms described by the usual DZ basis. The geometry of the square plane was constrained to be fixed to that generated by the RHF/DZ calculation, leaving only variation in the Rh–CH_3–I geometry possible in the optimization. This procedure generated a near-linear structure in which CH_3I was pushed slightly toward the iodide ligand side of the complex ($\theta = -4.5°$), and there was a substantial reduction in the leaving group distance from the standard basis prediction ($R_{LG} \approx 2.8$ Å).

The last result suggests that the late character and associated non-linearity of the MP2/DZ structure could, to some degree, be an artifact of an inadequate basis. It is difficult to pass judgement on correlation phenomena merely from inspecting molecular geometries, but a qualitative argument to explain these observations could be as follows. Although there is no precise dividing definition, Møller-Plesset theory will include both short-range (dynamic) and long-range (non-dynamic) electron correlation. The introduction of dynamic correlation should in principle allow electrons to become optimally close. Non-dynamic correlation, on the other hand, encourages electrons to remain with their parent atoms, and thus expands the molecular size. When just the standard DZ basis is used, there is a bias toward the description of non-dynamic correlation, since these effects arise from the combination of different states involving only the occupied valence orbitals. The outcome of this calculation is a late distorted TS in which too much electron density is localised on the atoms. The iodide leaving group holds a large negative charge (−0.88), which causes it to be pushed away to a large distance and off-set from the Rh–Cα axis by 40°. When extra polarization functions are included, short-range interactions can also be partly accounted for by allowing the deformation of density into regions of space not normally covered by the standard basis. In this way, the orbital basis has the necessary freedom to incorporate some virtual-state character into the electronic structure, and thus more properly express the dynamic correlation. This description of electron correlation yields a linear TS with

[1] The exponents of these functions had the standard values used throughout this work. They are tabulated in chapter 3 (Methods).

a significantly shorter Cα–I distance. Thus, providing the basis set is adequate, we contend that all of the *ab initio* methods will predict a TS geometry with a relatively small deviation from linearity ($\theta < 40°$).

The most significant contrast between the DFT and *ab initio* results, is the large angular distortion ($\theta > 40°$) which is a feature common to *all* these transition states, irrespective of the functional and basis used. The greatest distortions are found in the transition states generated by the pure DFT methods; typical values of θ are 50° to 70°. Concomitant with this non-linearity. are the long leaving group distances, small Rh–C distances and acute inversion angles–parameters associated with a late product-like TS. In most instances R_{LG} is greater than 3.5 Å, which represents an extraordinarily long extension from the C–I bond in free CH_3I (> 60%). These can be compared to the leaving group distances for the TS in the identity reaction calculated by the DFT methods (Table 5.3), which are in general smaller than 2.8 Å. The values of R_{Nu} for TSinv(Rh) lie in the range 2.05 to 2.10 Å, and γ is in each instance close to its fully inverted value. Also of note are the C–H bond distances which at each level of DFT , are larger than the distances in free CH_3I, and comparable to the values predicted for the overall product of oxidative addition. At the DZ level, the LDA, BLYP, and Becke3LYP functionals gave structures which were very similar. It is interesting that the 'exchange-only' HFS functional also predicts a very late and distorted transition structure. The most notable difference among the DFT results, is provided by the geometry optimized with the BHANDH functional which uses a combination of HF and HFS exchange potentials. The TS still retains a small value for R_{Nu} but θ and R_{LG} are both reduced relative to the other DFT-based methods.

Whereas for the MP2 scheme, a partial optimization employing an extended basis reduced the angular distortion and led to an earlier TS. the same procedure at the LDA level only served to exaggerate this distortion and did not converge to a local maximum. During the course of the optimization. the Cα–I bond became increasingly longer, until a point where all saddle-point character appeared to be lost and the calculation was aborted. Full DZ* optimizations at the LDA and Becke3LYP levels did succeed, but in each case yielded geometries which were not significantly changed from the parameters calculated with the DZ basis. Optimizing this TS with the semi-core ECP and DZ2 basis at the LDA level, also did not result in a significant structural change. Interestingly, the minimal basis LDA and Becke3LYP geometries show a smaller distortion than their DZ basis counterparts. An improved basis does not therefore appear to favour an earlier more linear structure, as in the case for the *ab initio* methods. Using a finer numerical integration grid made SCF convergence considerably slower and more difficult to obtain, such that the calculation was as expensive as a full MP2 optimization. A calculation carried out at the LDA/DZ level with the int=finegrid option, did not lead to a markedly different TS geometry.

The transition state geometries predicted for the iridium system are in general qualitatively similar to those described for rhodium. Comparison of the RHF/DZ structures for TSinv reveals that the iridium species has a larger metal–carbon distance, a shorter value for R_{LG}, and a value of γ which describes a less advanced C–H inversion. The CH_3 unit is displaced away from the metal and toward the leaving group by *ca.* 0.2 Å relative to the rhodium structure. These differences correspond to a significantly earlier TS. The deviation from Ir–Cα–I linearity is smaller than for rhodium, $\theta \approx 2°$. The DZ2 basis generated a slightly later structure, but did not introduce any significant non-linearity into the geometry as in the case for the rhodium TS. Applying the local density approximation to the computation of the iridium TS, resulted in similar geometrical changes to those described for rhodium. The LDA geometry of TSinv(Ir) is also late ($R_{Nu} \approx 2.2$ Å, $R_{LG} \approx 3.5$ Å) and significantly distorted ($\theta \approx 57°$).

It is clear from the results that there are discrepancies between the descriptions of the electronic structure of these species provided by the *ab initio* and DFT methodologies. As soon as the exact HF exchange term is replaced by any exchange-correlation functional, there is an immediate qualitative change in the form of the transition state toward a bent product-like species. This result is independent of the detailed form of the exchange-correlation term which only affects the quantitative value of the bend and the other quantitative features of the geometry. We suspect that this difference is not only due to the inclusion of electron correlation into the calculation since the effect also occurs at the HFS level, which does not explicitly contain a correlation functional in the exchange-correlation term. Introducing some HF exchange back into the DFT calculation results in a more HF-like structure, as demonstrated by the BHANDH calculation on TSinv(Rh).

Further insight into the properties of these transition states, can be gained by examining the computed imaginary frequencies and their associated normal mode vibrations. Numerical vibrational analysis of the RHF/DZ structure computed for TSinv(Rh) reveals a single imaginary frequency with a normal mode vibration which is symmetric with respect to the C_s plane of addition. This mode describes translation of the methyl unit toward the rhodium atom together with a small inversion of the CH_3 umbrella, in qualitative agreement with expectations of a reaction co-ordinate vibration for an S_N2 process. The magnitude of the imaginary frequency (-96 cm^{-1}) is, however, significantly lower than expected. Vetter *et al.* have computed frequencies of -525 and -324 cm^{-1} for the identity methyl transfer reactions involving fluoride and chloride ions [239]. The value for the rhodium nucleophile is also 187 cm^{-1} lower than the RHF/DZ frequency calculated for the identity reaction using the Los Alamos ECP, Table 5.3. The size of the imaginary frequency measures the curvature of the potential energy surface in the vicinity of the transition state, and thus provides an indication of the barrier width. Hence, a value of -96 cm^{-1} represents a maximum which is significantly less well-

defined than the sharp maxima that characterize other S_N2 processes. We would expect from this low value that the interacting fragments, in particular the Cα–I fragment of the substrate, are bound quite loosely at the TS. The RHF imaginary frequencies for the iridium structure, TSinv(Ir), are about three times the size of the corresponding rhodium values ($\nu_i \approx -300$ cm^{-1}). This is in qualitative agreement with the idea that an earlier TS is more tightly bound.

Examination of the imaginary frequencies calculated for the DFT structures, reveals that these maxima are even less well-defined. In fact, the pure DFT functionals, LDA and BLYP give *two* negative frequencies for TSinv(Rh), which rule them out as being true saddle point maxima[2]. The presence of an extra unwanted imaginary frequency normally indicates that a symmetry constraint has been imposed which is preventing the structure from reaching its global minimum. However, relaxing the C_s constraint did not have a significant effect on the geometries of these transition states when the parameters were reoptimized. The LDA, Becke3LYP and BHANDH schemes all exhibit a single conspicuously low imaginary frequency ($|\nu_i| < 50$ cm^{-1}) and are associated with normal mode vibrations which are quite different to the classical S_N2 vibrations displayed by the RHF structures. The main component of the DFT vibrations is a tilting of the Rh–Cα geometry toward the side of the complex containing the iodide leaving group and carbonyl ligands. There is no lengthening or shortening of the important bonds and it is difficult to conceive how these vibrations could correspond to a reaction co-ordinate mode. The DFT imaginary frequencies for TSinv(Ir) are also markedly lower than anticipated for an S_N2 transition state. These observations cast some doubt on the validity of interpreting the DFT transition states as chemically meaningful structures.

Retention of Configuration TSret

Retention of configuration in TSret (Figure 5.2b) results from a side-on approach of CH_3I towards the metal complex. We have located rhodium transition states for this mechanism at the RHF, LDA and Becke3LYP levels of theory. The absolute energies of these species are larger than the energies of the corresponding structures displaying inversion of configuration by *ca.* 50 to 90 kJ mol^{-1}. This indicates from the outset of the analysis that this type of mechanism is unlikely to compete with a mechanism which proceeds via a classical transition state of the form TSinv. Nevertheless, there is a great deal of experimental and theoretical interest in substitution reactions which can proceed with retention of stereochemistry [240, 241]. The computation of this TS is certainly useful from the point of view of comparing with the inversion TS and also with the experimental data.

[2]A saddle point is a maximum in one direction only on the potential energy surface. Two negative frequencies indicates a second-order transition state which is a maximum in two directions.

Apart from the Rh–Cα–I angle ($\theta \approx 92°$ to 95°) and the different I–Cα–H geometry, the other major structural difference with TSinv(Rh) is the long Rh–C distance. The RHF/DZ calculation predicts a value of R_{Nu} which is *ca.* 0.6 Å greater than for the linear structure, suggesting that TSret(Rh) is comparatively early with respect to metal–carbon bond formation. By contrast, the Cα–I bond is close to complete rupture, having a similar length to that computed for TSinv(Rh). For the retention TS, γ represents the compliment of the angle that the C–H1 bond makes with the Rh–Cα bond. This value is *ca.* 118°, demonstrating that the CH_3 umbrella has not undergone inversion at the transition state. The geometry computed for TSret(Ir) is slightly earlier relative to rhodium, indicated by a longer Ir–C bond and a shorter leaving group distance. The most noteworthy feature of the LDA structures is a contracted M–Cα–I geometry. The angles are generally quite similar to those in the RHF structures, but the M–Cα and Cα–I distances are both shorter by *ca.* 0.5 Å. The Becke3LYP bond distances in TSret(Rh) are intermediate between the RHF and LDA parameters.

The imaginary frequencies calculated for the bent retention TS are significantly larger than those for TSinv. Despite being considerably raised in energy, these stationary points are well-defined maxima on the potential energy surface. The RHF imaginary frequency for TSret(Rh) (-472 cm^{-1}) corresponds to a normal mode describing a rocking motion of the C–H units about the Cα–I axis together with a smaller vibration causing displacement of the CH_3 group towards rhodium. The DFT transition states for retention of configuration are also true saddle points. Vibrational analysis of the LDA and Becke3LYP structures in each case yielded a single imaginary frequency, which are *ca.* 150 cm^{-1} lower than the RHF values.

5.3.2 Reaction Pathways and Energetics

Intrinsic reaction co-ordinates (IRC) were computed for TSinv(Rh), TSinv(Ir) and TSret(Rh) at the RHF/DZ level. Figure 5.4a shows the reaction path computed for the inversion mechanism in the rhodium system, overlaid with the results from a similar calculation for iridium. Figure 5.4b shows the reaction path for retention of configuration which has been carried out for the rhodium system only. In these plots the zero of energy is taken as the combined energies of the isolated reactants CH_3I and $[M(CO)_2I_2]^-$. Attempts at tracing the IRC for the DFT methods from TSinv(Rh), failed in each case, even for species that were characterized by frequency analysis to be true saddle points. The calculations were only able to follow a few steps before terminating. Failure was probably due to there being only a very small, possibly spurious, imaginary frequency with which to compute the reaction path, reinforcing our earlier conclusions regarding the validity of these saddle points.

IRC for Inversion of Configuration

The IRC calculated for TSinv(Rh) (Figure 5.4a) is very unsymmetric, indicating that most of the bond making–breaking processes are concentrated on one side of the reaction path. In this case, the TS is late with a very short metal–carbon bond and a long carbon–iodine bond; bond making and breaking are therefore more concentrated on the reactant side. Accordingly, the reactant side of the path displays the greatest and most rapid energy change. The IRC for iridium has been extrapolated back to coincide with the rhodium path at the stationary point on the reactant side ($rx \sim -9$). The location of the maximum earlier along the reaction co-ordinate is consistent with the longer Ir–Cα and shorter Cα–I bond distances that were computed for TSinv(Ir).

Geometries taken from several selected points of the IRC calculated for the rhodium system are displayed in Figure 5.5. The reactant complex corresponding to the extreme left of the reaction co-ordinate ($rx \sim -9$), has the general form shown in (a). DFT complexes were obtained by initiating the optimization procedure with the RHF geometry as a starting guess. The most important parameters are collected in Table 5.5. For the RHF geometry, the Cα–I axis is aligned approximately in the horizontal plane of the rhodium complex with the iodine atom directed away from the metal. The smallest intermolecular distance occurs between the methyl hydrogen atoms and the iodide ligands ($\approx$ 3.5 Å) but none of the geometries indicate the interaction of C–H bonds with the metal centre. The Cα atom of the substrate is separated from the central metal atom by a rather larger distance, $R_{Nu} \approx 5.5$ Å. The geometries and atomic charge distributions of the CH_3I and $[Rh(CO)_2I_2]^-$ fragments are changed by only a small amount compared to the isolated molecules. In addition, the stabilization energies of these complexes (ΔE_c, Table 5.6) are generally small, lower than for example, those calculated for the identity reaction with I^- (Table 5.4). *Ab initio* estimates based on the RHF geometries lie in the range 20 to 28 kJ mol^{-1}. The DFT complexation energies are slightly larger (*ca.* 20 to 40 kJ mol^{-1}), reflecting the closer approach of the substrate to the metal centre found in the geometries predicted by these methods. Analysis of the fragment MO overlap populations reveals that there are no significant orbital interactions between the nucleophile and substrate at this point. Stabilization of the reactant molecules is therefore due to a modest electrostatic interaction between the positive carbon end of the CH_3I dipole and the negative charge residing on the iodide ligands in $[Rh(CO)_2I_2]^-$. These results differ from theoretical studies of oxidative addition of CH_4 to transition metals, where significant molecularly bound σ complexes were located preceding the transition states (see for example, references [220]-[222]).

Following the conformation of the molecules from $rx \sim -9$ to -2, shows a gradual rotation of CH_3I toward the axis perpendicular to the square plane. At $rx \sim -2$ (c), the preparation for charge-transfer is virtually complete. The Cα–I bond

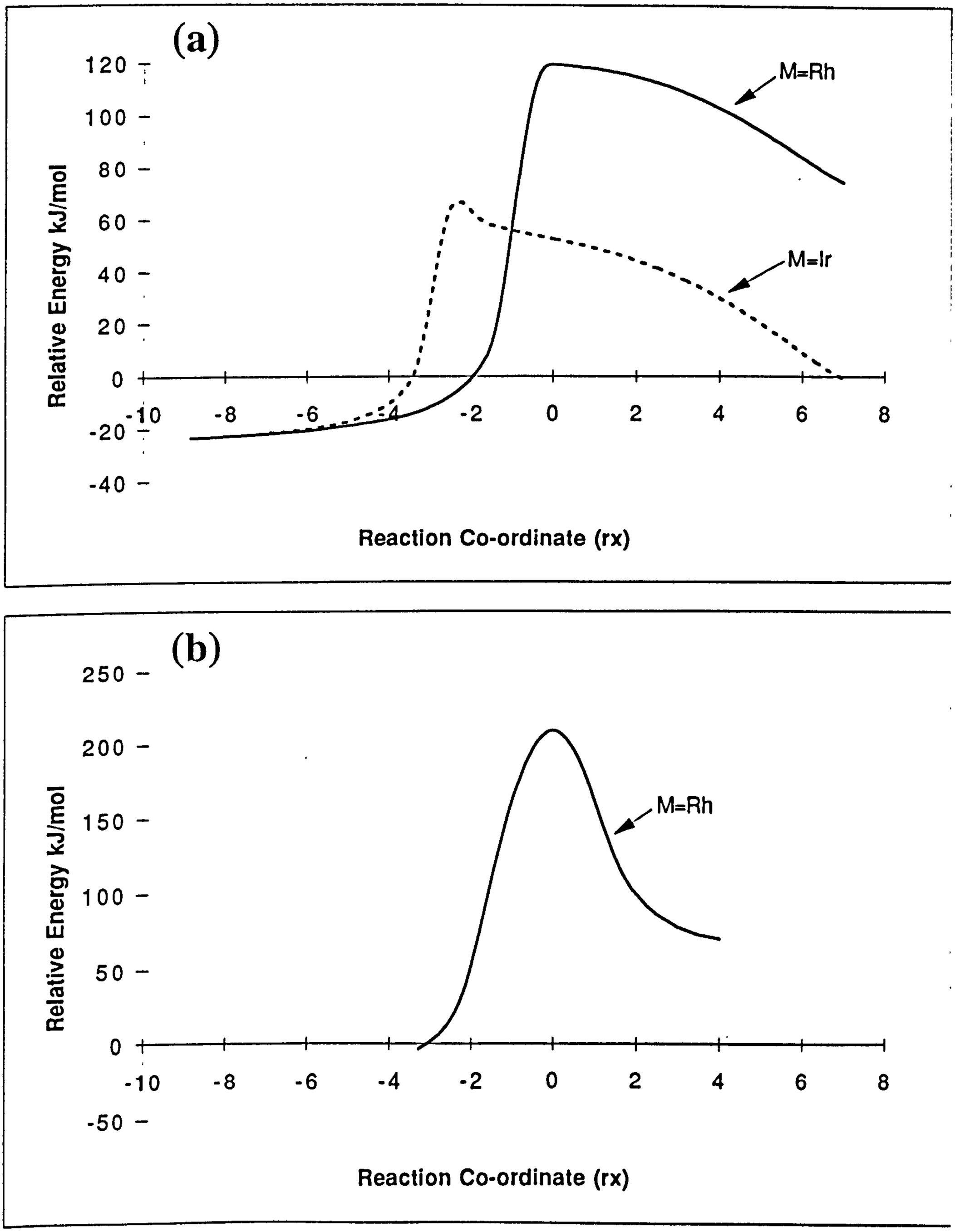

Figure 5.4: Intrinsic reaction co-ordinates for nucleophilic substitution of CH_3I by *cis*-$[M(CO)_2I_2]^-$: (a) inversion of configuration for rhodium (solid line) and iridium (dashed line) transition states; (b) retention of configuration, rhodium only. The vertical axis is the energy relative to the combined energies of the separated reactants. Data deduced from RHF/DZ calculations.

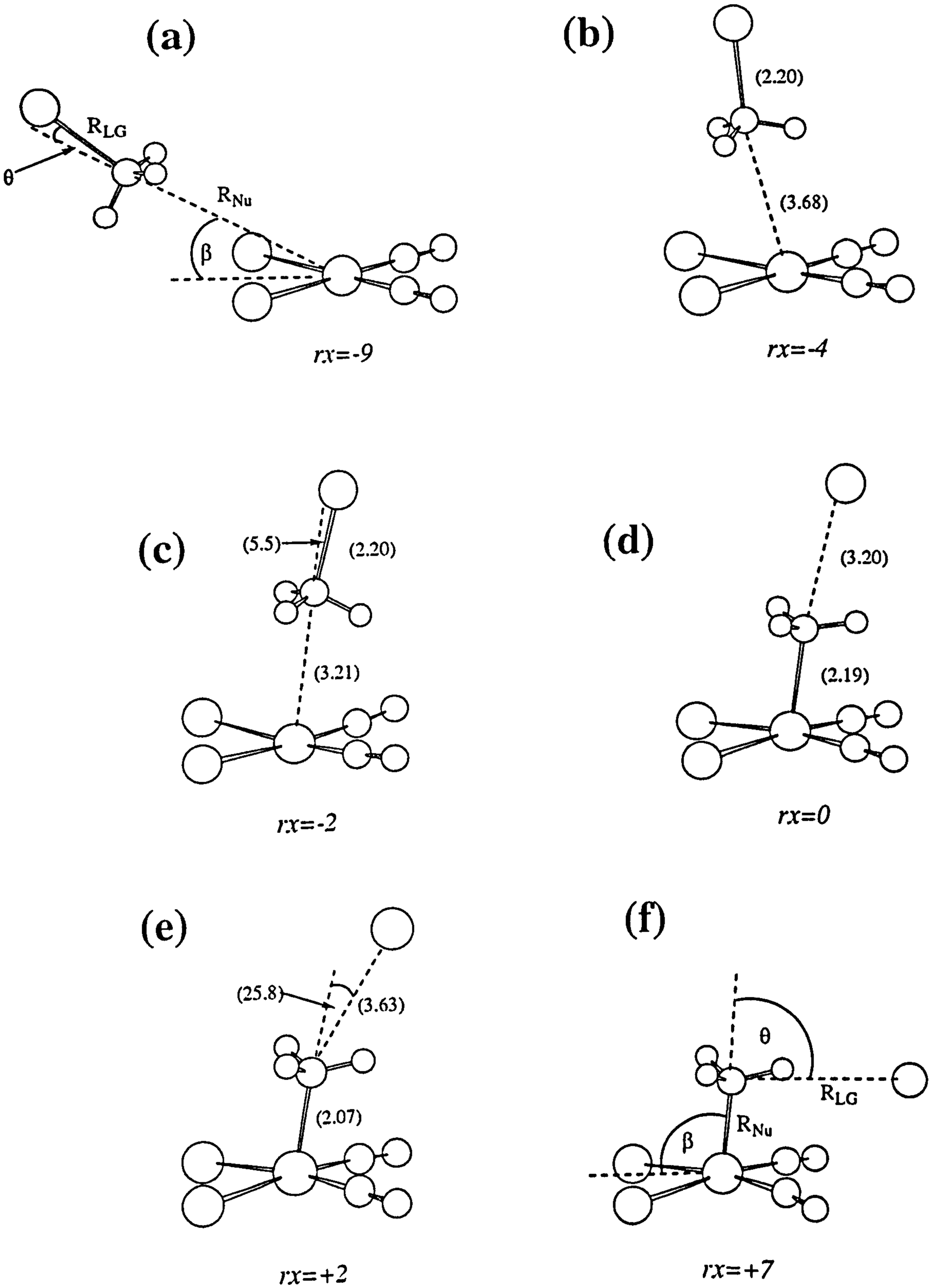

Figure 5.5: Optimized molecular geometries at six points along the reaction coordinate for TSinv(Rh).

length is still unchanged at *ca.* 2.2 Å, and the Cα–Rh bond (*ca.* 3.2 Å) is inclined at an angle of 92° to the plane containing rhodium and the iodide ligands. After this point the curvature of the path changes rapidly, rising steeply to the maximum as the major orbital interactions take place. Activation barriers computed for the forward nucleophilic substitution reaction ($\Delta E_f^{\ddagger}$) are presented in Table 5.6. Note that the energy data has not been corrected for zero-point vibrational contributions[3]. The RHF barriers are substantially larger than experimental solution values. This is not unexepected, however, since previous theoretical investigations of oxidative addition have indicated a substantial influence of electron correlation on the computed reaction energetics. Due to the difficulties encountered with full optimization of the TS at the MP2 level, we have preferred to use the RHF geometries with which to compute the correlated energies. For each basis, there is a significant reduction in the RHF barrier when correlation is included. Single-point MP2/DZ* calculations yield a barrier for nucleophilic substitution in the rhodium system of 71 kJ mol^{-1}, in reasonable quantitative agreement with experimental values ($\Delta H_{exp}^{\ddagger} \approx 55$ kJ mol^{-1}, Table 5.1). The large correlation energy can be attributed to changes in covalency on M–CH_3 formation. The DFT barriers are significantly higher and lie in the range *ca.* 90 to 120 kJ mol^{-1}. The activation barriers computed for oxidative addition in the iridium system, are systematically lower than the rhodium values by *ca.* 10 to 50 kJ mol^{-1}. The latter result is consistent with previous experimental and theoretical data for C–H activation by rhodium and iridium nucleophiles [223, 224]. However, experimental measurements for the addition of CH_3I to $[M(CO)_2I_2]^-$ complexes have indicated that the activation barriers are similar for both metals.

After the TS has been passed, substitution is completed by dissociation of the complex into a rhodium–methyl fragment and an iodide ion. This part of the reaction is characterized by an energy profile which describes a rather obtuse descent to another shallow minimum. Inspection of the geometry changes (d)→(f) indicates that the major component of the trajectory is taken up by motion of the iodide toward the positive potential provided by the carbonyl side of the molecule. Very little bond-making or breaking is involved, and thus, does not result in a rapid energy change with respect to the reaction co-ordinate. The contribution from this side of the reaction path results in a rather broad maximum, giving an indication of why the RHF imaginary frequency for this TS is small. The descent towards products leading from the iridium TS is initially quite steep. In the narrow region $rx \sim -2$ to -2.5, the width of the maxima is small, consistent with the larger imaginary frequency computed for this system. However, following rupture of the Cα–I bond, the path flattens out in a similar way to the rhodium profile.

Substitution does not lead directly to the final product of oxidative addition,

[3]RHF ZPEs were initially calculated, but were found to only change the barriers by *ca.* 1 – 2 kJ mol^{-1}.

$[CH_3M(CO)_2I_3]^-$. The initial minimum at $rx \sim 3$ corresponds to an ion-dipole complex (**f**) in which the leaving iodide ion associates with the unsaturated five co-ordinate alkyl fragment through a weak electrostatic interaction. Geometrical parameters computed for this complex are given in the lower half of Table 5.5. The axis formed by the Cα···I unit is roughly parallel with the bisector of the carbonyl ligands in the square plane. The leaving group distances vary from *ca.* 3.65 to 4.1 Å, with the DFT methods tending to generate the shortest values. At each level of theory, the ion-dipole product complex is raised in energy with respect to the reactant species, indicating that the substitution reaction is an endothermic process (ΔE_{sub}, Table 5.6.) This is the case for both metal systems, but generally less so for iridium. For example, the MP2/DZ* calculations predict that the reaction will be more endothermic for rhodium complexes by *ca.* 30 kJ mol^{-1}. A consequence of this endothermicity is that the barriers for the back reaction to nucleophilic substitution ($\Delta E_b^{\ddagger}$) are all rather low. In particular, the MP2/DZ* values (*ca.* 10 kJ mol^{-1}) suggest that elimination of CH_3I from the ion-dipole product is an extremely facile process. However. such a mechanism does not take

Table 5.5: Geometrical parameters computed for the reactant and product ion-dipole complexes involved in nucleophilic substitution of CH_3I by *cis*-$[M(CO)_2I_2]^-$. The RHF geometries have been located by following the reaction path to the extremes, and then reoptimizing to verify that these structures are global minima. The DFT stationary points have been optimized by using the RHF geometries as the initial guess. All data deduced from DZ basis calculations. Bond lengths Å, angles °.

Model	R_{Nu}	R_{LG}	θ	β
	$[Rh(CO)_2I_2]^-\cdots CH_3I$ (C_s)			
RHF	5.481	2.211	3.6	5.5
HFS	4.991	2.238	11.2	3.4
LDA	4.894	2.176	8.8	17.0
BLYP	5.223	2.242	6.6	4.1
BHANDH	4.915	2.171	8.1	2.8
Becke3LYP	5.137	2.215	8.0	5.5
	$[CH_3Rh(CO)_2I_2]\cdots I^-$ (C_s)			
RHF	2.014	4.082	93.3	98.1
HFS	2.027	3.651	102.1	93.6
LDA	1.983	3.641	103.1	97.2
BLYP	2.041	3.864	101.2	97.5
BHANDH	1.979	3.739	98.0	97.0
Becke3LYP	2.020	3.854	100.1	97.2

into account the co-ordination of ligands (iodide or solvent) to the vacant axial site *trans* to the CH_3 group which is also expected to be facile. In addition, the polarizing influence of a solvent medium is likely to aid dissociation of I^- and lead

to a stabilization on the product side of the energy profile. For these reasons, the 'gas phase' values of ΔE_{sub} and $\Delta E_b^{\ddagger}$ may only have real significance from the point of view of comparing the different methodologies.

The effect of electron correlation on the reaction co-ordinate for TSinv(Rh) has been examined by performing MP2/DZ* single-point calculations on several intermediate points taken from the RHF IRC. The results are presented in Figure 5.6, which shows the RHF reaction path overlaid with the additional MP2 points. The MP2 curve suggests that the original single-point estimates for the forward and back activation barriers were too low. Revised values can be obtained by interpolating the curve to locate the positions of the new minima and maxima. First, we note the position of a new reactant complex at about $rx = -4$, corresponding to the geometry denoted in Figure 5.5 as (b). This minimum is more well-defined than for the weakly bound RHF complex. There is a a significant ion-dipole interaction amounting to a stabilization of *ca.* 40 kJ mol^{-1} relative to the separate reactants. The inclusion of correlation at this level, displaces the position of the TS further along the reaction co-ordinate from $rx = 0$ to $rx \approx 2$, suggesting that a moderate bend in the Rh–Cα–I geometry of TSinv(Rh) does exist. The deviation from linearity at $rx = 2.0$ (e) is about 25°, which is intermediate between the deviations found in the fully optimized RHF/DZ and MP2/DZ geometries. The results are still consistent with the conjecture that an improved basis at the correlated level leads to a more linear TS. It is possible that additional enhancement beyond the DZ* level would cause a further reduction in the value of θ and locate the TS earlier along the reaction co-ordinate. The position of the product complex is essentially unchanged from the RHF location at $rx \sim 8$. It follows from Figure 5.6 that new MP2/DZ* values for the forward and reverse barriers to nucleophilic substitution are approximately 90 and 25 kJ mol^{-1}, respectively. This analysis has moved the theoretical activation barriers for the substitution reaction away from the experimental solution values ($\Delta H_{exp}^{\ddagger} \approx 55$ kJ mol^{-1}, Table 5.1), which could suggest the involvement of an additional stabilizing factor that has not yet been considered. Further stabilization could arise, for example, from the static effect of a polarizable medium, or from a dynamic effect in which solvent parameters participate directly in the reaction co-ordinate. Also worth investigating is the possible influence of an iodide ion which has been proposed to accelerate oxidative addition by interacting with the reactants or transition state.

IRC for Retention of Configuration

The IRC computed for TSret(Rh) is shown in Figure 5.4b. The saddle point is sharper and more symmetric than the energy profile described for the linear TS. Steep energy gradients on both sides of the maximum indicate that this mechanism involves a transition state which is relatively central with respect to bond

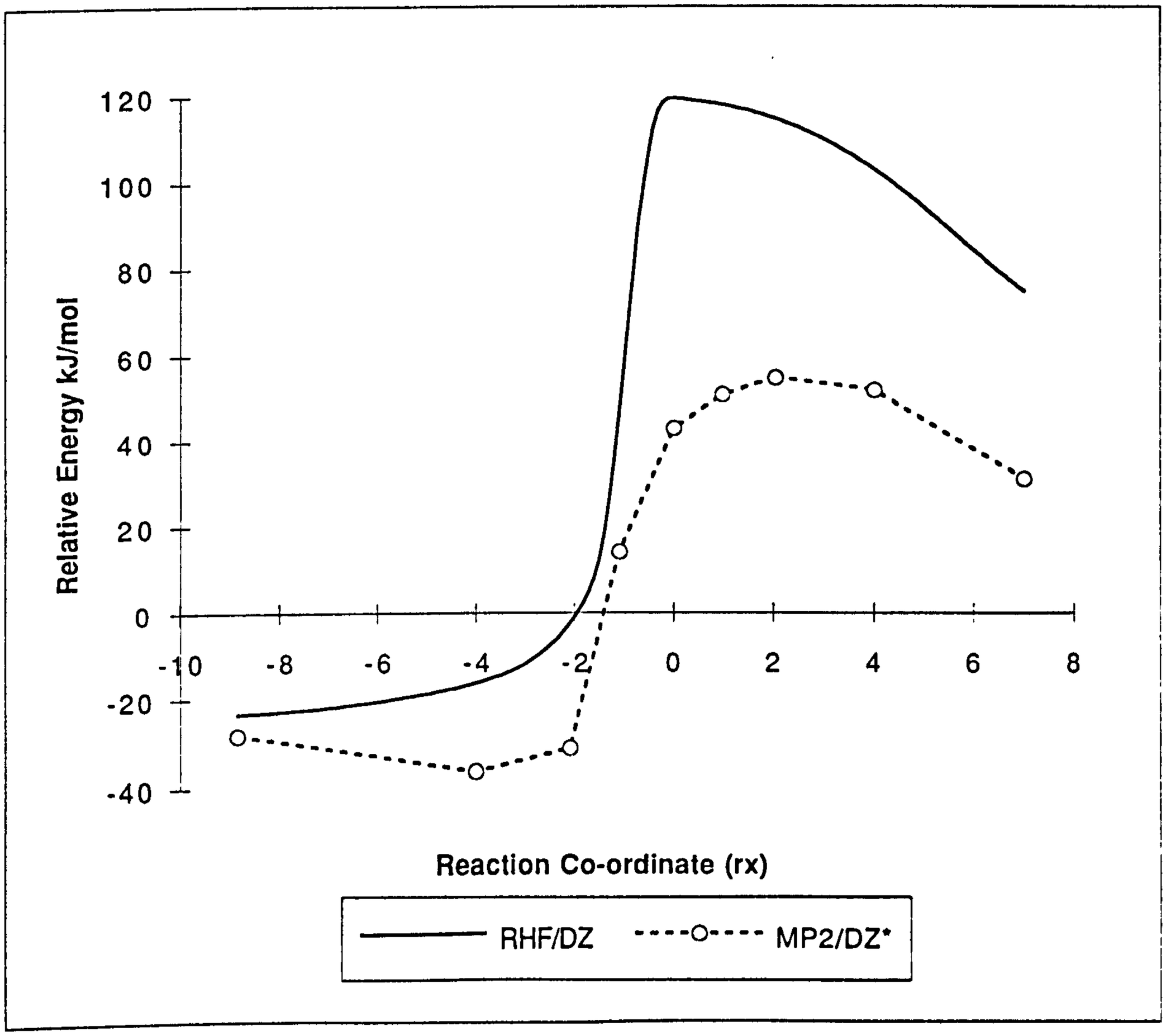

Figure 5.6: Effect of MP2 electron correlation (points) on the RHF reaction co-ordinate (solid line) for TSinv(Rh). Single-point calculations were performed using the DZ* basis on selected points of the RHF reaction co-ordinate.

making and breaking. The first point on the reactant side ($rx = -3.4$) is only 5 kJ mol^{-1} lower in energy than the combined energies of the isolated reactants, indicative of a precursor complex which is bound together through weak electrostatic forces. Examination of the geometry corresponding to this point reveals the molecular conformation (**a'**) displayed in Figure 5.7. The Cα–I axis of the substrate is situated parallel to and above the plane of the rhodium complex by about 3.6 Å. The Cα atom lies above the central metal, while I takes up a position above the carbonyl ligands. The geometries of the separate fragments are negligably changed from the isolated molecules. Note that although the atomic forces at this point of the IRC were all fairly small, this conformation is not a fully optimized structure. The IRC code could not compute the remainder of the reaction path, terminating at this point after exceeding the allowed number of optimization cycles. It is difficult to precisely locate minima in shallow regions of the potential energy surface. Taking the geometry of this last point, and allowing it to optimize to a global minimum (i.e. not constraining it to this reaction path), regenerated the reactant complex (**a**) (Figure 5.5) corresponding to the reaction path for TSinv(Rh). Since we cannot compute the IRC at every level of theory, the fully optimized reactant geometries for TSinv (Table 5.5), have been used for the purposes of calculating barrier heights and isotope effects (see section 5.3.4) for both reaction mechanisms. This should have a negligible effect on the results, since the two RHF conformations have virtually identical energies and in each case only describe a weak interaction between CH_3I and $[Rh(CO)_2I_2]^-$.

The barrier to substitution via a retention mechanism is substantially larger than for the linear TS, thus confirming our earlier expectations. This is clearly demonstrated in the plots for the IRC at the RHF level, and the same is true for every other level of theory ($\Delta E_f^{\ddagger}$, Table 5.6). The *ab initio* barriers are at least 90 kJ mol^{-1} in excess of the values predicted for TSinv(Rh). By contrast to the energy data for the inversion mechanism, the correlated MP2 calculations do not reduce the activation barrier from the RHF value. This suggests that TSret(Rh) has a comparable correlation energy to the initial reactant complex. Apart from the non-linearity, this TS differs from others that we have located most significantly in the quantitative value of the M–Cα bond length. R_{Nu} is *ca.* 0.6 Å longer than the corresponding value in TSinv(Rh), suggesting that short M···C partial bonds are associated with a rather larger correlation correction than long M···C bonds. The correlation energy for the C···I partial bond is probably approximately equal in TSinv and TSret, since R_{LG} is about the same value in each structure. MP2 calculations on the identity reaction of I^- with CH_3I (Table 5.3), have indicated that the correlation energy associated with the formation and breaking of C–I bonds is small. The activation barriers computed for TSret at the LDA and Becke3LYP levels are both lower than the *ab initio* estimates. The decrease in these energies correlates with smaller values of R_{Nu} and R_{LG}, indicating more stable, tightly bound structures.

(a')

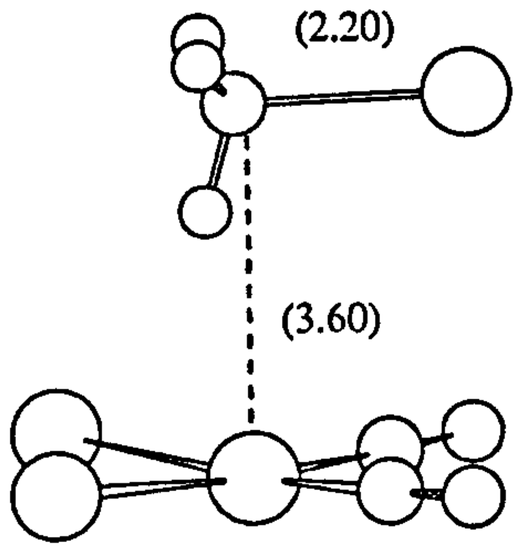

rx=-3.5

(b')

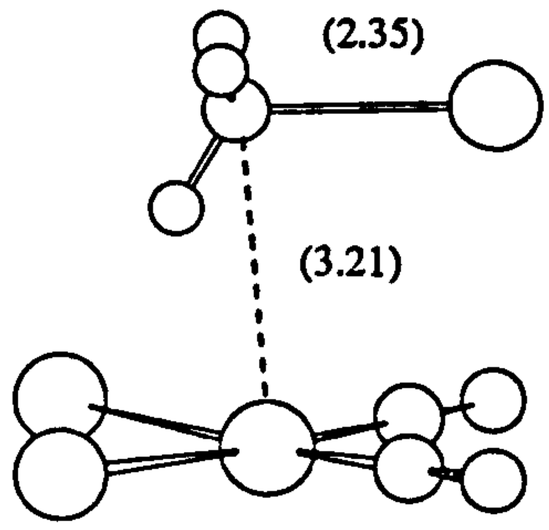

rx=-2

(c')

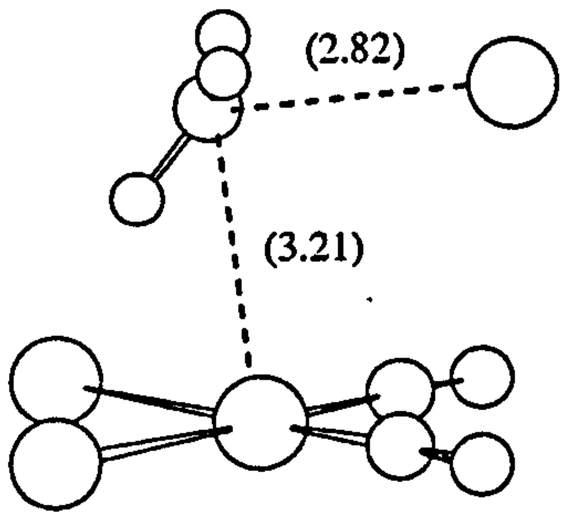

rx=-1

(d')

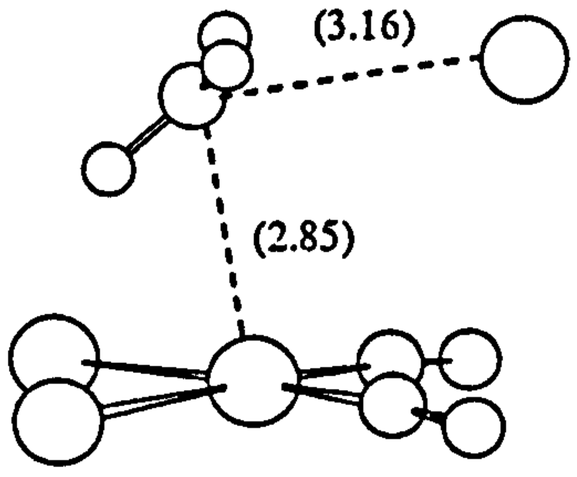

rx=0

(e')

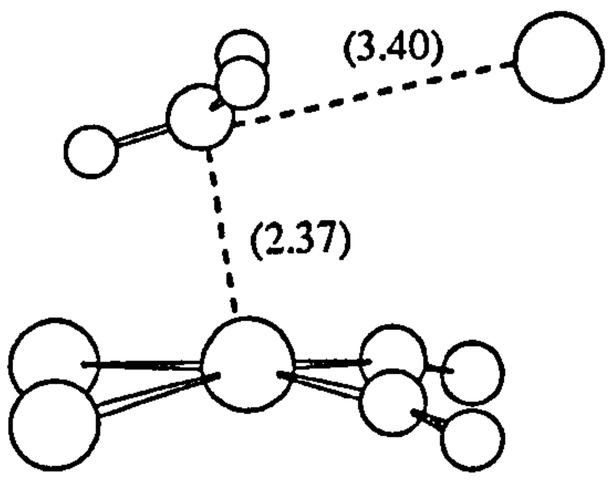

rx=+1

(f')

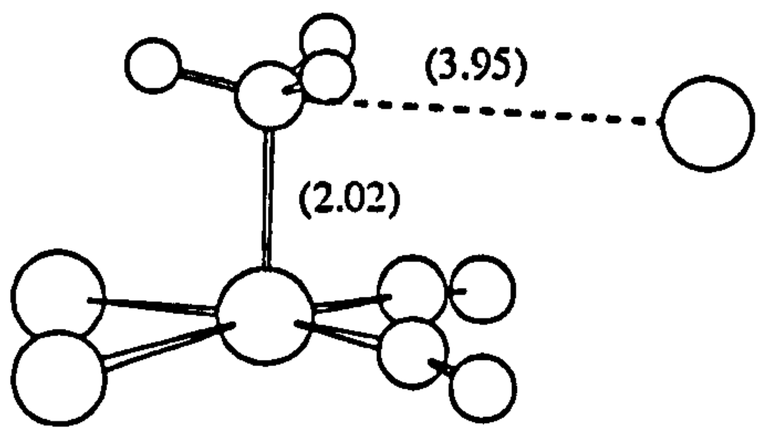

rx=+4

Figure 5.7: Optimized molecular geometries at six points along the reaction coordinate for TSret(Rh).

Inspection of the geometrical changes on the product side of the path, shows that TSret(Rh) also leads to the formation of a neutral five co-ordinate complex and a weakly bound iodide ion (f'). The only significant difference between this geometry and the product resulting from inversion of configuration is a trivial rotation of the CH_3 group around the M–Cα axis into the alternative C_s conformation. Both mechanisms are therefore properly described as S_N2 processes; the bent TS *does not* correspond to a concerted addition of CH_3I to the metal centre. Bickelhaupt *et al.* have argued in their recent publication on the model Pd + CH_3Cl system, that oxidative insertion can be viewed as frontside S_N2 substitution [234]. Our work appears to support this view to some extent, but differs in that for this system complete oxidative insertion does not occur. Insertion is prevented primarily due to the presence of the ligands which cause steric hindrance in addition to electronic effects. We return to this point in a later section.

5.3.3 Enthalpy Changes

Computed values of the energy change (ΔE_{add}) for the overall oxidative addition process

$$[M(CO)_2I_2]^- + CH_3I \rightarrow [CH_3M(CO)_2I_3]^- \qquad (5.3)$$

are shown in the right hand column of Table 5.6. The relative stabilities of the alkyl complexes has been ascribed as the key factor accounting for the different characteristics of the rhodium and iridium catalysed processes [55]. At the RHF level, the formation of the six co-ordinate alkyl complex, is found to be endothermic for rhodium but exothermic for iridium. These results are in qualitative agreement with experiment; salts of $[CH_3Ir(CO)_2I_3]^-$ are isolable, whereas the analogous rhodium complex is unstable with respect to loss of CH_3I and migratory insertion [15, 18]. The calculation of this energy change represents a severe test of the theory at any level, so it is surprising that the RHF method succeeds in reproducing the experimental behaviour. However, it should be noted that the entropy component of the free energy, which has been ignored until this point, could also make a significant contribution to the observed stabilities.

A slightly different picture emerges from the results obtained using the MP2 and DFT schemes. As for the RHF method, each calculation predicts the iridium alkyl complex to be the more thermodynamically stable species with respect to its initial reactants. Computed values of the energy difference ΔE_{add}(Rh)$-\Delta E_{add}$(Ir), are $\sim$ 30 to 50 kJ mol^{-1} for the MP2 scheme, $\sim$30 kJ mol^{-1} for LDA, and $\sim$ 15 to 35 kJ mol^{-1} for the Becke3LYP functional. Evidently, the correlated methods predict the relative stabilities of rhodium and iridium alkyl complexes to be quite finely balanced compared to the larger energy differences (*ca.* 80 kJ mol^{-1}) calculated with the RHF method. There is a large variation in the individual values of ΔE_{add} over the different methods employed. For the rhodium system, the non-local DFT

Table 5.6: Relative energies of stationary points computed for the oxidative addition of CH_3I to *cis*-$[M(CO)_2I_2]^-$. Parameters refer to those defined in Figure 5.8. All energies are in kJ mol^{-1}.

Model	Basis	ΔE_c	$\Delta E_f^{\ddagger}$	$\Delta E_b^{\ddagger}$	ΔE_{sub}	ΔE_{add}
			Inversion of configuration TSinv(Rh)			
RHF	DZ	−26.6	146.0	50.7	95.4	10.7
RHF	DZ2	−27.6	163.8	44.1	119.7	49.1
MP2[a]	DZ	−20.5	59.3	2.4	57.0	−61.5 (−56.7)[c]
MP2[a]	DZ*	−27.9	71.2	11.6	59.6	−69.3
MP2[a]	DZ2	−21.2	69.9	0.9	68.9	−48.2 (−57.1)[c]
HFS	DZ	−36.2	88.2	21.5	66.7	−23.6
LDA	DZ	−38.1	91.1	38.3	52.8	−38.4
BLYP	DZ	−22.3	110.8	19.4	91.4	41.4
BHANDH	DZ	−38.9	118.1	39.6	78.5	−36.0
Becke3LYP	DZ	−24.7	120.8	20.5	100.3	37.0
Becke3LYP[a]	DZ	−22.1	100.8	−3.4	104.2	45.9
			Inversion of configuration TSinv(Ir)			
RHF	DZ	−25.5	92.2	71.9	20.3	−69.0
RHF	DZ2	−24.7	118.5	49.7	68.8	−38.9
MP2[a]	DZ	−20.0	28.6	8.6	20.0	−96.1 (−102.3)[c]
MP2[a]	DZ*	−25.1	43.2	13.7	29.4	−100.4
MP2[b]	DZ2	−19.6	52.2	43.0	9.1	−85.8
MP2[b]	DZ2*	−24.5	69.9	21.7	48.2	−87.5 (−85.3)[c]
LDA	DZ	−39.0	59.1	66.1	−7.0	−69.4
Becke3LYP	DZ	−23.7	76.1	41.5	34.7	−10.0
Becke3LYP[b]	DZ2	−18.1	64.4	−2.7	67.1	−24.7
			Retention of configuration TSret(Rh)			
RHF	DZ	-	236.1	-	-	-
MP2[a]	DZ*	-	254.7	-	-	-
LDA	DZ	-	144.5	-	-	-
Becke3LYP	DZ	-	194.0	-	-	-
			Retention of configuration TSret(Ir)			
RHF	DZ	-	212.1	-	-	-
LDA	DZ	-	121.8	-	-	-

[a]Single-point energy calculations on optimized RHF/DZ geometries.

[b]Single-point energy calculations on optimized RHF/DZ2 geometries.

[c]Values in parentheses for ΔE_{add} denote values which have been obtained by fully optimizing CH_3I, $[M(CO)_2I_2]^-$ and $[CH_3M(CO)_2I_2]^-$ at the MP2 level.

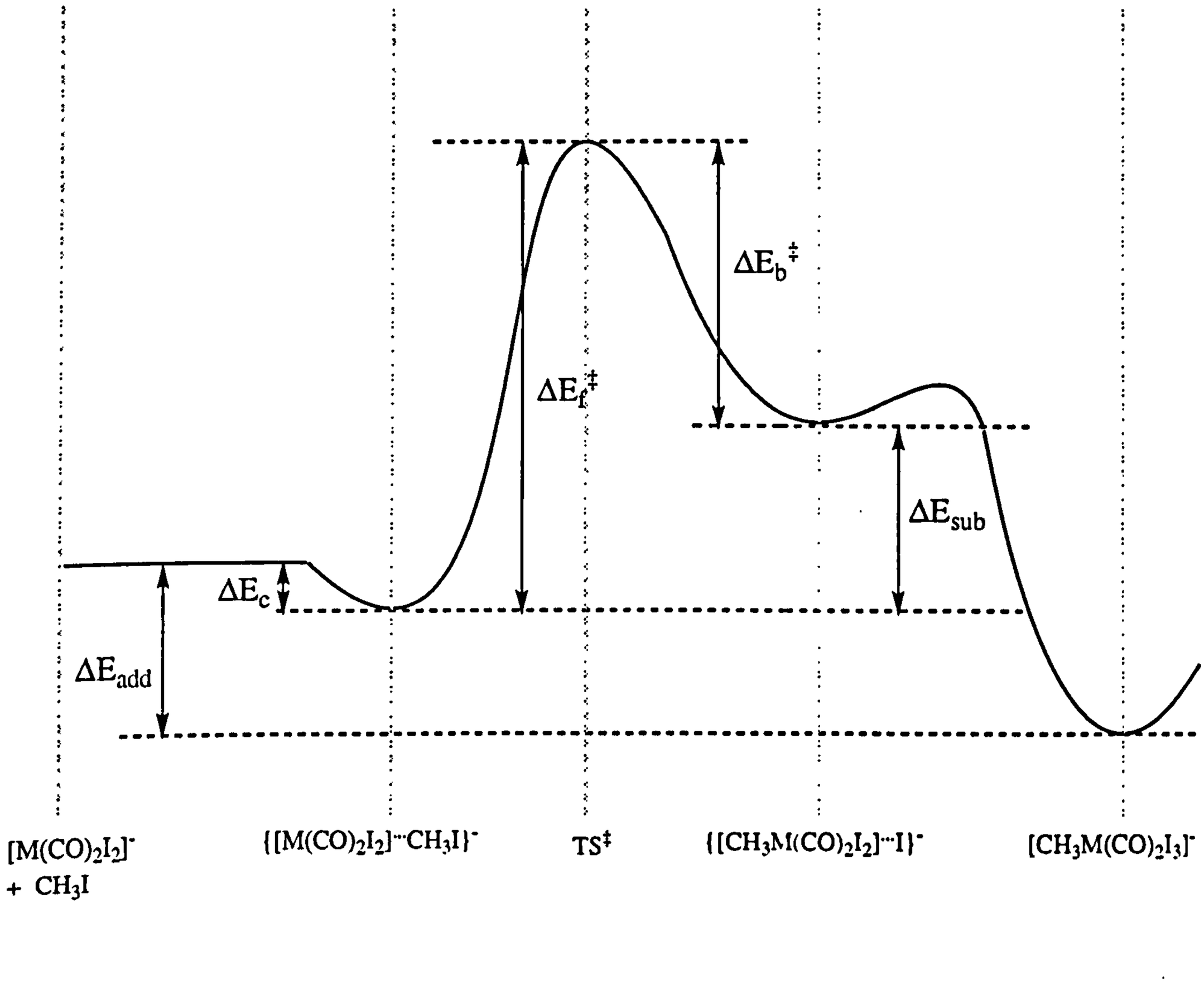

Figure 5.8: Schematic diagram of the energy profile for oxidative addition of CH_3I to $[M(CO)_2I_2]^-$ proceeding via an S_N2 pathway.

schemes are in agreement with the RHF method, predicting that overall oxidative addition is endothermic, $\Delta E_{add} \approx +40$ kJ mol^{-1}. By contrast, the MP2, LDA and BHANDH schemes predict that this process is exothermic by *ca.* −35 to −70 kJ mol^{-1}. For the iridium system, MP2 calculations yield energy changes which are large and negative suggesting a highly exothermic process ($\Delta E_{add} \approx -85$ to −100 kJ mol^{-1}). However, the Becke3LYP calculations predict a much smaller value, suggesting a rather less stable iridium species (−10 to −25 kJ mol^{-1}). In general, the predicted stabilities of $[CH_3M(CO)_2I_3]^-$ complexes decrease in the order: MP2 > local DFT > RHF > non-local DFT. This trend appears to hold for both metal systems. It is surprising that the MP2 and non-local DFT schemes, considered to be the highest quality theoretical methods, generate data which exhibit the greatest differences.

The enthalpy change for oxidative addition has not been measured directly for either metal system. However, Haynes has estimated a value for the rhodium system from extrapolated rate data, $\Delta H_{add} \approx -50$ kJ mol^{-1} [242]. Thus, oxidative addition of CH_3I to $[Rh(CO)_2I_2]^-$ is an exothermic process. A large negative entropy component is found to make ΔG_{add} positive, hence the instability of the rhodium alkyl intermediate. Since $[CH_3Ir(CO)_2I_3]$ is isolable, it should in principle be possible to calculate an experimental enthalpy change for the iridium system by difference of the forward and reverse activation barriers. However, this is prevented due to a lack of accurate rate data for reductive elimination, which is too slow to measure under normal conditions. An upper limit for the elimination barrier has been determined though, allowing an approximate value of ΔH_{add} to be estimated. Carrying out the necessary arithmetic leads to an enthalpy change for the iridium system which is exothermic by at least −75 kJ mol^{-1} [242]. Enthalpy changes and kinetic data are available for the reaction of CH_3I with a variety of Vaska-type complexes. The enthalpy change for the oxidative addition of CH_3I to *trans*-$[Ir(CO)Cl(PMe_3)_2]$ has been measured directly by solution calorimetry and is given as −117 KJmol^{-1} [243]. It is generally accepted that oxidative addition is promoted by increasing the electron density at the metal centre [11, 13]. The rate and exothermicity for this nucleophile, would therefore be expected to be higher than for $[Ir(CO)_2I_2]^-$ due to the presence of electron releasing PMe_3 ligands. The second order rate constant for the reaction of a similar Vaska complex (L=PEt_3) is 23×10^{-3} s^{-1}M^{-1} (benzene, 25 °C) [23]. This is significantly greater than the rate constant determined by Pearson for the reaction of CH_3I with $[Ir(CO)_2I_2]^-$, $k_2 = 3.09 \times 10^{-3}$ s^{-1}M^{-1} (dichloromethane 25 °C) [67].

To summarize, oxidative addition of CH_3I to $[Rh(CO)_2I_2]^-$ is exothermic by approximately 50 kJ mol^{-1}. Estimates based on rate data and related oxidative additions suggest an enthalpy change for the iridium system lying in the range $\sim$ −75 to −117 kJ mol^{-1}. It follows from the previous discussion and the values shown in Table 5.6 that the enthalpy changes computed by the MP2 scheme are

consistent with the experimental data. The DFT methods, on the other hand, tend to generate enthalpy changes for the oxidative addition which are too endothermic. The failure of the non-local functionals to reproduce comparable data to the MP2 scheme is disappointing in view of their good reported performances in energy calculations of a variety of other systems.

5.3.4 Secondary α-Deuterium Kinetic Isotope Effects

Hitherto, the results have not provided unambiguous proof for the geometry of the transition state, and hence the detailed mechanism, of the oxidative addition reaction. To recapitulate, the candidates for the TS and their proposers are:

- a nearly linear structure with inversion of configuration at carbon (RHF);
- a bent structure with inversion (DFT);
- a bent structure with retention (RHF and DFT);

Secondary α-Deuterium kinetic isotope effects have been widely used to probe transition state structure for S_N2 reactions and provide an alternative method for comparing theoretical to experimental observables. Computed secondary α-D KIEs, together with experimental values, are presented in Table 5.7 for the reaction of *cis*-$[M(CO)_2I_2]^-$ complexes with $C(H)D_3I$. Also included for comparison to the transition metal nucleophile results are the analogous data for the identity reaction of I^- with $C(H)D_3I$.

The calculated KIEs for the "linear" transition states, are in general small and normal (>1), consistent with classical S_N2 reactions, which typically exhibit inverse (<1) or small normal values of k_H/k_D. By contrast, much larger KIEs are computed for each of the bent transition states. The theoretical KIEs computed at the RHF/DZ level for the linear transition states are in excellent agreement with experiment. The values of $(k_H/k_D)_{calc}$ are 1.15 and 1.09 for rhodium and iridium, respectively, as compared to values of 1.16 and 1.06 determined experimentally. These results provide very strong evidence for an S_N2 inversion mechanism proceeding through a "linear" transition state. However, elongation of the leaving group distance and a small distortion in the M–Cα–I geometry appears to translate into a significant increase away from the experimental values. For example, the deviation from linearity in the structure of TSinv(Rh) calculated at the RHF/DZ2 level is *ca.* 26°, leading to a KIE which is too large by 0.07. The KIEs computed for the inversion transition states with the DFT methods[4] are larger still, the disagreement with experiment increasing to *ca.* 0.15–0.20. These increases correlate

[4]Note that we have used the HFS and Becke3LYP geometries since these were both characterized by frequency analysis to be true transition states.

with larger values of θ and R_{LG}; the local HFS scheme generates the most bent and product-like inversion TS, and hence, the largest KIE (1.40). From these observations it is not surprising that retention of configuration in the bent structures computed for TSret are characterized by even larger values of $(k_H/k_D)_{calc}$, which vary from 1.43 to 1.92. The KIE predicted by the LDA scheme is markedly smaller than the corresponding RHF value, probably as a result of the contracted geometry that was described earlier.

Table 5.7: Calculated secondary α-D kinetic isotope effects $(k_H/k_D)_{calc}$ for the reactions of *cis*-$[M(CO)_2I_2]^-$ and I^- with $CH(D)_3I$. In each case the computed KIE corresponds to transformation of the reactant ion-dipole complex into the TS. Experimental KIEs $(k_H/k_D)_{exp}$, are given for comparison.

Nucleophile	Model	Basis	$(k_H/k_D)_{calc}$[a]	$(k_H/k_D)_{exp}$
		Inversion of configuration TSinv		
$[Rh(CO)_2I_2]^-$	RHF	DZ	1.15	1.16±0.03[b]
$[Rh(CO)_2I_2]^-$	RHF	DZ2	1.22	
$[Rh(CO)_2I_2]^-$	HFS	DZ	1.40	
$[Rh(CO)_2I_2]^-$	Becke3LYP	DZ	1.34	
$[Ir(CO)_2I_2]^-$	RHF	DZ	1.09	1.06±0.03[c]
$[Ir(CO)_2I_2]^-$	RHF	DZ2	1.11	
I^-	RHF	DZ	1.07	1.05,1.10[d]
I^-	LDA	DZ	1.03	
		Retention of configuration TSret[e]		
$[Rh(CO)_2I_2]^-$	RHF	DZ	1.92	
$[Rh(CO)_2I_2]^-$	LDA	DZ	1.43	

[a]For the computation of the KIE, the Hartree-Fock frequencies were scaled by a standard factor of 0.89. Frequencies computed by the DFT methods were left unscaled.

[b]Experimental value, 25° in neat CH_3I [203].

[c]Experimental value, 25° in CH_2Cl_2 [203].

[d]Literature values for Nu=I^- measured at 20 °C in CH_3OH and H_2O, respectively [244].

[e]KIEs for retention of configuration have been computed using the same optimized reactant ion-dipole geometries that were used for TSinv.

We have analysed the origins of the computed KIEs for the transition states predicted at the RHF/DZ level. Table 5.8 shows the separated contributions from the C–H(D) bending and stretching vibrations and the contribution from the imaginary frequency. Also included are the calculated values of Wolfe's looseness parameter [177] and Westaway's R_{TS} parameter [179]. A definition of these parameters and a description of the vibrations used to partition the KIEs were given in chapter 3. The analysis shows that the computed KIEs are dominated by large, normal contributions from C–H(D) bending vibrations. For the linear rhodium transition states, the biggest contribution comes from the "umbrella" bending mode (Figure 5.3.4a), which is sterically unhindered in the large available space between nu-

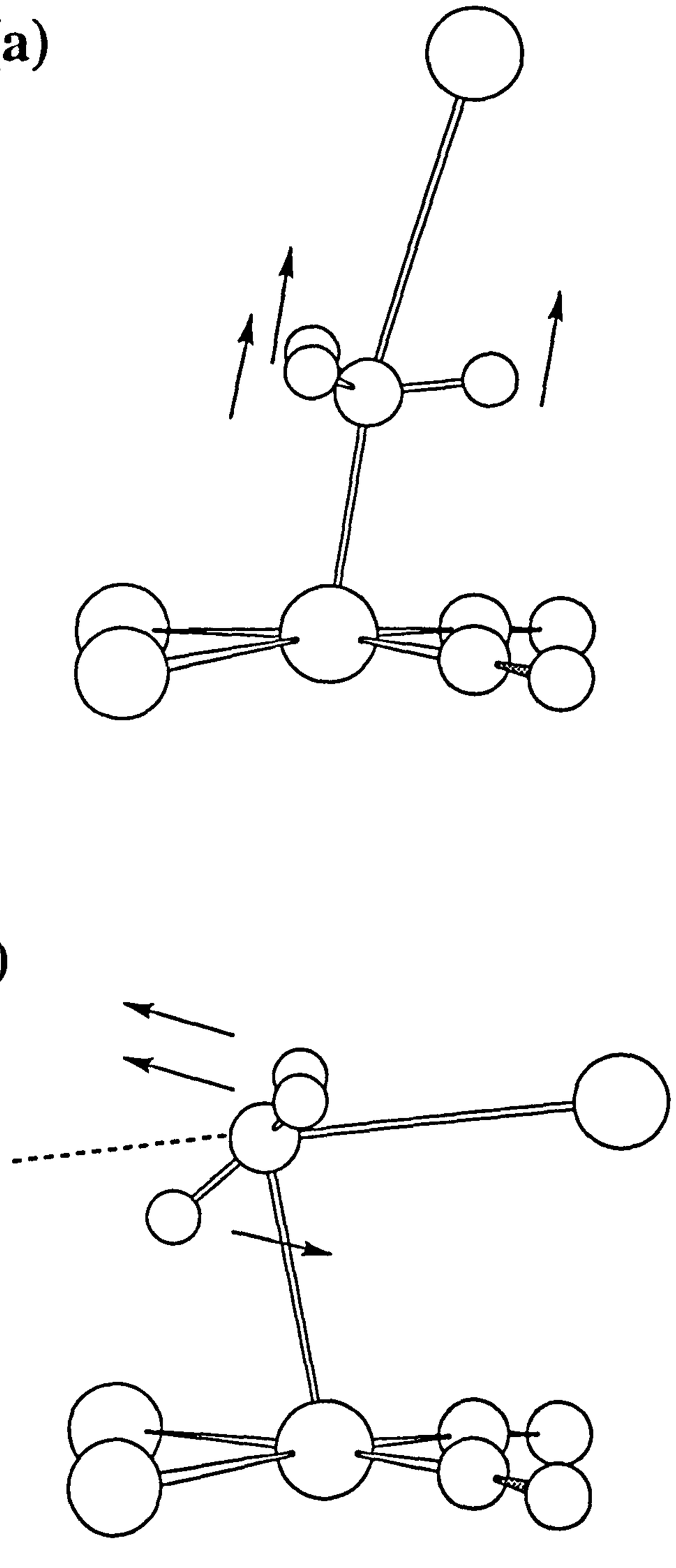

Figure 5.9: C–H(D) bending modes of principal importance in determining the computed secondary α-D KIEs for (a) TSinv and (b) TSret.

Table 5.8: Contributions to the computed KIEs from the C–H(D) bending (k_b) and stretching (k_s) vibrations. k_i is the imaginary vibration contribution. Also included are the L_{TS} and R_{TS} parameters (see text). All data deduced from RHF/DZ calculations.

Nucleophile	$(k_H/k_D)_{calc}$	k_b	k_s	k_i	L_{TS}	R_{TS}
Inversion of configuration TSinv						
$[Rh(CO)_2I_2]^-$	1.15	1.23	0.92	1.02	53.6	5.39
$[Ir(CO)_2I_2]^-$	1.09	1.27	0.85	1.01	47.1	5.37
I^-	1.07	1.26	0.83	1.01	49.3	5.57
Retention of configuration TSret						
$[Rh(CO)_2I_2]^-$	1.92	1.51	0.88	1.19	84.2	6.00

cleophile and leaving group. This supports our earlier conclusions in classifying TSinv(Rh) as a relatively late S_N2 transition structure. The considerably larger normal KIE for the bent retention TS originates principally from a rocking motion about the Cα–I axis (Figure 5.3.4b). The contribution from the imaginary frequency for TSret(Rh) is quite large (k_i = 1.19) since this mode also incorporates a significant rocking vibration of the CH_3 group. By contrast, the imaginary contributions for inversion of configuration are all small ($k_i \approx 1.01$). This is because these modes mainly describe an asymmetric stretch of the M–Cα–I geometry, accompanied by only a slight flattening of the methyl umbrella. The C–H(D) stretching contribution to the total KIE is inverse in all cases, in agreement with recent theoretical treatments of S_N2 reactions [177, 179].

The smaller observed KIE for the iridium nucleophile is correctly predicted by theory. This decrease correlates with smaller values of both L_{TS} and R_{TS}, indicating a tighter inversion transition state than for rhodium. The KIE computed for the identity reaction between I^- and CH_3I is also in good agreement with reported experimental data [244]. The observed and calculated KIEs for *cis*-$[Ir(CO)_2I_2]^-$ are similar to those for I^-, as are the respective contributions from the C–H(D) bending and stretching vibrations. Normal bending contributions are again dominant, but larger inverse stretching contributions bring the total KIEs below that for the rhodium nucleophile. Previous data have shown the nucleophilicity of *cis*-$[Ir(CO)_2I_2]^-$ to be *ca.* 2 orders of magnitude greater than that of *cis*-$[Rh(CO)_2I_2]^-$ and similar to that of iodide [18]. This suggests a correlation between KIE and nucleophilicity for both transition metal and other nucleophiles.

Concluding this section, the calculated KIEs for S_N2 inversion transitions states with the "linear" geometries predicted by the RHF method are in excellent agree-

ment with experiment. A distortion in the geometry of these transition states leads to an increase in the predicted KIE away from the observed values. The involvement of bent inversion transition states, as proposed by the DFT schemes, therefore appears to be very doubtful. Retention of configuration, also characterized by a bent transition state, is unlikely to compete with the inversion mechanism on energetic grounds and is associated with a considerably larger secondary α-D KIE.

The remainder of this chapter presents the results of further analysis of the oxidative addition reaction pathway, carried out using the RHF and MP2 methods. The majority of the calculations relate to the linear TS displaying inversion stereochemistry. Topics covered include the influence of a solvent medium, ligand effects, and an analysis of the electronic interactions that govern the substitution reaction.

5.3.5 Electronic Structure and Bonding

We have analysed the electronic structure of, and bonding between, $[M(CO)_2I_2]^-$ and CH_3I in the inversion and retention transition states, the substitution products and the oxidative addition products. First, we inspect the valence electronic structures of the separated reactants for the rhodium system which are displayed schematically in Figure 5.10. Orbitals of interest to the following discussion are displayed graphically. Note that the orbital counting for each molecule begins with the lowest *valence* orbital. The two lowest valence levels in CH_3I, $1a_1$ and $2a_1$, are essentially the bonding and anti-bonding combinations of carbon $2s$ and iodine $5s$ orbitals. The $1e_1$ and $3a_1$ MO levels are σ_{CH} and σ_{CI} bonding orbitals, respectively. The $2e_1$ degenerate orbitals accommodate the iodine lone pairs. The $4a1$ LUMO has strong σ_{CI} anti-bonding character. $[Rh(CO)_2I_2]^-$ exhibits a rather more complex set of MOs. We have approximated the energy level scheme by grouping together orbitals of similar character and energies to simplify the discussion. The two lowest valence orbitals $1A_1$ and $1B_2$ are C–O σ bonding combinations. $2A_1$ and $2B_2$ are the Rh–CO σ bonding orbitals. The $3A_1$ and $3B_2$ levels are Rh–I σ bonding orbitals. Rh–CO π back-donation is described to differing extents by the group of six orbitals with similar energy $4A_1$ to $5B_2$. The next three levels are essentially non-bonding Rh d orbitals; $6A_1$ is a $d_{x^2-y^2}$ in the plane, while $2A_2$ and $2B_1$ are out of plane d_{yz} and d_{xz} orbitals, respectively. $7A_1$ and $8A_1$ both contain significant d_{z^2} character. Situated between these is a Rh–I π bonding orbital, $6B_2$. The four highest occupied MOs are p type orbitals which accommodate iodide ligand lone pairs. The largest contribution to the LUMO comes from a p_z orbital centred on Rh.

A fragment molecular orbital (FMO) analysis identifies two occupied orbitals in $[Rh(CO)_2I_2]^-$ ($8A_1$ and $7A_1$), and a single virtual orbital in CH_3I ($5a_1$) as having the largest bonding interactions in TSinv(Rh). The overlaps and populations of

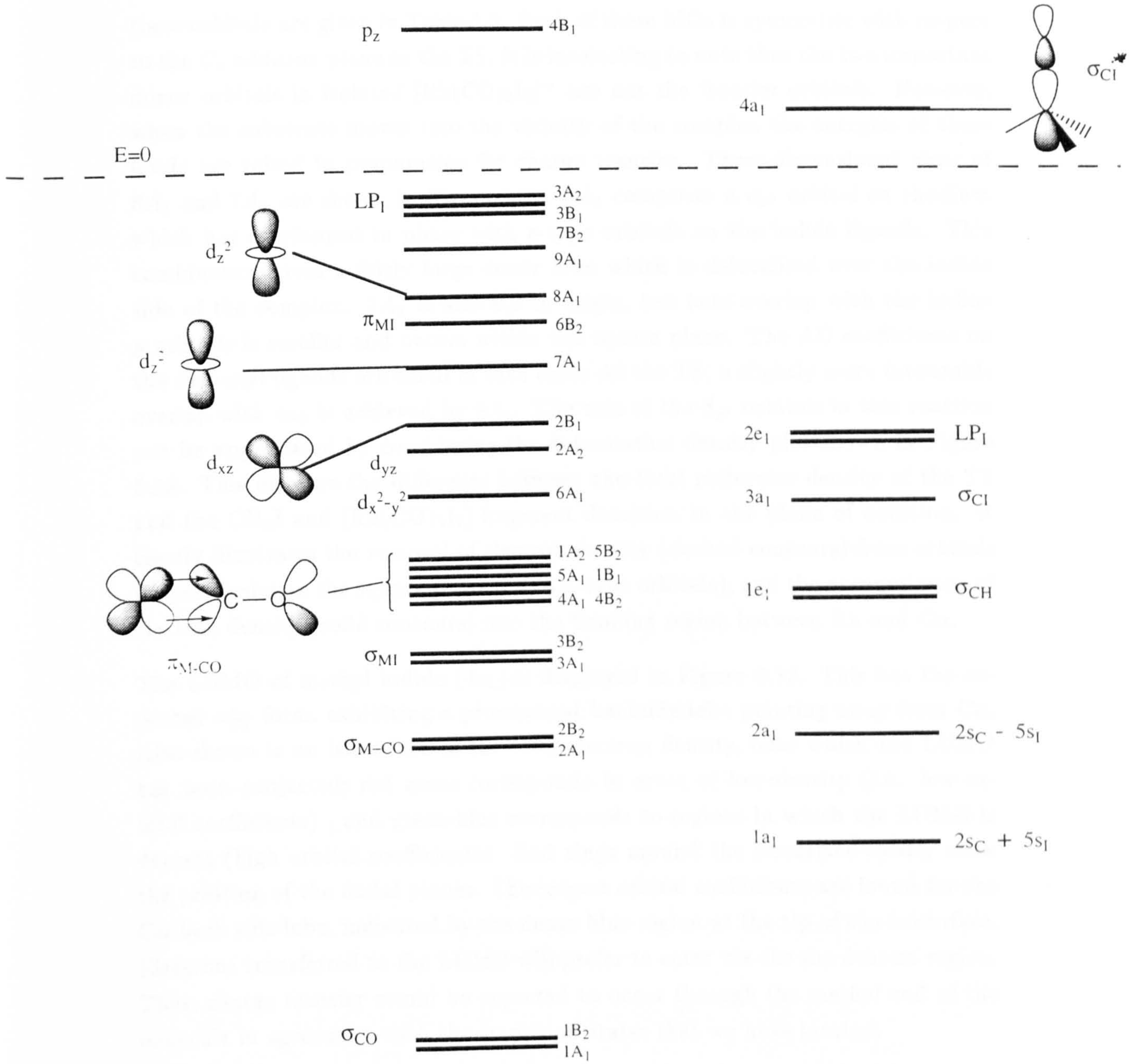

Figure 5.10: Valence MO scheme of $[M(CO)_2I_2]^-$ and CH_3I. Orbital counting begins with the lowest valence MO in each case.

these orbitals are given in Table 5.9. Each of these MOs is symmetric with respect to the C_s addition plane in the TS. It is interesting to note that the two important donor orbitals in isolated $[Rh(CO)_2I_2]^-$ are not the frontier orbitals. However, when the substrate moves into the vicinity of the complex the energies of these levels are raised in preparation for charge transfer. Three-dimensional plots of $8A_1$ and $7A_1$ are shown in Figure 5.11. $8A_1$ comprises a d_{z^2} orbital on rhodium which has overlapped in phase with p-type orbitals on the iodide ligands. This combination gives a fairly large donor lobe which is delocalised over the iodide side of the complex. $7A_1$ is also d_{z^2} in origin, but here overlap with the iodine p orbitals is smaller and occurs within the square plane. The AO coefficients on the carbonyl ligands are small in each case. At the TS, a slightly more favourable overlap with $4a_1$ is achieved by $8A_1$. The role of the d_{z^2} orbitals in this reaction can be appreciated by considering the deformation density plot shown in Figure 5.12. This displays the difference between the total molecular density of the TS and the CH_3I and $[Rh(CO)_2I_2]$ fragment densities, in the plane of addition. It clearly illustrates the removal of electron density (dashed contours) from orbitals perpendicular to the square plane (i.e. d_{z^2}-type orbitals), and the accumulation of electron density (solid contours) into the bonding region between Rh and Cα.

The LUMO of methyl iodide ($4a_1$) is displayed in Figure 5.13. This has the expected σ^*_{CI} form, exhibiting a pronounced backside lobe pointing away from Cα. Also shown is an isosurface of the total electron density, onto which the LUMO has been projected; red areas corresponds to areas of low density (i.e. low orbital coefficients) , and green-blue corresponds to regions in which the LUMO is densest (high orbital coefficients). Red rings around the isosurface clearly show the position of the nodal planes. The largest orbital coefficients are found for the Cα back side lobe, indicated by the dense blue region at the tip of the isosurface. Electrons transferred to the LUMO will prefer to enter via the the densest region. Thus, charge transfer would be expected to occur through the methyl end of the molecule in agreement with the transition states that we have located.

FMO analysis of the iridium transition state TSinv(Ir), indicates similar interactions between metal d_{z^2}-type orbitals and the CH_3I LUMO. In this case however, the higher energy orbital $8A_1$ appears to dominate the interaction with the LUMO. This is indicated by the favourable $\langle 8A_1|4a_1\rangle$ overlap of 0.26, which is about four times the corresponding value for $7A_1$. The strength of this interaction is also reflected by the large depopulation of $P(8A_1) = 1.72$, which accounts for the greater part of the density transferred to the LUMO in the TS ($P(4a_1) = 0.42$). This differs from the rhodium system where the results suggest that both orbitals make an equal contribution to the charge transfer. The reasons for this become clearer when the three-dimensional plots of the iridium orbitals are examined, Figure 5.11. Here, $8A_1$ is a d_{z^2} orbital which extends further into the region perpendicular to the square plane than does its rhodium counterpart; there is a small contribution from

iodide p orbitals, but most of the d_{z^2} character is retained. By contrast, in $7A_1$ the proportion of d_{z^2} is significantly diminished and delocalised to a greater extent over the ligands. These observations correlate with the computed metal–carbon distances in the transition states. The major donor orbital in the iridium nucleophile can protrude further and interact with the substrate orbitals at a larger distance from the square plane. Hence, Ir–C bond formation can occur earlier along the reaction path than for rhodium. This also has the advantage of reducing the exchange repulsion between occupied d orbitals and the CH_3 σ orbitals. The sum of the overlaps of the $1a_1$ and $1e_1$ CH_3 orbitals with the six highest metal d orbitals ($6A_1$ to $8A_1$) which are most involved in this repulsion. is reduced relative to the value for TSinv(Rh), Table 5.9. Closer inspection of the AO coefficients for the iridium nucleophile, reveals that $8A_1$ has a significant contribution from a metal s orbital. An in-phase s component to a d_{z^2} orbital can augment the main lobes and project it further into the perpendicular bonding region. This is probably due to the relativistic effect for the $5d$ metals which lowers the energy of the atomic $6s$ orbital, enhancing its participation in metal–ligand bonding.

From the geometry of TSret(Rh), one might expect qualitatively similar donor-acceptor interactions to those reported by Bickelhaupt *et al.* in the TS for the model reaction between Pd and CH_3Cl [234]. These workers described an oxidative insertion mechanism which was facilitated by the favourable overlap of a Pd d_{xz} hybrid with the LUMO on CH_3Cl, Figure 5.14. They argued that insertion in organometallic chemistry is analogous to *frontside* S_N2 substitution between alkyl halides and main-group bases in organic chemistry. For main-group bases only backside S_N2 substitution is feasible due to the unfavourable overlap of the p-type HOMO with the nodal structure of the σ^* LUMO of the substrate. For metal bases, it was suggested that frontside attack could be favourable due to the presence of valence d orbitals of the correct symmetry.

Our results however, suggest that this type of interaction may be limited to bare metal atoms, or to sterically uncrowded complexes. The most significant bonding interactions in TSret(Rh) are once again between the d_{z^2}-type orbitals, $7A_1$ and $8A_1$, and the substrate LUMO, $4a_1$. There is a single non-bonding d_{xz} orbital $2B_1$, but this is lower in energy and does not protrude to a great extent into the region above the square plane where charge transfer is invoked. Appreciable steric hindrance prevents CH_3I from approaching close enough for the LUMO to form a favourable overlap with this orbital. In fact, the net overlap in the TS is not even bonding. TSret(Rh) does benefit from a reduced electron repulsion between σ_{CH} and metal d electrons on account of the larger Rh–C distance. However, this is negated by significantly larger overlaps between occupied orbitals of the complex and occupied substrate orbitals associated with the iodide leaving group. To obtain a qualitative impression of the magnitude of these interactions, we have summed the overlaps between the lone pair orbitals $2e_1$ and the Cα–I σ bonding

(a) M=Rh

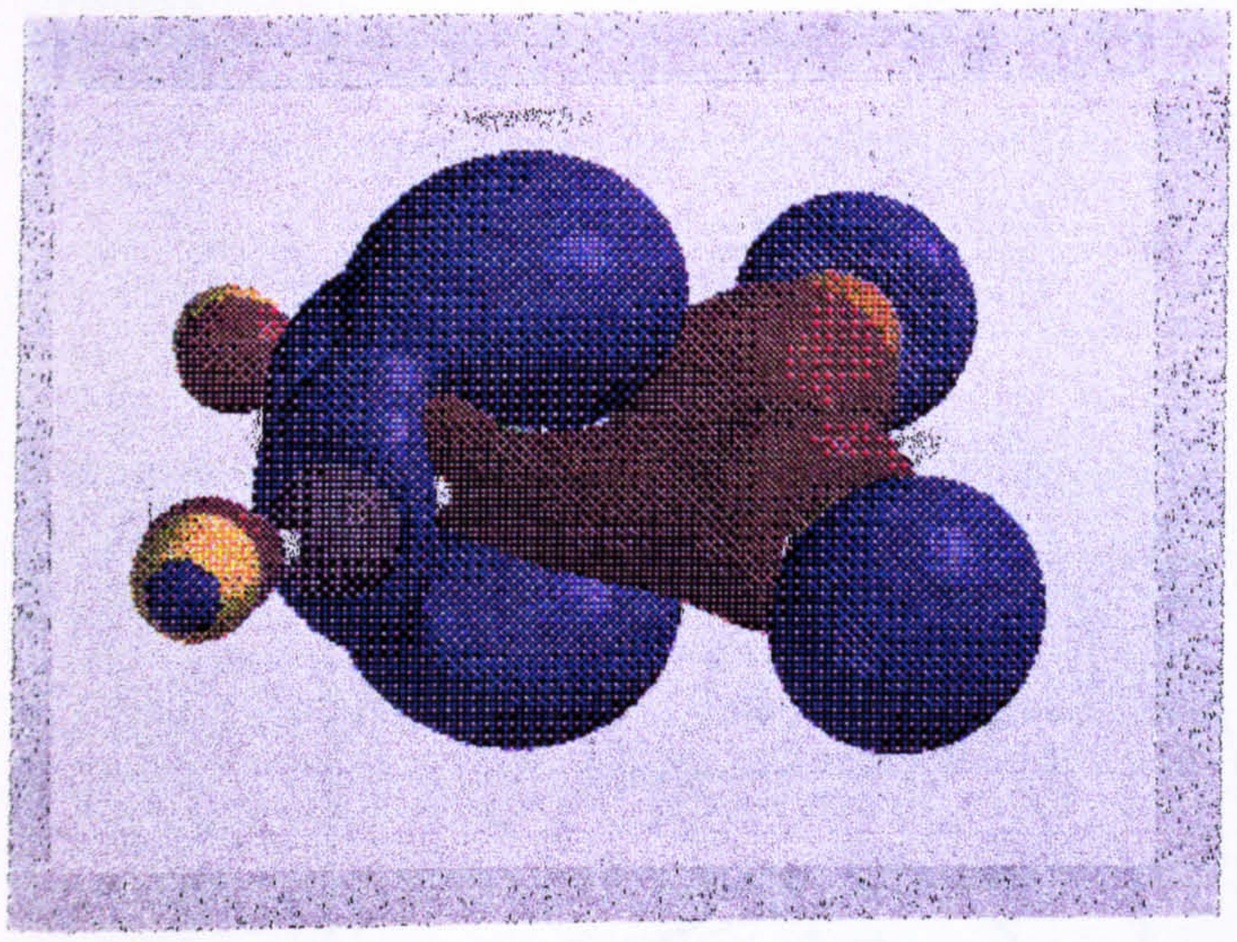

$7A_1$

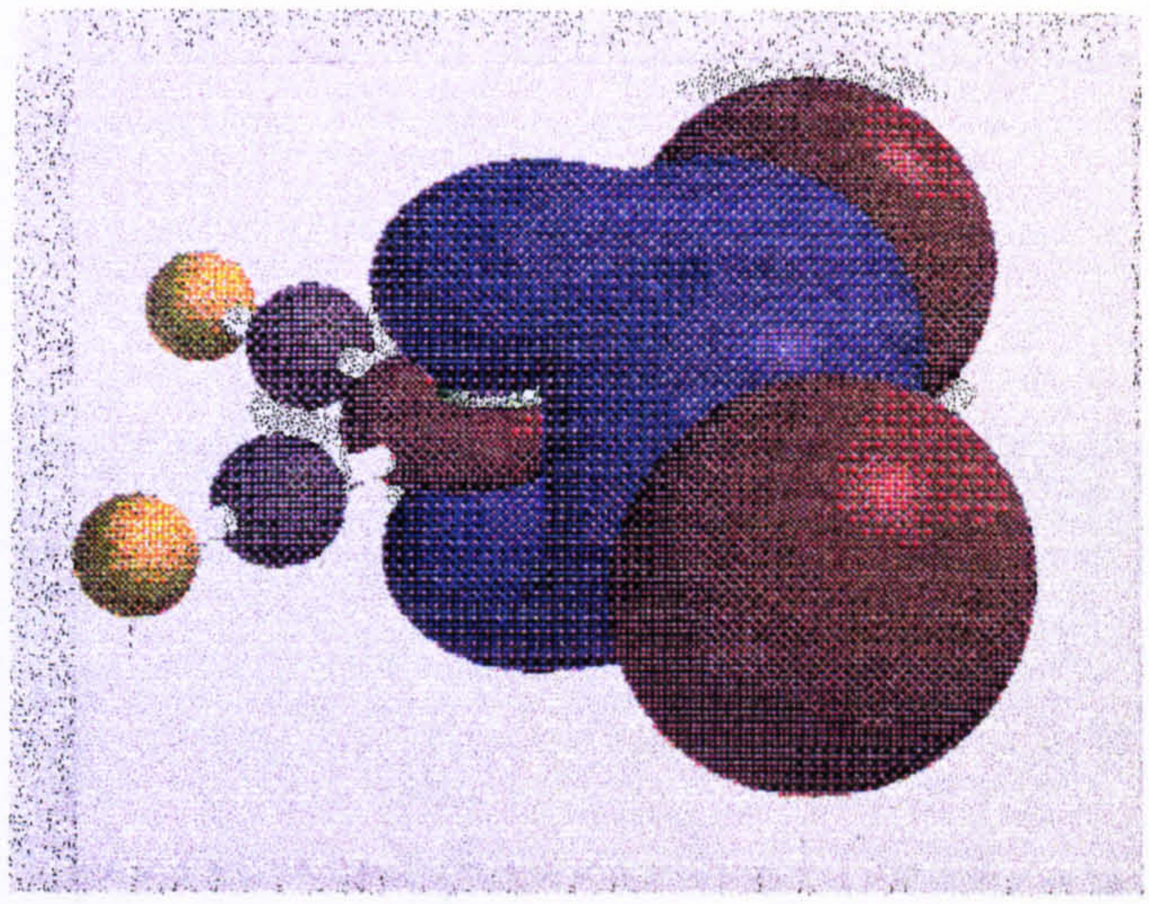

$8A_1$

(b) M=Ir

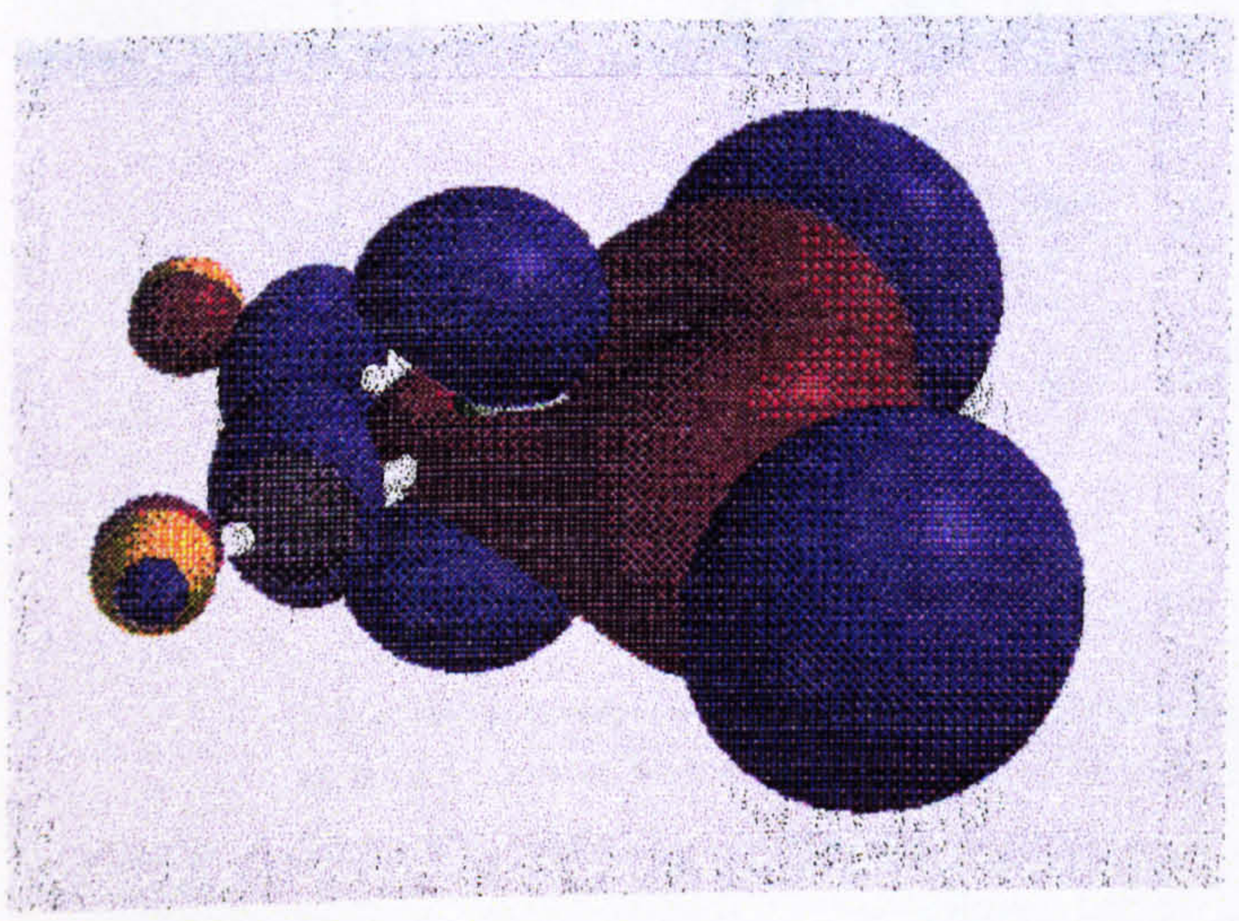

$7A_1$

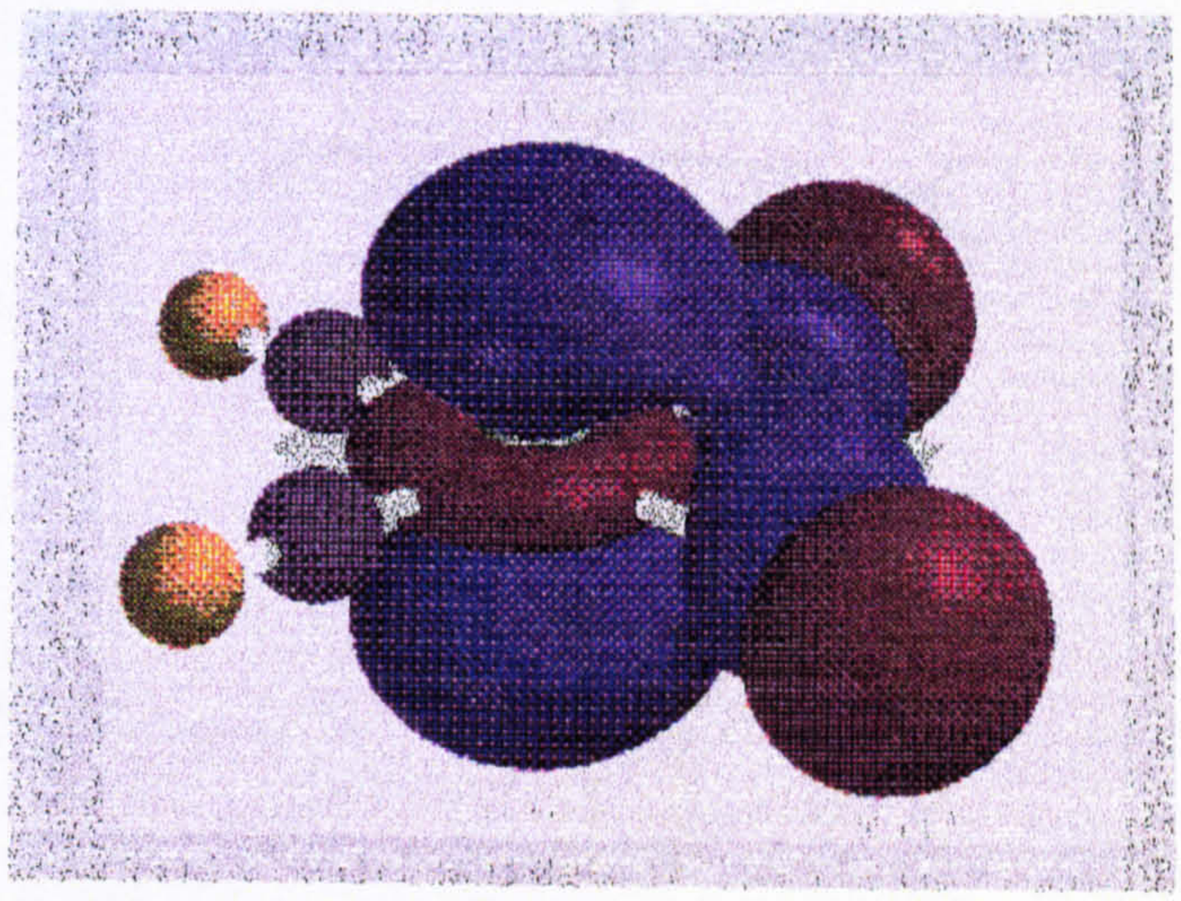

$8A_1$

Figure 5.11: Three-dimensional representation of the important donor orbitals ($7A_1$ and $8A_1$) in (a) $[Rh(CO)_2I_2]^-$ and (b) $[Ir(CO)_2I_2]^-$. Data deduced from RHF/DZ calculations.

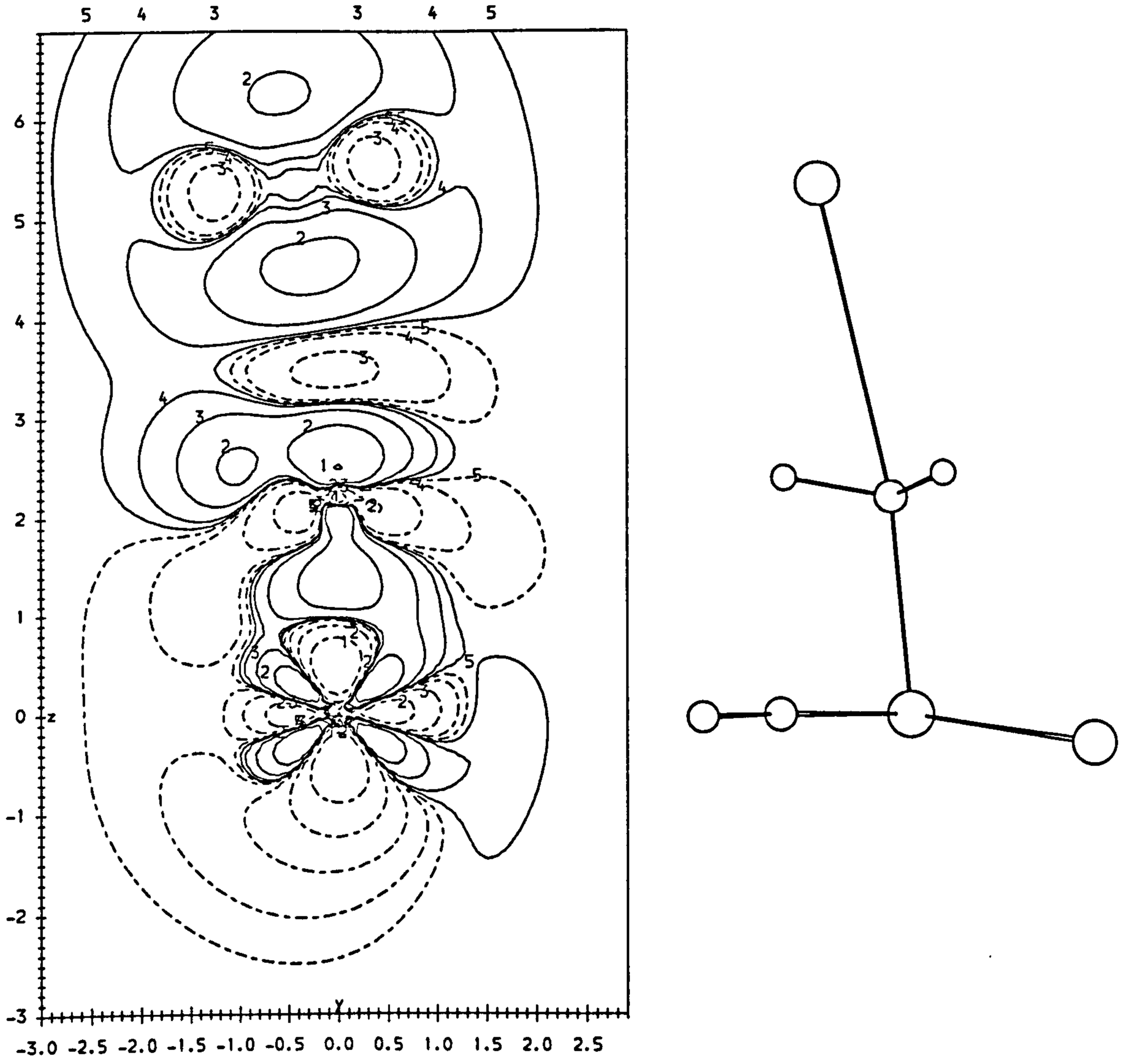

Figure 5.12: Deformation density: $\rho(\mathrm{TSinv(Rh)}) - \rho(CH_3I) - \rho([Rh(CO)_2I_2]^-)$. The plot is taken from the C_s addition plane containing the Rh–Cα–I unit. The contours are geometric differing by a factor of 4, with the value of the smallest positive and negative contour equal to $\pm 1.58\times10^{-4}\ e/a_0^3$. Negative contours are dashed. Data deduced from RHF/DZ calculations.

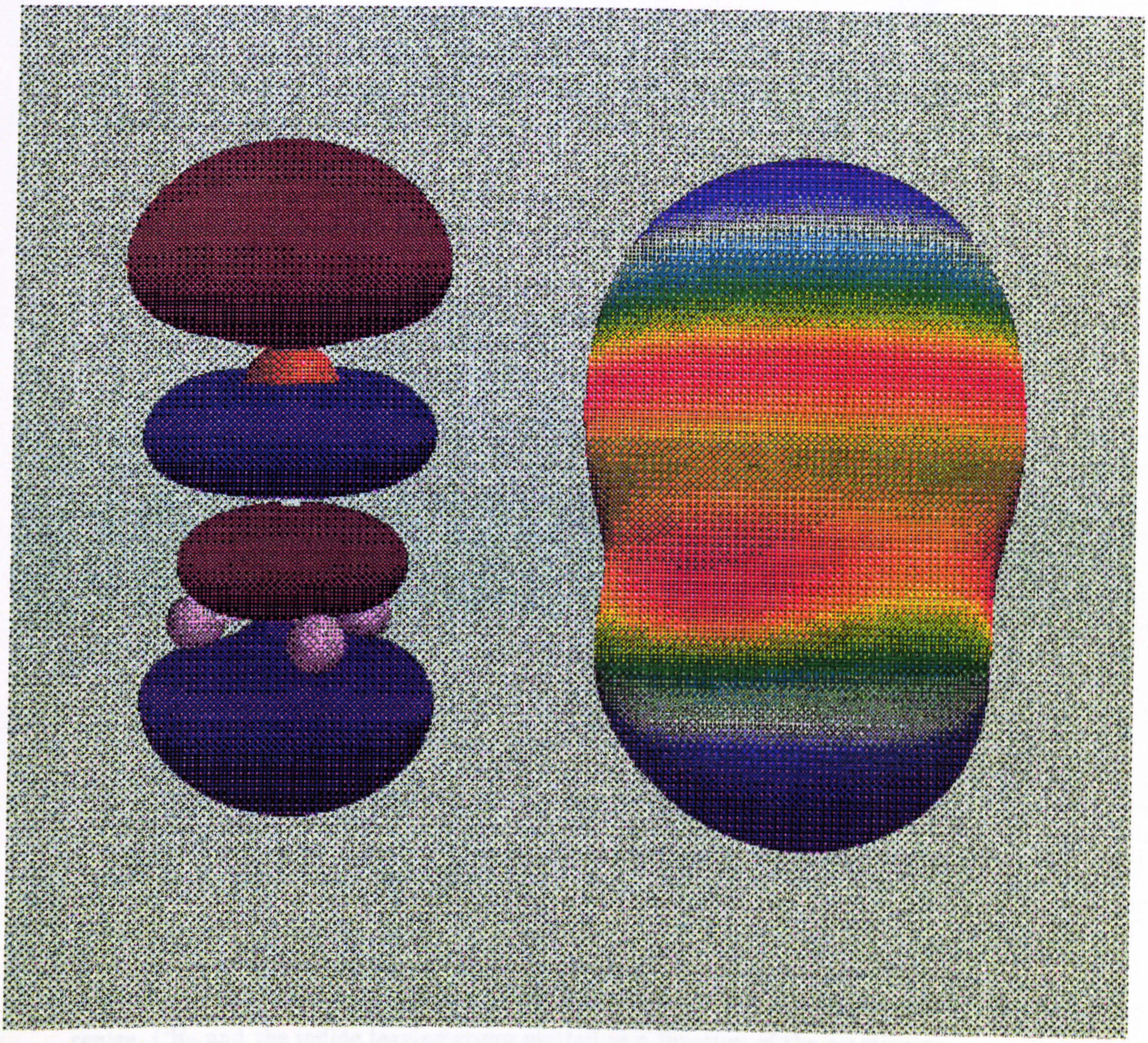

Figure 5.13: Three-dimensional representation of the LUMO ($4a_1$) in CH_3I. Also shown is an isosurface of the total density onto which the AO coefficients of the LUMO have been encoded; blue represents dense areas, while red represents areas where the coefficients are small. Data deduced from RHF/DZ calculations.

orbital $3a_1$ with *all* of the occupied orbitals on the metal complex. It is clear from Table 5.9 that the repulsion is much larger in the bent retention TS than either of the linear inversion transition states. A large component of this repulsion appears to occur between the iodide lone pairs and the CO π^* acceptor orbitals which causes the oxygen atoms to turn outwards by *ca.* 4°. The bonding interactions in TSret are not large enough to compensate for the destabilizing repulsion, and consequently there is a larger energy penalty to the activation barrier than for inversion of configuration.

Table 5.9: Fragment Molecular Orbital (FMO) analysis of the bonding mechanism in the transition states for oxidative addition. Data deduced from RHF/DZ calculations.

	TSinv(Rh)	TSinv(Ir)	TSret(Rh)
Fragment MO Overlaps			
Bonding Interactions			
$\langle 7A_1 \vert 4a_1 \rangle$	0.20	0.07	0.16
$\langle 8A_1 \vert 4a_1 \rangle$	0.23	0.26	0.16
Electron Repulsion			
$\sum\langle\psi\vert\phi\rangle^a$	0.34	0.30	0.20
$\sum\langle\psi\vert\phi\rangle^b$	0.17	0.18	0.47
Fragment MO occupation numbers (electrons)			
$P(7A_1)$	1.78	1.97	1.91
$P(8A_1)$	1.77	1.72	1.91
$P(4a_1)$	0.59	0.42	0.26

[a]Summed overlaps between σ_{CH} orbitals ($1a_1$ and $1e_1$) and six metal occupied *d* orbitals $6A_1$, $2A_2$, $2B_1$. $7A_1$, $6B_2$ and $8A_1$ which are mainly non-bonding in character.

[b]Summed overlaps of the iodide lone pair orbitals ($2e_1$) and the C–I σ orbital ($3a_1$) with the complete set of occupied MOs in $[M(CO)_2I_2]^-$.

Next, we examine the bonding changes that occur along the reaction co-ordinate of the nucleophilic substitution. Figure 5.15a shows the Mulliken charges on the metal centre, CH_3 and the iodide leaving group plotted as a function of the reaction co-ordinate for TSinv(Rh) and TSinv(Ir). Each curve is fairly uniform up to about $rx = -2$. The methyl group holds a small positive charge of *ca.* +0.05 with iodine holding an equal negative charge. There is a substantial negative charge on the metal of *ca.* −0.50. The reaction co-ordinate at this point corresponds to structure (c) shown in Figure 5.5, in which the Cα–I axis is roughly perpendicular to the square plane and the M–Cα distance is about 3.2 Å. After $rx = -2.0$ the charges on the methyl group and iodine grow rapidly in opposite directions resulting in a significant charge separation at the TS. By contrast, the charges on the metal atoms remain fairly constant. Formally, the metal is said to undergo a

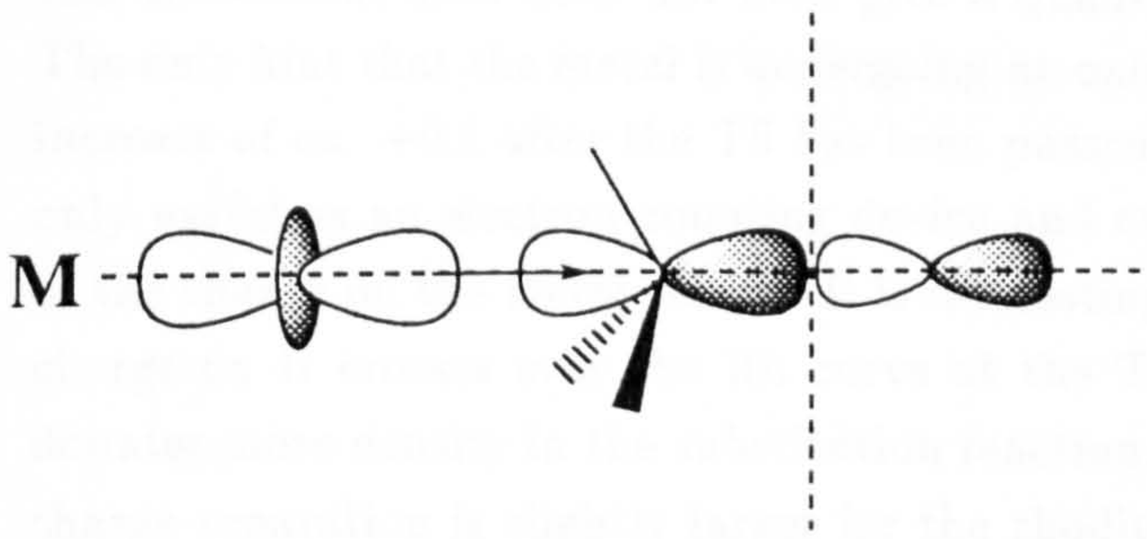

Backside Attack
(Metal Base)

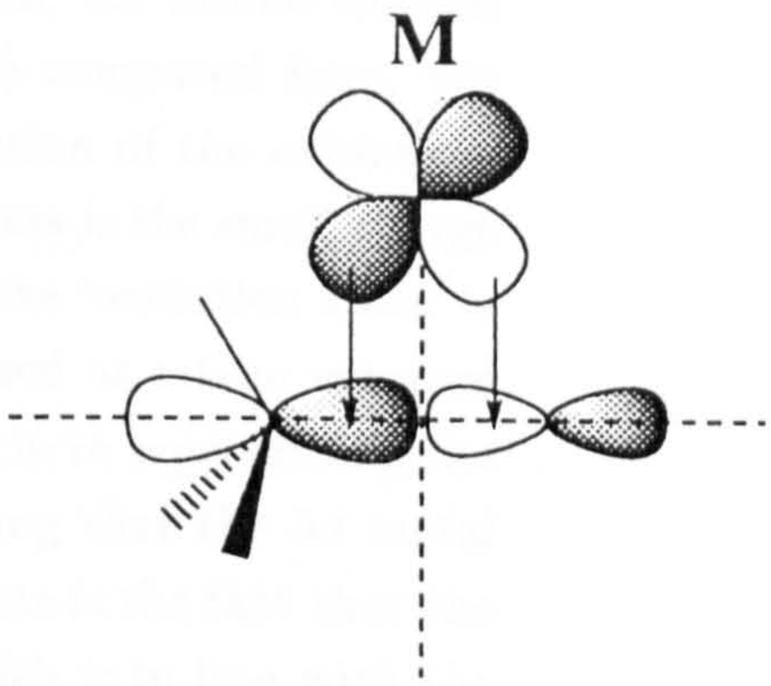

Frontside Attack
(Metal Base)

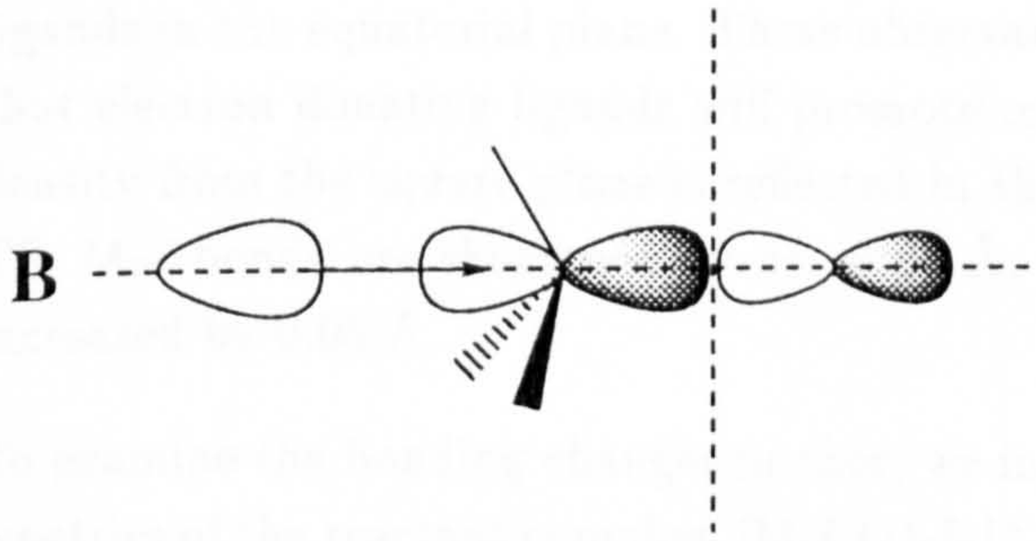

Backside Attack
(Main Group Base)

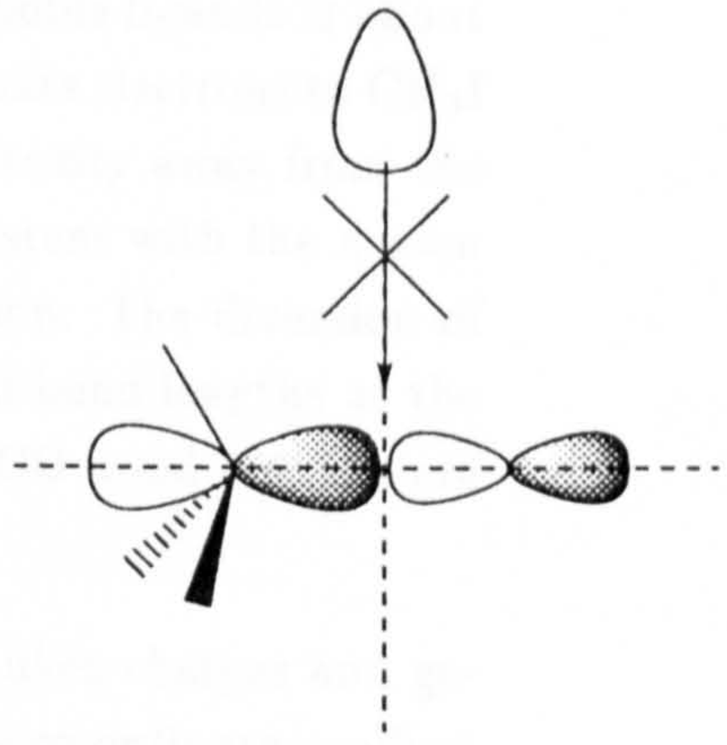

Frontside Attack
(Main Group Base)

Figure 5.14: Donor-acceptor orbital interactions of transition metal and main group bases with alkyl halides.

transformation from an M(I) to an M(III) species. Of course, the formal charges will be more pronounced than we would expect from those computed here, but this theoretical data does not even give a qualitative reflection of the oxidation. The only hint that the metal is undergoing an oxidative process is the small charge increase of *ca.* +0.1 after the TS has been passed. Clearly, the 'oxidation state' is only useful as an electron counting device and cannot be used as a true measure of the charge on the metal centre. It is interesting that the curve representing the charge on Ir crosses over the Rh curve at the TS, suggesting that the 5*d* metal donates more density in the substitution reaction. Also of note is the fact that the charge separation is slightly larger for the rhodium TS, which is in line with the later structure computed for TSinv(Rh).

The charge must of course be conserved in the reaction. If the metal does not increase its positive charge to balance the net negative charge on $[CH_3\cdots I]$, then significant reorganization must also occur in the metal-ligand electronic structure. The missing charge density can be accounted for by examining the plots in Figure 5.15b which show the charges on the iodide and carbonyl ligands. also plotted as a function of the reaction co-ordinate. Note that the points represent the summed charges for $(CO)_2$ and I_2. In each case, the ligand charges become more positive as the new metal–carbon bond is formed. The effect on the iodide ligands is about double that for the carbonyl groups. Hence, the metal can donate electrons to CH_3I and retain its negative charge by polarizing extra electron density away from the ligands in the equatorial plane. These observations are consistent with the notion that electron donating ligands will promote oxidative addition. The diversion of density from the square plane is reflected in the metal–ligand bond lengths at the TS; M–I bonds are shortened by *ca.* 0.07 Å, while the M–CO bond lengths are increased by 0.05 Å.

To examine the bonding changes further, we inspect the Mulliken charges and geometries of the reactant complex, $[M(CO)_2I_2]^-$, the initial five co-ordinate product of nucleophilic substitution, $[CH_3M(CO)_2I_2]$, and the overall product of oxidative addition, $[CH_3M(CO)_2I_3]^-$. The structures are shown in Figure 5.16 annotated with bond lengths computed at the RHF/DZ level. The main concern here is the *change* in the M–L bond lengths that occur in going from M(I) to M(III) species, and not the absolute values; more accurate parameters obtained at the correlated level can be found in chapter 3. Table 5.10 shows the calculated charges on the metal and ligands for these complexes.

Addition of CH_3I to $[M(CO)_2I_2]^-$ has a significant effect on the M–I and M–CO ligand geometries. Going from four co-ordinate Rh(I) to five co-ordinate Rh(III), the Rh–I bonds are reduced by 0.11 Å, while the Rh–CO bonds are elongated by 0.09 Å. The C–O distances are slightly reduced by *ca.* 0.02 Å. Similar changes are observed for iridium. These geometry changes are consistent with oxidation of the central metal atom. Removal of electron density from the metal centre to be

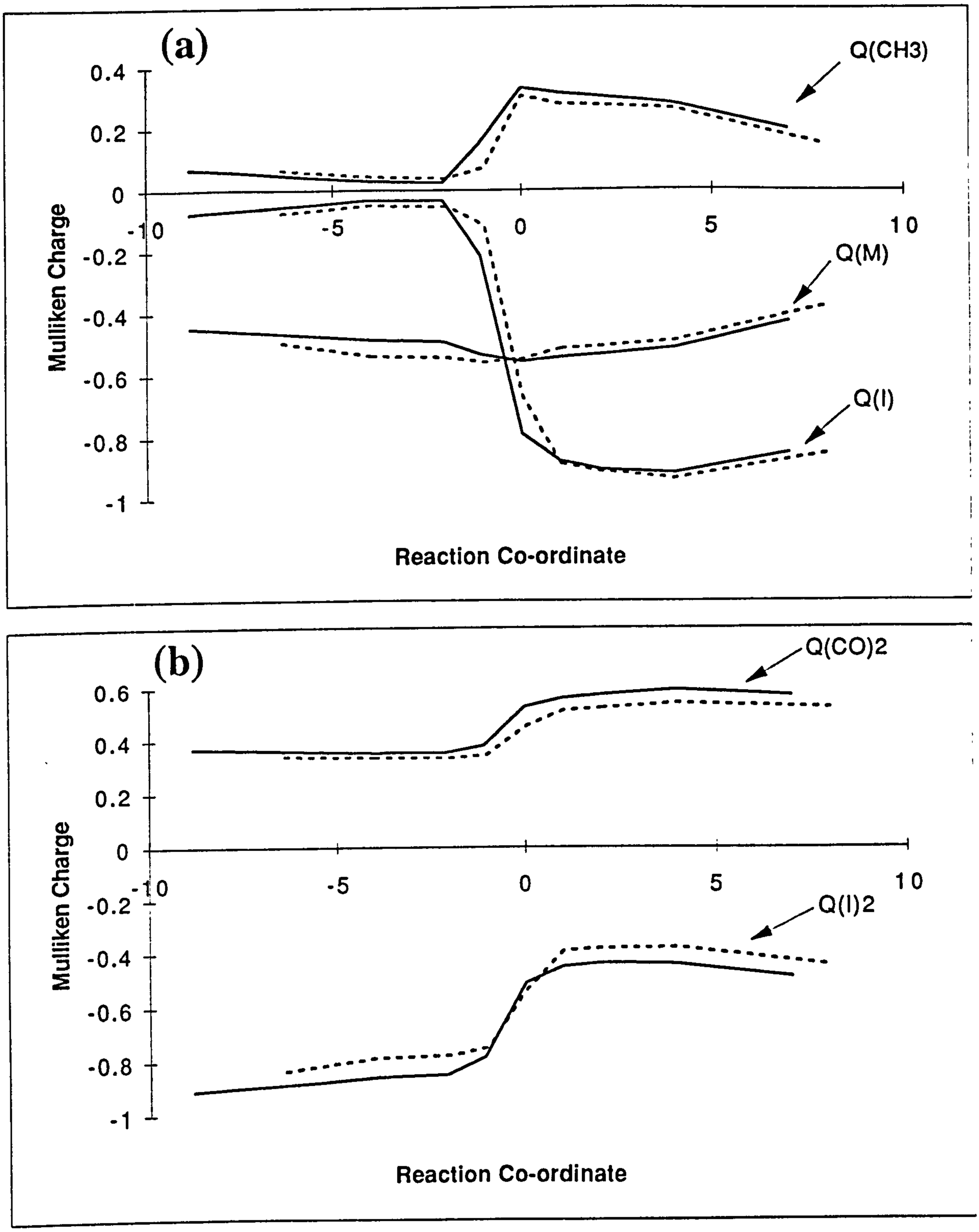

Figure 5.15: Mulliken charges plotted as a function of the reaction co-ordinate for TSinv(Rh) (solid) and TSinv(Ir) (dashed). Plot (a) shows the charges on CH_3, I and M; (b) shows the summed charges on the iodide ligands and the carbonyl ligands. Note that $rx = 0.0$ corresponds to the TS in each case.

(a)

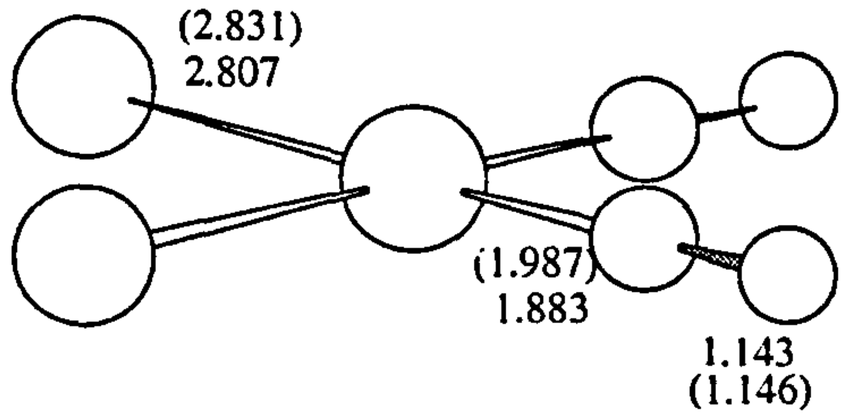

(b)

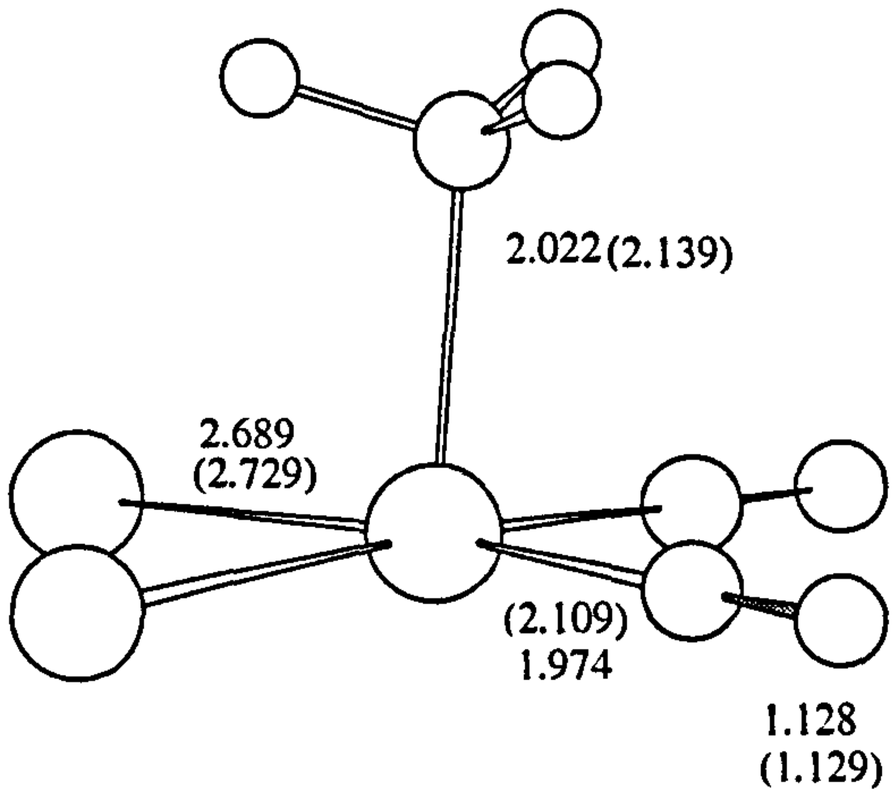

(c)

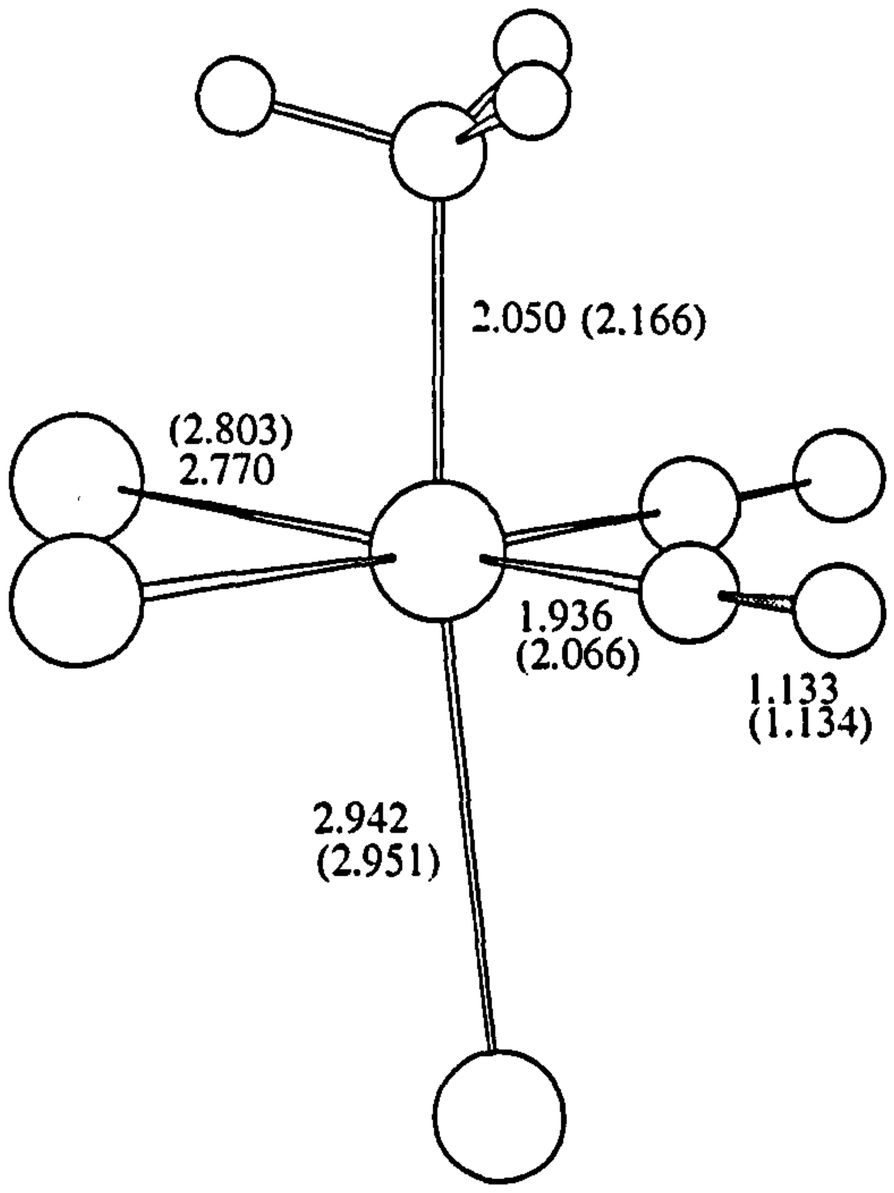

Figure 5.16: Optimized geometries of $[Rh(CO)_2I_2]^-$, $[CH_3Rh(CO)_2I_2]$, and $[CH_3Rh(CO)_2I_3]^-$. Values in parentheses are bond lengths for the corresponding Ir complexes. All geometric data has been deduced from RHF/DZ calculations.

utilised in M–CH_3 bonding allows the iodide ligands to enter into greater M–I σ bonding. This is reflected by a decreased negative charge ($\Delta Q_I \approx +0.55$) and a reduction in the energies of the M–I σ bonding orbitals. Oxidation of the metal penalises M–CO bonding, since there is less density available for the π-acceptor ligands to strengthen their bonds through back-donation. Consequently, the positive charge on the CO ligands increases by *ca.* 0.20. The energies of the π^* acceptor orbitals are also lowered in the five co-ordinate M(III) complex, but inspection of their composition reveals that they incorporate significantly less metal character. The iridium analogue of the substitution product $[CH_3Ir(CO)_2I_2]$ can be prepared by abstracting I^- from the stable complex $[CH_3Ir(CO)_2I_3]^-$. Pearson has measured the terminal carbonyl stretching frequencies [67], which are given as 2118 and 2071 cm^{-1} [67]. These are 72 and 109 cm^{-1} higher than the frequencies in $[Ir(CO)_2I_2]^-$, consistent with a reduced M–CO back-donative interaction. By contrast to the transition states, where the negative charge on the metal was slightly increased relative to $[M(CO)_2I_2]^-$, the metal charges here on five co-ordinate M(III), do imply an oxidative process. Of course though, $[CH_3M(CO)_2I_2]$ is a neutral species, and we would expect this to be reflected in the electron populations. Note that the energy of the LUMO for this complex, which is mainly a p_z orbital pointing out of the square plane, is close to zero Hartrees. The 16-electron fragment therefore has a high electron affinity and would prefer to exist as a co-ordinatively saturated complex by capturing an electron donating ligand such as iodide. This is in line with the fact that the S_N2 intermediate has not been observed during the oxidative addition process for either metal. Calculation of an approximate reaction co-ordinate by stepwise removal of I^- from $[CH_3(CO)_2I_3]^-$, has suggested that this co-ordination can proceed without a barrier.

When iodide co-ordinates to the vacant axial site, the effects described above are partially cancelled as the complex shifts back to an anionic species. The negative charge at the metal centre increases which favours π over σ bonding and the metal–ligand geometry changes accordingly. M–I and C–O bonds are both weakened and the bond lengths increase back toward similar values found in the M(I) complexes. M–CO bonds are strengthened exhibiting a small length decrease. The observed carbonyl frequencies for this species are consistent with the predicted geometric and electronic structure changes. The terminal ν(CO) bands for $[CH_3Ir(CO)_2I_3]^-$ at 2098 and 2045 cm^{-1} lie between those of the four and five co-ordinate complexes.

The valence electronic structure of the final alkyl product is shown schematically in Figure 5.17. To a first approximation, the metal–alkyl bonding can be described by the orbital interactions between an open-shell $[M(CO)_2I_3]^-$ fragment and a methyl radical. The most important bonding interaction is between a singly occupied metal d_{z^2}-type orbital and the singly occupied HOMO on CH_3 ($2\sigma_{CH_3}$). In the full MO scheme this combination gives the highest energy occupied orbital incorporating CH_3 character, $12A'$. The metal component is derived from a mod-

ification to the lower energy donor orbital $7A_1$ in $[M(CO)_2I_2]^-$. $8A_1$, which incorporated a large d_{z^2} component in the reactant nucleophile, changes its character in the product to become solely involved in M–I bonding ($13A'$). The metal orbitals change their function as the oxidative addition proceeds. In the entrance channel to nucleophilic substitution the higher energy orbital with the largest radial lobes is most important, since this is closer matched in energy with the LUMO and can interact at greater distances from the other occupied d orbitals to minimize the exchange repulsion. In the product a more favourable bonding is achieved with the smaller lobes of the lower energy d_{z^2} orbital which can concentrate density more efficiently in the bonding region between metal and carbon.

In addition to a half-filled σ orbital, the methyl radical has three fully-occupied bonding orbitals. $1\sigma_{CH_3}$ is dominated by a large $2s$ component on carbon, with smaller in-phase $1s$ contributions from each of the hydrogens. In the valence scheme this is the lowest CH_3 orbital, $2A'$. Situated above the CO π^* acceptor orbitals are two π_{CH_3} orbitals, $7A''$ and $9A'$. The influence of these orbitals on the M–CH_3 bond is primarily stabilizing as electron density is donated from π_{CH_3} to empty orbitals on the metal. The occupied $1\sigma_{CH_3}$ orbital will on the other hand destabilize the M–CH_3 bond since this will be involved in repulsive interactions with the metal electrons. Ziegler has cited the main reason for the instability of M–CH_3 bonds in saturated metal methyl complexes as being due to a four-electron two-orbital repulsive interaction between $1\sigma_{CH_3}$ ($2A'$) and the M–CH_3 σ-bonding orbital ($12A'$) [247, 248]. In this interaction the energy of $1\sigma_{CH_3}$ is lowered, at the expense of a larger destabilization to $12A'$, and consequently a net destabilization to the M–CH_3 bond. This was related to the polarity of the $M^{\delta+}$—$C^{\delta-}$ σ bond, where it was argued that higher polarities would afford the greatest stabilities. This is supported by the fact that the early first row transition metals form stronger M–CH_3 bonds than their middle to late transition metal analogues on account of their reduced electronegativity and d electron populations. From our detailed orbital analysis it is difficult to identify any change in the orbital populations as being uniquely associated with the different reactivities of Rh and Ir alkyl complexes. It should also be noted that these arguments were originally devised to rationalize trends in bond strengths of neutral and positively charged first row transition metal alkyls. Nevertheless, it follows from Table 5.10 that we do note a different polarity in the Rh–C and Ir–C bonds. The difference is most significant in $[CH_3M(CO)_2I_3]^-$ where Cα is more negatively charged than the metal centre by 0.03 and 0.12 for M=Rh and M=Ir, respectively. Hence, this analysis would suggest that the rhodium species suffers from larger destabilizing interactions to the M–CH_3 bond.

In both the five and six co-ordinate metal alkyl complexes, the iridium metal centre is predicted to hold a smaller negative charge than rhodium. This is an indication that the $5d$ metal is more easily oxidised. Inspection of the orbital populations in

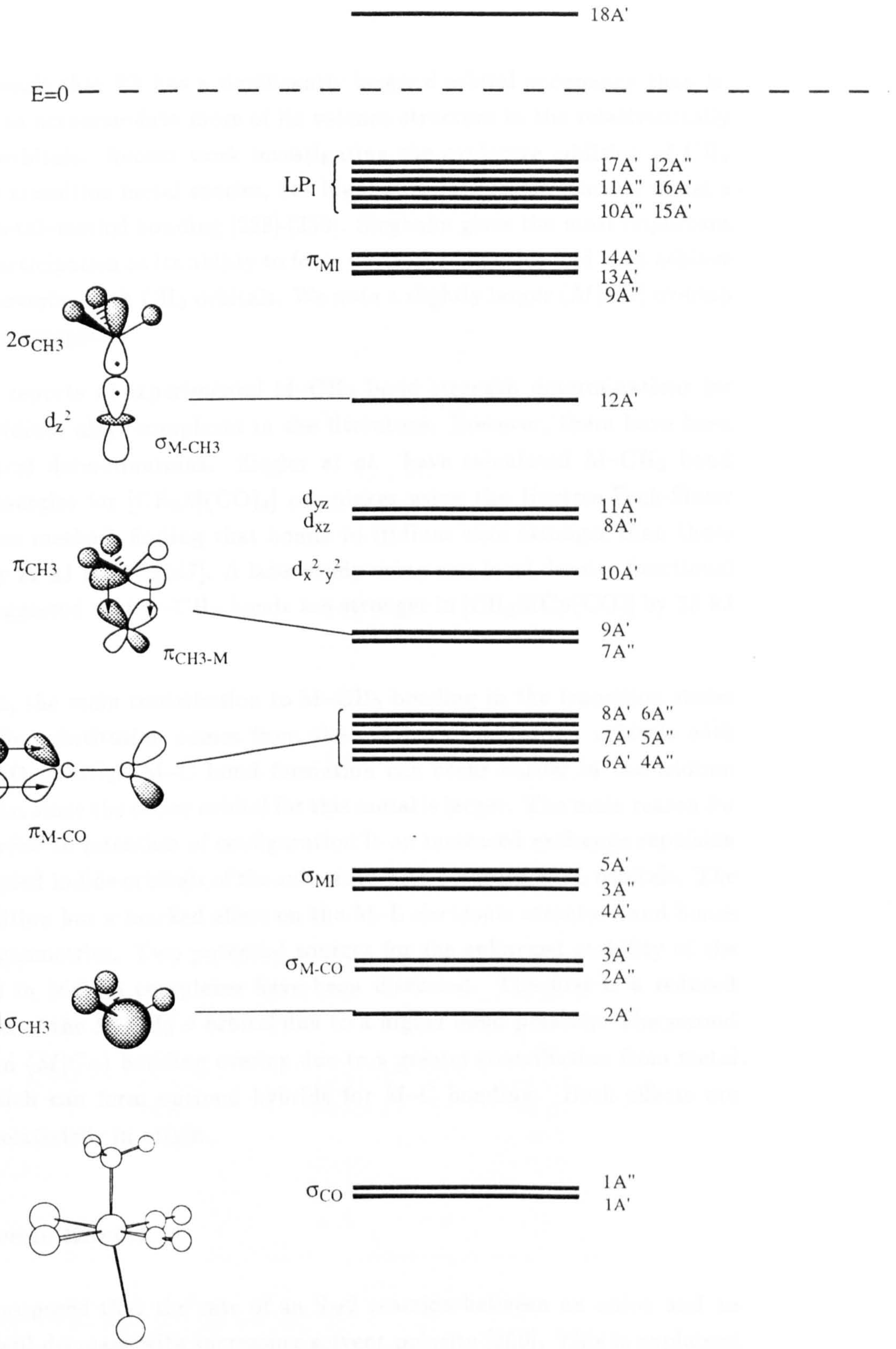

Figure 5.17: Valence MO scheme of $[CH_3M(CO)_2I_3]^-$. Orbital counting begins with the lowest valence MO.

Table 5.10, reveals that Rh has a significantly larger *d* orbital occupancy than Ir, which prefers to accommodate more of its valence structure in the relativistically contracted *s* orbitals. Recent work investigating the oxidative addition of CH_4 to second row transition metal species, has highlighted the importance of metal *s* electrons in metal–methyl bonding [228]-[233]. Siegbahn gives the most important reason for *s* participation as its ability to form optimal *sd* hybrids and thus achieve more efficient overlap with CH_3 orbitals. We note a slightly larger $\langle M|C\alpha\rangle$ overlap for the iridium complexes.

There are no reports of experimental M–CH_3 bond strength determinations for rhodium or iridium alkyl complexes in the literature. However, there have been some theoretical determinations. Ziegler *et al.* have calculated M–CH_3 bond dissociation energies for $[CH_3M(CO)_4]$ complexes using the Hartree-Fock-Slater transition state method, finding that bonds to iridium were stronger than those to rhodium by 22 kJ mol^{-1} [247]. A later study using non-local density functional theory, has suggested that Ir–CH_3 bonds are stronger in $[CH_3MCp(CO)]$ by 33 kJ mol^{-1} [249].

To summarize, the main contribution to M–CH_3 bonding in the transition states for nucleophilic substitution comes from the overlap of metal d_{z^2} orbitals with the σ^*_{CI} LUMO of CH_3I. M–C bond formation can occur earlier in the iridium transition state, since the donor orbital for this metal is larger. The main reason for the larger barrier to retention of configuration is an increased exchange repulsion between occupied iodide orbitals of the substrate with occupied M–L orbitals. The oxidative addition has a marked effect on the M–L electronic structure and hence on the M–L geometries. Two potential sources for the enhanced stability of the M–CH_3 bond in iridium complexes have been discussed. The first is a reduced destabilization of the M–CH_3 σ orbital due to a higher bond polarity. The second is an increased $\langle M|C\alpha\rangle$ bonding overlap due to a greater contribution from metal *s* orbitals which can form optimal hybrids for M–C bonding. Both effects are presumably relativistic in origin.

5.3.6 Solvent Effects

It has been proposed that the rate of an S_N2 reaction between an anion and an alkyl halide will decrease with increasing solvent polarity [250]. This is explained in terms of the change in charge between the reactants and the transition state. In the reactant complex there is expected to be localised charge on one of the groups ($Y^{-}\cdots CH_3X$), whereas in the TS this charge is dispersed ($Y^{\delta-}\cdots CH_3\cdots X^{\delta-}$). Hence, a polar solvent should stabilize the reactant more than the TS, leading to an increase in the activation barrier and a decrease in the rate. These qualitative arguments are based on studies of organic reactions but can also be applied to the reactions of transition metal nucleophiles. However, the experimental obser-

Table 5.10: Mulliken population analysis of the transition metal complexes involved in the oxidative addition reaction. Shown are the charges on the fragments, the metal *s*, *p* and *d* gross orbital populations and the metal–carbon overlap populations. The analysis is based on the optimized RHF/DZ geometries with the larger DZ* basis.

	$[M(CO)_2I_2]^-$	$[CH_3M(CO)_2I_2]$	$[CH_3M(CO)_2I_3]^-$
		M=Rh	
Q_M	−0.36	−0.26	−0.42
s	0.50	0.38	0.37
p	0.66	0.88	1.15
d	8.20	8.00	7.90
$Q_{(CO)}$[a]	+0.37	+0.55	+0.58
Q_I[b]	−1.01	−0.46	−0.71
Q_I[c]	-	-	−0.47
Q_{CH_3}	-	+0.17	+0.02
$Q_{C\alpha}$	-	−0.35	−0.45
$\langle M\|C\alpha\rangle$	-	0.19	0.22
		M=Ir	
Q_M	−0.37	−0.23	−0.36
s	0.58	0.46	0.45
p	0.73	0.93	1.17
d	8.06	7.84	7.74
$Q_{(CO)}$[a]	+0.34	+0.51	+0.53
Q_I[b]	−0.97	−0.43	−0.68
Q_I[c]	-	-	−0.47
Q_{CH_3}	-	+0.15	−0.02
$Q_{C\alpha}$	-	−0.38	−0.48
$\langle M\|C\alpha\rangle$	-	0.20	0.23

[a]Charges summed for both carbonyl ligands.
[b]Charges summed for both iodide ligands.
[c]Charge on the iodide ligand *trans* to the CH_3 group in $[CH_3M(CO)_2I_3]^-$.

vations for oxidative addition of CH_3I to $[M(CO)_2I_2]^-$ complexes do not support such a simple theory. For the rhodium process, a five-fold increase in rate has been observed on going from methyl acetate to methanol [54], whereas in the iridium system, the opposite behaviour is observed, with increasing solvent polarity generally causing a small rate decrease [67].

The self-consistent reaction field (SCRF) model has been applied to the stationary points and to several intermediate points along the reaction co-ordinates for TSinv(Rh) and TSinv(Ir). In this way, new potential energy profiles have been constructed in static media of different dielectric strength. Figure 5.18 shows the rhodium reaction path for a vacuum ($\epsilon_r = 1.0$), CH_3I ($\epsilon_r = 7.0$), CH_3OH ($\epsilon_r = 32.64$) and H_2O ($\epsilon_r = 78.54$). The zero of energy is taken as the RHF/SCRF energy for given ϵ_r, of the first point on the reactant side of the path. Several interesting features emerge:

- Each of the reaction fields creates a significant change in the gas phase profile, irrespective of the specified dielectric constant.
- The stabilization in the energy profile reflects the polarity of the particular medium: $H_2O > CH_3OH > CH_3I$. However, these differences are small compared to the change on going from a vacuum to any of the condensed media with $\epsilon_r > 1$.
- The position of the TS is displaced slightly earlier along the reaction co-ordinate.
- A new minimum exists on the product side at $rx \approx 1.0$.

Evidently, there is a general medium effect on the energetics of the nucleophilic substitution reaction. When a reaction field is introduced there is a marked change in the qualitative features of the energy profile, and the effect is not only limited to media with high dielectric constants. These observations can be understood by re-examining the evolution of the Mulliken charges along the gas phase reaction co-ordinates, Figure 5.16. The negative charge on the reactants is spread over the iodide ligands and the metal atom, with the carbonyl groups holding a net positive charge. CH_3 and I are essentially neutral. Thus, charge separation in the reactant complex occurs in the plane of $[Rh(CO)_2I_2]^-$. The reaction fields cause a modest stabilization of the reactants, amounting to about 10 kJ mol^{-1}. As the reaction progresses the charge separation in the square plane is superseded by that in the C_s addition plane. In the late transition state, the iodide leaving group holds a substantial negative charge ($Q_I = -0.79$) and is separated from the positive methyl group ($Q_{CH_3} = +0.33$) by *ca.* 3.2 Å. The strongly polarized TS therefore has a large dipole moment ($\mu_{RHF} = 11.5$ D), which leads accordingly to a stabilization of *ca.* 50 kJ mol^{-1} when a solvent reaction field is applied. The gas phase

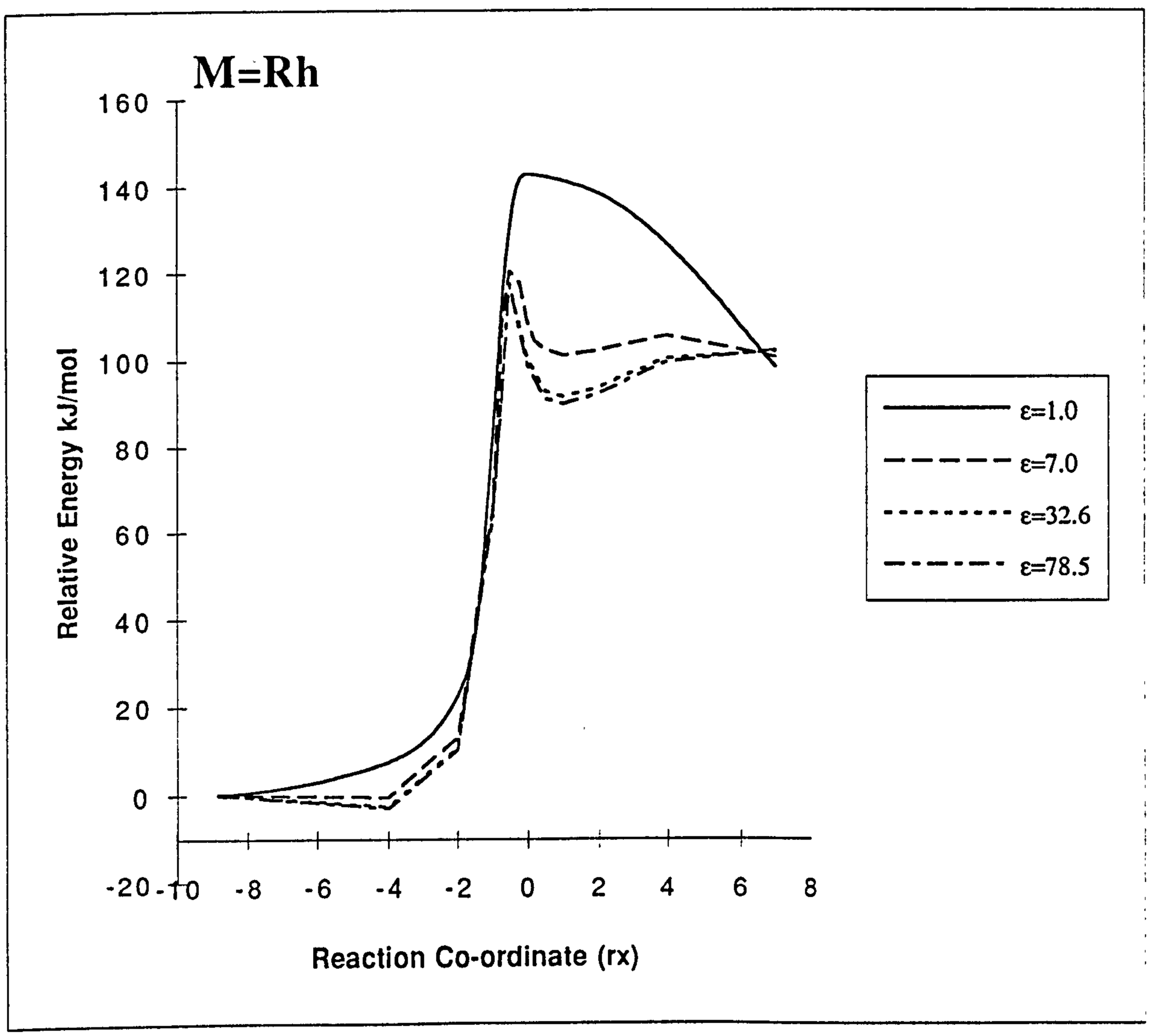

Figure 5.18: Effect of a static solvent medium on the RHF reaction co-ordinate for TSinv(Rh). Profiles corresponding to the gas phase ($\epsilon_r = 1.0$). methyl iodide ($\epsilon_r = 7.0$), methanol ($\epsilon_r = 32.63$) and water ($\epsilon_r = 78.54$) are shown. Data deduced from RHF/DZ SCRF calculations.

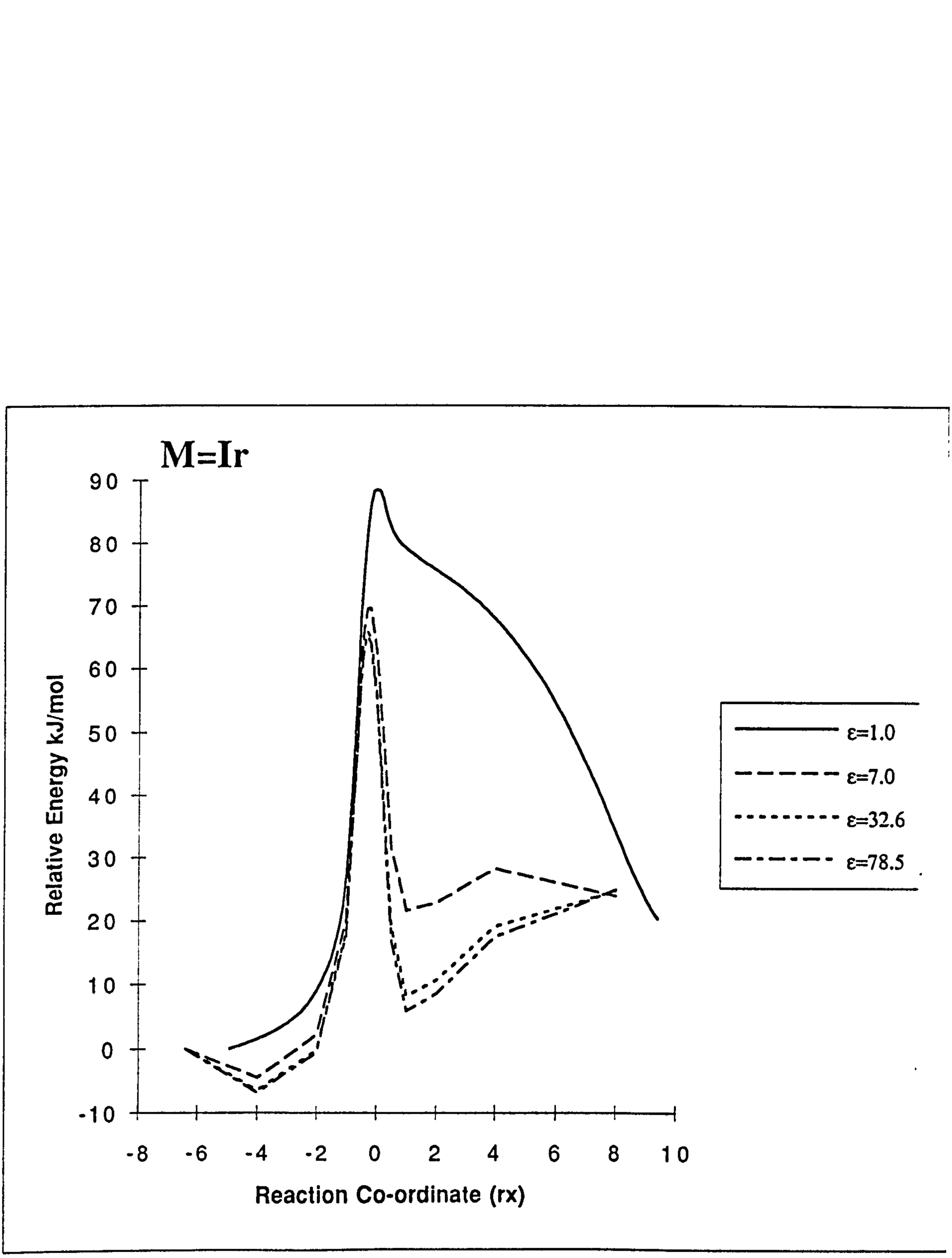

Figure 5.19: Effect of a static solvent medium on the RHF reaction co-ordinate for TSinv(Ir). Profiles corresponding to the gas phase ($\epsilon_r = 1.0$), methyl iodide ($\epsilon_r = 7.0$), methanol ($\epsilon_r = 32.63$) and water ($\epsilon_r = 78.54$) are shown. Data deduced from RHF/DZ SCRF calculations.

geometry of TSinv(Rh) at $rx = 0.0$ does not however, correspond to the highest energy conformation in the reaction fields. The RHF SCRF calculations predicts new maxima located earlier along the co-ordinate at $rx \approx -0.5$. This point corresponds to a geometry with Rh–Cα and Cα–I bond distances of *ca.* 2.52 and 2.87 Å, respectively. Stabilization of this conformation is still more than double that of the reactants, leading to a significant reduction in the barrier to nucleophilic substitution. It follows from Figure 5.18 and Table 5.11, that nucleophilic substitution in the rhodium system is predicted by the RHF SCRF method to have an activation barrier of *ca.* 120 kJ mol^{-1} in each solvent field. This stabilization differs from the qualitative view, since without a detailed theoretical knowledge of the geometry, the true late nature of the TS and the associated charge separation could not have been expected.

Table 5.11: Calculated relative energies for the oxidative addition of CH_3I to $[M(CO)_2I_2]^-$ in the presence of a solvent reaction field of dielectric constant ϵ_r. The activation barriers for the substitution reaction are calculated with respect to the point of lowest energy on the reactant side of the path. For the reverse barrier and the substitution reaction energy change, the ion-dipole product is assumed to be completely dissociated and we use the summed energies of $[CH_3M(CO)_2I_2]$ and I^-. The oxidative addition enthalpy change is calculated with respect to the separated reactants.
Energies in kJ mol^{-1}.

	RHF [a]				MP2 [b]	
ϵ_r	1.00	7.00	32.63	78.54	7.00	32.63
			TSinv(Rh)			
$\Delta E_f^{\ddagger}$	+146.0	+121.0	+120.3	+120.1	+69.2	+63.5
$\Delta E_b^{\ddagger}$	(+50.7)[c]	+92.3	+114.2	+117.5	+50.7	+104.2
ΔE_{sub}	(+95.4)[c]	+28.7	+6.1	+2.6	+18.5	−40.7
ΔE_{add}					−64.2	−60.7
			TSinv(Ir)			
$\Delta E_f^{\ddagger}$	+92.2	+74.0	+72.2	+71.9	+54.9	+53.6
$\Delta E_b^{\ddagger}$	(+71.9)[c]	+119.0	+140.0	+141.6	+70.3	+92.3
ΔE_{sub}	(+20.3)[c]	−45.0	−67.8	−69.7	−15.4	−38.7
ΔE_{add}					−87.6	−89.4

[a]RHF SCRF energy data deduced from DZ basis calculations.

[b]MP2 SCRF energy data for the rhodium system deduced from DZ basis calculations on geometries taken from the RHF/DZ reaction co-ordinate. MP2 SCRF energy data for the iridium system deduced from DZ2 basis calculations on geometries taken from a RHF/DZ2 reaction co-ordinate.

[c]The combined energy of the *separated* products in the gas phase is higher than the energy of the TS. The numbers in parentheses are the gas phase values calculated with respect to the product ion-dipole complex.

The solvent field has an even larger influence on the gas phase energy profile leading to products. The greatest change is the stabilization of a substitution product $[CH_3Rh(CO)_2I_2]\cdots I^-$ with a shorter C$\alpha\cdots$I distance and a more linear Rh–C$\alpha\cdots$I geometry located at $rx \approx 1.0$. This would tend to suggest, that a solvent medium would aid dissociation of I^- away from Cα along an axis roughly perpendicular to the square plane. In addition, the specified polarity of the medium does appear to make a significant difference to the stability of the species in this region. For example, the energy of the complex at $rx = 1.0$ is lower in CH_3OH than CH_3I by *ca.* 10 kJ mol^{-1}. In the region $rx > 1.0$ the gas phase RHF IRC is probably not sufficient to give a qualitative description of the process occurring in the condensed phase because it does not incorporate the geometry of a $[CH_3Rh(CO)_2I_2]$ species which is separated by a large distance (> 3.0 Å) from I^-. We have therefore performed extra computations on the two *isolated* substitution products in the different media. For the interaction of the dipole of the neutral rhodium species with the solvent medium, the usual SCRF method has been used. For I^-, which does not have a dipole moment, the solvation energy has been estimated from an expression based on the simple Born treatment of a point charge in a spherical cavity [246]. In SI units the monopole energy of a charge Q in a medium of dielectric constant ϵ_r, can be written:

$$\Delta E_Q = -\frac{1}{2}\left(1 - \frac{1}{\epsilon_r}\right)\frac{1}{4\pi\epsilon_0}\frac{Q^2}{a_0}. \qquad (5.4)$$

The effective cavity radius a_0 is calculated in the same way as for the SCRF procedure. Adding the Born term to the gas phase energy of I^- and combining this with the energy for $[CH_3Rh(CO)_2I_2]$ derived from the SCRF calculation, yields an approximate energy for the solvated products. In this way new values of the barrier for the back reaction to nucleophilic substitution of $[M(CO)_2I_2]^-$ on CH_3I (i.e. the barrier for nucleophilic attack of I^- on the methyl group of $[CH_3M(CO)_2I_2]$), $\Delta E_b^{\ddagger}$, and the substitution reaction exothermicity, ΔE_{sub}, in the different media have been estimated, Table 5.11. Note that this analysis assumes a solvent medium will assist *complete* dissociation of the products into separate $[CH_3Rh(CO)_2I_2]$ and I^- fragments. The reverse barrier to nucleophilic substitution is raised substantially in the solvent fields. $\Delta E_b^{\ddagger}$ is significantly larger in CH_3OH and H_2O (114–118 kJ mol^{-1}) than in CH_3I (92 kJ mol^{-1}). This stabilization results in the substitution reaction becoming essentially thermoneutral in the more polar solvents.

Solvent effects on the reaction co-ordinate for iridium have also been examined, Figure 5.19. For this system, the RHF SCRF calculations predict a slightly smaller effect on the energy and location of the TS. The forward energy barrier is reduced by *ca.* 20 kJ mol^{-1} and the maximum is relocated at $rx = -0.3$. This correlates with the smaller dipole moment in TSinv(Ir) ($\mu_{RHF} = 10.0$). The reverse barriers are elevated as for rhodium, with new minima likewise occurring at $rx = 1.0$. Values of $\Delta E_b^{\ddagger}$ computed with respect to the dissociated products, range from 119

kJ mol^{-1} in CH_3I to 142 kJ mol^{-1} in H_2O, and the five co-ordinate iridium alkyl complex is predicted to be stable with respect to the starting materials in each medium.

A more expensive MP2 SCRF algorithm is implemented in GAUSSIAN for estimating solvation energies at the correlated level [165]. We have used this method to investigate the combined effect of electron correlation and a solvent field on the reaction pathways. Recall that the approximate MP2/DZ* gas phase reaction co-ordinate for rhodium (Figure 5.6) led to a forward barrier which was still 35 kJ mol^{-1} higher than experimental solution values. The TS was also predicted to be later than the RHF structures, exhibiting a significantly bent Rh–Cα–I geometry. MP2/DZ SCRF calculations of several points on the RHF reaction path yield the rather different energy profiles shown in Figure 5.20a. The solid line representing the reaction in CH_3I, describes a sharp maximum at $rx = -0.5$, stabilization of an ion-dipole complex at $rx = -4.0$ and a minimum on the product side at $rx = 0.0$. The forward barrier is estimated to be 69 kJ mol^{-1}. Considering the approximate nature of the technique, this value is in good quantitative agreement with the experimental solution values ($\Delta H^{\ddagger}_{exp} \approx 55$ kJ mol^{-1}, Table 5.1). Calculation of the separated products at this level, gives a smaller barrier for the assumed back reaction of *ca.* 51 kJ mol^{-1}. The reaction is therefore predicted to be an endothermic process in the low polarity medium ($\Delta E_{sub} = 18$ kJ mol^{-1}).

Next, inspecting the dashed profile representing the reaction in CH_3OH, a slightly smaller forward barrier of 63 kJ mol^{-1} can be interpolated. The MP2 SCRF scheme predicts that the barrier for the back reaction is *doubled* upon moving from CH_3I to CH_3OH; $\Delta E^{\ddagger}_{b}$ is raised dramatically to 104 kJ mol^{-1} and the substitution reaction becomes exothermic by 41 kJ mol^{-1}. Thus, on the basis of these results, competition to nucleophilic substitution of $[Rh(CO)_2I_2]^-$ on CH_3I from the reverse process of nucleophilic attack of I^- on the neutral five co-ordinate alkyl complex would be expected to be significantly reduced when a more polar medium is employed.

For the quantitative analysis of the correlation and medium effect in the iridium system a slightly different procedure has been employed; namely, the use of the semi-core DZ2 basis to compute, a new RHF reaction co-ordinate, and the MP2 SCRF energies of the selected points along this path. Our choice of ECP for this sytem is based primarily on the performance of the full and semi-core bases in conjunction with the RHF method for optimizing equilibrium complexes (chapter 4). For rhodium, the conventional DZ basis appeared to give the most accurate geometrical parameters. For iridium however, comparison of the computed structures with experimental data suggested that the DZ basis was generating Ir–C bond lengths which were consistently too long by *ca.* 0.1 Å. More accurate values were obtained by moving to the semi-core ECP. Extension to the DZ2 basis for iridium is therefore necessary so that the reaction path includes structures which

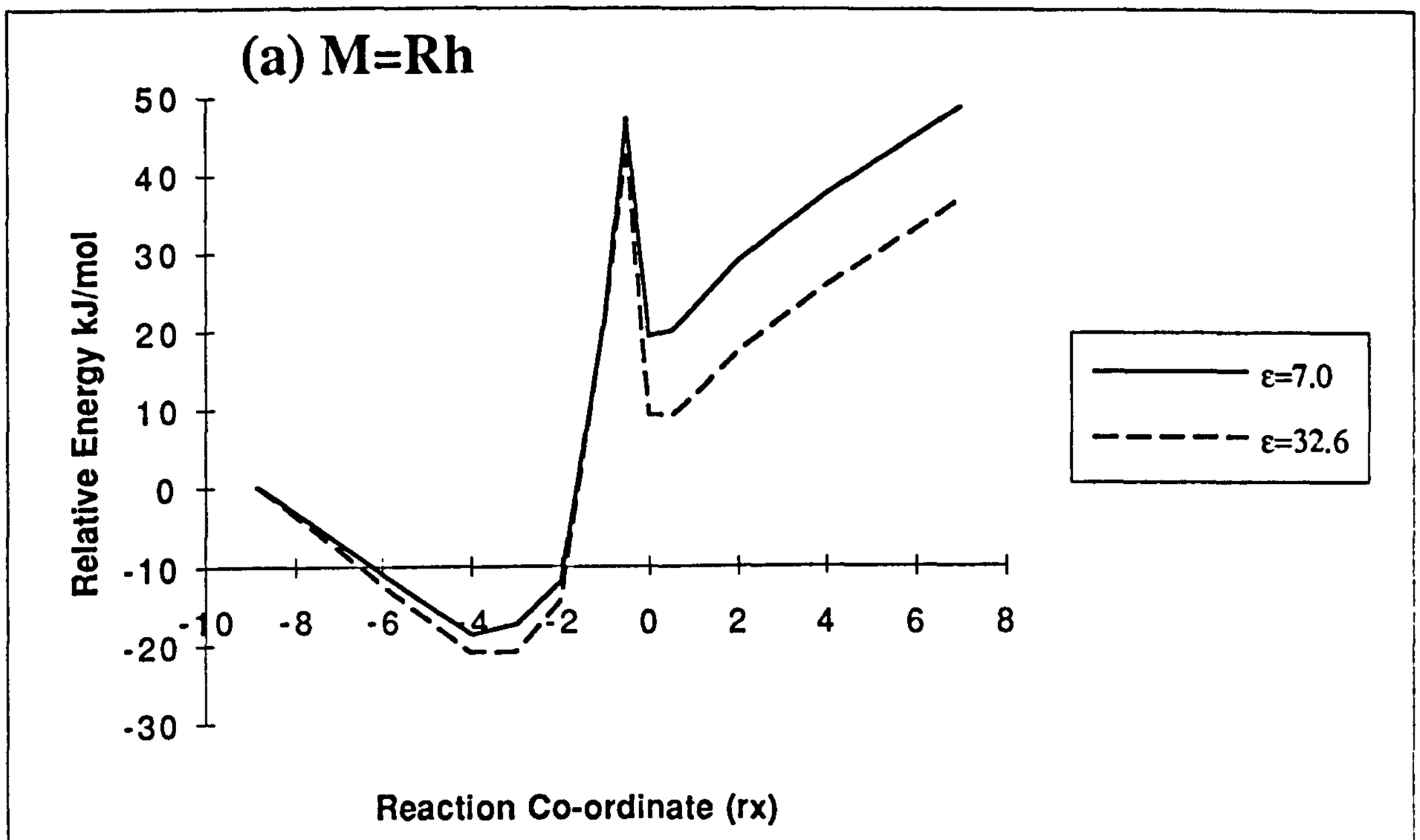

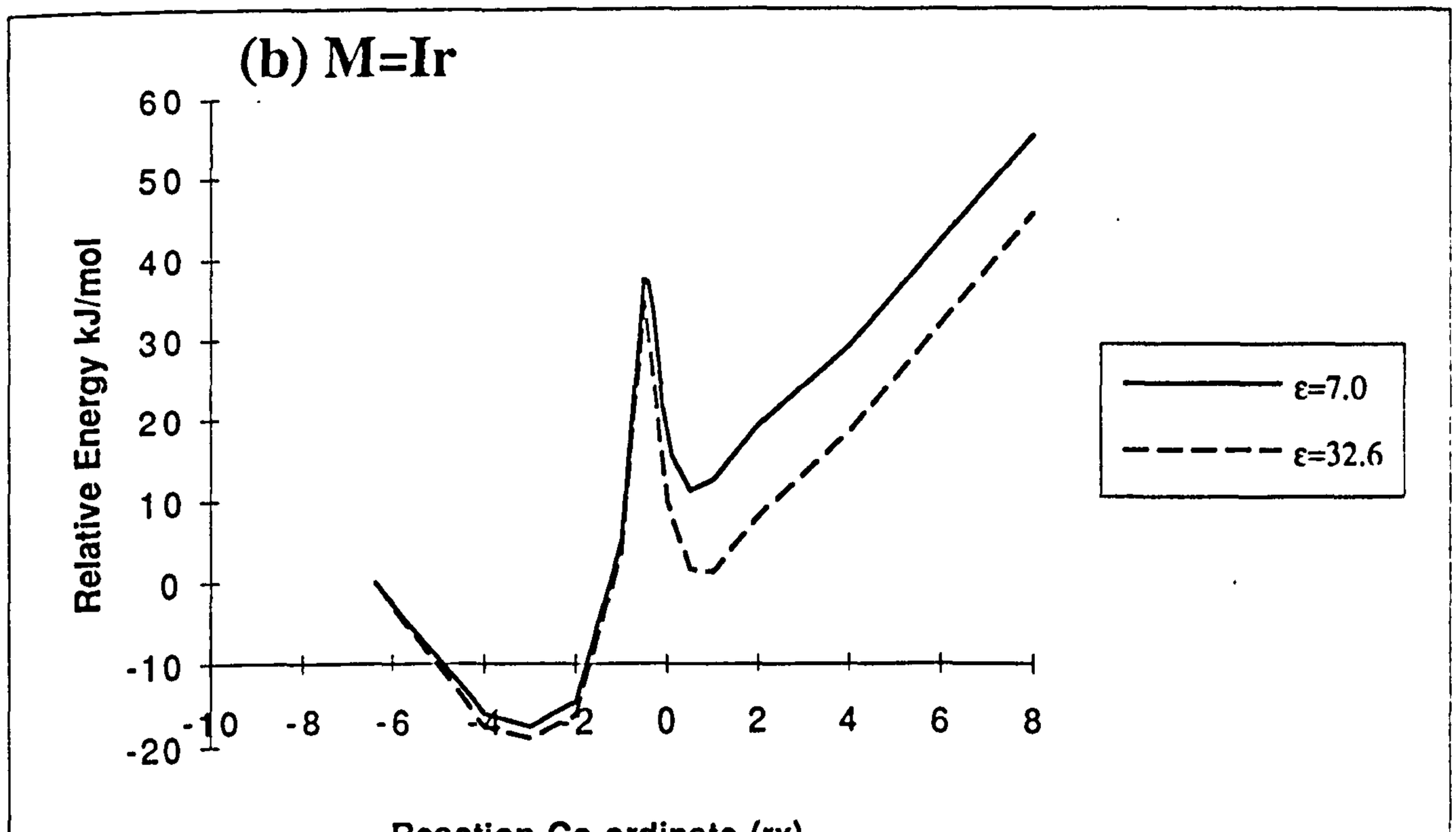

Figure 5.20: Combined effect of a solvent field and MP2 electron correlation on the RHF reaction co-ordinate for (a) TSinv(Rh) and (b) TSinv(Ir). Solvent parameters corresponding to CH_3I and CH_3OH have been used. Also shown for comparison are the RHF gas phase reaction co-ordinates. Data for rhodium deduced from DZ basis calculations. Data for iridium deduced from DZ2 basis calculations.

adequately describe the critical M–C bond formation. There is also some evidence to suggest that the ECP without the outermost core orbitals can overestimate the correlation energy [245]. Preliminary calculations on the DZ path for TSinv(Ir) suggested that this was the case, with MP2/DZ SCRF corrections yielding estimates of the barrier which were too low by *ca.* 15 to 25 kJ mol^{-1}.

Computed reaction co-ordinates incorporating electron correlation and medium effects for the iridium system are shown in Figure 5.20b. The solid line representing the reaction in a CH_3I medium, is similar to the profile calculated for rhodium. The location of the maximum is slightly more central between the two minima indicating that the iridium TS is earlier, in line with the previous gas phase calculations. The transition structure at the new maximum has a forming Ir–CH_3 bond distance of 2.65 Å, and a C–I leaving group distance of 2.74 Å. The latter is very close to the leaving group distance computed at the MP2/DZ level in the TS for the identity S_N2 reaction between CH_3I and I^- (Table 5.3). This correlates with similar values of the measured and computed KIEs for $[Ir(CO)_2I_2]^-$ and I^- and is a further indication of the similar nucleophilicities of these species with respect to C–I activation. The activation barrier of 55 kJ mol^{-1} predicted for the forward substitution reaction (Table 5.11) is in excellent agreement with experiment but is lower than the barrier computed for rhodium by 15 kJ mol^{-1}. Nucleophilic substitution in the iridium system is predicted to be an exothermic process, even in the low polarity medium ($\Delta E_{sub} = -15$ kJ mol^{-1}). This is consistent with the experimental observation that $[CH_3Ir(CO)_2I_2]$ can be prepared in dichloromethane ($\epsilon_r = 9.1$), existing as either a stable solvate or dimer, and reacts with I^- to give only $[CH_3Ir(CO)_2I_3]^-$ [67].

Moving to the higher polarity CH_3OH medium appears to have a negligible effect on the forward activation barrier, but increases the reaction exothermicity by about 20 kJ mol^{-1}. This increase is, however, significantly lower than the corresponding change computed for the rhodium system and only serves to reinforce an already dominant forward substitution process.

The MP2 SCRF data suggests that the proposed neutral S_N2 intermediate has different reactivity for the two metals: $[CH_3Ir(CO)_2I_2]$ is a relatively stable species in either low or high polarity media; $[CH_3Rh(CO)_2I_2]$ on the other hand, only appears to be stable in high polarity media such as methanol. These findings are compatible with the experimentally observed solvent effects on the rate of oxidative addition. In particular, the observed rate acceleration for rhodium in the presence of methanol [54] could be explained by a stabilization of the substitution products, inhibiting the reverse process of nucleophilic attack of I^- on the S_N2 intermediate. However, it should be stressed that such an explanation assumes loss of CH_3I would occur most favourably by I^- abstracting CH_3 directly from $[CH_3Rh(CO)_2I_2]$. It remains to be proven that an alternative lower energy pathway to *reductive elimination* of CH_3I (from $[CH_3Rh(CO)_2I_3]^-$, for example) does not

exist.

The dipole moments computed at the RHF level for the ground state complexes, $[M(CO)_2I_2]^-$ and $[CH_3M(CO)_2I_3]^-$, are small compared to the dipole moments in the S_N2 transition states. The energetics for the overall oxidative addition process are therefore not expected to have a substantial dependence on the polarity of the solvent medium. The MP2 SCRF estimates of the enthalpy changes shown in Table 5.11 confirm these expectations. In CH_3I, ΔE_{add} for rhodium is 3 kJ mol^{-1} smaller than the gas phase value obtained by full optimization of the separated reactants and alkyl complex. Incorporating a stronger CH_3OH field causes a further modest decrease. Similarly, the enthalpy change in the iridium system is only marginally affected by the solvent field. Here we note increases of 2 and 4 $kJmol^{-1}$ in media corresponding to CH_3I and CH_3OH, respectively. The predicted values are still in good agreement with the projected enthalpy changes obtained from extrapolated rate data.

The MP2 SCRF approach has yielded data which are in reasonable quantitative agreement with experiment. The only notable disparity, which has not been observed, is the prediction of a smaller activation barrier for oxidative addition in the iridium system. The maxima in the reaction profiles computed using the MP2 SCRF scheme correspond to transition structures which are slightly earlier than those optimized at the RHF level. This displacement should translate into slightly tighter TS geometries and therefore yield smaller KIEs. The RHF gas phase structures gave KIEs which were in general slightly larger than experiment, so the location of a maximum anywhere in the region $rx = -0.5$ to 0.0 will probably correspond to a good approximation for the geometry of the true transition state. The substantial and competing, correlation and medium effects that we have described suggest that this system is a very difficult one to model. Correlation pushes the TS to the product side of the reaction co-ordinate generating structures with late features such as long leaving group distances and bent M–Cα–I geometries. The solvent field, and probably to a lesser extent an extension of the basis set, are factors which tend to cement the interacting groups together and locate the TS earlier along the reactants side. In the gas phase some degree of non-linearity would therefore be expected to occur and the TS would be expected to be late and rather loosely bound. On the basis of the MP2 SCRF results, it would appear therefore, that the prediction of a linear TS in roughly the correct region of the reaction co-ordinate by the RHF gas phase calculations is fortuitous.

The rationale for the distortion in the MP2 gas phase structures raises an important question: is the lack of medium also the reason why the DFT transition states were late and bent? The distortion in these structures was, however, rather more pronounced and the effect also occurred at the HFS level which does not formally contain a correlation term in the exchange-correlation functional. To investigate this, single-point SCRF calculations on the RHF/DZ reaction path for TSinv(Rh)

were carried out at the LDA and Becke3LYP levels. The outcome of these calculations was spurious; the Becke3LYP functional predicted a curve with no saddle point, just a constantly rising energy, while the LDA energies of the selected points varied by as much as ± 200 kJ mol^{-1}. The reasons for this behaviour are unclear. It could be due to either an instability of the DFT SCRF code or that the DFT functionals employed for the present study are not suitable to compute this reaction. The latter could be true as a consequence of the late and product-like nature of the gas phase S_N2 TS, in particular, the loosely bound C···I fragment of the substrate. Recent studies have suggested that the capabilities of currently used functionals reach their limits in the region of weak molecular interactions [113, 114], and it is seems likely that this transition state is an example of such a system.

5.3.7 The Effect of Iodide

A large concentration of added iodide has been found to increase the rate of oxidative addition in the rhodium system by a factor of *ca.* 2 [42, 61, 62]. It was postulated that the rate enhancement was due to the presence of a small, steady state concentration of $[Rh(CO)_2I_3]^{2-}$, formed by co-ordination of I^- to $[Rh(CO)_2I_2]^-$. The rationale was based upon the concept that additional electron density enhances the nucleophilicity of the metal centre, thus promoting oxidative addition. There is however, no spectroscopic evidence to verify the existence of such a species.

All attempts at optimizing a structure for $[Rh(CO)_2I_3]^{2-}$ failed. Irrespective of the starting geometry, *cis* or *trans*, square pyramidal or trigonal bypyramidal, RHF, MP2 and DFT calculations all followed the same course in which the structure was found to rapidly dissociate an iodide ligand to reform $[Rh(CO)_2I_2]^-$. Incorporating diffuse functions in the basis (DZ+) to give a better description of the dianonic character did not result in different behaviour. Optimization in the presence of a solvent reaction field also dissociated I^-. The computational evidence therefore strongly suggests that the postulated tri-iodide is unstable and would not exist to any significant concentration in reaction mixtures.

However, this does not rule out the possibility of a stabilizing influence of I^- on the S_N2 transition state. The LUMO of TSinv(Rh) exhibits a fairly large acceptor lobe pointing toward the vacant site, *trans* to the forming M···CH_3 bond. Therefore, it does not seem unreasonable that iodide could co-ordinate to the metal centre at this juncture. We have fully optimized a TS with an extra iodide in this location at the RHF/DZ level, Figure 5.21. The weakly bound iodide ion has an optimized Rh–I distance (4.64 Å) which is much longer than expected for a co-ordinated ligand and is displaced toward the carbonyl side of the molecule making an angle of *ca.* 38° with the square plane. Interestingly though, this interaction causes a significant change in the Rh–Cα–I geometry; Cα–I is shortened by 0.27 Å, Rh–Cα

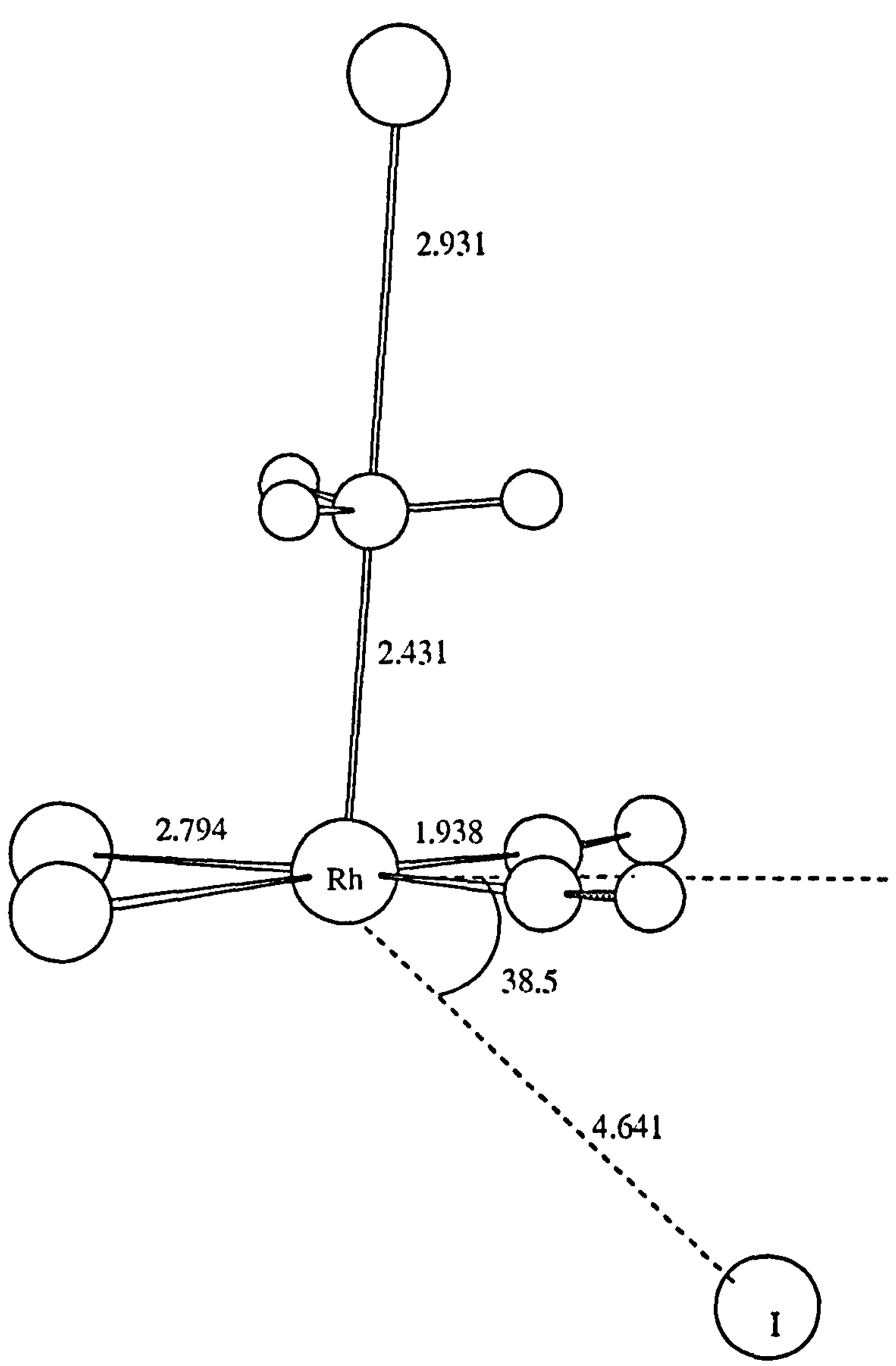

Figure 5.21: Optimized geometry of an S_N2 TS involving an extra iodide in the site *trans* to the forming $Rh\cdots CH_3$ bond.

is elongated by 0.24 Å and the deviation from linearity in the Rh–Cα–I axis is essentially removed. On the basis of this result, one might conclude that added iodide could cause the TS to be located earlier along the reaction path. However, the energy of this species is elevated relative to the combined energies of the fragments TSinv(Rh) and I^- by *ca.* 100 kJ mol^{-1}. Moreover, the influence of a solvent medium would be expected to favour a removal of weakly interacting I^- from the co-ordination sphere. Single-point RHF SCRF calculations on the fragments and composite molecule for a medium of dielectric strength $\epsilon_r = 7.0$ support this view, increasing the energy difference to 146 kJ mol^{-1}. The earlier geometry of this TS could be due to the field of the anion in this position causing a similar effect to that observed by introducing a solvent reaction field, as discussed in the previous section.

5.3.8 Substituent Ligand Effects

Siegbahn and co-workers have carried out a systematic investigation of ligand effects on C–H activation by second-row transition metal species [228]-[233]. A series of publications have led to a number of interesting conclusions concerning the electronic factors which govern metal–carbon bond formation and the stability of the metal–methyl complex. The conclusions most relevant to the present study are outlined below.

In the first of these studies, the reactivity between the naked transition metal atoms and methane was investigated [228]. It was found that the main state involved in the binding in the insertion products (CH_3MH) was the s^1 state. The *s* orbital is larger than the *d* orbitals and therefore has better overlap with the incoming orbitals. More importantly, the *s* orbital in the s^1 state can mix with the *d* orbitals and form optimal bonding hybrids. The second main conclusion from the early work was that in the transition state for C–H activation the s^0 state also plays a key role, since this is the state with least repulsion toward methane. It was argued that the presence of this low-lying state led to the lowest barriers for atoms to the right of the periodic table. In particular, the lowest barrier was found for rhodium and this has both low-lying s^0 and s^1 states.

In later studies, hydride and chloride ligands were employed to model the effects of covalent and electronegative ligands on the oxidative addition [230, 231]. For the metals to the right of the periodic table, substitution of a hydride by a halide was found to have a significant effect on both the barrier to addition and the stability of the insertion product. For example, replacing the hydride in $RhH(HCH_3)$ by a chloride ligand, $RhCl(HCH_3)$, led to a destabilization of this complex by *ca.* 60 kJ mol^{-1}. The transition state was also destabilized, resulting in a barrier increase of *ca.* 41 kJ mol^{-1}. The effect of halides on the products can be explained in terms of an increased cationic charge on the metal centre. The bonding s^1 state

is higher in energy for the cations than for the neutral atoms to the right, and therefore, the halide species will promote a smaller metal *s* population and form weaker M–C bonds than the more neutral metal hydride complexes. The elevation of the energy barrier observed for this substitution cannot be so easily interpreted. In the transition state region, Siegbahn argues that easy access to the s^0 state, which is the ground state of the cations to the right, is an advantage. One might therefore expect the halide complex to afford a lower barrier for C–H activation. However, the final size of the barrier is determined by a combination of how low the repulsion in the entrance channel is, and how strong the bonds are in the product.

Another interesting effect in the previous study was found when lone pair ligands were added [232]. It was found that for the atoms to the right, carbonyl ligands in general have a stabilizing effect on methane activation. This can be ascribed to a delocalisation of the repulsive *d* electrons whilst preserving the important *s* population at the metal centre.

In order to test if these hypotheses also apply to oxidative addition of C–I bonds to rhodium complexes, we have fully optimized the square planar reactants, the S_N2 transition states, and the alkyl products involved in the oxidative addition of CH_3I to $[Rh(CO)_2X_2]^-$ complexes, for X=I, Cl and H. The geometries are displayed in Figure 5.22. Single-point MP2/DZ calculations have been carried out on these geometries to obtain better quantitative estimates of the barrier heights and reaction energies. This data along with the metal *s* and *d* populations in the reactant complex $[Rh(CO)_2X_2]^-$ are presented in Table 5.12. For the sake of completeness, we also include the metal populations of the square planar tetracarbonyl[5] $[Rh(CO)_4]^-$. A transition state for the addition of CH_3I to this complex in the square planar geometry could not be located.

Table 5.12: Gross metal *s* and *d* orbital populations in the complexes $[Rh(CO)_2X_2]^-$. Also shown are the barrier heights $\Delta E_B^{\ddagger}$ and reaction energies ΔE_{add} for the oxidative addition of CH_3I to these nucleophiles. Note that *both* values have been calculated with respect to the separated reactants.

	Population[a]	$\Delta E_B^{\ddagger}$ [b]	ΔE_{add}^{b}
X=I	$5s(0.50)4d(8.26)$	+39.0	−61.5
X=Cl	$5s(0.47)4d(8.19)$	+47.2	−45.6
X=H	$5s(0.90)4d(8.30)$	−7.5	−148.3
X=CO	$5s(0.46)4d(8.65)$	-	-

[a]Population analysis based on RHF/DZ density.

[b]Energies deduced from MP2/DZ single-point calculations on RHF/DZ optimized geometries.

[5]Note that the tetracarbonyl $[Rh(CO)_4]^-$ is formally in a lower oxidation state (-I) and is expected to be tetrahedral since it is isoelectronic with 18-electron $[Ni(CO)_4]$.

(a) X=I

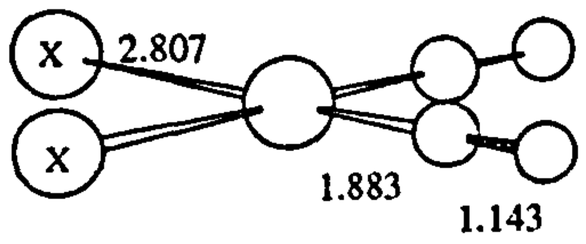

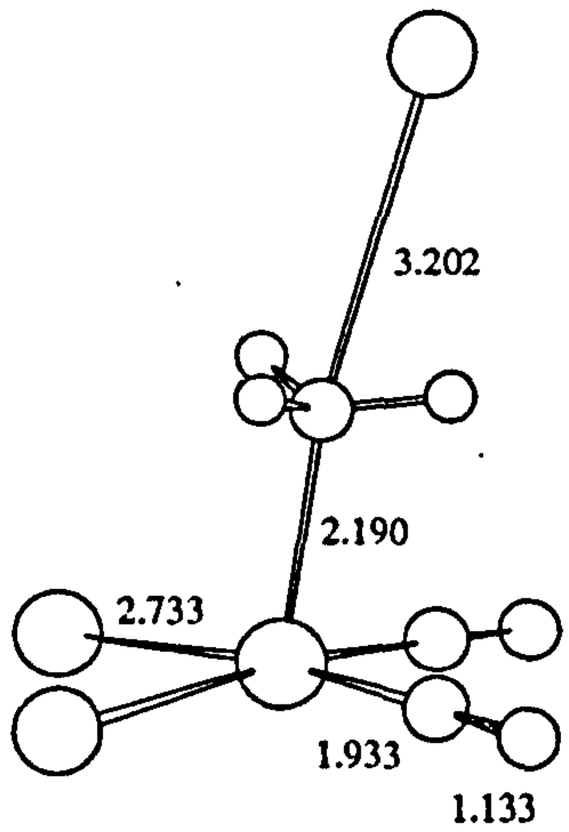

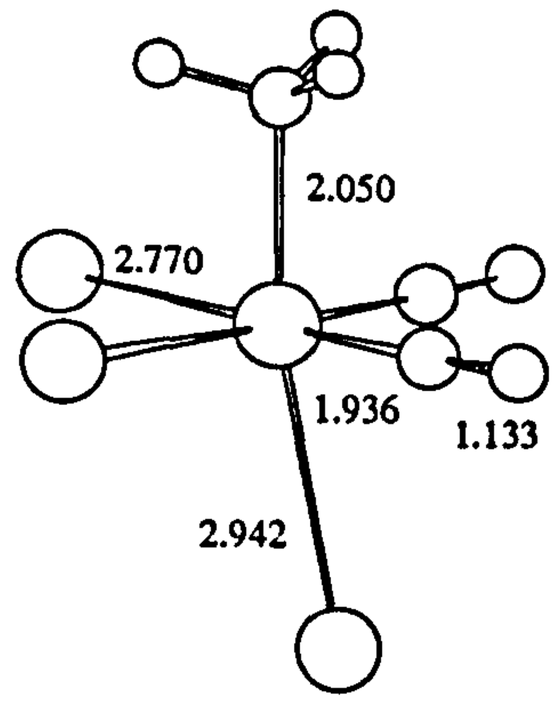

θ=9.2 β=99.7 γ=79.6

(b) X=Cl

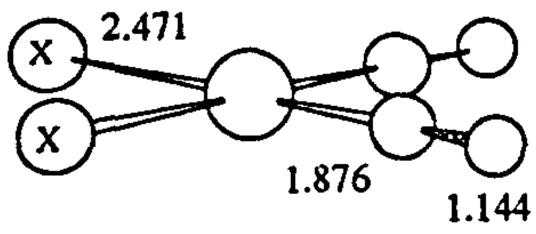

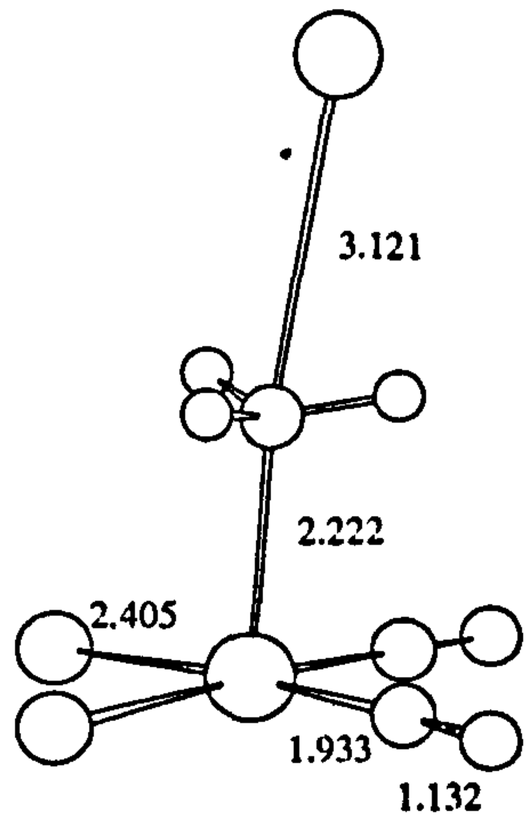

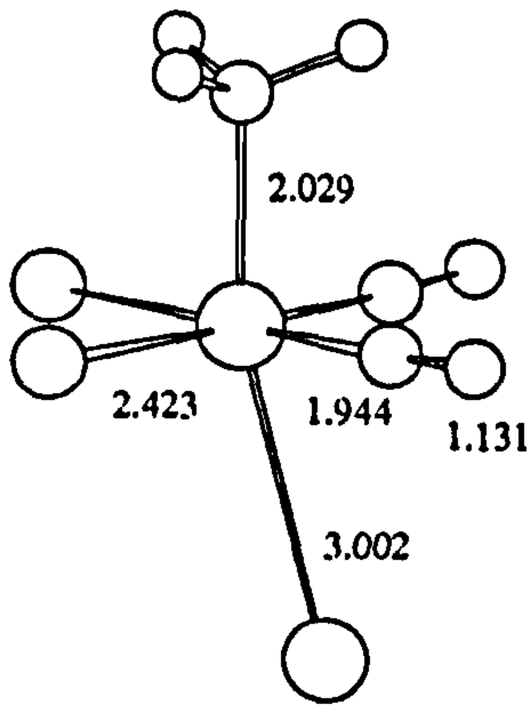

θ=5.8 β=95.2 γ=81.9

(c) X=H

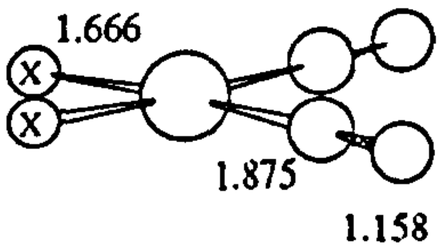

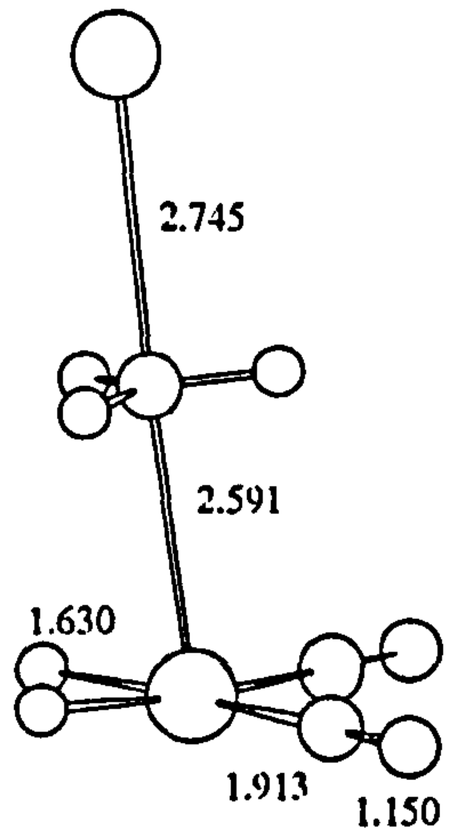

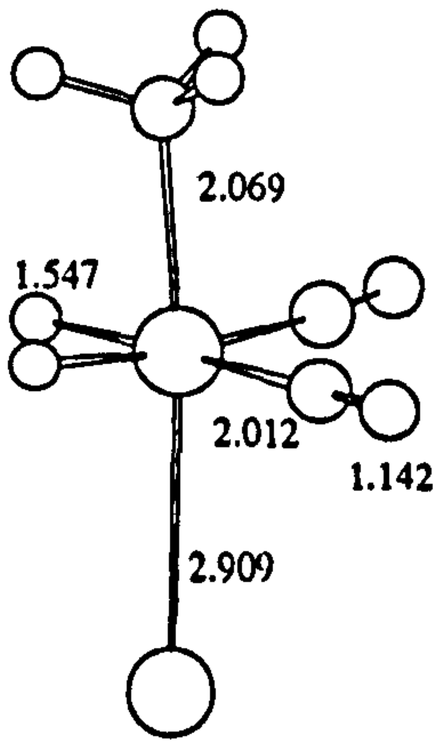

θ=1.8 β=80.3 γ=90.5

Figure 5.22: Optimized geometries of the reactant, TS and alkyl product for the reaction of CH_3I with $[Rh(CO)_2X_2]^-$, X=I, Cl and H. Parameters deduced from RHF/DZ optimizations.

First, the results of the population analysis are examined. Of the different ligands considered, hydrides appear to promote the largest metal valence *s* population. A greater covalent bonding leads to rhodium increasing its 5*s* population by 0.40 relative to that computed for $[Rh(CO)_2I_2]^-$. Replacing the iodide ligands by chlorides results in a much smaller change. In this case, the 5*s* population is decreased by 0.03 due to the greater electronegativity of the lighter halide. These population differences are consistent with the cationic promotion effect, described above. The tetracarbonyl has the smallest metal *s* population and the largest *d* population. Four mutually *trans* carbonyl ligands compete against each other for the metal *d* electrons, and thus, are not a good combination for efficient M–CO π back-donation. Such a high *d* population is expected to lead to instability of the metal complex. In fact, all known 18-electron four co-ordinate tetracarbonyls, only exhibit tetrahedral geometries in their ground states.

As we have theorized, promotion of the s^1 state should lead in principle to greater stability of the metal–carbon bond and therefore a more stable metal–alkyl product. This is indeed the case, with the hydride complex exhibiting both the highest rhodium 5*s* population and the largest computed exothermicity for the oxidative addition reaction. $[CH_3Rh(CO)_2H_2I]^-$ is stable by 148 kJ mol^{-1} relative to the separated reactants, as compared to the much lower exothermic energy change of 62 kJ mol^{-1} predicted for the analogous iodide system. Substituting the iodide ligands by chlorides leads to a small decrease in the reaction exothermicity, consistent with the slightly smaller metal *s* electron population. Surprisingly, the stabilities of the alkyl complexes are not reflected in the optimised M–CH_3 bond lengths, Figure 5.22. Even in the hydride alkyl complex which is substantially lower in energy, and the least sterically crowded, the computed M–CH_3 bond distance is comparable to that in the corresponding iodide species.

Next, we turn our attention to the optimized transition state geometries and the influence that ligand substitution has on the calculated energy barriers. Note that the *barrier heights* shown in Table 5.12, $\Delta E_B^{\ddagger}$, have been calculated with respect to the *separated* reactants and not from the ion-dipole minima. Experience suggests that complexation energies arising from the electrostatic interaction of the anionic charge on $[M(CO)_2X_2]^-$ with the dipole of CH_3I tend to be small and quite similar for each nucleophile (≈ -25 to -40 kJ mol^{-1}). It is therefore reasonable to infer relative reactivities from the barrier heights that we have computed. Replacement of the iodide ligands by chlorides leads to an earlier transition structure, as indicated by the slightly longer forming Rh–CH_3 bond and the shorter breaking C–I bond, Figure 5.22. However, this structural difference is modest and may be mainly due to a steric effect since the predicted energy barrier is still higher than the value computed for the bulkier $[Rh(CO)_2I_2]^-$ nucleophile. By contrast, hydride ligands have a marked effect on both the geometry and energy of the transition state. In this case, the S_N2 TS exhibits a linear geometry for the Rh–Cα–I fragment which

is tilted toward the hydride side of the complex. The CH_3 unit is displaced toward the iodide leaving group along the Rh–Cα–I axis by *ca.* 0.4 Å relative to the geometry found in the TS for iodide ligands. Hence, increasing the *s* population at the metal centre appears to leads to a much earlier transition state. At the MP2 level, the energy of this TS is lower than the energy of the separated reactants, $\Delta E_B = -7$ kJ mol^{-1}, suggesting that nucleophilic substitution of $[Rh(CO)_2H_2]^-$ on CH_3I could proceed without a significant barrier even in the gas phase.

The low-lying s^0 state of rhodium does not have an obvious stabilizing influence on the computed barrier heights. Chloride ligands which are expected to promote this state yield the least stable transition structures. The most important factor governing the ease of C–I addition to $[M(CO)_2X_2]^-$ complexes is therefore the effective population of the s^1 state. In this context it is interesting to recall the results of analyses carried out on the rhodium and iridium $[M(CO)_2I_2]^-$ nucleophiles reported in section 5.3.5. The iridium nucleophile was found to have a larger proportion of metal valence *s* electrons (Table 5.10) and a larger donor orbital (Figure 5.11). This appeared to lead to an earlier transition state and a smaller activation barrier. However, it should be noted that although the difference in transition state geometries are consistent with the experimental KIEs, a significant difference for the activation barriers has never been observed. It is possible that the low-lying s^0 state for rhodium is not described well theoretically and this is, in fact, the reason why the observed barriers are similar for both transition metals.

5.3.9 Reductive Elimination

Elimination of a CH_3 ligand from the metal centre in catalyst reaction mixtures could, in principle, occur by several different pathways. We have considered the four mechanisms depicted in Figure 5.23. The first, (a), is the reverse of the nucleophilic substitution mechanism, that is I^- abstracting CH_3 directly from the S_N2 intermediate $[CH_3M(CO)_2I_2]$. Figure (b) represents the reaction that could occur if I^- were to attack the methyl group of the six co-ordinate alkyl intermediate $[CH_3M(CO)_2I_3]^-$. Figures (c) and (d) represent intramolecular processes where mutually *cis* CH_3 and I ligands are eliminated from the co-ordination spheres of $[CH_3M(CO)_2I_3]^-$ and $[CH_3M(CO)_2I_2]$, respectively. Note that although each pathway involves the formation of CH_3I and a decrease in the oxidation state of the metal, only the last two mechanisms can be formally classified as *reductive elimination* reactions.

The transition structure for a reaction proceeding by the process (a), is, of course, the same structure shared by the forward nucleophilic substitution reaction (TSinv). MP2 SCRF calculations suggested that this reaction in the rhodium system would take place with a relatively low activation barrier for a low polarity medium, but that increasing the dielectric strength of the medium would significantly increase

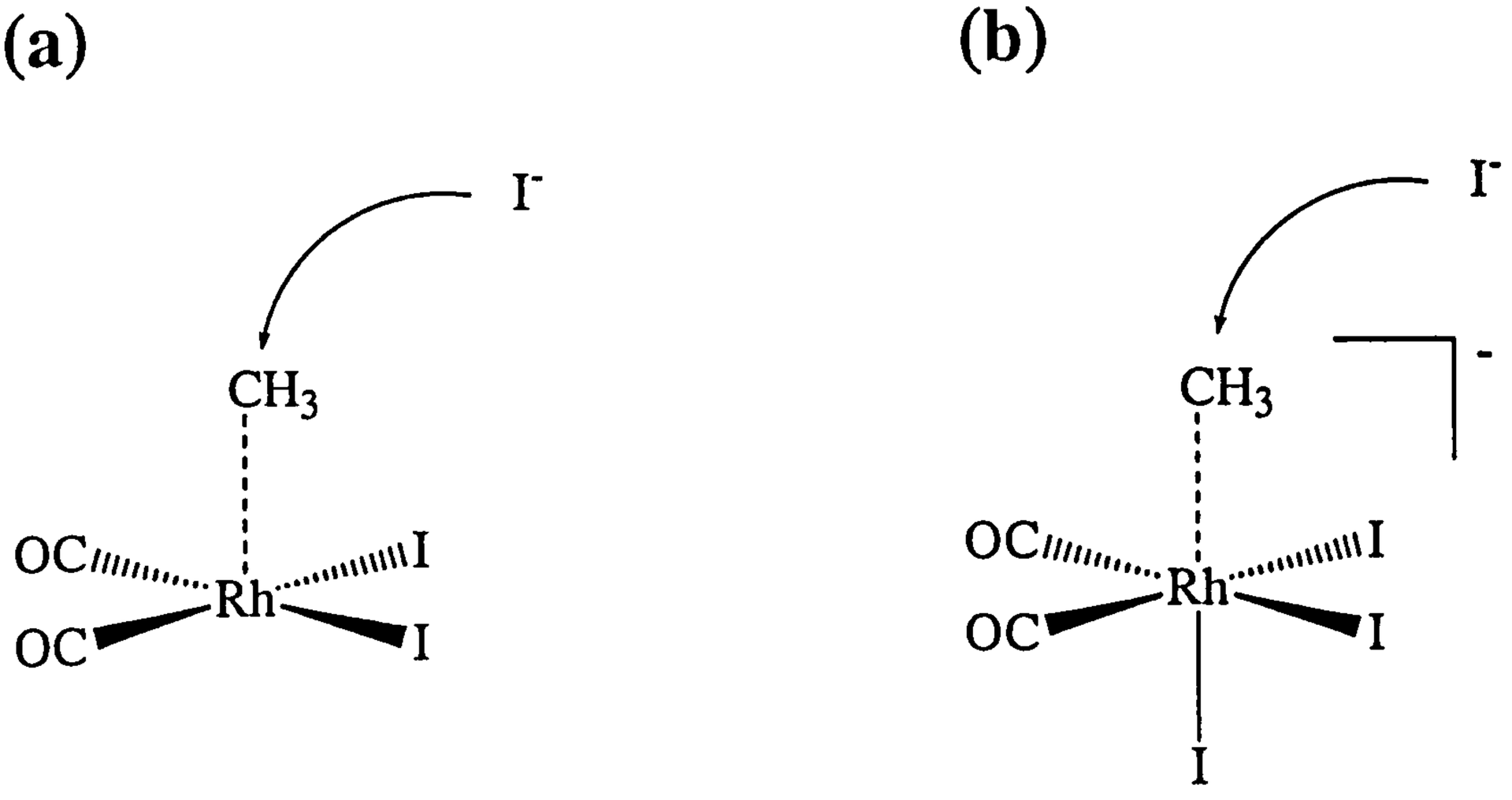

Figure 5.23: Proposed mechanisms of elimination of CH_3I; (a) nucleophilic attack of I^- on $[CH_3Rh(CO)_2I_2]$; (b) nucleophilic attack of I^- on $[CH_3Rh(CO)_2I_3]^-$; (c) concerted reductive elimination of CH_3I from $[CH_3Rh(CO)_2I_3]^-$; (d) concerted reductive elimination of CH_3I from $[CH_3Rh(CO)_2I_2]$.

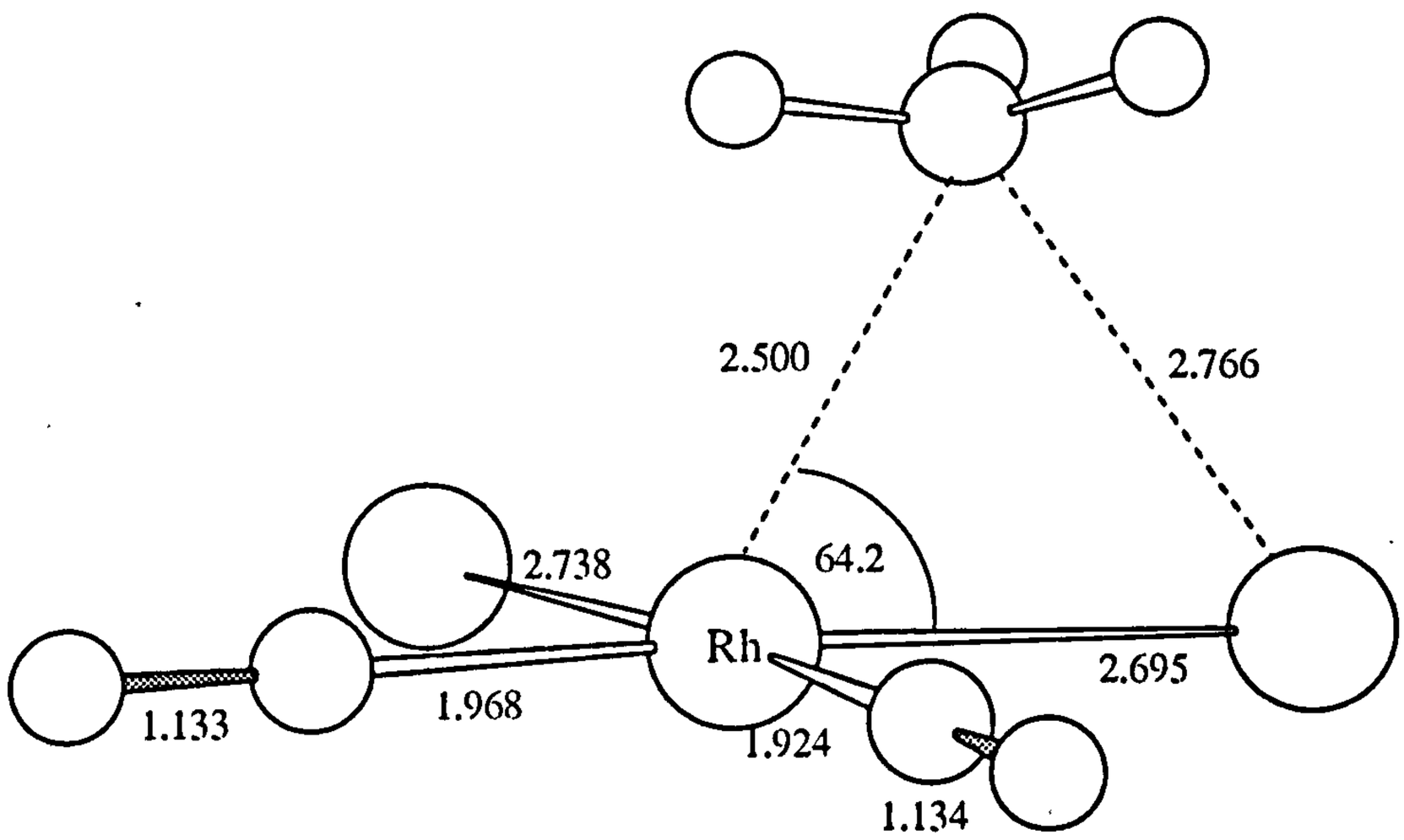

Figure 5.24: Geometry of the TS for intramolecular concerted reductive elimination of CH_3I from $[CH_3Rh(CO)_2I_2]$. Data deduced from RHF/DZ calculations.

this barrier. In the iridium system, nucleophilic substitution of $[Ir(CO)_2I_2]^-$ on CH_3I was predicted to dominate in both low and high polarity media. (See section 5.3.6.)

A stable transition state for an elimination of CH_3I from the six co-ordinate alkyl complex $[CH_3M(CO)_2I_3]^-$ could not be located, despite an extensive search of the potential energy surface. Initial calculations did reveal a transition structure involving a weakly interacting iodide in the site *trans* to CH_3 ($Rh\cdots I \approx 4.6$ Å) which could be related to the mechanism depicted in (b). (This is the same structure we located when investigating the effect of iodide on the S_N2 TS, Figure 5.21.) However, the energy of this conformation was at least 100 kJ mol^{-1} higher than the combined energies of the fragments TSinv(Rh) and I^-, and an electrostatic medium was found to favour complete dissociation of the iodide from this site.

Attempts to locate a saddle point for an intramolecular reductive elimination from the six co-ordinate alkyl complex, mechanism (c), were similarly unfruitful. The most common course of these optimizations was also the rejection of the iodide ligand *trans* to the methyl group when the M–CH_3 bond was elongated in the guessed structures. The energies of the estimated structures and the forces acting on the atoms in the initial stages of the optimization were both very high. It appears that an iodide ligand cannot co-ordinate to the metal in the axial site when the CH_3 group *trans* to this position is only partially co-ordinated. One reason for this could be that the extra density at the metal centre from co-ordination of I^- can only be stabilized by the formation of a complete bond in the *trans* position. These observations suggest that no transition state, or at least no stable theoretical transition state, exists for reductive elimination of CH_3I from the six co-ordinate alkyl complex. In one respect the failure to locate a TS for an intramolecular elimination is encouraging, since it reinforces our earlier conclusion that oxidative addition can only proceed via a stepwise nucleophilic substitution pathway. The failure to compute an elimination pathway from $[CH_3M(CO)_2I_3]^-$ also supports the hypothesis put forward to explain the solvent effects on oxidative addition in the rhodium system.

Optimization of a TS for the final mechanism (d), involving elimination of CH_3I from the S_N2 intermediate, $[CH_3M(CO)_2I_2]$, did succeed, yielding the structure for rhodium shown in Figure 5.24. The geometry and imaginary vibration for this TS are indicative of a CH_3 migration onto an iodide ligand. The Rh–CH_3 bond is elongated relative to that in the five co-ordinate complex by 0.48 Å and the forming $CH_3\cdots I$ bond has a length of 2.77 Å. Interestingly, the Rh–$I(H_3C)$ bond is shorter than the *cis* Rh–I ligand bond by 0.04 Å and is virtually unchanged from that in $[CH_3Rh(CO)_2I_2]$. At the MP2/DZ level, the energy of this transition state is 130 kJ mol^{-1} higher than the ground state of $[CH_3Rh(CO)_2I_2]$. This would suggest a rather energetically unfavourable reaction, although the three co-ordinate product $[Rh(CO)_2I]$ of this elimination has been implicated as an intermediate in

the catalytic process [242]. Intramolecular reductive elimination and the potential influence of a three co-ordinate rhodium species on the oxidative addition could be addressed in a future study.

5.4 Conclusions

An effective core potential study of the oxidative addition of CH_3I to *cis*-$[M(CO)_2I_2]^-$ (M=Rh, Ir) has been carried out by *ab initio* and DFT computational methods employing the same Gaussian bases. Several conclusions have been reached which are summarized below.

The RHF method predicts that the lowest energy pathway to oxidative addition is via a "linear" S_N2 transition state leading to inversion of configuration at carbon. Computed secondary α-D kinetic isotope effects for this mechanism are in excellent agreement with experiment for both metal complexes, giving very strong evidence for a classical S_N2 inversion mechanism. The main contribution to M–C bonding in the transition states comes from the interaction of a d_{z^2}-type orbital on the metal centre with the anti-bonding σ^*_{CI} LUMO of the substrate. A "bent" S_N2 transition state involving a side-on bonding of CH_3I to the metal centre and leading to retention of configuration, has also been located on the potential energy surface. However, this structure is unstable due to increased steric repulsion between the substrate and the ligands, and yields a computed KIE which is considerably larger than the experimental values.

Both electron correlation and a solvent reaction field have a stabilizing influence on the nucleophilic substitution energetics. The former can be attributed to an increased covalent bonding on M–C bond formation, while the latter is due to the charge separation in the strongly polarised TS and the products. MP2 SCRF calculations predict forward barriers of 69 and 55 kJ mol^{-1} for rhodium and iridium nucleophiles, respectively. The correlation and medium effects tend to balance each other with respect to the geometry of the TS, leading to maxima in roughly the same region of the reaction co-ordinate as the gas phase RHF calculations. This lends further support to the validity of the qualitative features of the RHF transition structures, in spite of their somewhat fortuitous prediction. Perhaps the most significant effect of a solvent field on this reaction is the stabilization of the energy profile leading to the substitution products. Increasing the polarity of the medium from $\epsilon = 7.00$ (CH_3I) to $\epsilon = 32.63$ (CH_3OH) in the rhodium system, doubles the barrier for nucleophilic attack of I^- on $[CH_3Rh(CO)_2I_2]$, thus shifting the energy balance strongly in favour of the forward reaction. This is compatible with the experimental observation that the rate of oxidative addition in the rhodium system is increased when a more polar solvent is employed.

At the MP2 level, the overall oxidative addition process is predicted to be exothermic for both metal systems, in agreement with projected enthalpy changes from extrapolated rate data. For rhodium, the reaction has a calculated exothermicity of -50 to -70 kJ mol^{-1}, while for iridium the alkyl product is more stable, yielding computed energy changes of -85 to -100 kJ mol^{-1}. The increased stability of iridium alkyl complexes is probably due to the greater participation of metal *s* electrons in M–CH_3 bonding.

No tangible computational evidence could be found to support rate changes associated with the interaction of I^- with either the reactant complex or the S_N2 transition state. However, oxidative addition can be promoted by substituting the iodide ligands in $[Rh(CO)_2I_2]^-$ by more covalent ligands such as hydrides.

An objective of this work has been to test the performance of the GAUSSIAN implementation of DFT in calculations of the Monsanto acetic acid cycle. The results of this chapter show that *ab initio* methods, albeit with some experience in their use and knowledge of their limitations, can be used to optimize transition states and model the oxidative addition with some success. By contrast to their good performance in calculations of the strongly bound ground state complexes, the DFT methods that we have applied here fail to give even a qualitative description of the important features of this reaction. The S_N2 inversion transition states are rather more bent and product-like than either the RHF or MP2 structures. The kinetic isotope effects are significantly larger than those obtained by experiment or those computed for the linear structures. The code could not compute a reaction co-ordinate or model the solvent effect. Enthalpy changes for the oxidative addition computed at the non-local level of DFT (BLYP and Becke3LYP) are in poor agreement with values extrapolated from experimental rate data.

Chapter 6

Migratory Insertion

This chapter presents the results of calculations performed on the important migratory insertion step of the Monsanto catalytic cycle. Optimized transition structures and reaction pathways are reported for the reaction:

$$[CH_3M(CO)_2I_3]^- \rightarrow [(COCH_3)M(CO)I_3]^- \qquad M = (Rh, Ir). \tag{6.1}$$

Theoretical results are also presented for a migratory insertion in the neutral tricarbonyl species $[CH_3Ir(CO)_3I_2]$, which has been implicated as a step in the iridium cycle for methanol carbonylation.

6.1 Mechanistic Aspects of Migratory Insertion Reactions

Examples of migratory insertion reactions that transform alkyl-carbonyl complexes into acyl complexes are known for all of the transition metals [11]. Due to their importance in catalytic processes, numerous experimental investigations have been carried out. One of the most interesting questions concerning this reaction is whether it takes place by migration of an alkyl group to a CO ligand, Figure 6.1a, or by literal insertion of CO into a metal–alkyl bond, Figure 6.1b. Early studies focused on the carbonylation reaction:

$$[CH_3Mn(CO)_5] + CO \rightarrow [(CH_3CO)Mn(CO)_5]. \tag{6.2}$$

Calderazzo *et al.* [252] and Flood *et al.* [25] have studied the stereochemical course of this reaction by infra red and ^{13}C NMR techniques, respectively. By analysis of the product distribution between the possible stereochemical forms, it was deduced in both studies that the acylation process proceeded via a methyl migration. The entering CO ligand was observed to occupy the position previously occupied by

the methyl group *cis* to the acyl. Their results suggested the formation of a square pyramidal intermediate which was rigid over the time scale of the reaction. Studies of a variety of other systems have also found alkyl migration to be the dominant mechanism although cases of carbonyl insertion are known [25, 253].

There are several reported cases of the incoming ligand co-ordinating in the position *trans* to the forming acyl group [254]-[256]. For example, this occurs in the reaction:

$$[IrCl_2Et(CO)_2L] + L' \rightarrow [IrCl_2(COEt)(CO)LL'], \qquad (6.3)$$

where L and L′=$As(CH_3)_mPh_n$ ($m = 1, 2$; $n = 1, 2$). To account for this observation, Glyde and Mawby proposed that the migratory insertion took place by a concerted movement of the alkyl and carbonyl groups, accompanied by a widening of the bond angle *trans* to the interacting ligands [255]. This is illustrated schematically in Figure 6.2.

Mechanistic studies of migratory insertion in $[CH_3Rh(CO)_2I_3]^-$ have led to the reaction scheme shown in Figure 6.3 [39, 40]. Following migratory insertion, the first detectable species is the five co-ordinate acyl complex $[(COCH_3)Rh(CO)I_3]^-$ (**C**), which exists as either a dimer or a solvate if no incoming ligand is available. In the presence of CO, the stable product is the *trans* dicarbonyl complex $[(COCH_3)Rh(CO)_2I_3]^-$ (**E**); the *cis* dicarbonyl (**D**) is not observed. A *cis* isomer with *facial* stereochemistry (**F**) can be formed by reacting $[Rh(CO)_2I_2]^-$ with acetyl iodide, as shown in the lower reaction sequence. However, this species undergoes a slow isomerisation to form the stable *trans* complex which is inconsistent with the rapid conversion **A**→**E** that is actually observed. This suggests that subsequent to migration, the external CO ligand enters *trans* to the newly formed acyl to generate the kinetic product (**D**) which then rapidly isomerises to form the *trans* dicarbonyl complex (**E**). Note that these observations do not indicate the nature of the intramolecular combination of the alkyl and carbonyl ligands. Figure 6.3 displays the initial acyl product **B** with stereochemistry that would result from a methyl migration. However, complex **C** could be formed directly from the six co-ordinate alkyl complex if the migratory insertion took place by a concerted mechanism as proposed by Glyde and Mawby [255].

Forster [66] proposed that migratory insertion in the iridium system actually occurred in a neutral tricarbonyl species, $[CH_3Ir(CO)_3I_2]$, as shown in Figure 6.4. In this mechanism, the first step is reversible dissociation of an axial iodide ligand to form complex **2**, followed by co-ordination of CO to form the tricarbonyl, complex **3**. The axial iodide should be the most labile due to the *trans* influence of the methyl group, and is therefore the ligand most likely to be replaced by CO. Hence, the predominant tricarbonyl species is expected to be the *fac-cis-* isomer shown in Figure 6.4. Under normal reaction conditions (i.e. in aprotic solvents), dissociation of the iodide is expected to be slow and contribute to the rate de-

(a)

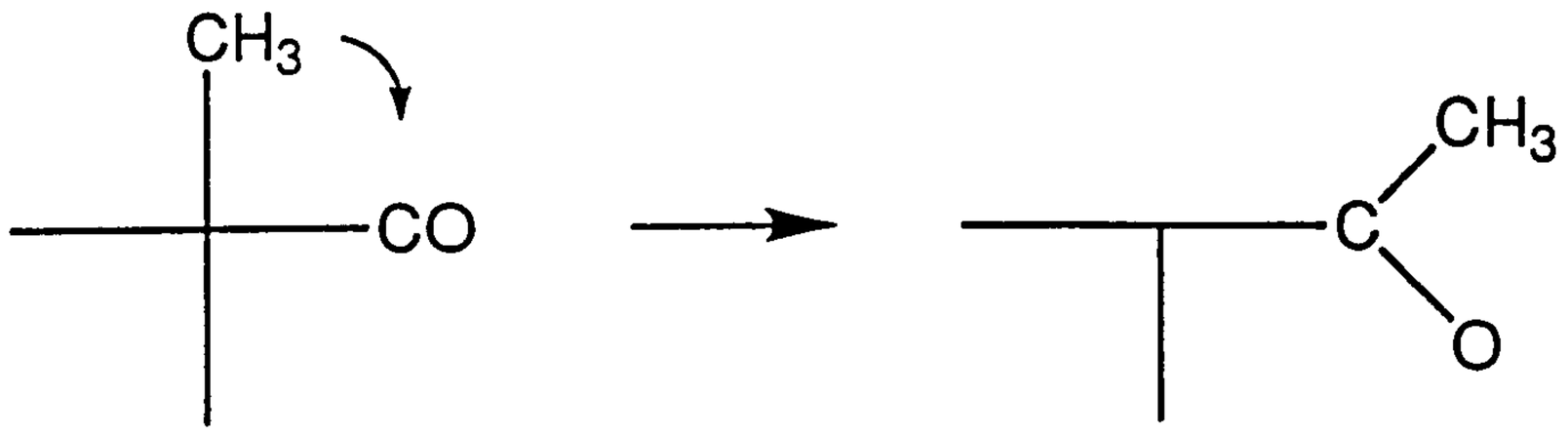

(b)

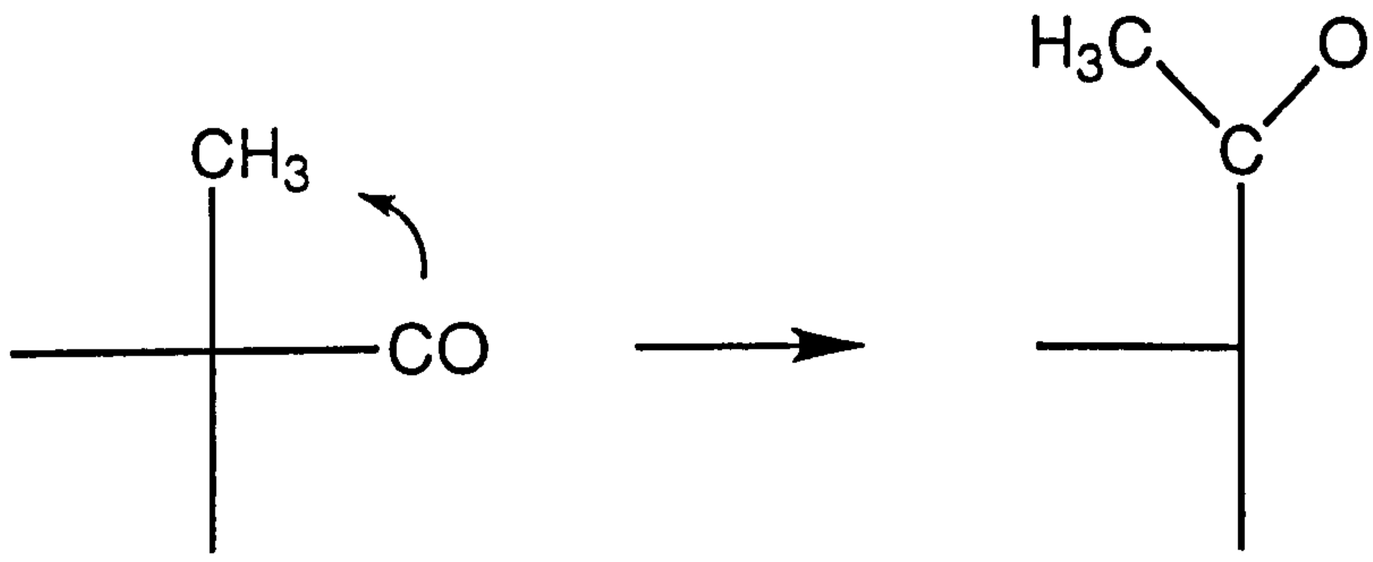

Figure 6.1: Mechanisms of migratory insertion: (a) methyl migration; (b) carbonyl insertion.

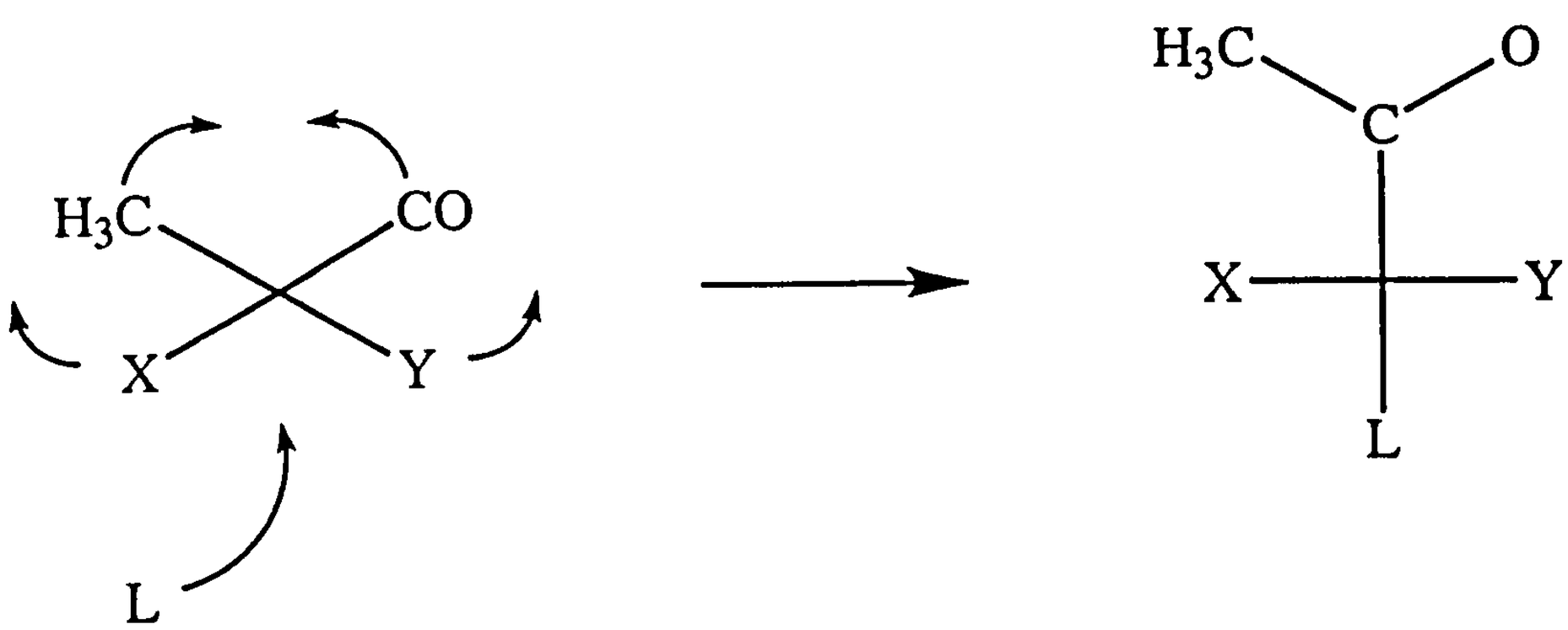

Figure 6.2: Concerted migratory insertion of alkyl and carbonyl ligands accompanied by a widening of the X–M–Y bond angle allowing *trans* addition of the external ligand. Apical ligands have been omitted for clarity.

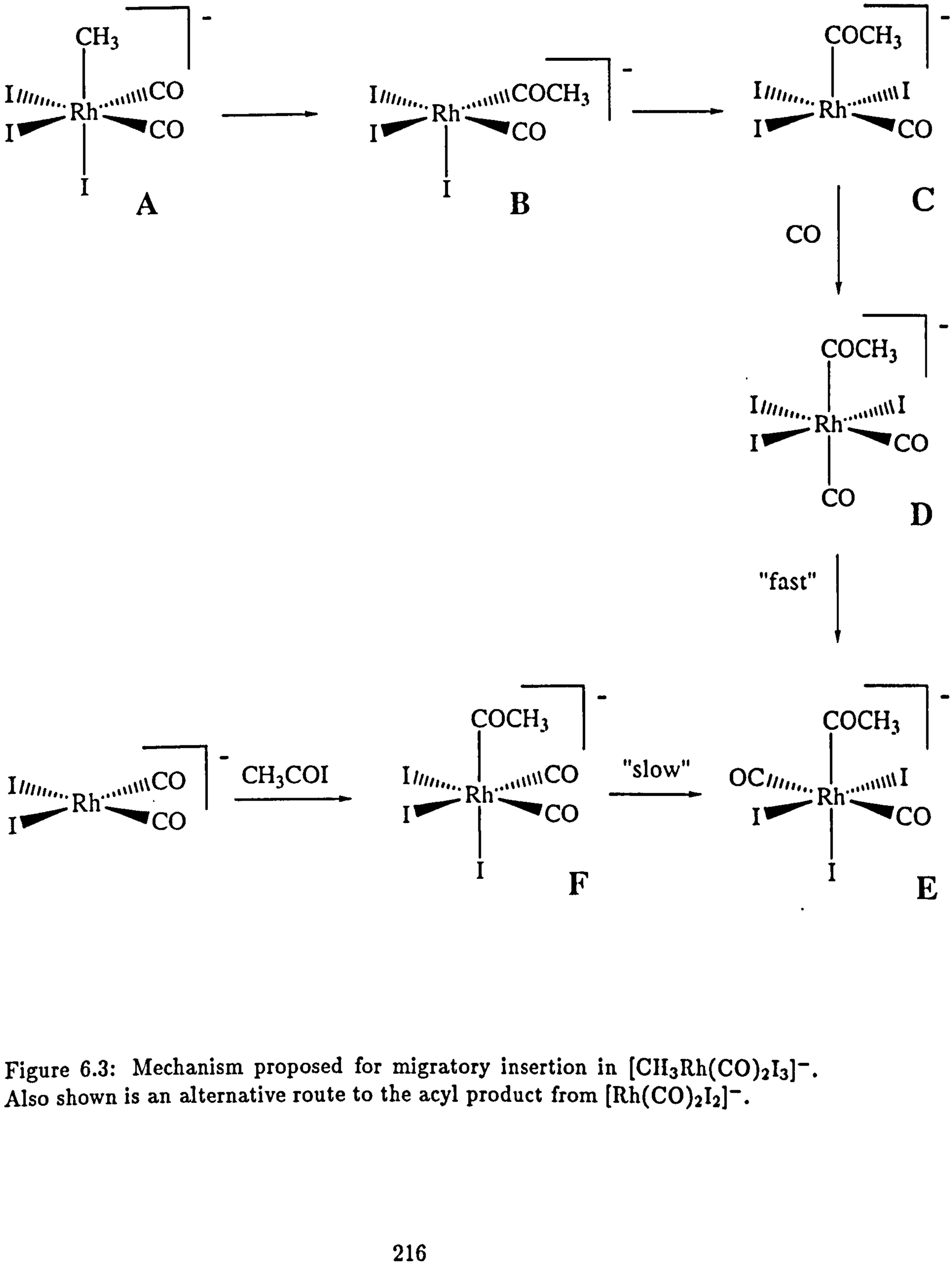

Figure 6.3: Mechanism proposed for migratory insertion in $[CH_3Rh(CO)_2I_3]^-$. Also shown is an alternative route to the acyl product from $[Rh(CO)_2I_2]^-$.

termining step. The tricarbonyl species (**3**) has never been observed, either in working catalyst solutions or model reactions, leading to the suggestion that once formed migratory insertion in this complex is rapid. The initial five co-ordinate acyl product will have the stereochemistry as shown in complex 4 if methyl migration takes place, and complex 5 if concerted migratory insertion takes place. In either case, iodide co-ordinating into the free site will form the dicarbonyl acyl complex with *fac-cis-* stereochemistry (**6**). It is also possible that migratory insertion in $[CH_3Ir(CO)_2I_3]^-$ could proceed via a similar mechanism to that proposed for rhodium. If this is the case, the major acyl product would be a *trans* iridium dicarbonyl species, analogous to complex **E** shown in Figure 6.3.

Pearson has analysed the carbonylation of $[CH_3Ir(CO)_2I_3]^-$ using infra red spectroscopy and concluded that migratory insertion in this complex can proceed via both of the mechanisms described above [67]. The reaction conditions employed were found to dictate which mechanism predominated. In neat chlorobenzene it appeared that both mechanisms were operating simultaneously. Stereochemical analysis of the acyl products indicated that migratory insertion in approximately 50% of the reactants proceeded via the mechanism proposed by Forster involving prior dissociation of an iodide ligand to form the tricarbonyl. Migratory insertion in the remaining 50 % appeared to take place directly in the tri-iodide by an analogous mechanism to that proposed for rhodium. On addition of iodide to the reaction mixture only the *trans* dicarbonyl acyl product was observed, indicating that the iodide loss mechanism had been suppressed. The rate was approximately halved which is consistent with migratory insertion only taking place in $[CH_3Ir(CO)_2I_3]^-$.

The key difference between rhodium and iridium catalysed methanol carbonylation arises in the migratory insertion step of the cycle. In the rhodium process, the conversion of $[CH_3Rh(CO)_2I_3]^-$ into $[(COCH_3)Rh(CO)I_3]^-$ is rapid even under ambient conditions. By contrast, the analogous transformation in the iridium system is rate determining, typically requiring temperatures of greater than 80 °C to proceed in aprotic solvents and can only occur in the presence of CO pressure. It has recently been estimated that migration of methyl onto carbonyl is a factor of *ca.* 10^5 faster for Rh(III) than for Ir(III) in comparable systems [257]. The impetus behind any investigation of the iridium process therefore lies in making the migratory insertion step more competitive.

Several methods for accelerating migratory insertion are known. Donor solvents have frequently been found to give significant rate enhancements in migratory insertion reactions. Such effects are usually explained in terms of solvent stabilization of the unsaturated acyl intermediate generated after the alkyl migration step [30]. Acid catalysis has been proposed to exert a stabilizing influence on the transition states and products in CO migratory insertion reactions. It is possible that an electrophile attacking the oxygen atom of a forming acyl ligand could reduce

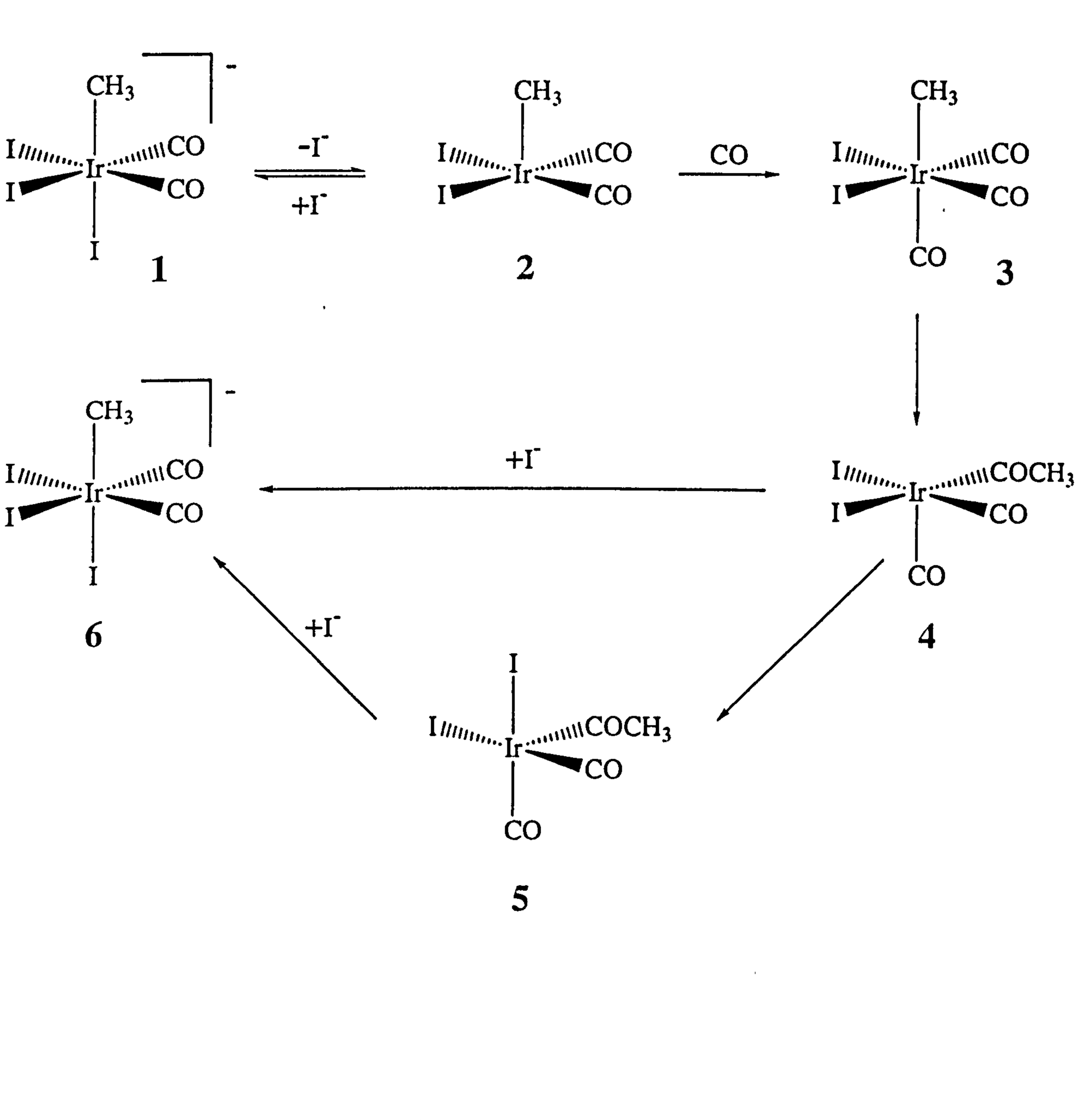

Figure 6.4: Proposed mechanism for migratory insertion in $[CH_3Ir(CO)_2I_3]^-$.

destabilizing repulsive interactions by polarizing some of the carbonyl lone pair electron density away from the C–C bond forming region. Butts *et al.* reported that dichloroacetic acid enhanced the rate of migratory insertion in $[CH_3Mn(CO)_5]$ [258]. They postulated that the acid was involved in a hydrogen bonding interaction with the acyl oxygen, thereby stabilizing the transition state relative to the ground state by *ca.* 8 to 12 kJ mol^{-1}. Cation assisted migratory insertion has been observed in anionic metal carbonyl species. Collman *et al.* reported a threefold increase in the rate of migratory insertion in $[Fe(CO)_4R]^-$ when Na^+ was replaced by Li^+ [259]. The rate increase was of the order of 10^3 on replacing a large non-co-ordinating organic cation with Li^+. It was proposed that the promotional effects were due to the co-ordinatively unsaturated acyl complex being favoured over the alkyl complex in the presence of smaller cations which bind more tightly to the acyl oxygen. Strong lewis acids such as $AlCl_3$, $AlBr_3$ and BF_3 have been found to induce rapid alkyl migration in a variety of metal carbonyls [260]. It has been proposed that the acid lowers the activation barrier of the migratory insertion reaction by co-ordinating with the oxygen of a carbonyl ligand prior to alkyl migration.

Dramatic acceleratory effects have been observed on the rate of migratory insertion in $[CH_3Ir(CO)_2I_3]^-$. Pearson *et al.* reported that the rate of this reaction was increased by a factor of 10^4 on addition of small quantities of methanol and by a factor of 200 on addition of the Lewis acid SnI_2 [67, 68]. The acceleration was not proposed to arise from either the donor properties of the solvent or from acid catalysis at the acyl oxygen. Kinetic measurements of the promoted reactions gave rather different activation parameters to those measured in neat chlorobenzene, with much lower values of $\Delta H^{\ddagger}$ and large negative values of $\Delta S^{\ddagger}$. This suggested that there had been a change in the nature of the rate determining step from a dissociative to an associative mechanism. The explanation put forward was that both of these species activated an Ir–I bond prior to alkyl migration. Methanol was proposed to aid dissociation of an iodide ligand through hydrogen bonding interactions

$$[CH_3Ir(CO)_2I_3]^- + CH_3OH \rightleftharpoons [CH_3Ir(CO)_2I_2] + CH_3OH\cdots I^-, \quad (6.4)$$

leading to facile formation of the tricarbonyl complex $[CH_3Ir(CO)_3I_2]$ in which migratory insertion is believed to be rapid. The Lewis acid was proposed to insert into an iridium iodide bond forming a $Ir–SnI_3$ species

$$[CH_3Ir(CO)_2I_3]^- + SnI_2 \rightarrow [CH_3Ir(CO)_2I_2(SnI_3)]^-, \quad (6.5)$$

labilising the *trans* methyl group toward a more rapid migration.

6.2 Theoretical Aspects of Migratory Insertion Reactions

Two recent reviews of theoretical studies of carbonyl migratory insertion reactions have been published [207, 261]. The first theoretical study of migratory insertion in an alkyl-carbonyl complex was undertaken by Berke and Hoffmann [26] within the framework of the extended Hückel model of electronic structure. They examined the reaction path for a methyl migration reaction in $[CH_3Mn(CO)_5]$ and extended the analysis to the more general case of organometallic migration reactions. A full optimization of all the degrees of freedom was not carried out but an approximate reaction path was extrapolated from several exploratory calculations that constrained the interacting groups to a C_s migration plane. The simulated reaction path gave an activation barrier that was in reasonable agreement with experiment and contained a five co-ordinate intermediate which was close in energy to the transition state. The potential stabilizing interaction of donating solvent molecules was investigated. Analysis showed that a suitable low energy acceptor orbital was not created until after the transition state was passed. This suggested that an incoming ligand or solvent molecule could stabilize the unsaturated acyl intermediate but not the transition state. The effect of changing the metal centre was also examined in this work. Substitution of Mn by Re caused a substantial increase in the activation energy, suggesting that migration should be more difficult as one proceeds down a triad. The 5*d* metals are usually found to form stronger M–CH_3 bonds than their 4*d* analogues but Berke and Hoffman have also suggested that the heavier metals will be penalised more in the migratory insertion due to a greater reduction in stabilization arising from M–CO π back-donation.

In early *ab initio* studies, migratory insertion reactions in square planar complexes of the group 10 transition metals were investigated. Sakaki *et al.* studied reaction (6.6) at the RHF level of theory [262].

$$[CH_3Pt(CO)(F)(PH_3)] \rightarrow [(COCH_3)Pt(F)(PH_3)]. \qquad (6.6)$$

The geometry of the Pt complex was changed stepwise to simulate reaction paths corresponding to methyl migration, carbonyl insertion and a concerted migratory insertion with simultaneous opening of the F–Pt–PH_3 angle. From the energy changes along the assumed reaction paths it was concluded that the most energetically favourable mechanism was methyl migration and that the least favourable was carbonyl insertion.

Similar conclusions have been reached by Koga and Morokuma [263] who investigated migratory insertion in d^8 square planar complexes. They considered the

model Pd and Pt migratory insertion reactions:

$$[CH_3M(CO)(H)(PH_3)] \rightarrow [(COCH_3)M(H)(PH_3)] \quad (M = Pd, Pt). \quad (6.7)$$

A full optimization with the energy gradient method at the RHF level has shown that the reaction path is a methyl group migration passing through a three-centred transition state. An extensive search of the potential energy surface failed to locate a transition state corresponding to a carbonyl insertion mechanism. The preference for methyl migration over carbonyl insertion was explained in terms of a reduced destabilizing repulsion between a carbonyl lone pair and an occupied metal *d* orbital. Single-point calculations carried out at the correlated MP2 level, revealed that the reaction was more endothermic and the activation barrier higher for the Pt complex. This was ascribed to the difference of M–CH_3, M–CO and M–$COCH_3$ bond strengths between Pd and Pt complexes arising from relativistic effects in the electronic structure of the heavier transition metal atom. The Pt bond strengths were estimated to be stronger by *ca.* 30, 47 and 38 kJ mol^{-1}, respectively, than the corresponding ones in the Pd complexes. Note that in this study the Los Alamos full-core ECP and associated Gaussian bases due to Hay and Wadt (LANL1DZ) was used for the lighter Pd atom [144] but for the quantitative calculations in the Pt system, a different ECP due to Noell and Hay was employed [264]. Their calculations showed that the LANL1DZ basis predicted Pt–CO bond lengths that were longer than the corresponding Pd bonds by *ca.* 0.2 Å. These workers therefore felt it necessary as we have in the present study, to use different ECPs for the 4*d* and 5*d* transition metals.

Dedieu *et al.* [265] have carried out *ab initio* complete active space SCF (CASSCF)[1] calculations to examine the effect of electron correlation on the model migration reaction:

$$[HMn(CO)] \rightarrow [(HCO)Mn]. \quad (6.8)$$

Analysis of the CASSCF wavefunction has demonstrated that the correct description of π back-donation in the Mn complexes requires a multi-determinantal wavefunction such as in CI, MCSCF or Møller-Plesset perturbation theory. The Hartree-Fock method is well known to underestimate the π back-donation in transition metal carbonyl complexes [183]. In the reactant, [HMn(CO)], there is both in-plane and out-of-plane Mn–CO π back-donation. In the formyl product, however, only out-of-plane π back-donation can take place since the in-plane CO π^* orbital changes to the C–H σ bond orbital during the reaction. The difference in bonding between the reactant and product could not be adequately described by the HF calculations; π back-donation was underestimated more in the hydride reactant leading to an energy profile incorrectly favouring the formyl product.

[1]CASSCF is a multi-configurational SCF (MCSF) method designed to take care of near-degeneracy effects in transition metal systems.

Carbonyl migratory insertion reactions have also been investigated using density functional theory. Versluis *et al.* have studied reaction (6.9) using the Hartree-Fock-Slater method [266].

$$[CH_3Co(CO)_4] \rightarrow [(COCH_3)Co(CO)_3]. \qquad (6.9)$$

They optimized the structures of the reactants and products and constructed approximate reaction paths using a linear synchronous transit procedure. The energy barrier for a methyl migration was significantly lower than for a carbonyl insertion. The high barrier for insertion was attributed to the repulsion between CO lone pair electrons and non-bonding *d* electrons in accordance with the study by Koga and Morokuma on the d^8 square planar complexes.

A very recent publication has examined carbonyl migratory insertion in octahedral rhodium complexes. Margl *et al.* have carried out non-local density functional calculations on the stationary points for reaction (6.10) using the ADF code [267].

$$[CH_3Rh(CO)Cl(H)(PH_3)_2] \rightarrow [(COCH_3)RhCl(H)(PH_3)_2] \qquad (6.10)$$

Migratory insertion occurring in both the *cis* and *trans* rhodium complexes was investigated. For the reaction in the complex with *cis* phosphine ligands (leading to a *cis* product), the calculated activation barrier and enthalpy change were 114 and -13 kJ mol^{-1}, respectively. Migratory insertion in the *trans* species had a similar enthalpy change of -13 kJ mol^{-1} and a higher activation energy of 129 kJ mol^{-1}. Interestingly, the stereochemistry of the optimized transition states and acyl products reported in this study are consistent with a concerted migratory insertion mechanism (Figure 6.2). The calculated reaction paths led in each case to the formation of an acyl group in the apical site and the hydride ligand was found to move from a *trans* to a *cis* position with respect to the carbonyl carbon atom. This differs from methyl migration reactions in octahedral complexes such as $[CH_3Mn(CO)_5]$, which are characterized by the formation of square pyramidal species with the acyl ligand in a basal site.

6.3 Theoretical Investigation of Migratory Insertion in $[CH_3M(CO)_2I_3]^-$ (M=Rh, Ir)

6.3.1 Transition States

We have attempted to optimize transition states for the migratory insertion reaction in $[CH_3M(CO)_2I_3]^-$ using the Hartree-Fock and density functional methods. Despite investing a considerable amount of computational effort the DFT calculations did not yield any–spurious or otherwise–optimum transition states for this

reaction. By contrast, it proved quite straightforward a task to optimize a transition state at the RHF level, providing that the force constants and a judicious estimate of the geometry were supplied to initiate the calculation. Initiating DFT optimizations from the optimum RHF TS geometries and force constants led to rather unsymmetrical high-energy structures that were not stationary points on the potential energy surface. This was the case for each of the local and non-local functionals employed. Increasing the resolution of the numerical integration grid or extending the basis set did not lead to a significant improvement. The reasons for this behaviour are unclear. One plausible explanation could be that there is no TS for migratory insertion at the levels of DFT that were considered. That is, the energy of any intermediate structure on the reaction path is lower than the energy of the reactant alkyl complex leading to a migratory insertion reaction that proceeds without a barrier. This would imply that the DFT schemes had underestimated the energy of the TS. This argument could be reasonably applied to processes with very low activation barriers, say less than 20 kJ mol^{-1}. However, the experimentally measured activation enthalpies for the migratory insertion reaction are moderate to large, having values of *ca.* 60 and 150 kJ mol^{-1} in the rhodium and iridium systems, respectively. The absence of a TS could be due to deficiencies in the exchange potentials of the density functionals in the critical C–C bond formation region. One other explanation which we do not believe is true but nevertheless cannot be ruled out, is simply that our efforts were not thorough enough to locate the position of a TS for migratory insertion at this level. Our experience of transition state optimization is that it is rather more difficult to locate saddle points using DFT than the conventional *ab initio* methods. Whatever the reason, the failure to optimize a transition state for this reaction adds further doubt to the applicability of the Gaussian implementation of DFT to practical calculations of the catalytic steps in the Monsanto acetic acid cycle. The rest of this chapter will concentrate on the results of *ab initio* calculations performed on the migratory insertion reaction.

The *ab initio* methods of calculation that have been used for investigating the migratory insertion reaction were chosen on the basis of their performance in calculations of the equilbrium structures and of the oxidative addition reaction described in previous chapters. For geometry optimization and calculation of the intrinsic reaction co-ordinate we have only used the RIIF method. Transition state optimizations at the MP2 level were not attempted in view of their expensive dependence on the inclusion of polarization functions. The MP2 scheme is reserved for single-point energy calculations on the reaction pathways. The choice of ECP for each transition metal is not a trivial one. It would obviously be desirable to carry out calculations on the rhodium and iridium systems using the same Gaussian bases. However, there is some evidence to suggest that the full-core ECP basis (DZ) is inadequate for a quantitative description of processes which involve changes in Ir–C bonding. In particular, comparison of Ir–CO bond lengths com-

puted at the RHF/DZ level to related experimental crystal data suggested that they were overestimated by *ca.* 0.1 Å (for example, in the equilibrium geometries of $[Ir(CO)_2I_2]^-$ and $[CH_3Ir(CO)_2I_3]^-$; see chapter 4). Correlated MP2/DZ calculations of the activation barrier for oxidative addition of CH_3I to $[Ir(CO)_2I_2]^-$ were too low by *ca.* 25 kJ mol^{-1}. Both the geometrical parameters and the reaction energetics were significantly improved upon moving to the semi-core ECP. By contrast, previous results for the rhodium system have indicated the opposite behaviour, with the standard full-core ECP basis yielding the best geometrical parameters, and energetics which were in good agreement with the experimental values. An adequate description of the metal–carbon bonding is essential for an investigation of the migratory insertion process. At the risk of presenting a slightly nonuniform set of results, we have therefore decided to use different ECP bases for each metal atom. For rhodium the full-core Los Alamos ECP and associated DZ basis have been used, while for iridium all of the calculations have been carried out with the semi-core ECP and DZ2 basis.

As has been described previously, there are three possible transition states for migratory insertion: one for CH_3 migration. one for CO insertion and the other for concerted migration of both CO and CH_3. After an extensive search of the potential energy surface starting from several initial guess geometries, only one stable transition structure for migratory insertion in $[CH_3M(CO)_2I_3]^-$ could be found. This is shown for both rhodium and iridium in Figure 6.5. Also shown for comparison with the transition states are the geometries of the alkyl reactants calculated at the same levels of theory. The RHF structures were verified by vibrational analysis to be true saddle point maxima, exhibiting in each case a single imaginary frequency of *ca.* -500 cm^{-1}.

As expected, the reaction involves substantial changes in the M–CH_3 and M–CO geometries. The imaginary frequency vibrations describe a significant translation of *both* the methyl and carbonyl groups. The methyl group, with its local C_3 axis kept nearly vertical, moves about halfway along the M–CO bond. The carbonyl group is displaced upwards towards the methyl group as if to facilitate its migration and reorientates its M–C–O axis such that the oxygen atom points away from the C–C bond forming region. The H_3C–M–CO bond angles in the transition states are 52.0° and 48.2° for rhodium and iridium. respectively. The M–CH_3 bonds are lengthened and the M–CO bonds shortened relative to the computed parameters in the reactant alkyl complex. For rhodium, the Rh–CH_3 bond distance is increased by 0.28 Å and the Rh–CO distance reduced by 0.10 Å. The corresponding iridium process involves a slightly greater elongation in the Ir–CH_3 bond of 0.30 Å and a smaller reduction in the Ir–CO bond of 0.03 Å. The extent of acyl formation appears to be more advanced in the iridium TS. This is indicated by a shorter C–C bond length of 1.84 Å and a slightly longer C–O length of 1.18 Å, compared to the corresponding values in the rhodium TS which are 1.89 and 1.17 Å, respectively. In

(a) M=Rh

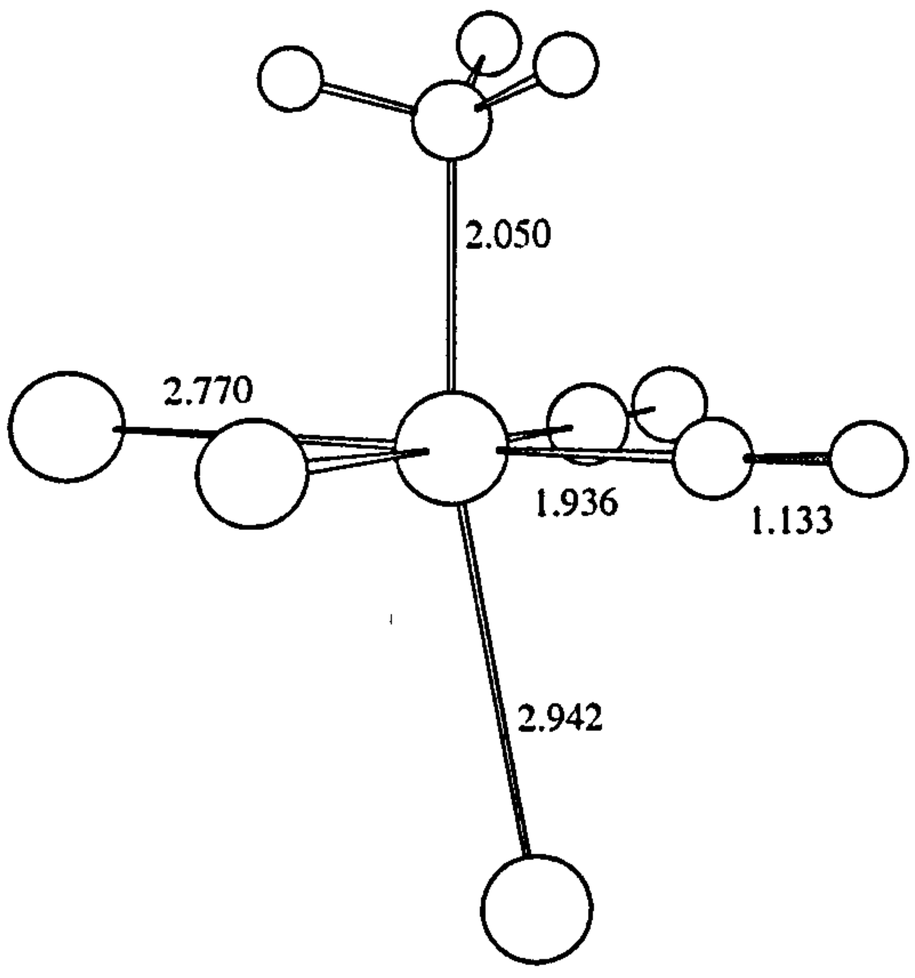

reactant

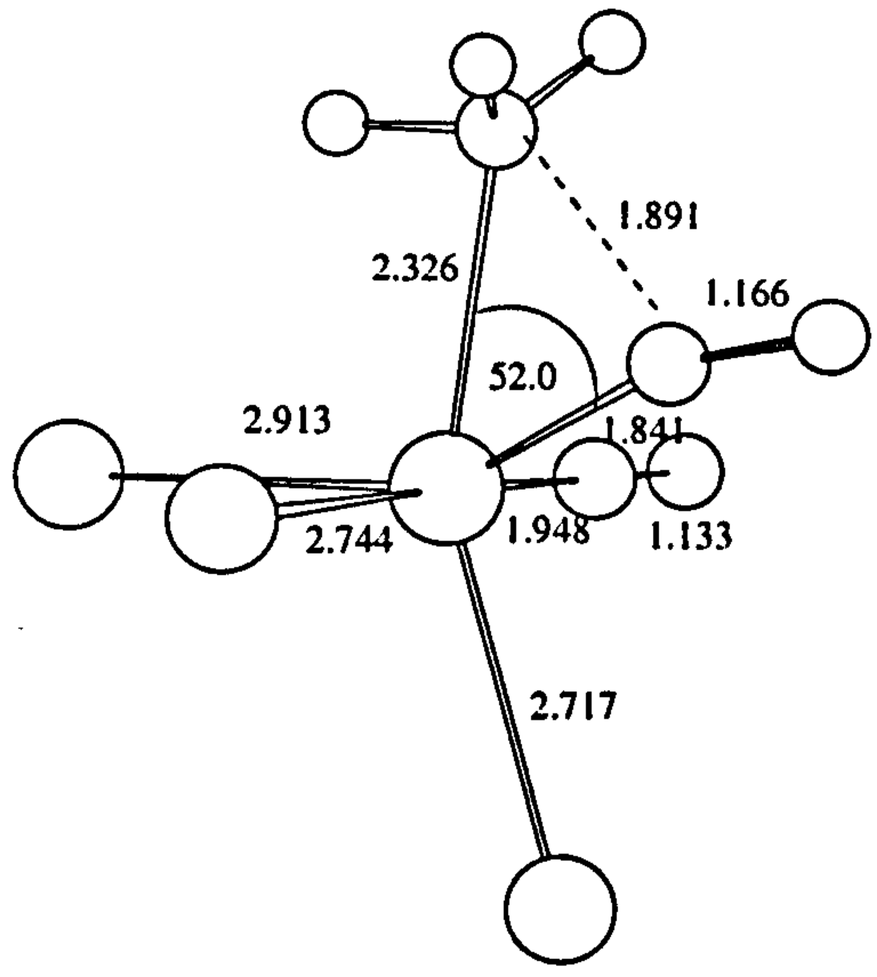

TS (ν_i=-502 cm^{-1})

(b) M=Ir

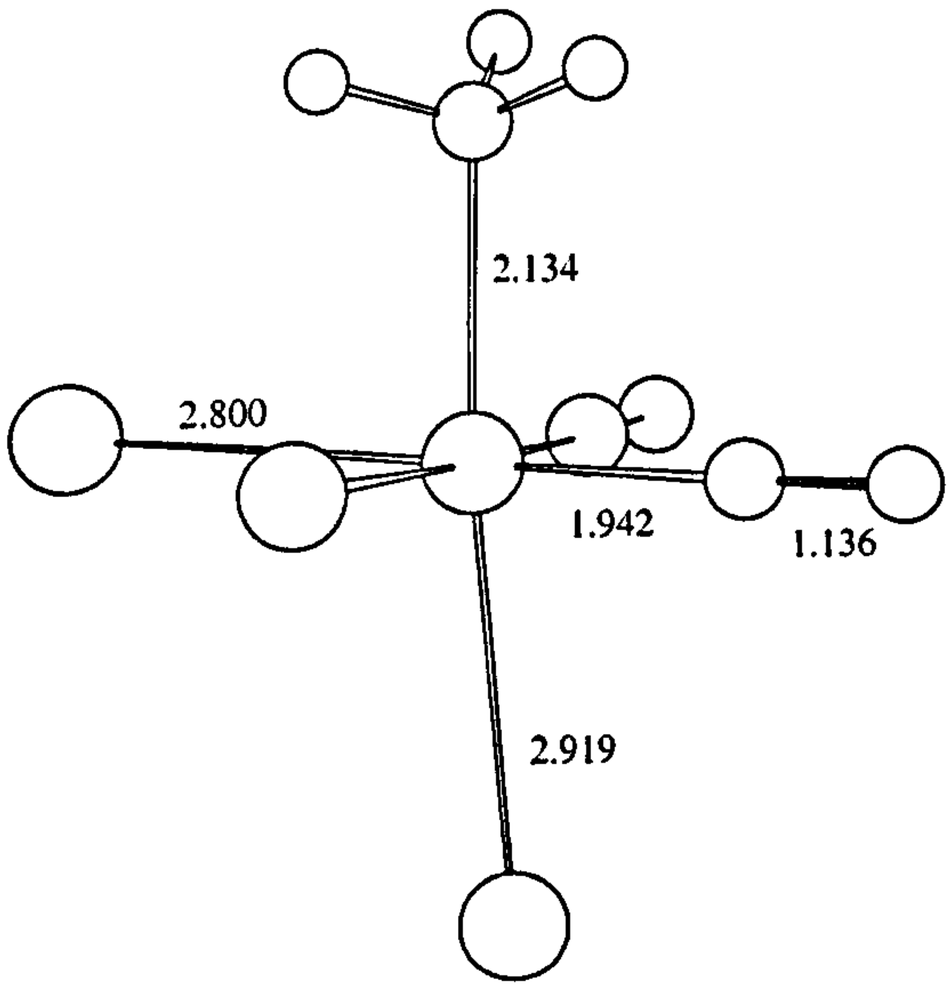

reactant

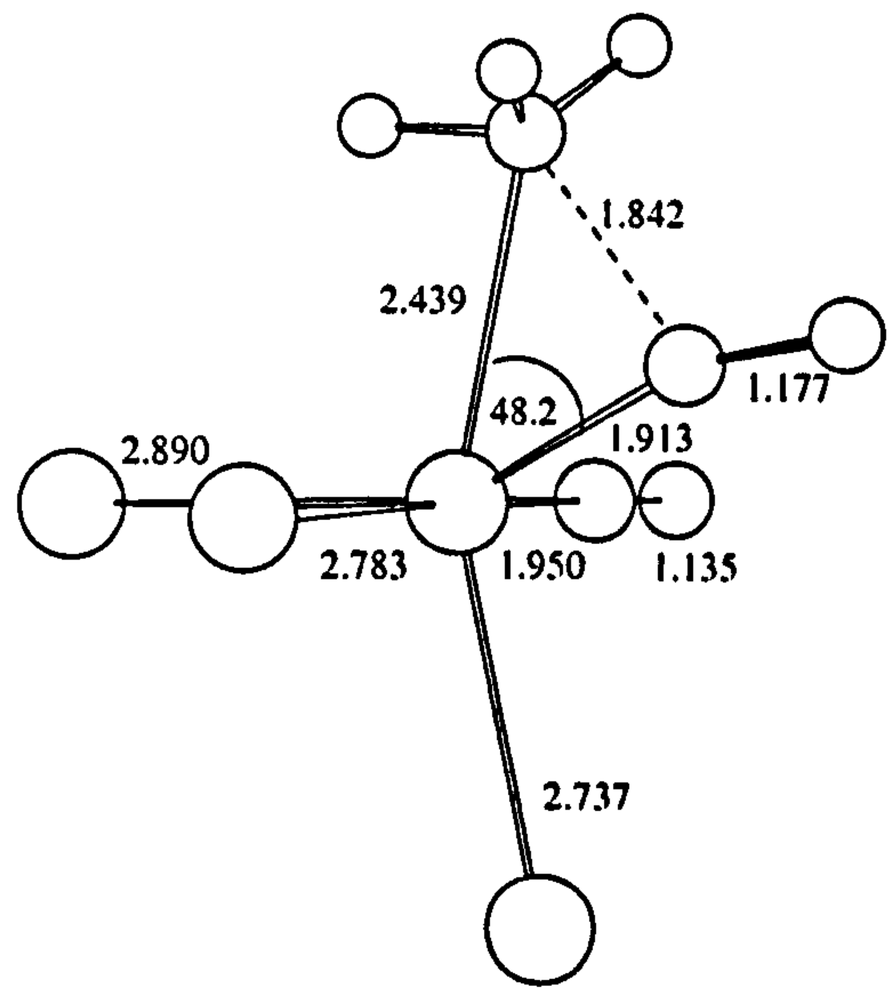

TS (ν_i=-529 cm^{-1})

Figure 6.5: Optimized geometries of reactants and transition structures for the migratory insertion reaction in $[CH_3M(CO)_2I_3]^-$. The parameters for rhodium (a) were obtained from RHF/DZ calculations and for iridium (b) from RHF/DZ2 calculations.

addition to the geometry changes in the ligands directly involved in acyl formation, there are also significant changes observed in the iodide ligands that were *trans* to CH_3 and CO in the alkyl complex. The iodide originally *trans* to CO is lengthened in each case by *ca.* 0.1 Å and the iodide *trans* to CH_3 is shortened by *ca.* 0.2 Å. There also appears to be some translation in these groups but this is difficult to interpret without calculating the reaction co-ordinate. The geometry of the apical I–M–CO fragment is essentially unchanged by the transformation of the reactants into the TS.

6.3.2 Reaction Pathways and Energetics

Intrinsic reaction co-ordinates have been computed for the migratory insertion reaction in $[CH_3M(CO)_2I_3]^-$ at the RHF/DZ level for rhodium, and at the RHF/DZ2 level for iridium. These are shown superimposed upon one another in Figure 6.6. The energy profiles exhibit well-defined maxima which are situated slightly closer to the alkyl side of the reaction co-ordinate. The steepest energy gradient is found for the transformation of the alkyl reactants into the TS with a more gentle slope describing the descent to acyl products. The IRC for iridium has been extrapolated so that it coincides with the rhodium path at the stationary point corresponding to the starting alkyl complex ($rx = -4.7$). The location of the maximum later along the reaction co-ordinate ($rx \approx +0.5$) is consistent with the computed TS geometries which suggested C–C bond formation was more advanced in the iridium system. This differs from the results of calculations on the nucleophilic substitution reaction described in the previous chapter, which indicated that the iridium TS for M–C bond formation was earlier than for rhodium.

Geometries taken from several selected points of the IRC calculated for the rhodium system are displayed in Figure 6.7. The transformation (a)→(b) corresponding to the initial flat region of the path ($rx \sim -5.0$ to -2.0) involves a slight tilting up, *ca.* 10°, of the carbonyl ligand toward the CH_3 group. At $rx \approx -1.0$ (c) the methyl group has also started to move, bending towards the CO ligand by 10° while stretching its bond with rhodium by *ca.* 0.1 Å. The CO ligand is involved in further upward motion by another 10° and the Rh–CO bond is shortened by *ca.* 0.1 Å. Contraction of this bond causes a significant lengthening of 0.12 Å in the Rh–I bond situated in the *trans* position. These observations suggest that the Rh–CO bond is getting stronger in the early stages of the reaction and is exerting a greater *trans* influence. Interestingly, at this point, the CH_3 group has rotated around its local C_3 axis so that the C–H bonds are congruent with the formation of a pseudo C_s symmetry plane in which the migration takes place. The most rapid energy change in the profiles occurs in the region $rx \sim -1.0$ to 0.0, (c)→(d), approaching the transition state. The major component of the reaction co-ordinate appears to be a lengthening of *ca.* 0.2 Å in the Rh–CH_3 bond together with a

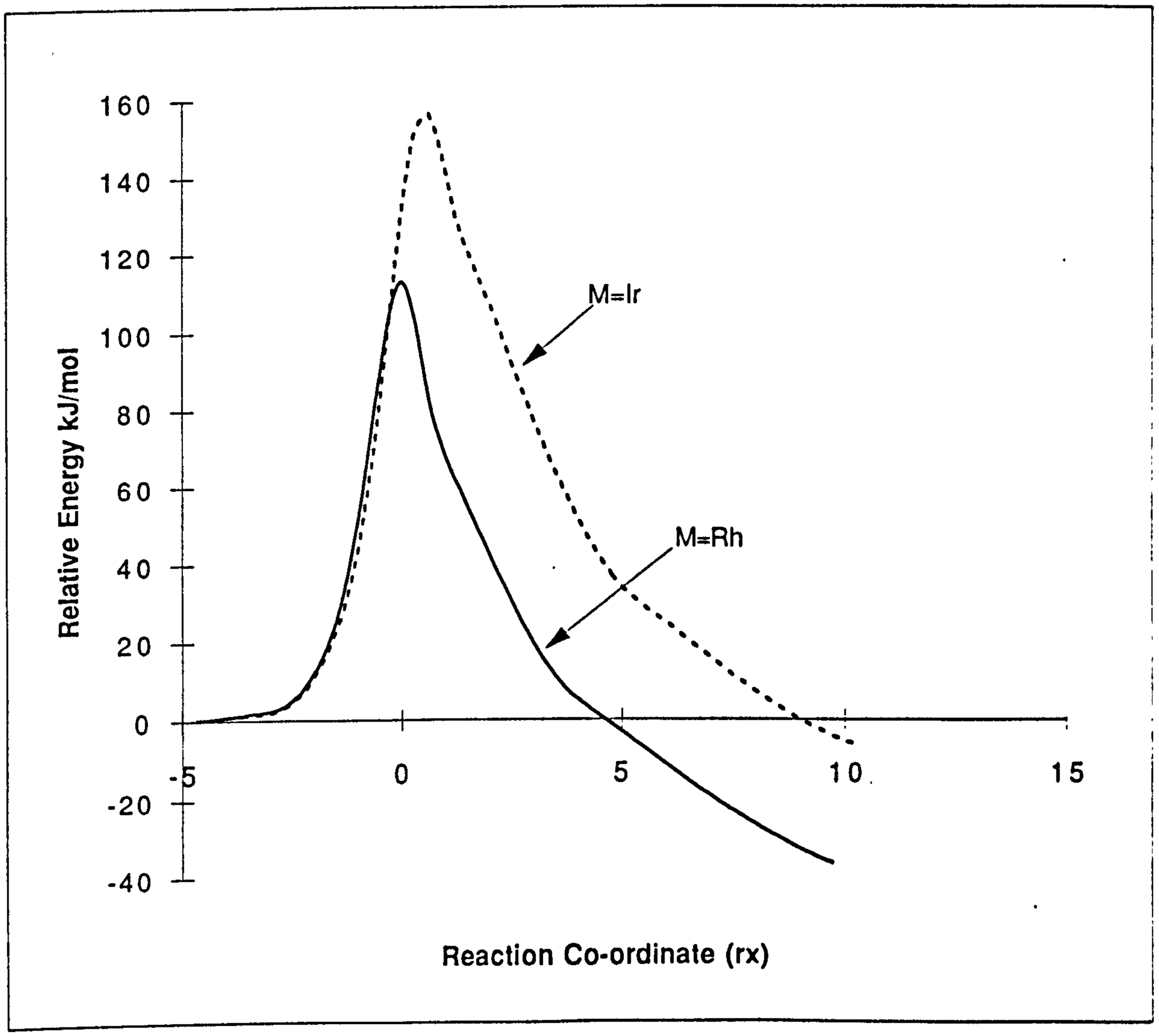

Figure 6.6: Intrinsic reaction co-ordinates for migratory insertion in $[CH_3M(CO)_2I_3]^-$ calculated at the RHF level of theory. The solid line is the reaction path for rhodium which has been computed using the DZ basis; the dashed line is the path for iridium calculated using the DZ2 basis. The zero of energy is taken as the energy of the reactant alkly complex.

reduction of *ca.* 0.15 Å in the *trans* Rh–I bond. Smaller contributions come from further bending of the CH_3 and CO ligands toward each other. Soon after the transition state has been passed the majority of the bond making and breaking involved in acyl formation has already taken place. In structure (e) at $rx \approx 1.0$, the C–C bond is nearly formed (1.55 Å), the Rh–CH_3 bond is essentially broken (2.52 Å) and the new Rh–$COCH_3$ bond begins to lengthen towards its equilibrium geometry (1.91 Å). Following the reaction path from $rx \sim 1.0$ to 6.0 reveals a substantial increase in the I–Rh–I bond angle from 110° in (e) to 156° in (f). The geometrical result of this movement is a distorted square pyramidal structure in which the iodides occupy basal sites *trans* to each other and the axial position is now taken up by the acyl ligand. In the latter part of the reaction path ($rx \sim 6.0$ to 9.0), the newly formed acyl group rotates out of the migration plane such that the acyl C–O bond is aligned above the carbonyl Rh–CO bond. The final product (g) is square pyramidal with C_s point group symmetry. These geometry changes describe a *concerted* migratory insertion mechanism very similar to that proposed by Glyde and Mawby [255]. The process can be divided into three consecutive stages:

- concerted movement of the CH_3 and CO groups to form the C–C bond;
- opening of the *trans* I–M–I angle to form a square pyramidal structure with the acyl ligand in the axial site;
- rotation of the acyl ligand to form a product with C_s symmetry.

The reaction co-ordinate for migratory insertion in the iridium alkyl complex displays the same qualitative features as those described above for the rhodium system. The main quantitative differences appear to be a reluctance of the Ir–CO bond to strengthen in the early stages of the reaction and a large extension in the Ir–CH_3 bond approaching the TS. Contraction of the Ir–CO bond is about half that observed in the rhodium complex at corresponding points in the region $rx \sim -5.0$ to -1.0. The Ir–CH_3 bond extends 0.1 Å more than Rh–CH_3 during the rapid energy change $rx \sim -1.0$ to 0.0. The RHF optimized structures of the rhodium and iridium five co-ordinate acyl complexes resulting from concerted migratory insertion are shown in Figure 6.8. The geometries of these species calculated using the MP2 method and several DFT-based schemes were reported in chapter 4. The most notable difference in the structures is the longer metal–acyl distance calculated for the iridium complex. This effect occurs at each of the levels but could be due to a basis set effect. A stable structure with the acyl ligand in a basal site could not be located on the potential energy surface. This is in line with the fact that all crystal structure determinations of square pyramidal acyl complexes to date, have only found species incorporating acyl ligands in the axial position. This is a reflection of the strong *trans* influence of the acyl ligand. The total energy of the square pyramidal complexes was found to have a fairly small

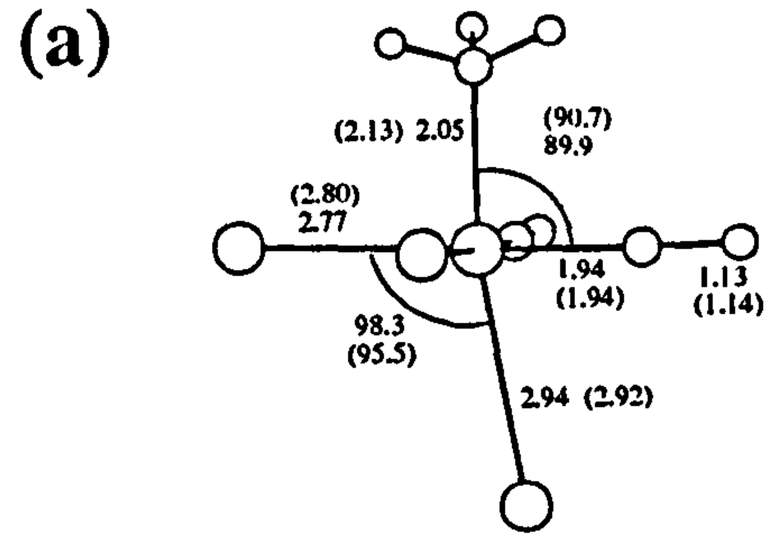

rx=-5

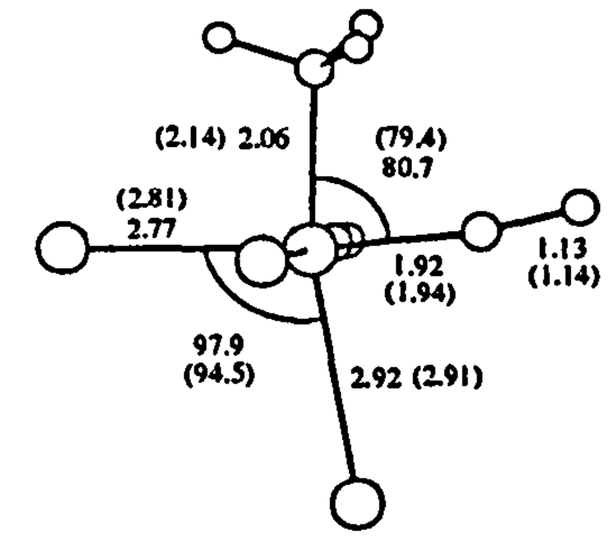

rx=-2

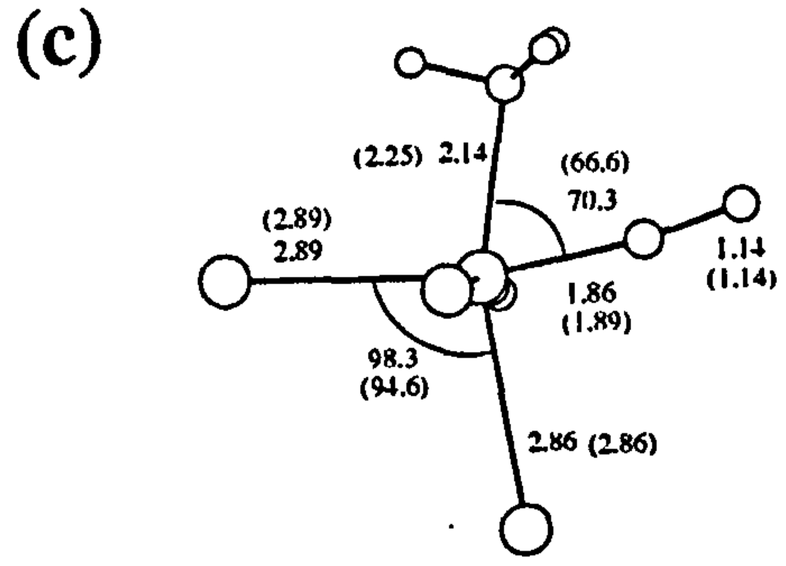

rx=-1

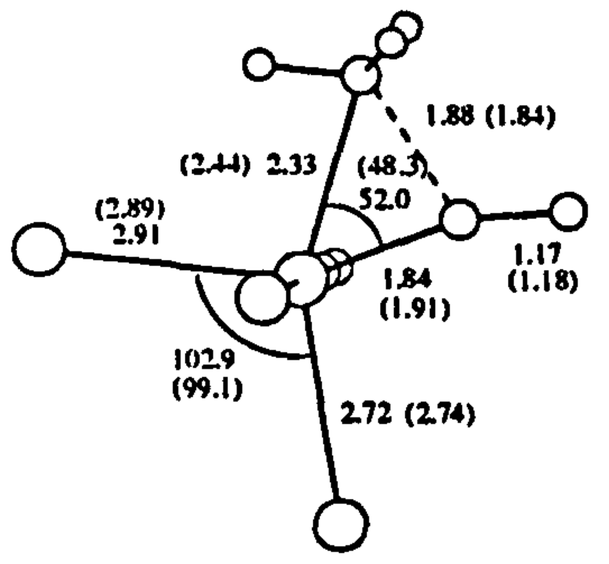

rx=0

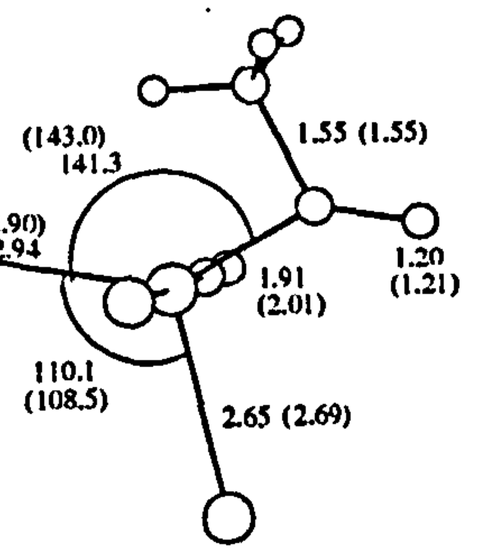

rx=+1

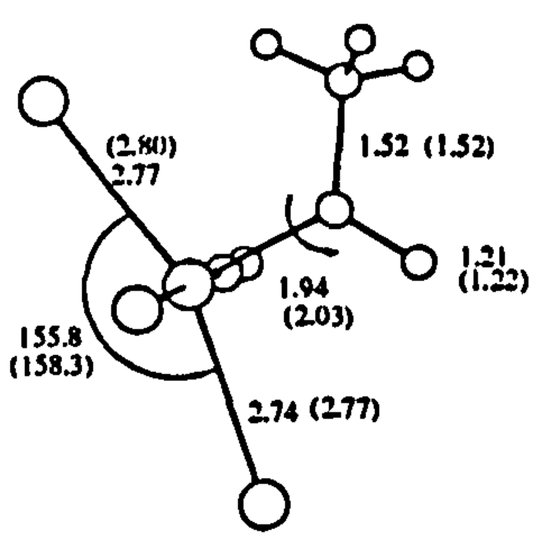

rx=+6

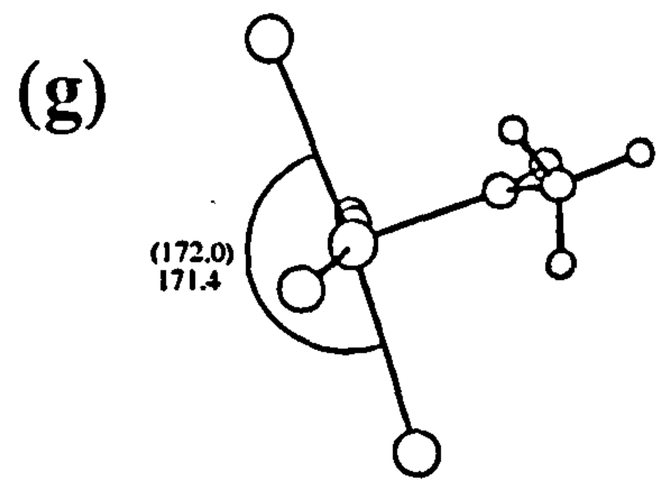

rx=+9

Figure 6.7: Optimized molecular geometries at seven points along the reaction co-ordinate for migratory insertion in $[CH_3Rh(CO)_2I_3]^-$. The numbers in parentheses are the corresponding parameters taken off the reaction co-ordinate for iridium.

(a) M=Rh

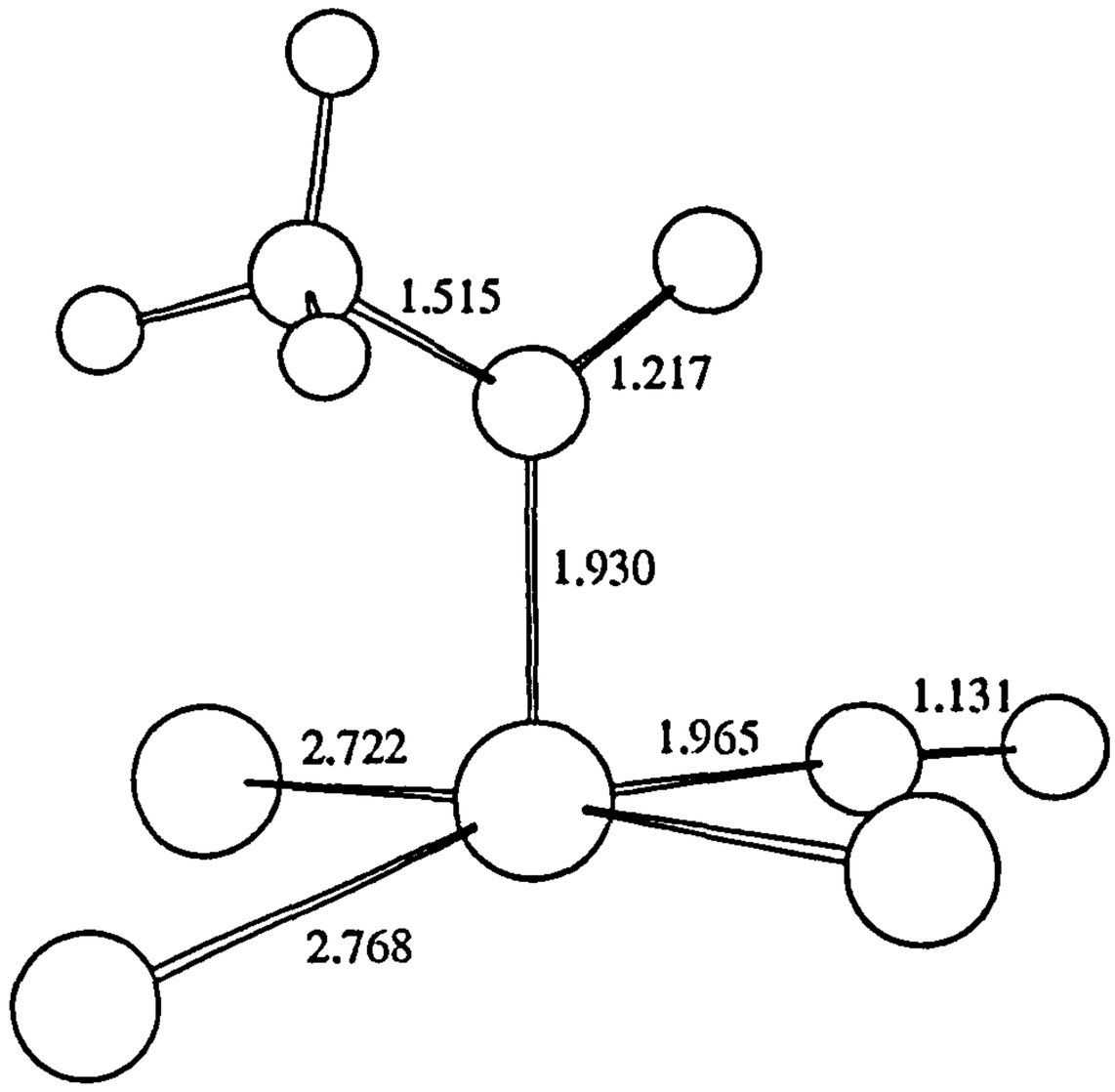

(b) M=Ir

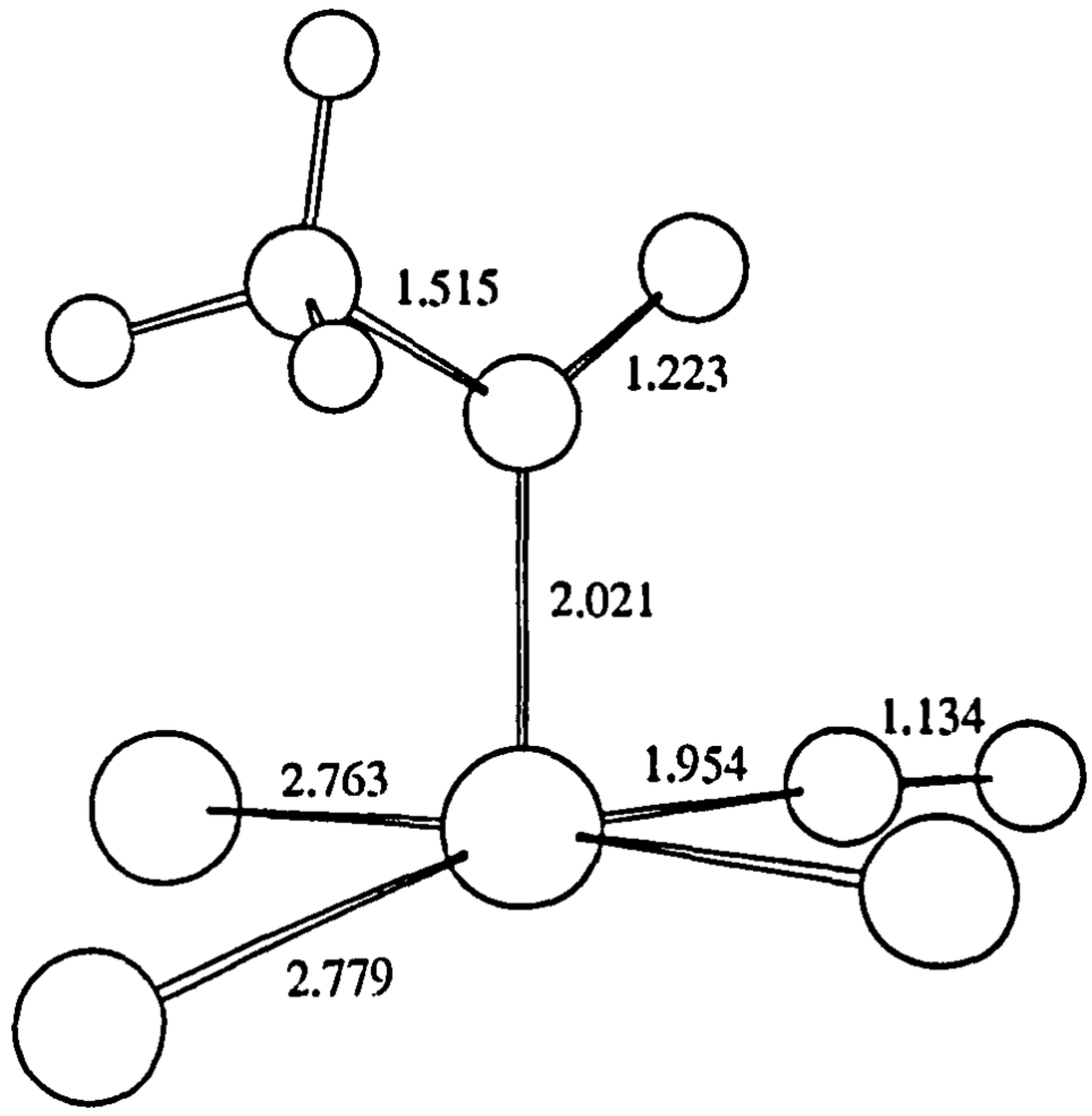

Figure 6.8: Optimized geometries of the five co-ordinate acyl complex $[(COCH_3)M(CO)I_3]^-$ resulting from migratory insertion. The parameters for rhodium (a) were obtained from RHF/DZ calculations and for iridium (b) from RHF/DZ2 calculations.

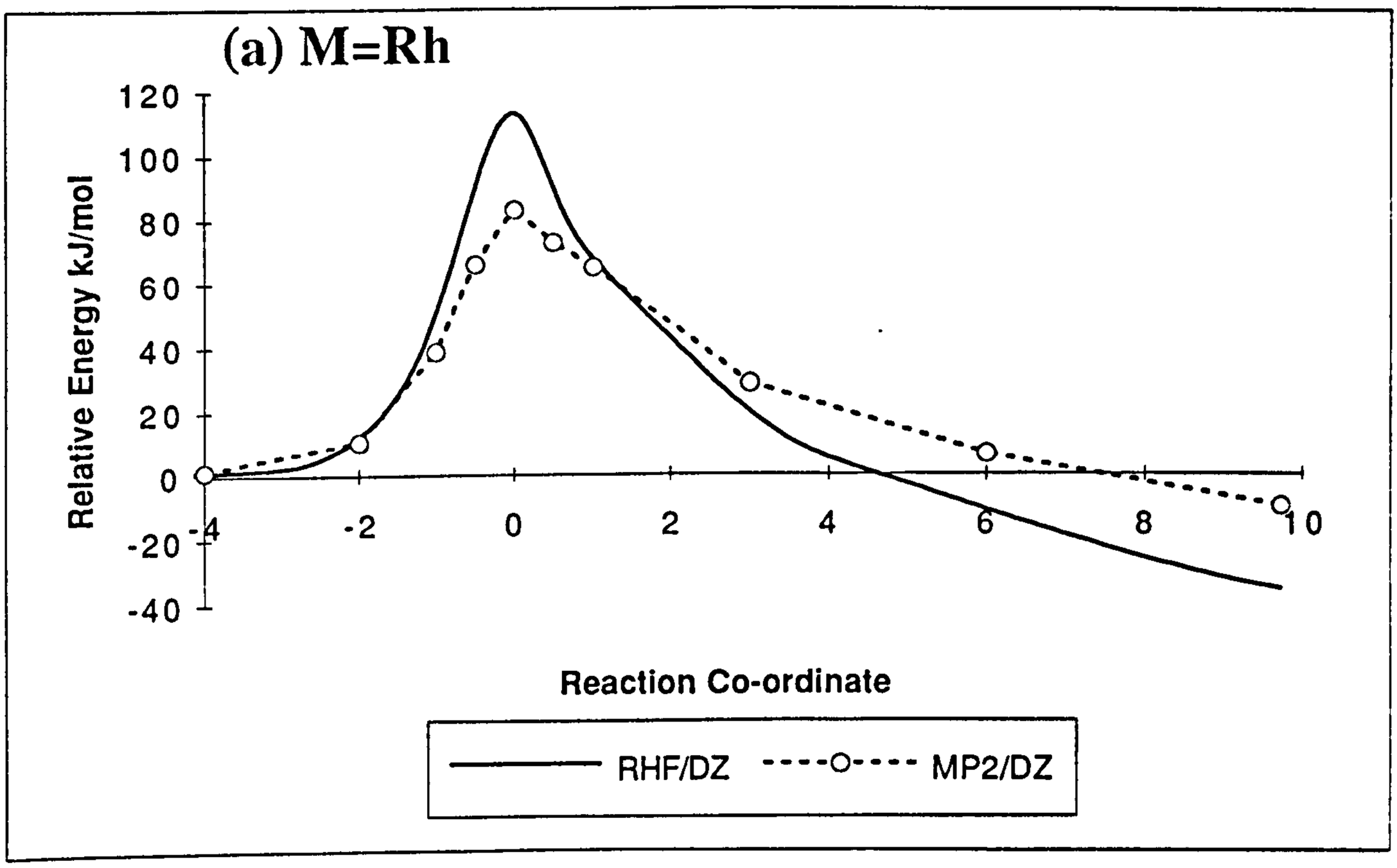

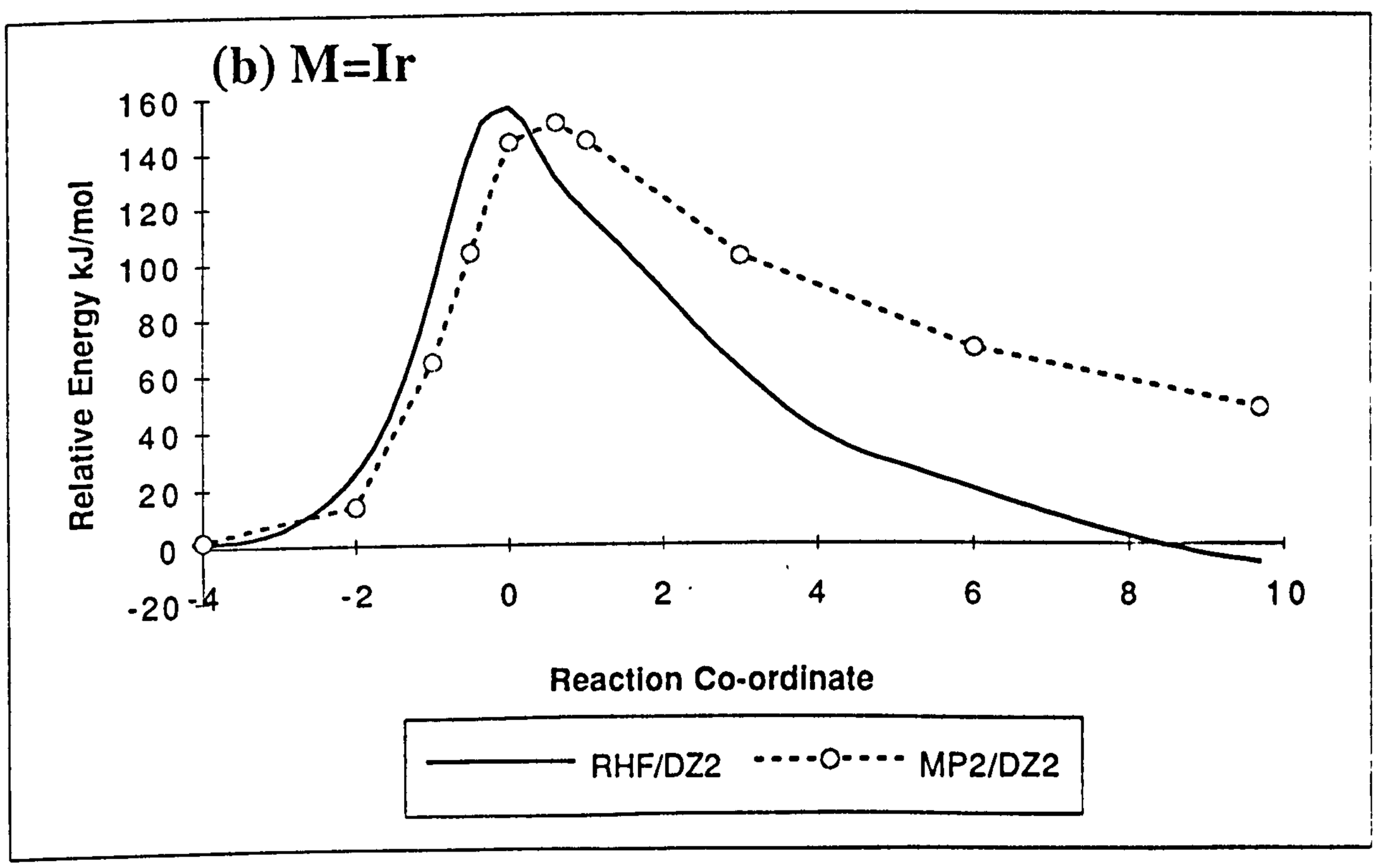

Figure 6.9: Effect of MP2 electron correlation (dashed line) on the RHF reaction co-ordinates (solid line) for migratory insertion in (a) $[CH_3Rh(CO)_2I_3]^-$ and (b) $[CH_3Ir(CO)_2I_3]^-$. Data has been obtained using the DZ basis for rhodium and the DZ2 basis for iridium.

Table 6.1: Relative energies of stationary points computed for the migratory insertion reaction: $[CH_3M(CO)_2I_3]^- \rightarrow [(CH_3CO)M(CO)I_3]^-$. Parameters refer to those defined in Figure 1.10.
All energies are in $kJmol^{-1}$.

Model	Basis	$\Delta E_f^{\ddagger}$	$\Delta E_b^{\ddagger}$	ΔE_{mig}
		M=Rh		
RHF	DZ	113.3	152.3	−39.0
MP2[a]	DZ	82.6	92.6	−10.0
MP2[a]	DZ*	63.0	108.5	−45.5
		M=Ir		
RHF	DZ2	156.9	166.1	−9.2
MP2[b]	DZ2	161.7	105.6	+56.1
MP2[b]	DZ2*	131.1	86.4	+44.7

[a]Single-point MP2 calculations on optimized RHF/DZ geometries.
[b]Single-point MP2 calculations on optimized RHF/DZ2 geometries.

dependence on the rotation of the acyl group around the M–C axis. Rotation of this ligand by 180° into the alternative C_s conformation with the C–O unit above a basal iodide caused the greatest destabilization of *ca.* 15 kJ mol^{-1} (MP2/DZ calculations).

The energetics of the migratory insertion reaction calculated at the RHF and MP2 levels of theory are given in Table 6.1. At the RHF level, the migratory insertion reaction in $[CH_3Rh(CO)_2I_3]^-$ has a calculated forward barrier of 113 kJ mol^{-1}, a barrier for the reverse process, 'deinsertion', of 152 kJ mol^{-1} and an exothermicity of −39 kJ mol^{-1}. The iridium system has a rather larger forward barrier of 157 kJ mol^{-1}, a similar deinsertion barrier of 166 kJmol $^{-1}$ and an exothermicity of −9 kJ mol^{-1}. The effect of electron correlation on the reaction co-ordinates has been examined by carrying out single-point MP2 calculations on selected geometries taken from the pathways computed at the RHF level. The results are displayed in Figure 6.9. In the IRC calculated for the rhodium system there is a significant reduction in the energy of the TS and an increase in the energy of the acyl product. The corresponding profile for iridium displays an even greater destabilization in the product but only a minor reduction in the energy of the TS which is also displaced slightly later along the reaction co-ordinate. The marked effect of electron correlation on the reaction energetics is primarily due to changes in covalent bonding between the central metal and the carbonyl ligand (see section 6.3.3).

To obtain more reliable energetics we have carried out single-point MP2 calculations on the stationary points using the extended DZ* and DZ2* basis sets which incorporate a set of polarization functions for each atom. The forward and reverse

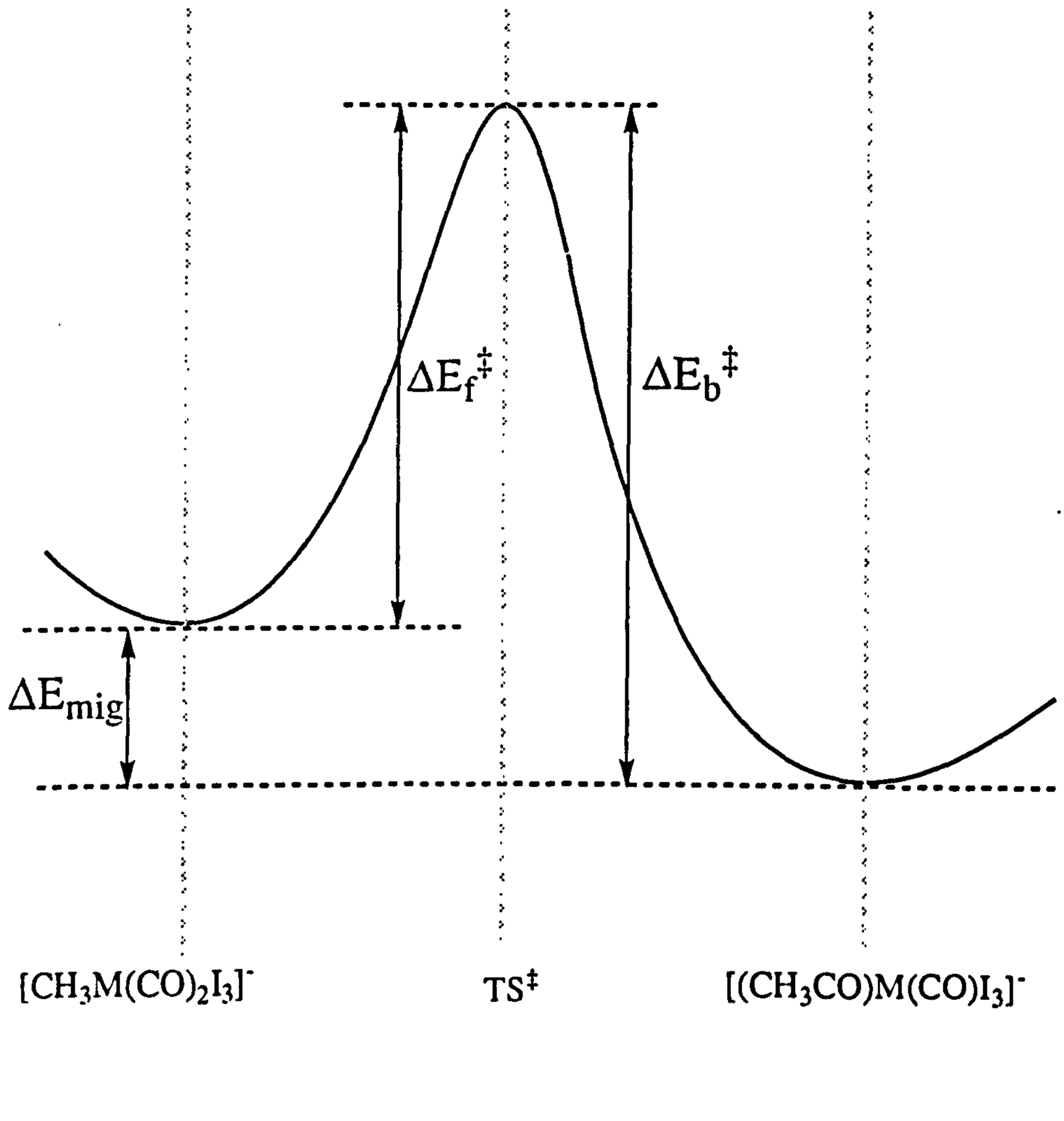

Figure 6.10: Schematic diagram of the energy profile for migratory insertion in $[CH_3M(CO)_2I_3]^-$.

barriers for the rhodium system calculated using this scheme are 63 and 109 kJ mol^{-1}, respectively. These values are in excellent agreement with the experimental activation enthalpies measured in neat CH_3I by Haynes *et al.* [15], which are 63 and 100 kJ mol^{-1}, respectively. The forward activation barrier for the iridium process has been measured in neat PhCl as 155 kJ mol^{-1} [67, 68]. This appears to agree fairly well with the value of 131 kJ mol^{-1} calculated here but the comparison may be complicated by the participation of an iodide dissociative pathway; that is, migratory insertion occurring directly in the anion, $[CH_3Ir(CO)_2I_3]^-$, and also in the neutral tricarbonyl, $[CH_3Ir(CO)_3I_2]$, following dissociation of an iodide ligand. If both of these mechanisms contribute to the overall rate then the activation enthalpy will be a combination of the enthalpies for the two mechanisms. Notwithstanding, migratory insertion in $[CH_3Ir(CO)_2I_3]^-$ alone would certainly be expected to have a significantly larger activation barrier than for the corresponding reaction in the rhodium alkyl complex. The calculated barrier for deinsertion from the iridium acyl complex at the MP2/DZ2* level is substantially lower than the forward barrier at 86 kJ mol^{-1}. Thus, migratory insertion in $[CH_3Ir(CO)_2I_3]^-$ is predicted to be endothermic by 48 kJ mol^{-1}. These values are consistent with the experimental observations. In the absence of CO pressure, migratory insertion in $[CH_3Ir(CO)_2I_3]^-$ does not take place, even when the temperature is elevated beyond 100°C [67]. This can be explained by the lower barrier to deinsertion which will cause all species undergoing migratory insertion to rapidly revert back to their original alkyl state. CO is required to trap any acyl complex formed by coordinating in the vacant site, leading to formation of the stable octahedral species $[(COCH_3)Ir(CO)_2I_3]^-$.

6.3.3 Electronic Structure and Bonding

We have examined the electronic structure changes that take place during the migratory insertion reaction. Several orbital interactions that contribute to the activation barrier and the stability of the acyl products can be identified. The most important of these are illustrated schematically in Figure 6.11, labelled (i) to (x).

In the reactant the most important component of the M–CH_3 bonding is the interaction of a d_{z^2}-type orbital centred on the metal with a σ_{CH_3} orbital on the methyl group. This gives rise to the M–CH_3 σ bonding orbital shown schematically in (i). A three-dimensional representation of the Rh–CH_3 σ orbital calculated from the Hartree-Fock wavefunction is displayed in Figure 6.12a. The M–CO bonding is similarly provided by a σ interaction directed along the M–CO axis (ii) but there are also significant contributions from carbonyl to metal π back-donation. For a qualitative analysis, the π bonding can be reduced to one in-plane and one out-of-plane component, as shown in (iii) and (iv), respectively.

(i)

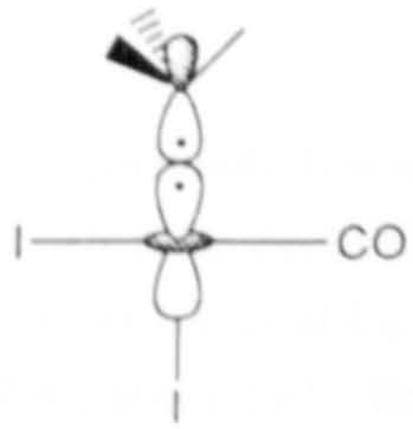

(ii)

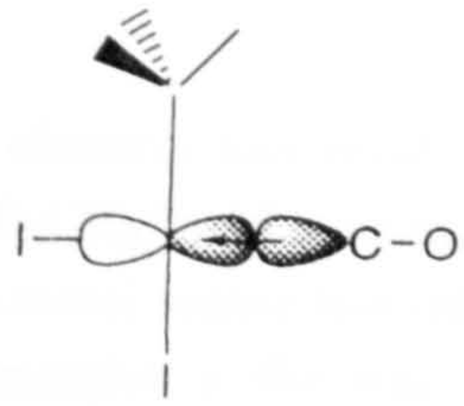

(iii)

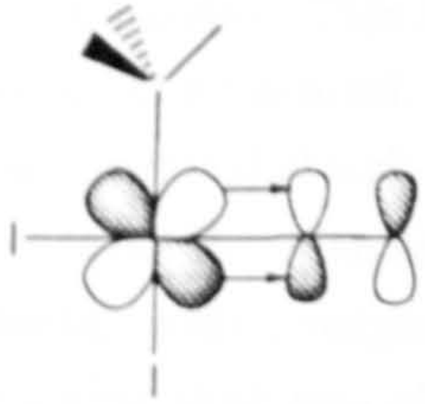

(iv)

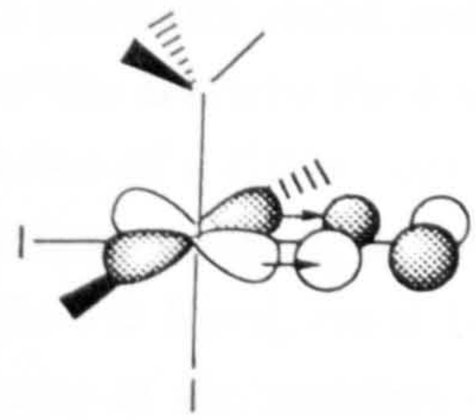

(v)

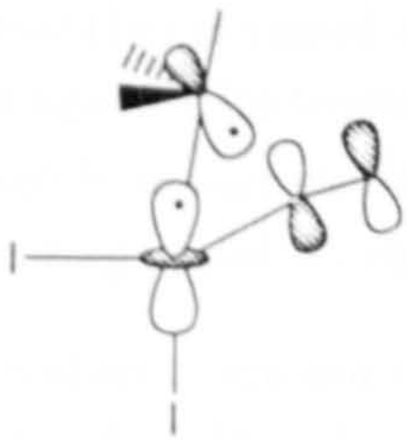

(vi)

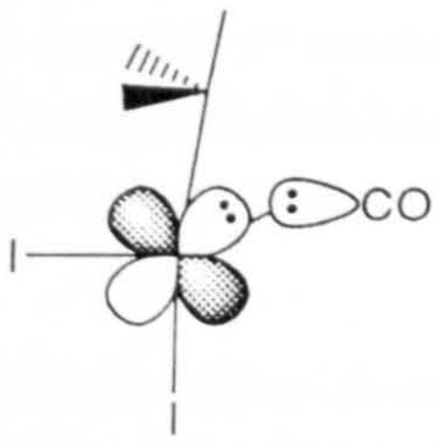

(vii)

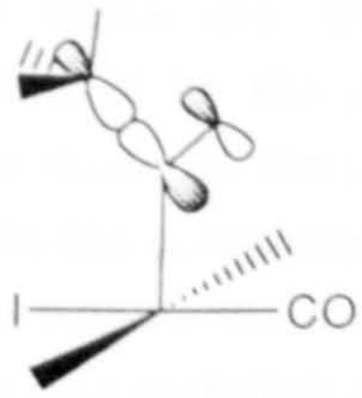

(viii)

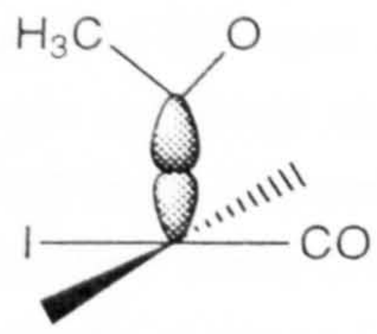

(ix)

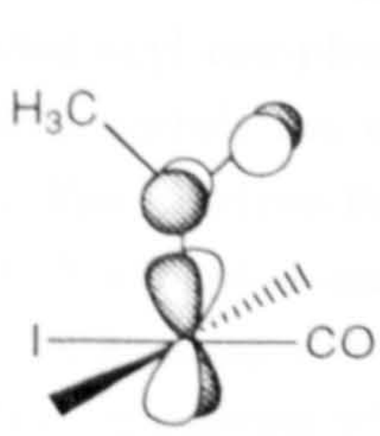

(x)

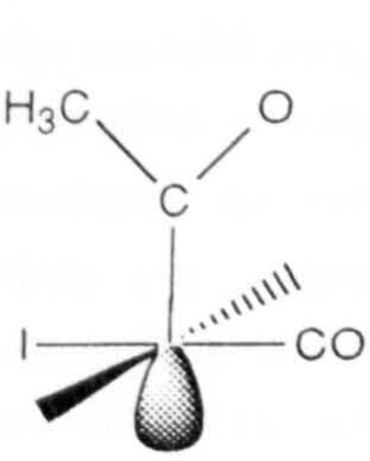

Figure 6.11: Schematic illustration of the molecular orbitals relevant to the migratory insertion reaction.

As the reaction proceeds toward the transition state, the electron pair residing in the M-CH_3 σ orbital is destabilized. This is because the M-CH_3 bond is elongated and has to reorient its local C_3 axis slightly away from the metal centre toward the carbonyl carbon atom (v). Examination of the orbital energies in the reactants and the TS reveals that this destabilization is the greatest of any orbital involved in the migratory insertion and is therefore expected to be the major contributor to the activation barrier. This interaction can, however, be partially stabilized by involvement of a CO π^* orbital, as indicated in (v). A plot of the Hartree-Fock Rh-CH_3 σ molecular orbital clearly demonstrates the participation of a CO π^* orbital at the TS, Figure 6.12b. Also note the π-type bonding overlap developing between CO and the metal, which suggests a strengthening of the Rh-CO bond, consistent with the shortening that was observed during the early stages of the reaction co-ordinate. There are two other significant destabilizing interactions that occur on the reactant side of the pathway. The energy of the metal *d* electrons in the in-plane π orbital (iv) is raised by the reduction in the metal *d* to CO π^* overlap as the carbonyl ligand tilts towards the methyl group. There is also a destabilization of the carbonyl lone pair electrons as these enter into greater repulsive interactions with non-bonding metal *d* orbitals (vi).

In the acyl product there are two new bonding interactions which can be identified as a C-C σ bond (vii) and a M-C(OCH_3) σ bond (viii). The former is derived from the increased interaction between the occupied σ_{CH_3} orbital and the vacant in-plane π^* orbital centred on CO. The latter is formed from a modification to the M-CO σ orbital (ii). One electron pair residing in an out-of-plane metal *d* orbital is stabilized by the interaction with a π^* orbital on the CO unit of the acyl group, as shown in (ix). The energy of this orbital is not markedly changed with respect to the corresponding orbital in the alkyl reactant (iv). However, the other electron pair in the *d* orbital coincident with the migration plane (iii) has completely lost its stabilizing back-donative interaction since the in-plane CO π^* orbital becomes completely involved in the C-C σ bond on the acyl group. The loss of the in-plane π bonding component is mainly responsible for the instability of the unsaturated acyl complexes. This is also the reason for the destabilizing effect of MP2 electron correlation on the product side of the RHF reaction co-ordinates (Figure 6.9). The Hartree-Fock model significantly underestimates the extent of covalent M-CO π back-donation[183]. When MP2 corrections are applied, the species with the greatest π bonding will be stabilized the most, which will clearly favour the alkyl complexes with both in-plane and out-of-plane metal to carbonyl π back-donation.

In the course of the migratory insertion a low-lying virtual orbital pointing toward the vacant site of the five co-ordinate acyl intermediate is created (x). This is an acceptor orbital with mainly d_{z^2} character, suggesting that an incoming ligand or donating solvent could have a stabilizing influence on the reaction energetics.

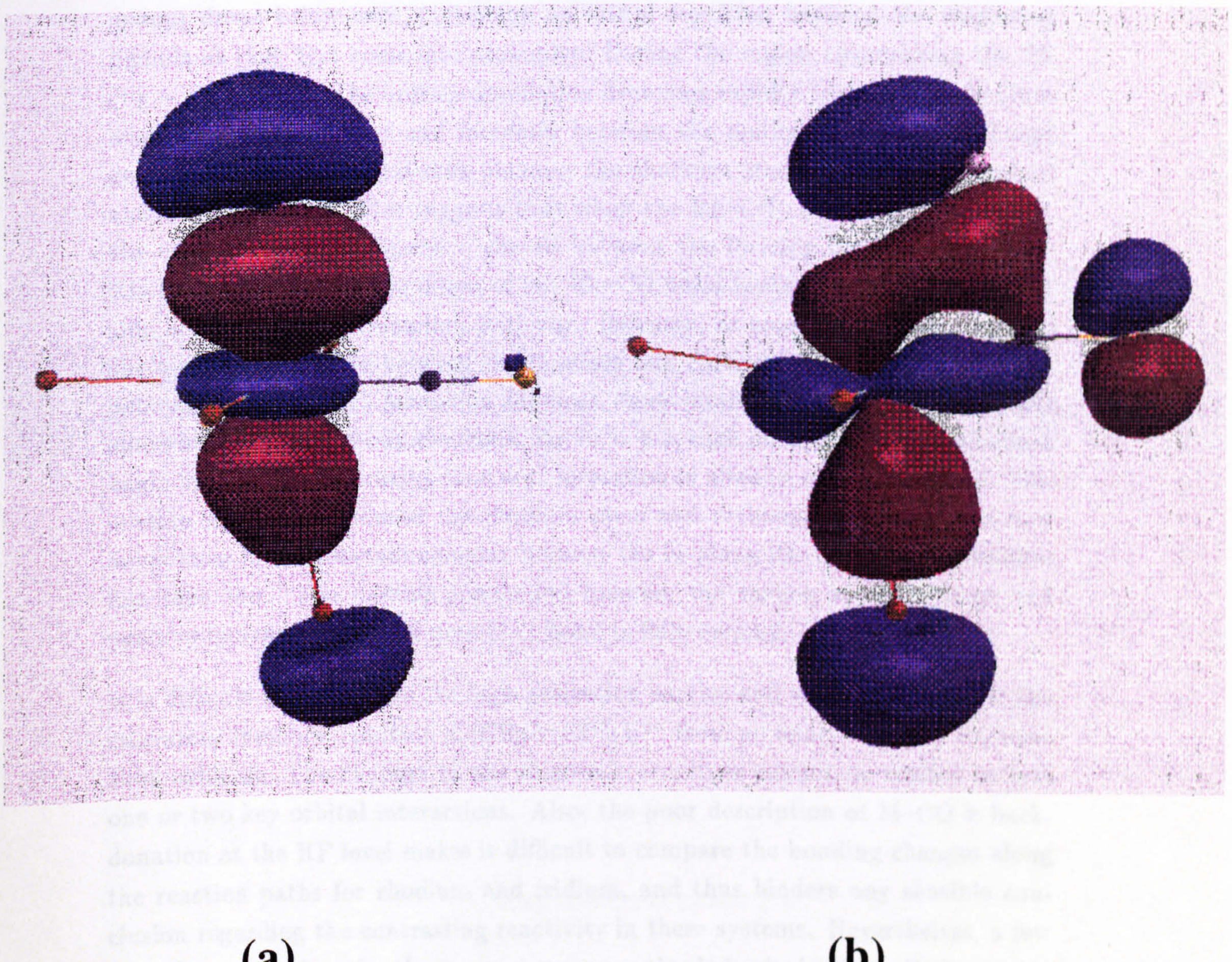

Figure 6.12: Three-dimensional plots of the Rh–CH_3 σ bonding orbital in (a) $[CH_3Rh(CO)_2I_3]^-$ and (b) the migratory insertion TS. The latter shows the involvement of a CO π^* orbital which stabilizes the TS during Rh–CH_3 rupture.

However, it is important to note that this orbital is not established until the intermediate is nearly fully formed and in particular that the energy of this orbital is high in the TS region.

The bonding changes can perhaps be put in a clearer perspective by examining the results of a Mulliken population analysis. Figure 6.13 shows the ⟨Rh|C(H_3)⟩, ⟨Rh|C(O)⟩ and ⟨C|C⟩ atomic overlap populations plotted as a function of the migratory insertion reaction co-ordinate for the rhodium system. In the early stage of the reaction ($rx \sim -5.0$ to -2.0), the overlap between the methyl and carbonyl groups drops below zero, indicating an initial repulsion between the migrating ligands as they first come into proximity. During the region approaching the TS ($rx \sim -2.0$ to 0.0), the overlap population decreases rapidly between the rhodium atom and methyl group and increases between the methyl group and carbonyl group. The overlap population between the rhodium atom and carbonyl carbon atom also increases. This suggests that when the Rh–CH_3 bond begins to break, the electron density released is shared between the forming C–C bond and the Rh–CO bond. This is the origin of the Rh–CO bond contraction on the reactant side of the migratory insertion pathway. However, as soon as the TS is passed, the overlap population between the rhodium and carbonyl carbon atom starts to decrease as C–C bond formation becomes more established and takes a greater share of the methyl group electrons. By $rx = 2.0$, each of the overlap populations begin to level off, indicating that acyl formation is already nearly complete. The overlap population between the rhodium atom and carbonyl carbon atom is now lower than in the reactant complex because the in-plane Rh–CO π back-donation has been lost. The overlap population between the carbon atoms is large and positive indicating that the acyl C–C bond is fully formed.

It is difficult to rationalize the high activation barrier and endothermicity for the migratory insertion reaction in $[CH_3Ir(CO)_2I_3]^-$ from an analysis of the Hartree-Fock orbitals. The changes in the electronic structure cannot be related to just one or two key orbital interactions. Also, the poor description of M–CO π back-donation at the HF level makes it difficult to compare the bonding changes along the reaction paths for rhodium and iridium, and thus hinders any sensible conclusion regarding the contrasting reactivity in these systems. Nevertheless, a few tentative suggestions for the poor migratory aptitude in the iridium alkyl complex can be made.

In chapter 6 two reasons for the apparently increased strength of Ir–CH_3 bonds compared to Rh–CH_3 bonds were discussed. The first was a larger bond polarity which has been suggested leads to a reduced destabilization of M–CH_3 bonds for the heavier transition metal [247, 248]. The second argument was based on the increased participation of metal *s* orbitals which can form optimum hybrids with the *d* orbitals and thus form stronger M–CH_3 bonds [228]-[233]. Both arguments, in particular the latter one, can probably be linked to the relativistic effect for the 5*d*

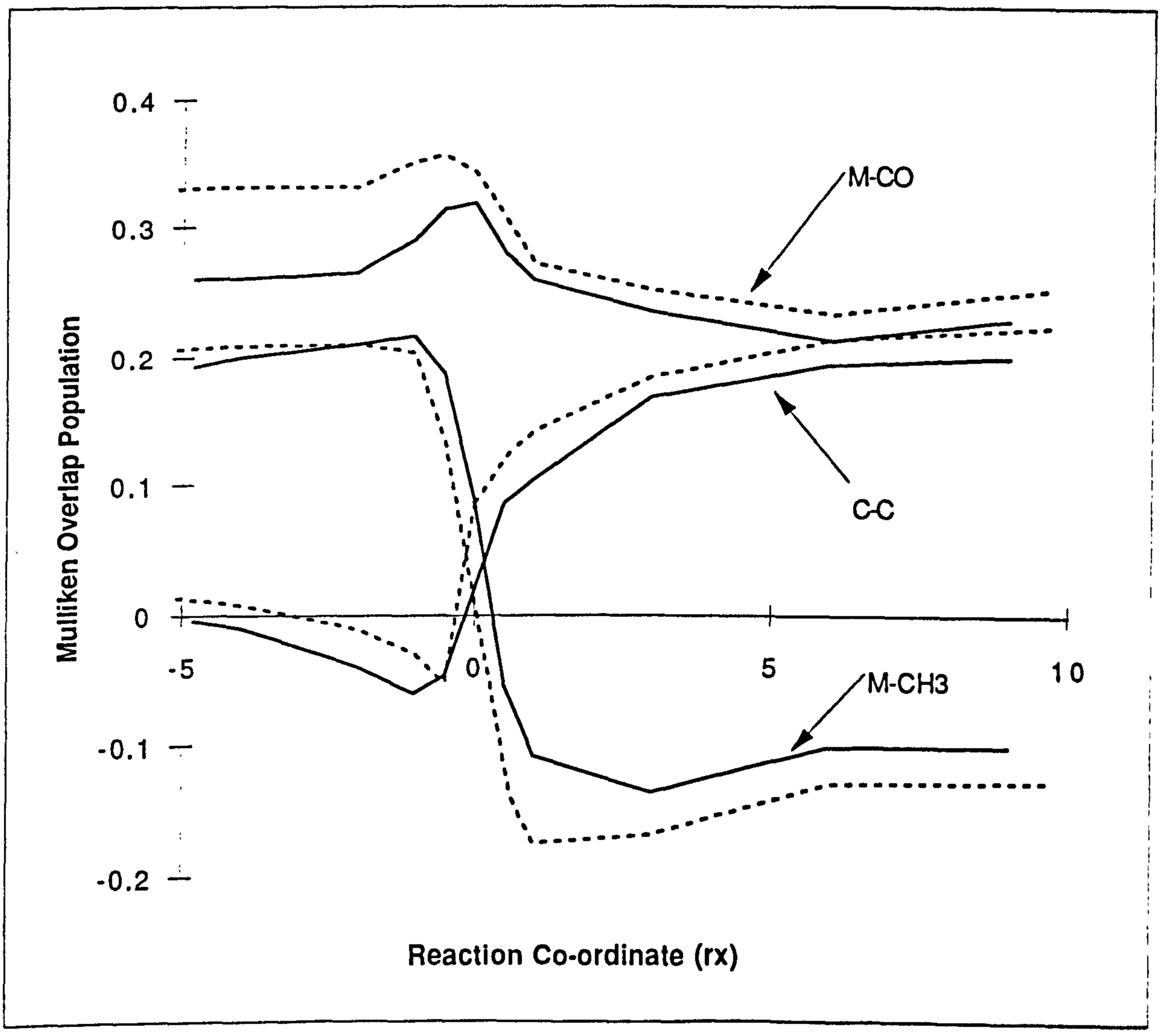

Figure 6.13: M–CH_3, M–CO and C–C Mulliken overlap populations plotted as a function of the reaction co-ordinate for migratory insertion in $[CH_3Rh(CO)_2I_3]^-$ (solid line; RHF/DZ) and $[CH_3Ir(CO)_2I_3]^-$ (dashed line; RHF/DZ2). Note that $rx = 0.0$ corresponds to the TS in each case.

metals. Ziegler has calculated M–CH_3 bond dissociation energies in $[CH_3M(CO)_4]$ and $[CH_3MCp(CO)]$ using DFT and found that the bonds to iridium were stronger by 20 to 30 kJ mol^{-1} than in the corresponding rhodium complexes [247, 249]. The inertness of $[CH_3Ir(CO)_2I_3]^-$ can therefore be partly rationalized in terms of a greater M–CH_3 strength. This is the most generally accepted explanation for the different reactivity that is observed. We note in this regard, that the energy of the Ir–CH_3 σ orbital is raised slightly more in the TS than the corresponding orbital in the rhodium system. However, the substantial difference in the calculated activation barriers (*ca.* 70 kJ mol^{-1} at the MP2 level) would tend to suggest the involvement of another factor.

While both systems derive their greatest contribution to the activation barrier from a destabilization of the key M–CH_3 σ orbital, migratory insertion in the iridium system also appears to cause substantial destabilization (greater than for rhodium) to several orbitals which have M–CO π bonding components. The relativistic effect causes atomic *d* orbitals to become higher in energy and more diffuse in space. The expansion of the 5*d* orbitals in the iridium alkyl complex leads to a larger overlap between metal *d* orbitals and the carbonyl π^* orbitals. Such a larger overlap could make the back-donative interaction more favourable and thus the Ir–CO bond stronger. Infra red spectroscopic data for the $[CH_3M(CO)_2I_3]^-$ (M=Rh, Ir) complexes support this view, where it is found that the C–O stretching frequencies are smaller for the iridium species. Previous theoretical investigations have also provided evidence for stronger M–CO bonds in the 5*d* transition metals. Koga and Morokuma calculated mean relative metal–carbon bond strengths in the $[CH_3M(CO)(H)(PH_3)]$ (M=Pd, Pt) complexes [263]. At the MP2 level the M–CO bond was predicted to be stronger in the Pt complex by *ca.* 47 kJ mol^{-1}. Thus, it is reasonable to conclude that Ir–CO bonds are stronger than Rh–CO bonds in $[CH_3M(CO)_2I_3]^-$ and that changes to this bonding will also lead to a more significant contribution to the activation barrier for migratory insertion in the iridium system. The computed enthalpy changes also suggest that the iridium complexes have a greater dependence on π back-donation for their stability. In the transformation of alkyl to acyl species, loss of the in-plane π back-donative interaction is associated with a larger energy penalty, the computed enthalpy change for iridium being more endothermic at the MP2 level by 90 kJ mol^{-1}.

The Mulliken overlap populations plotted as a function of the migratory insertion reaction co-ordinate for the iridium system are shown in Figure 6.13. A careful comparison with the corresponding graph for rhodium reveals that the greatest difference is actually for the metal to carbonyl overlap populations, rather than the metal to methyl overlap populations. In the reactant complex ($rx \sim -5.0$) the $\langle Ir|C(O)\rangle$ overlap is significantly larger (0.33) than the corresponding value for rhodium (0.26). This difference is much greater than that between the rhodium and iridium metal–methyl overlap populations (0.01). The Mulliken scheme would

therefore imply that the difference between Ir–CO and Rh–CO bond strengths in the $[CH_3M(CO)_2I_3]^-$ complexes is greater than the difference between Ir–CH_3 and Rh–CH_3 bond strengths. The increase in the ⟨Ir|C(O)⟩ overlap population is lower than for rhodium in the region $rx \sim -5.0$ to 0.0, which correlates with the smaller Ir–CO bond contraction that was observed along the iridium reaction co-ordinate. One possible explanation for this latter observation is that the iridium *d* electrons are reluctant to release the CO π^* orbital from the π back-donative interaction. This could inhibit the stabilizing interaction of the CO π^* orbital with the Ir–CH_3 σ orbital at the TS, and also reduce the electron density transferred to the Ir–CO bond that occurs during the part of the reaction. Another significant difference is observed for the net reduction in the ⟨M|C(O)⟩ overlap population from the alkyl reactant to acyl product species resulting from the loss of the in-plane π back-donative interaction. The reduction for iridium is about twice that observed along the rhodium reaction co-ordinate which correlates with the unfavourable enthalpy change computed for migratory insertion in the iridium system.

To summarize, the largest contribution to the activation barrier for migratory insertion in $[CH_3M(CO)_2I_2]^-$ comes from a destabilization of the M–CH_3 σ orbital. The energy of this orbital can be lowered to some extent in the TS by the involvement of a CO π^* orbital. The transformation of alkyl to acyl complexes results in the loss of one M–CO π back-donative interaction. The difference in reactivity between rhodium and iridium $[CH_3M(CO)_2I_3]^-$ complexes can be ascribed to the greater strength of M–C bonds for a 5*d* transition metal. Analysis of the orbital energies and atomic overlap populations has suggested that the high activation barrier and unfavourable enthalpy change in the iridium system can be related to both stronger Ir–CH_3 *and* Ir–CO bonds.

6.3.4 Solvent Effects

There are several potential ways in which a solvent could influence the migratory insertion reaction in $[CH_3M(CO)_2I_3]^-$:

(i) Co-ordination of a donating solvent molecule at either the TS or in the vacant site of the unsaturated acyl intermediate;

(ii) Stabilization of localised areas of charge by the static effect of a polar medium;

(iii) Acid catalysis occurring by, for example, hydrogen bonding to the oxygen atom of the forming acyl ligand;

(iv) Facilitation of the removal of an iodide ligand to form an alkyl species which is more labile with respect to migratory insertion.

These points are discussed in turn below.

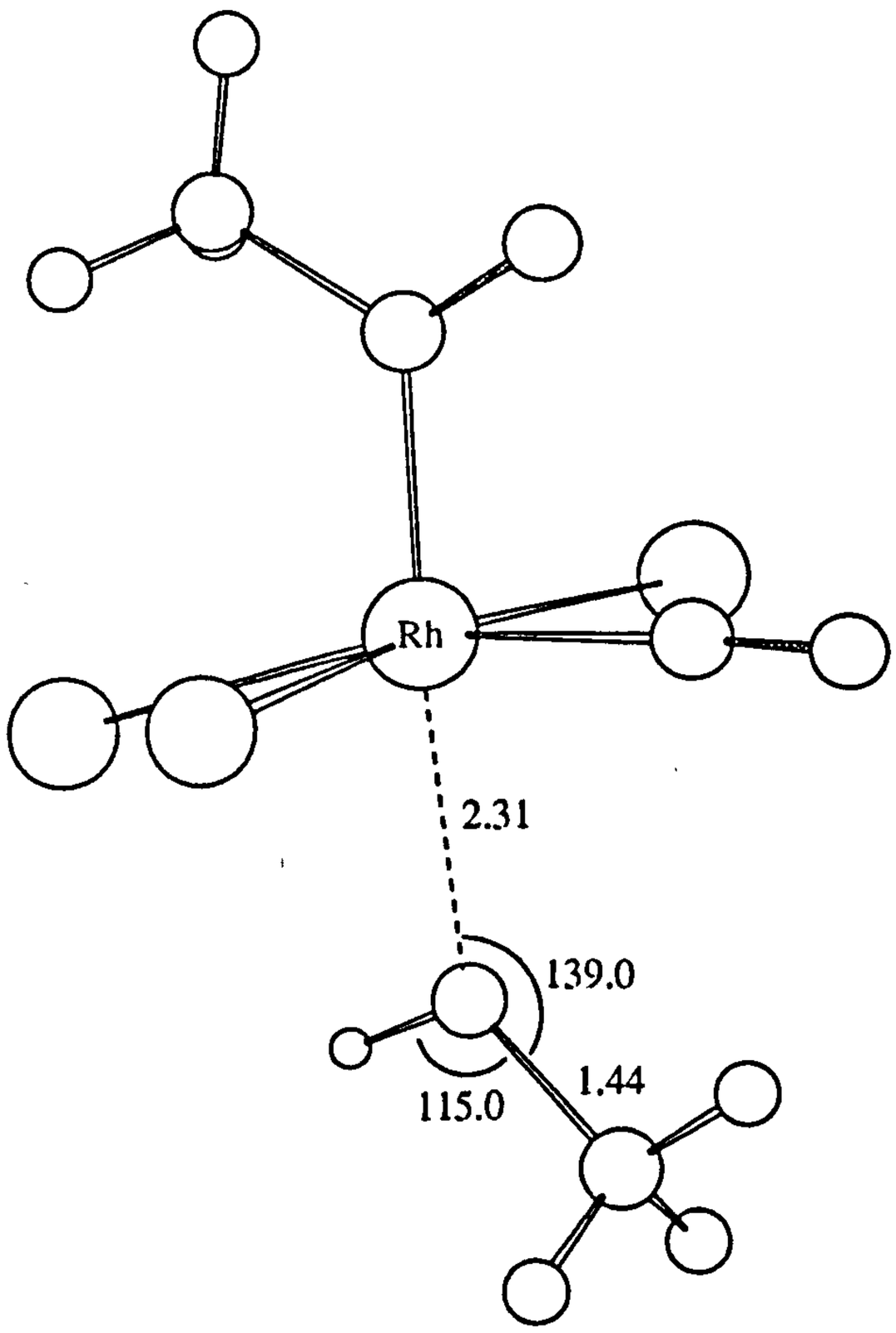

Figure 6.14: Geometry of $[(COCH_3)Rh(CO)(CH_3OH)I_3]^-$. Note that only the parameters for CH_3OH were allowed to vary. The geometry of the five co-ordinate acyl fragment was frozen at the geometry computed at the RHF/DZ level (Figure 6.8).

Co-ordination of Donating Solvent Molecules

Analysis of the orbital changes along the reaction co-ordinate showed that a suitable acceptor orbital that could be utilised by a stabilizing solvent molecule was not created until after the TS had been passed. Hence, an incoming solvent molecule would be expected to stabilize the five co-ordinate acyl intermediate but not the transition state for the migratory insertion reaction. Mann *et al.* have studied the solution behaviour of $[(COCH_3)Rh(CO)I_3]^-$ using ^1H and ^{13}C NMR spectroscopy [199]. In non-co-ordinating solvents it exists as a dimer held together through bridging iodide ligands. Co-ordinating solvents such as methanol can split the iodide bridges to form the monomeric solvated species $[(COCH_3)Rh(CO)(CH_3OH)I_3]^-$. We have optimized the geometry of a CH_3OH molecule in the vacant site of a (frozen) rhodium acyl complex $[(COCH_3)Rh(CO)I_3]^-$. The resulting structure incorporating methanol as a ligand is shown in Figure 6.14. The CH_3OH molecule aligns itself in the C_s symmetry plain of the acyl complex, with the CH_3 group favouring the carbonyl side. The $Rh\cdots O(HCH_3)$ distance is 2.31 Å. The total stabilization due to this interaction at the MP2/DZ level is *ca.* 44 kJ mol^{-1}.

The Static Solvent Effect

We have investigated the effect of a static solvent medium on the RHF reaction co-ordinates using the MP2 SCRF method. The results for dielectric media corresponding to a vacuum, CH_3I and CH_3OH are illustrated in Figure 6.15. The curves are nearly identical for each of the dielectric media considered, suggesting that this reaction is independent of the solvent polarity. This is the case for both the rhodium and iridium reaction profiles. These observations are consistent with the computed dipole moments which do not change to a significant extent during the migratory insertion reaction. In fact, the acyl intermediate appears to be slightly less stable in the more polar media but this effect is probably negligible compared to the stabilization that would result from co-ordination of a donating solvent molecule, as indicated by the calculation described above.

Acid Catalysis

The potential stabilizing influence of acid catalysis has been investigated by attaching a proton to the acyl oxygen atom in the transition state. A fully optimized TS computed for migratory insertion in the iridium complex with a proton in this position is shown in Figure 6.16. The single imaginary frequency confirmed that this was a true saddle point and the associated normal mode vibration displayed the characteristic bending of CH_3 and CO groups toward each other. The position

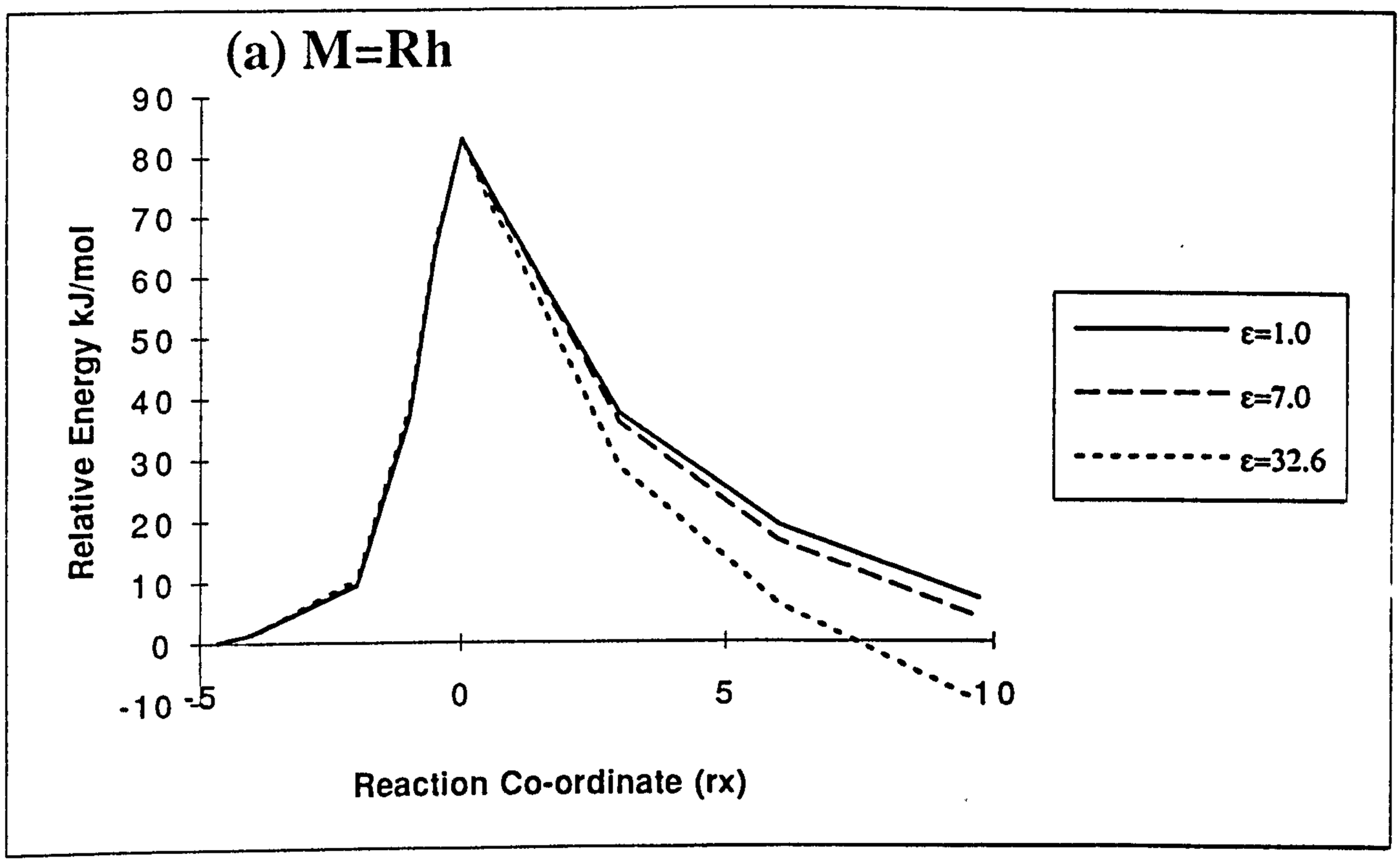

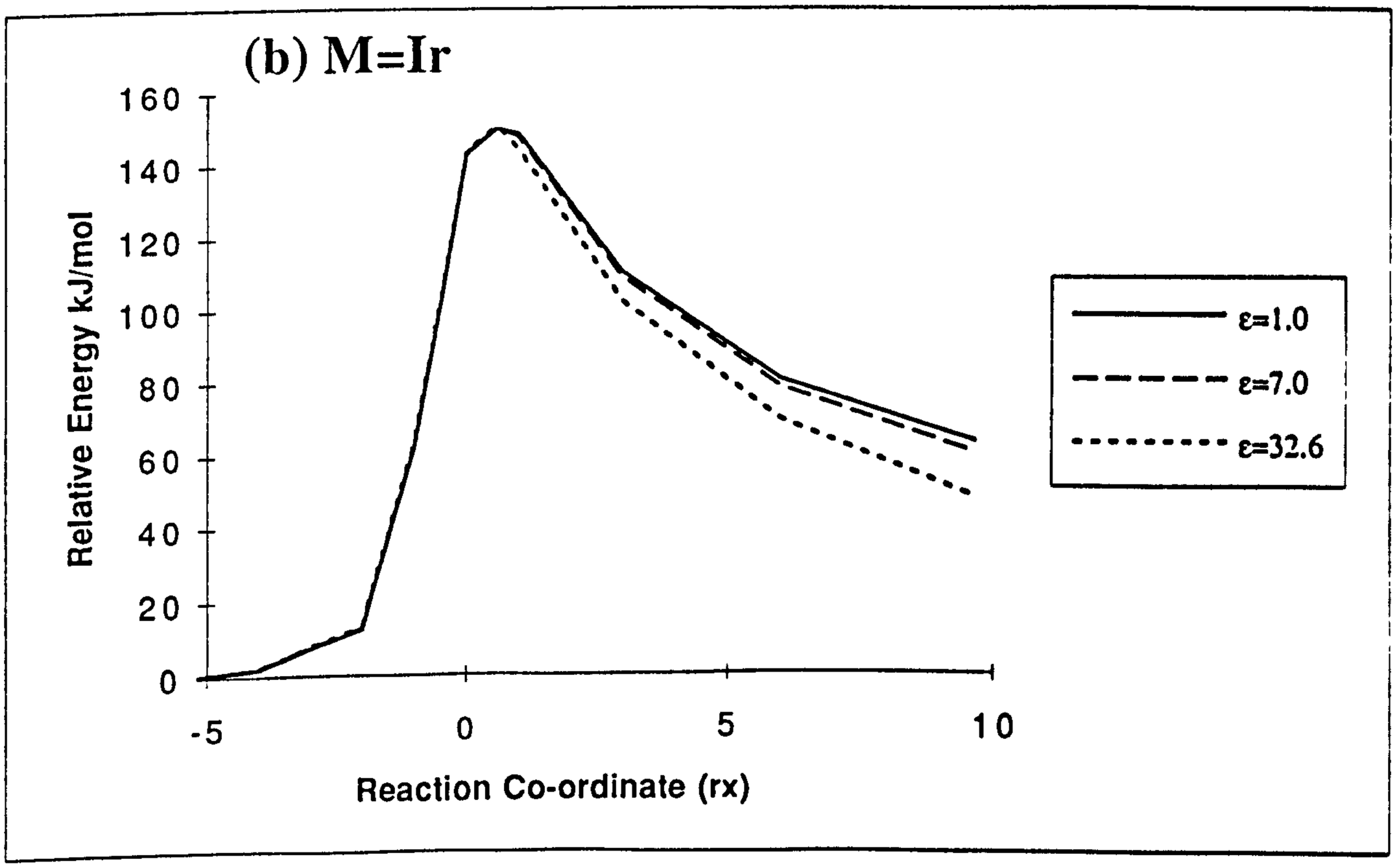

Figure 6.15: Effect of a static solvent medium on the reaction co-ordinate for migratory insertion in (a) $[CH_3Rh(CO)_2I_3]^-$ and (b) $[CH_3Ir(CO)_2I_3]^-$. Profiles corresponding to the gas phase (ϵ_r=1.0), methyl iodide (ϵ_r = 7.0) and methanol (ϵ_r = 32.63) are shown. Data deduced from MP2 SCRF calculations.

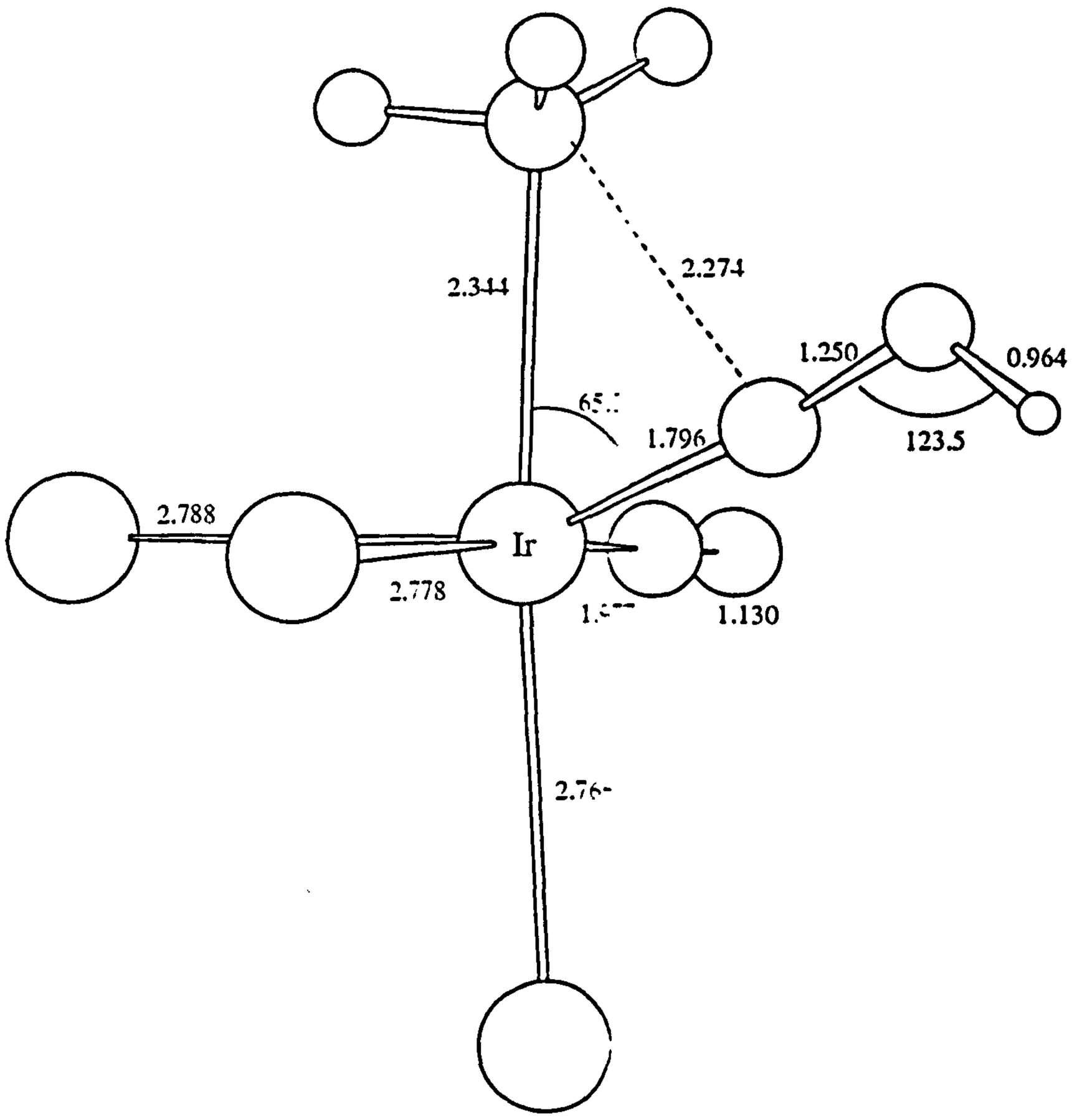

Figure 6.16: Effect of attaching a proton to the acyl oxygen in the transition structure for migratory insertion in $[CH_3Ir(CO)_2I_3]^-$. The geometry was optimized at the RHF/DZ2 level.

of the proton optimizes in the plane of migration with an O–H distance of 0.96 Å and a H–O–C angle of *ca.* 124°. The C–O bond is weakened, indicated by a lengthening of 0.07 Å, and tilts upward towards the methyl group. The rest of the parameters suggest that the action of the proton causes this transition state to be significantly earlier compared to the unperturbed structure described previously (Figure 6.5b). The forming C–C acyl bond is longer by 0.4 Å and the angle between the migrating groups is greater by 17°. The Ir–CH_3 bond is extended relative to the equilibrium geometry by *ca.* 0.2 Å compared to an elongation of 0.3 Å in the absence of the proton. Perhaps the most significant geometrical change though, is the enhanced contraction in the Ir–C(O) bond at 1.80 Å. The proton can delocalise the carbonyl lone pair electrons and reduce their repulsive interaction with metal *d* electrons (Figure 6.11(vi)). This allows the CO group to penetrate further in toward the metal centre which could also facilitate the stabilizing interaction of the CO π^* orbital with the M–CH_3 σ orbital (Figure 6.11(v). An intrinsic reaction co-ordinate for this TS was unstable and could not be calculated for more than a few steps. Also, a stable minimum energy structure for the reactant with a proton attached to the carbonyl ligand could not be optimized. These observations suggest that a proton can only interact with an acyl oxygen atom when migratory insertion is already underway.

Dissociation of an Iodide Ligand

Forster proposed that the rate determining step in the iridium catalytic cycle was the dissociation of an iodide ligand from $[CH_3Ir(CO)_2I_3]^-$ prior to a rapid migratory insertion in the tricarbonyl complex $CH_3Ir(CO)_3I_2$] [66] (Figure 1.5). It has recently been reported that added methanol can accelerate the rate of migratory insertion in this system by a factor of 10^4 [68]. The acceleration was proposed to arise from methanol aiding the slow dissociation of iodide by virtue of hydrogen bonding interactions (equation (6.4)).

To obtain an estimate of the activation barrier for iodide dissociation from the iridium alkyl complex, $[CH_3Ir(CO)_2I_3]^-$, we performed a series of calculations in which the axial Ir–I bond was increased stepwise while allowing the geometry of the five co-ordinate alkyl fragment to relax at each intermediate point. The simulated reaction paths for a vacuum and static solvent fields corresponding to CH_2Cl_2 and CH_3OH are shown in Figure 6.17. Note that this analysis does not take into account the specific hydrogen bonding interaction but the polarizing effect of the solvent medium would be expected to stabilize the charge separation and thus facilitate iodide dissociation. Pearson found that polar aprotic solvents such as acetonitrile, that do not have the facility to hydrogen bond, did cause a small but significant rate enhancement for migratory insertion in $[CH_3Ir(CO)_2I_3]^-$ [67]. It follows from Figure 6.17 that dissociation of an axial iodide ligand from

$[CH_3Ir(CO)_2I_3]^-$ is energetically unfavourable in a vacuum. There is no maximum in the profile, just a continuously rising energy. At infinite separation the energy change calculated at the RHF/DZ2 level is *ca.* +180.0 kJ mol^{-1}. In the low polarity medium, CH_2Cl_2 ($\epsilon_r = 9.08$), the profile is similar but begins to levels off at a Ir–I separation of about 4.5 Å. In the solvent field corresponding to CH_3OH, the profile assumes a slightly more familiar shape with a broad maximum occurring at *ca.* 4.3 Å. The approximate activation barrier is 64 kJ mol^{-1} suggesting that a polar medium would indeed facilitate iodide dissociation through the static solvent effect if nothing else.

The enthalpy change for reaction (6.11) has been estimated at the MP2/DZ2 level with and without the inclusion of solvent fields.

$$[CH_3Ir(CO)_2I_3]^- + CO \rightleftharpoons [CH_3Ir(CO)_3I_2] + I^-. \qquad (6.11)$$

The computed enthalpy changes in a vacuum, CH_2Cl_2 and CH_3OH are −80, −89 and −102 kJ mol^{-1} respectively. Thus, the reaction appears to be energetically favourable even when a solvent field is not included.

The ability of a polar solvent to facilitate iodide dissociation has never really been in dispute. A more pertinent issue, is concerned with whether substitution of iodide with carbonyl has a significant effect on the migratory insertion reaction. In particular, can migratory insertion in $[CH_3Ir(CO)_3I_2]$ take place with a low activation barrier and a favourable exothermicity? These questions are addressed in the next section.

6.3.5 Migratory Insertion in $[CH_3Ir(CO)_3I_2]$

Figure 6.18 shows the optimized alkyl reactant, transition state and acyl product for a migratory insertion reaction in the neutral tricarbonyl $[CH_3Ir(CO)_3I_2]$. First, inspecting the geometry of the reactant molecule one finds, perhaps surprisingly, that the optimized parameters are not markedly different to the corresponding parameters calculated for the anionic complex $[CH_3Ir(CO)_2I_3]^-$ (Figure 6.5b). In particular, the Ir–CH_3 bond is only 0.01 Å longer which does not suggest that this bond has been significantly weakened. Furthermore, the atomic overlap population between iridium and the methyl carbon is not reduced relative to the value calculated in the anionic complex. Replacing the iodide by a carbonyl ligand might be expected to weaken the Ir–CH_3 bond due to a greater *trans* influence. A slightly larger change relative to the geometry of $[CH_3Ir(CO)_2I_3]^-$ is observed in the equatorial Ir–CO bonds which are lengthened by 0.03 Å. This can be ascribed to a greater competition for the metal *d* electrons when an extra strong π accepting ligand is co-ordinated. The new axial carbonyl ligand has the longest Ir–CO length at 2.11 Å but this is probably a significant overestimate at the uncorrelated RHF

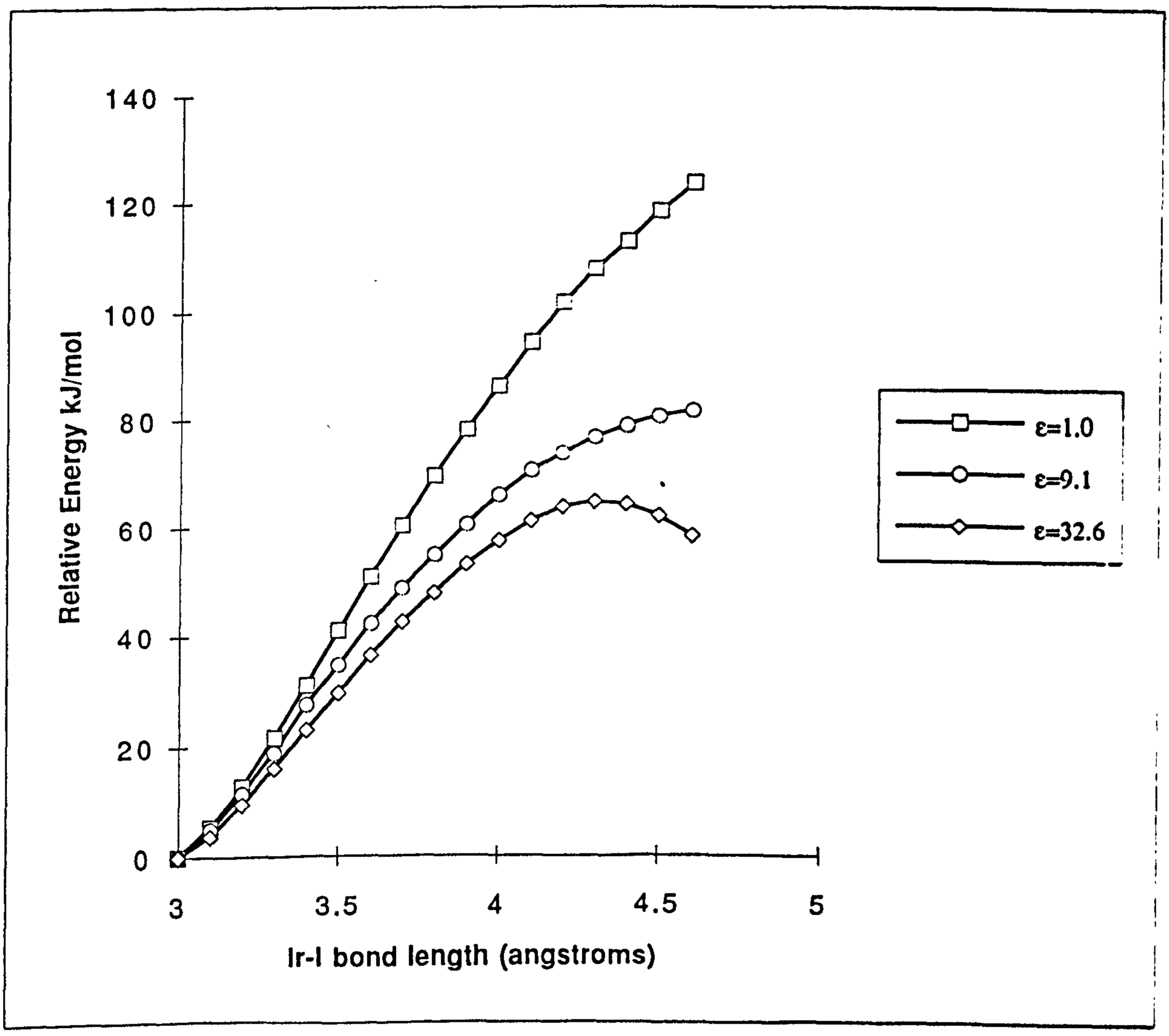

Figure 6.17: Simulated reactions paths for dissociation of the axial iodide ligand from $[CH_3Ir(CO)_2I_3]^-$ in a vacuum, and static solvent fields corresponding to CH_2Cl_2 and CH_3OH.

level. Electron correlation is more important in the description of axial carbonyl bonds since these involve additional correlation effects arising from the penetration of lone pair electrons into the metal *d* shells [268].

Only one transition state for migratory insertion in the tricarbonyl complex could be located, Figure 6.18. The imaginary vibration displays a bending motion of both the CH_3 and CO ligands toward each other, indicative of a concerted mechanism. Apart from the different axial Ir–CO geometry, the optimized parameters in this transition structure are generally similar to those computed for migratory insertion in $[CH_3Ir(CO)_2I_3]^-$ (Figure 6.5b). The most significant quantitative difference that can be identified, is a slightly smaller elongation in the Ir–CH_3 bond of 0.28 Å compared to 0.30 Å in the anionic TS.

The geometry of the five co-ordinate acyl complex $[(COCH_3)Ir(CO)_2I_2]$ is shown in Figure 6.18. This is also similar to the structure reported for the square pyramidal anion $[(COCH_3)Ir(CO)I_3]^-$ (Figure 6.8b). The most significant difference between these structures is the longer Ir–C(OCH_3) bond distance (2.06 Å) in the neutral species. This is understandable since the acyl group is now competing with two carbonyl ligands, rather than just one, for the metal *d* electrons.

The intrinsic reaction co-ordinate computed for migratory insertion in the tricarbonyl is shown in Figure 6.19. The maximum appears to be located earlier along the reaction co-ordinate than in the corresponding profile for the anionic species. Geometries of the tricarbonyl at several intermediate points along the reaction co-ordinate are shown in Figure 6.20. On the reactant side of the pathway, $rx \sim -4.0$ to 0.0, the main process is again a concerted migration of the methyl and carbonyl ligands toward each other to form the acyl C–C bond. The region following the TS, $rx \sim 0.0$ to 6.0, is dominated by opening of the bond angle *trans* to the migrating groups. The remainder of the path, $rx \sim 6.0$ to 9.0, involves rotation of the acyl ligand into the C_s symmetry plane yielding the square pyramidal product. The geometrical changes along the reaction path are also generally similar to those described previously for the anionic system. However, there is one difference that could conceivably signal a variation in the behaviour of these systems. In structure (e) at $rx \approx 1.0$, the I–Ir–C(OCH_3) angle corresponding to the site vacated by the methyl ligand is significantly larger in the tricarbonyl (151°) than in the anionic species (143°). This difference does not become apparent until after the TS is passed and only occurs briefly in the high energy region on the product side of the reaction co-ordinate. The reason for this geometrical change is presumably the stronger *trans* influence of the axial carbonyl group which hinders the iodide ligand from taking up its position in the (*trans*) basal site of the square pyramid. It is interesting to note in this context, that the energy of the LUMO for this geometry is very low ($\approx$ 0.0 Hartree), suggesting that an incoming ligand or donor solvent could stabilize the complex at this point. However, examination of the LUMO's composition did not reveal a substantial acceptor lobe which could have

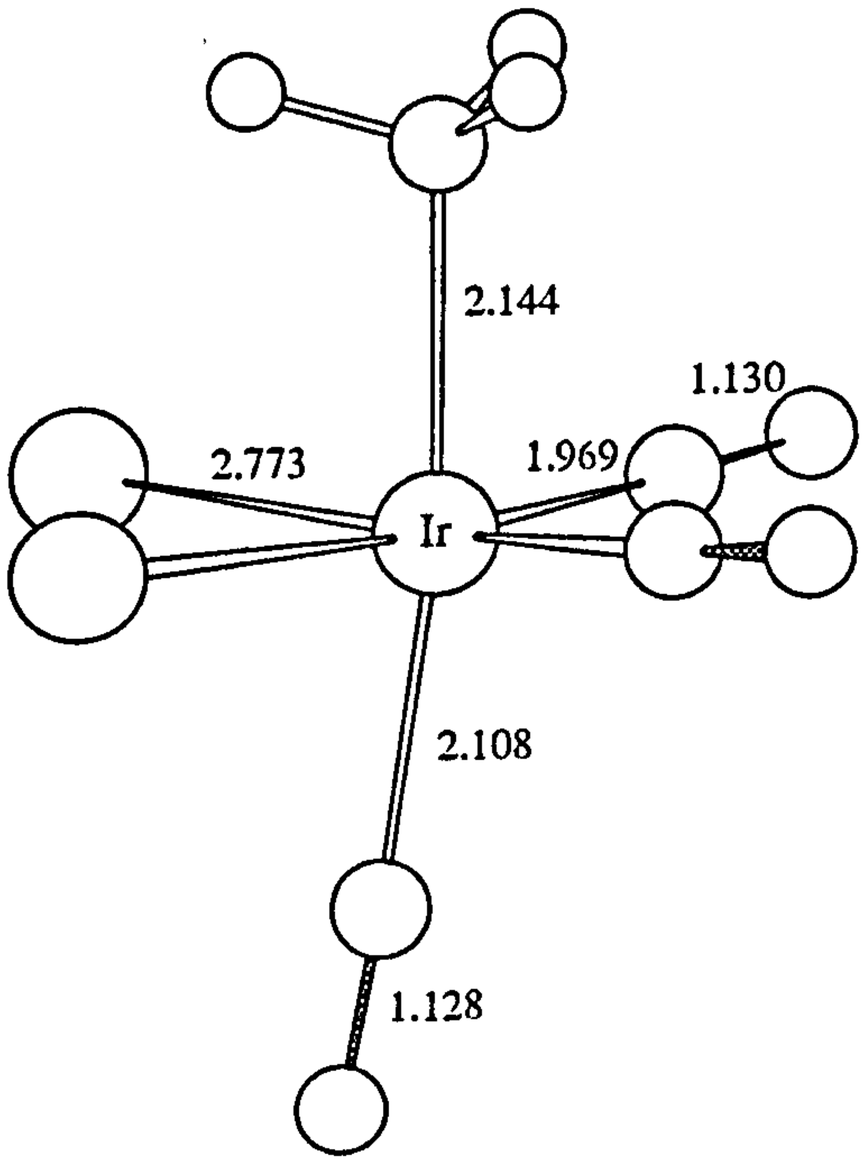

reactant

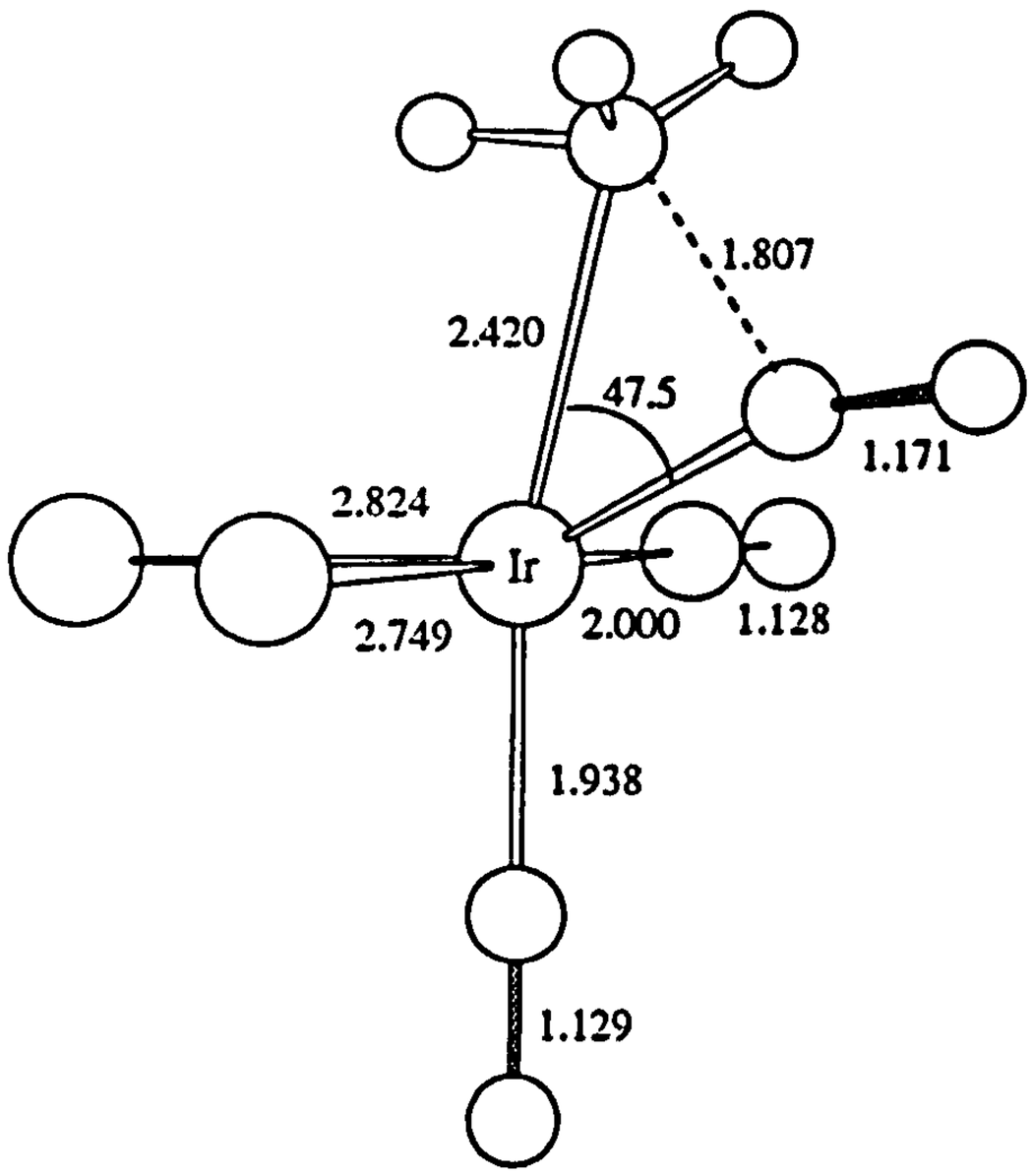

TS (ν_i=-527 cm^{-1})

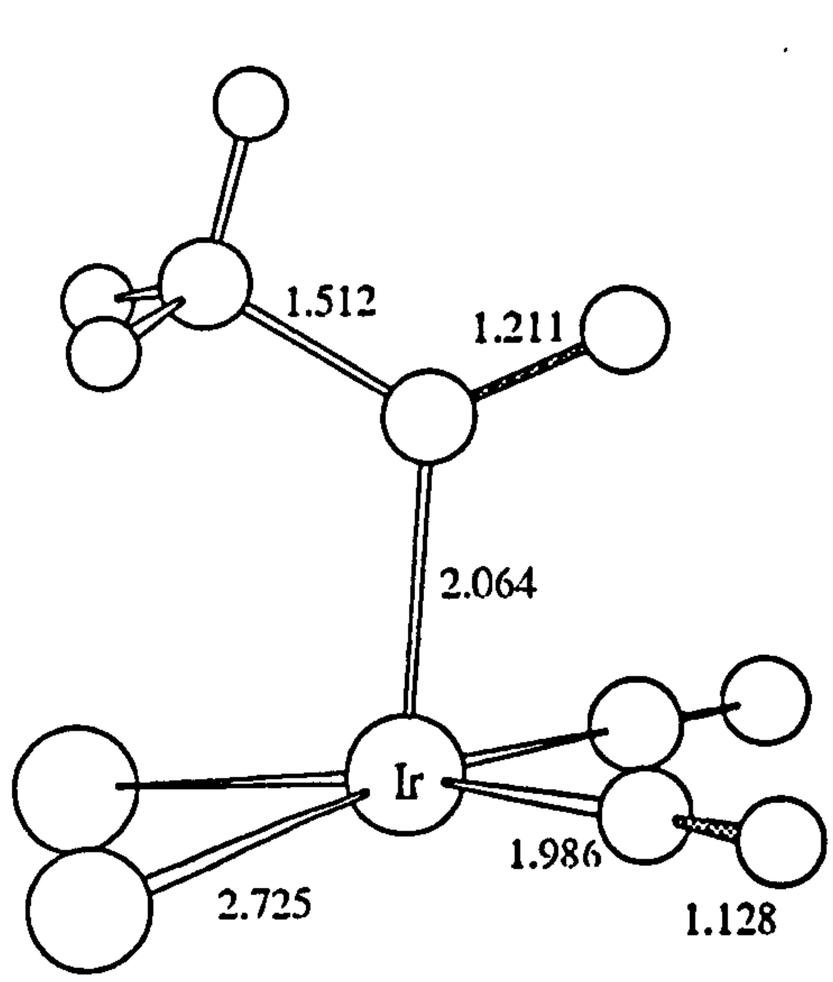

product

Figure 6.18: Optimized geometries of reactants, transition structures and acyl products for the migratory insertion reaction in $[CH_3Ir(CO)_3I_2]$. Parameters deduced from RHF/DZ2 calculations.

supported a solvent assisted mechanism for the migratory insertion reaction in the tricarbonyl system.

The relative energies of the stationary points for the migratory insertion reaction in $[CH_3Ir(CO)_3I_2]$ are given in Table 6.2. The activation barrier predicted by the RHF/DZ2 method is again very high at 140 kJ mol^{-1}. MP2/DZ2 calculations on selected points of the reaction co-ordinate yield a slightly smaller value of 128 kJ mol^{-1}. At the highest level of theory, incorporating both electron correlation and polarization functions, the MP2/DZ2* scheme predicts that migratory insertion in the tricarbonyl will take place with an activation barrier of 100 kJ mol^{-1} and be endothermic by +27 kJ mol^{-1}. Although the activation barrier is reduced by *ca.* 30 kJ mol^{-1} and the enthalpy change is slightly less endothermic by *ca.* 18 kJ mol^{-1}, these parameters *do not* suggest that replacement of iodide by carbonyl in $[CH_3Ir(CO)_2I_3]^-$ would lead to a dramatic acceleration in the rate of migratory insertion. The theoretical data presented here does not, therefore, correlate with the conclusions from mechanistic studies which have always maintained that migratory insertion in the tricarbonyl proceeds via a low energy pathway. The most important implication of these results is that the dramatic acceleration observed when methanol is added to the iridium system could be arising from another promotional effect in addition to the activation of an Ir–I bond. Associative activation parameters, such as those that have been reported, could be realised by, for example, methanol co-ordinating to the metal centre in the course of migratory insertion (i.e. a solvent assisted migratory insertion) or by the methanol hydrogen bonding to the forming acyl oxygen (i.e an acid catalysed migratory insertion). However, no firm evidence could be found to substantiate either of these suggestions.

The slightly more favourable activation barrier that was calculated for the tricarbonyl system can be attributed to a smaller destabilization of the Ir–CH_3 σ orbital in the migratory insertion TS. When there are three, rather than two, carbonyl ligands co-ordinated to the metal centre, the π back-donative interaction for the Ir–CO bond involved in acyl formation will be smaller. This could allow the CO π^* orbital to participate more freely in the interaction with the Ir–CH_3 σ orbital at the transition state (Figure 6.11(v)) and thus, afford a greater stabilization of the energy barrier.

One would hope to have confidence in the results obtained from the present study, but experience would suggest that the tricarbonyl system is more difficult to compute with limited theoretical methods. The greater degree of π back-donation arising from the replacement of an iodide with a carbonyl ligand will lead to a poorer description of the geometrical changes for this process by the Hartree-Fock scheme. A correlated method for both geometry optimization and energy determination may therefore be necessary to give an adequate theoretical description of this system. Further work is clearly required before definitive conclusions regarding the reactivity of $[CH_3Ir(CO)_3I_2]$ and the effect of methanol on the migratory

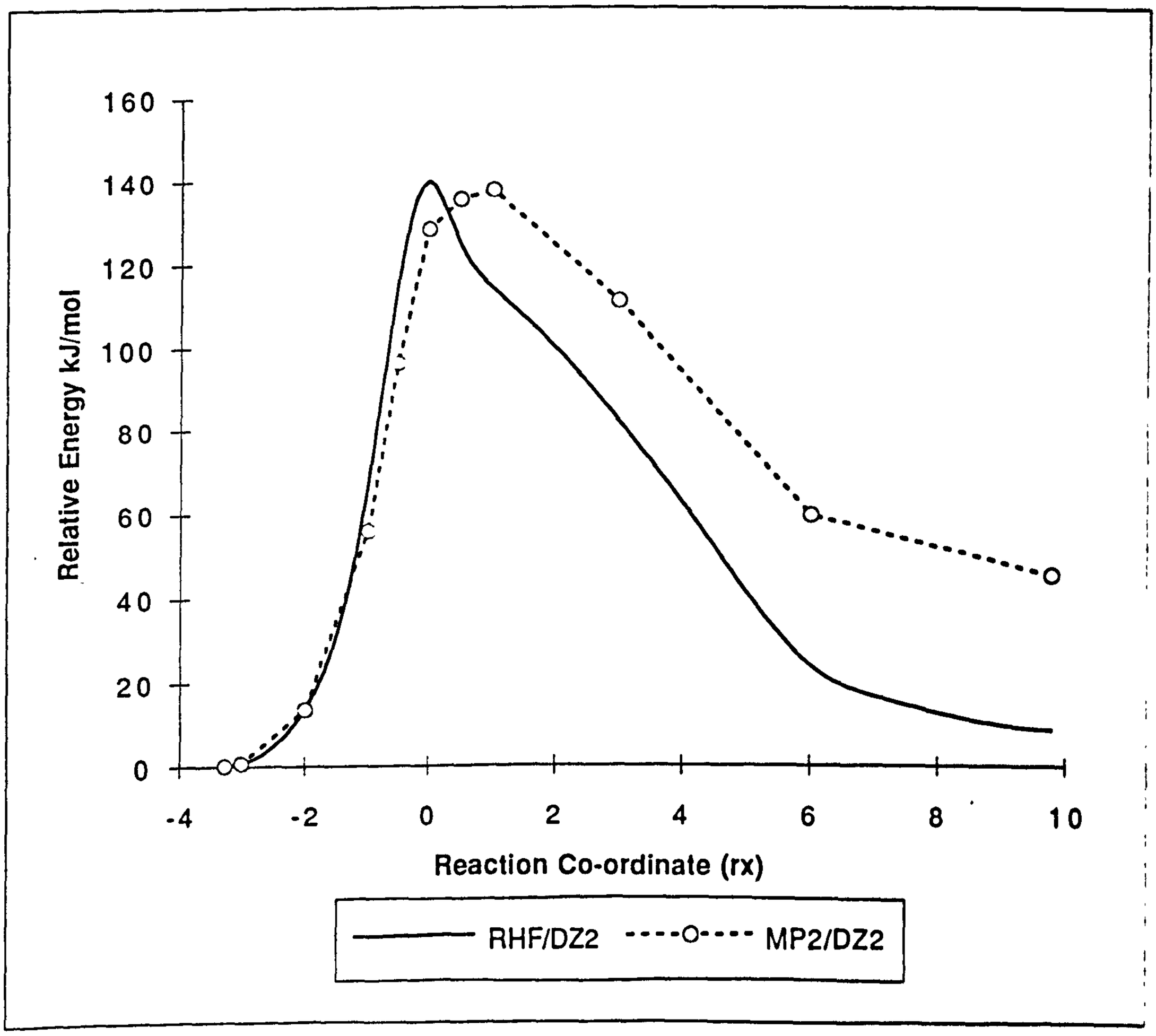

Figure 6.19: Intrinsic reaction co-ordinate for migratory insertion in $[CH_3Ir(CO)_3I_2]$. The solid line is the RHF/DZ2 reaction path; the dashed line represents the effect of MP2/DZ2 electron correlation on this path.

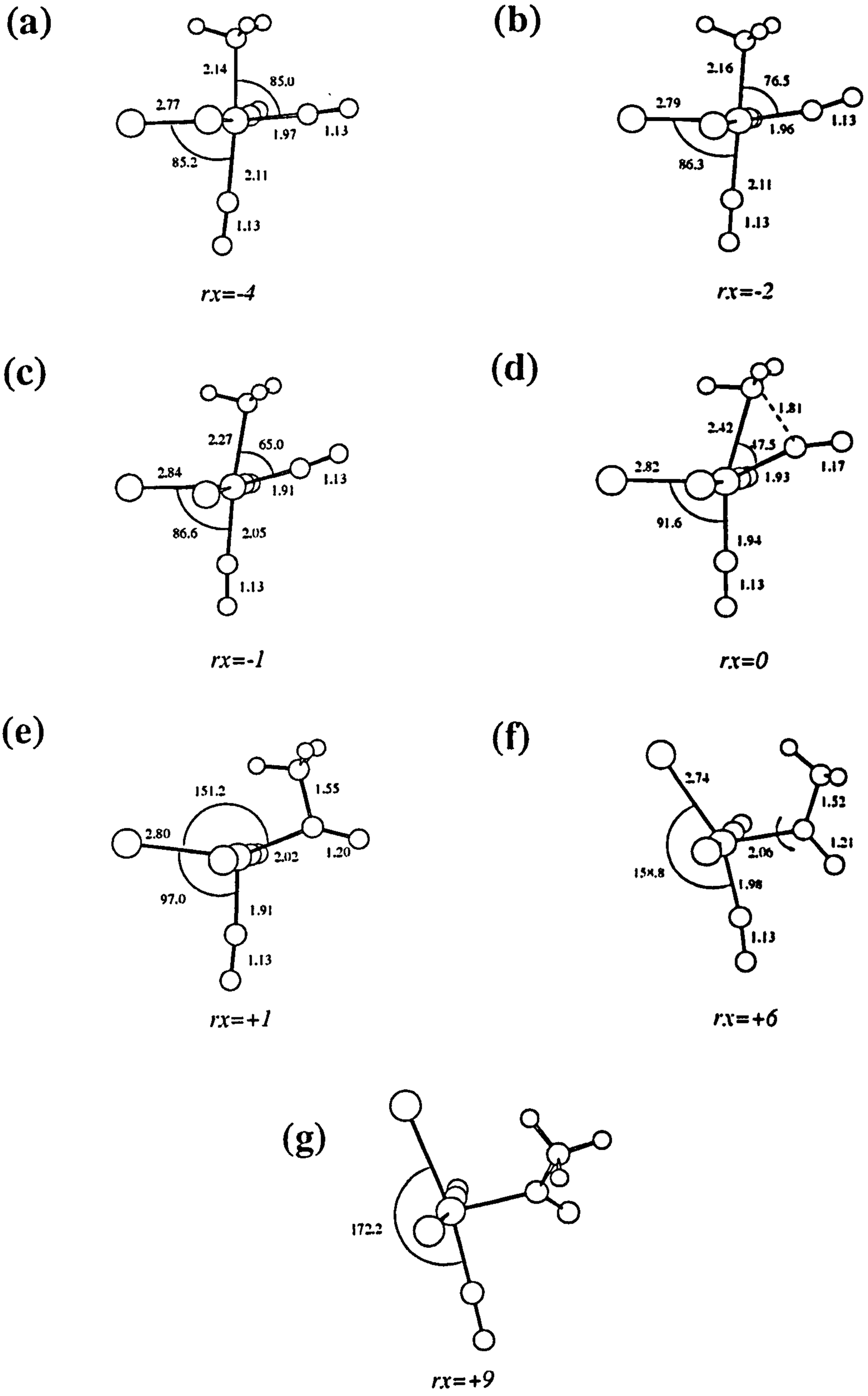

Figure 6.20: Optimized molecular geometries at seven points along the reaction co-ordinate for migratory insertion in $[CH_3Ir(CO)_3I_2]$.

insertion reaction in $[CH_3Ir(CO)_2I_3]^-$ can be made.

Table 6.2: Relative energies of stationary points computed for the migratory insertion reaction: $[CH_3Ir(CO)_3I_2] \rightarrow [(CH_3CO)M(CO)_2I_2]$. Parameters refer to those defined in Figure 6.10.
All energies are in $kJmol^{-1}$.

Model	Basis	$\Delta E_f^{\ddagger}$	$\Delta E_b^{\ddagger}$	ΔE_{mig}
RHF	DZ2	140.1	131.4	−8.6
MP2[a]	DZ2	128.4	82.6	+45.8
MP2[a]	DZ2*	100.1	73.6	+26.6

[a]Single-point MP2 calculations on optimized RHF/DZ2 geometries.

6.4 Conclusions

The migratory insertion reaction in $[CH_3M(CO)_2I_3]^-$ (M=Rh, Ir) has been investigated using the RHF and MP2 *ab initio* methods in conjunction with effective core potential basis sets. Transition states for these reactions could not be located using density functional theory. Transition structures and reaction pathways optimized at the RHF level of theory indicate that the mechanism is a concerted migratory insertion involving translation of both the CH_3 and CO groups together with opening of the *trans* I–M–I bond angle. The five co-ordinate species, $[(COCH_3)M(CO)I_3]^-$ resulting from concerted migratory insertion is square pyramidal with the acyl ligand occupying the axial site.

The calculated MP2/DZ* activation barriers for the forward and back reactions in the rhodium system are 63 and 109 kJ mol^{-1}, respectively. These are in excellent agreement with experimental solution values. The activation barrier calculated for migratory insertion in $[CH_3Ir(CO)_2I_3]^-$ is substantially higher at 131 kJ mol^{-1} and the reaction is predicted to be endothermic by +45 kJ mol^{-1}. These values are consistent with the observed low reactivity of the iridium alkyl species. The different behaviour in the rhodium and iridium systems has been ascribed to different metal–carbon bond strengths. The analysis has suggested that Ir–CH_3 and Ir–CO bonds are stronger than the corresponding rhodium bonds in the reactant alkyl complexes.

The effect of solvent on the migratory insertion reaction has been investigated. A donating solvent molecule such as methanol can stabilize the five co-ordinate acyl product by co-ordinating in the vacant axial site but a low energy acceptor orbital that could be utilised to lower the activation barrier was not created until after the TS had been passed. The static solvent effect was found to have a negligible influ-

ence on the migratory insertion reaction co-ordinates. Acid catalysis, investigated by attaching a proton to the oxygen atom of the forming acyl group, appeared to make the iridium transition structure earlier.

Migratory insertion in the iridium tricarbonyl complex $[CH_3Ir(CO)_3I_2]$ was investigated using the *ab initio* methods. The theoretical calculations did not, however, predict the expected lability of this complex. The geometries of the alkyl reactant and transition structure were very similar to those computed for $[CH_3Ir(CO)_2I_3]^-$. The MP2/DZ2* activation barrier was smaller than in the anionic system but still high at 100 kJ mol^{-1}. The computed enthalpy change at this level was endothermic by +27 kJ mol^{-1}. Further work is necessary to clarify the effect that substitution of iodide by carbonyl has on migratory insertion in the iridium system, and also to elucidate the correct mechanism by which methanol promotes this reaction.

Chapter 7

General Conclusions

An extensive theoretical study of the catalytic cycles for methanol carbonylation by rhodium- and iridium-iodo-carbonyl complexes has been undertaken. A variety of results have been obtained, which are interesting and useful from both the point of view of comparing the performances of the models of electronic structure employed and for developing a better understanding of the important physical processes occurring.

Effective core potential calculations have shown that certain density functionals in conjunction with moderate Gaussian valence basis sets can provide very good estimates of molecular properties for ground state complexes relevant to the catalysis. The local density approximation (LDA) and the GAUSSIAN implementation of Becke's simplest hybrid scheme (BHANDH) yield optimized geometrical structures and carbonyl vibrational frequencies which are in general superior to the results obtained from the traditional Hartree-Fock *ab initio* method and superior or comparable to the results from the correlated MP2 method in the same basis. The gradient-corrected nonlocal density functionals, on the other hand, do not appear to be reliable for such calculations. It is noteworthy that the sophisticated BLYP functional generates equilibrium structures with metal-ligand bonds which are systematically too long, overestimated typically by more than 0.1 Å.

All of the theoretical data lead to the conclusion that oxidative addition of CH_3I to *cis*-$[M(CO)_2I_2]^-$ complexes proceed via a nucleophilic substitution pathway. The RHF method predicts two distinct S_N2 transition states: a "linear" structure resulting from classical backside nucleophilic attack of the metal centre on the substrate leading to inversion of configuration at carbon; a "bent" structure resulting from a side-on approach of CH_3I towards the metal complex leading to retention of configuration at carbon. The former is energetically preferred, and yields computed secondary α-deuterium kinetic isotope effects which are in excellent agreement with experiment. Given the sensitivity of the KIE technique

to changes in transition state geometry, the theoretical data presented provides very strong evidence for a classical S_N2 inversion mechanism in these reactions. The transition structure for the iridium system is predicted to be earlier than for rhodium, consistent with both smaller experimental and theoretical KIEs, and also with the higher nucleophilicity of *cis*-$[Ir(CO)_2I_2]^-$. It is suggested that the difference arises from a relativistic effect which enhances the main lobes of the important d_{z^2} donor orbital of the heavier transition metal species.

The reaction mechanism corresponding to the bent retention transition state has a significantly higher activation barrier due to destabilizing electron repulsion between occupied orbitals of the iodide leaving group of the substrate and occupied orbitals involved in metal–ligand bonding. Furthermore, this mechanism is associated with a considerably larger theoretical KIE. These facts taken together with the failure to locate a TS for a concerted one-step addition of CH_3I to the square planar complexes, suggest that a mechanism for oxidative addition involving a side-on approach of the substrate can be discounted under normal reaction conditions.

Analysis of the inversion mechanism using the *ab initio* methods has revealed both a substantial influence of electron correlation and solvent medium on the nucleophilic substitution reaction energetics. Single-point MP2 SCRF calculations carried out on the RHF reaction co-ordinates for a solvent field with dielectric constant corresponding to CH_3I, yield activation barriers of 69 and 55 kJ mol^{-1} for rhodium and iridium nucleophiles. respectively. These are in good agreement with experimental solution values ($\Delta H^{\ddagger} \approx 55$ kJ mol^{-1}), although a significant difference between the activation enthalpies for the two metal systems has never been observed. The correlation and solvent effect appear to balance each other with respect to the geometry of the TS, leading to structures which are similar to those obtained at the RHF level in the gas phase. Increasing the dielectric constant from 7.0 (CH_3I) to 32.6 (CH_3OH) in the theoretical calculations is found to change the substitution reaction in the rhodium system from an endothermic to an exothermic process, while for iridium increasing the solvent polarity only reinforces an already dominant forward substitution reaction. It is proposed that the experimentally observed rate acceleration of oxidative addition in the rhodium system upon moving to a more polar solvent is due to stabilization of the substitution products which inhibits the reverse process of nucleophilic attack of I^- on the methyl group of $[CH_3Rh(CO)_2I_2]$.

The overall oxidative addition process is predicted at the MP2 level to be exothermic for both metal systems, but more so for iridium ($\Delta E_{add} \approx -50$ to -70 kJ mol^{-1} Rh; $\Delta E_{add} \approx -85$ to -100 kJ mol^{-1} Ir). The predicted exothermicity for rhodium is surprising in view of the highly labile nature of the alkyl intermediate $[CH_3Rh(CO)_2I_3]^-$. However. extrapolated rate data support this result, suggesting that a large negative entropy component to the free energy change is

the main source of the instability. The results of population analyses carried out at the Hartree-Fock level are consistent with a stronger M–CH_3 bond in the iridium alkyl complex. The higher stability of $[CH_3Ir(CO)_2I_3]^-$ compared to the analogous rhodium species is probably due to a relativistic stabilization of the iridium 6*s* orbital which is considered to be important in M–CH_3 bonding.

No firm theoretical evidence could be found to support the favourable interaction of ionic iodide with either $[Rh(CO)_2I_2]^-$ or the transition state for nucleophilic substitution. However, substituting the the iodide ligands in $[Rh(CO)_2I_2]^-$ by more covalent ligands such as hydrides appears to promote oxidative addition by changing the character of the occupied metal orbitals. In particular, increasing the 5*s* population at the metal centre seems to result in an earlier TS, a smaller activation barrier and a more favourable energy change for the overall oxidative addition process. This result further highlights the importance of metal *s* electrons to M–CH_3 bonding.

A transition state for a reductive elimination of CH_3I from $[CH_3M(CO)_2I_3]^-$ could not be located on the potential energy surface. Loss of CH_3I can be achieved, however, by either the reverse of the nucleophilic substitution pathway, or by a concerted reductive elimination from the neutral complex $[CH_3Rh(CO)_2I_2]$. The transition state optimized at the RHF level for the latter mechanism is interesting, since it presumably leads to the formation of a three co-ordinate rhodium intermediate, $[Rh(CO)_2I]$. Notwithstanding, MP2 single-point calculations have suggested that this mechanism is associated with a rather large energy penalty, and that nucleophilic attack of I^- on the neutral five co-ordinate alkyl complex is the most favourable CH_3I loss mechanism competing with oxidative addition.

Attempts at probing the potential energy surface of the oxidative addition reaction using density functional theory, have not been successful. Transition structures computed for the inversion mechanism are considerably later and more distorted than those generated with the Hartree-Fock method. The result is independent of the particular DFT scheme employed, and occurs even when the calculations are carried out with the HFS exchange-only functional. Reaction pathways leading from the DFT transition states could not be computed and the results of DFT SCRF solvent field calculations on structures taken from the RHF intrinsic reaction co-ordinates were spurious. Moreover, the imaginary frequencies computed for the DFT transition states were either very small, or there were two, and the corresponding normal mode vibrations do not resemble the expected asymmetric stretch that characterize S_N2 processes. It is proposed that the gas phase inversion TS in the oxidative addition reaction is an example of a weakly interacting system, which cannot be modelled by the current functionals due to the well known deficiencies in their exchange-correlation potentials. In addition to the problems encountered for the transition state, which is clearly a difficult system to study, it is also disturbing that the nonlocal DFT functionals do not yield energy changes

for overall oxidative addition which are consistent with the estimates based on extrapolated rate data. The results of this work add to the growing number of reports in the literature of systems where approximate DFT has failed to give an adequate description, and suggest that a great deal more effort is required in the construction of new functionals before DFT can be applied as routinely, and to as broad a range of chemical problems, as conventional *ab initio* techniques.

Migratory insertion in $[CH_3M(CO)_2I_3]^-$ complexes has been studied using the RHF and MP2 methods. Transition states for this reaction could not be located using any of the DFT-based schemes. Determination of transition structures and the associated intrinsic reaction co-ordinates at the RHF level indicate that the mechanism is a concerted migratory insertion of methyl and carbonyl groups toward each other followed by opening of the I–M–I bond angle. The product of this mechanism is a square pyramidal complex with the acyl ligand occupying the axial site.

The forward and reverse activation barriers calculated for the rhodium system at the MP2 level of 63 and 109 kJ mol^{-1}, respectively, are in excellent agreement with experimental solution values. Migratory insertion in $[CH_3Ir(CO)_2I_3]^-$ is found to have a significantly larger forward barrier of 131 kJ mol^{-1} and the reaction is predicted to be endothermic by 45 kJ mol^{-1}. The theoretical data for the iridium system is compatible with the experimental observation that migratory insertion can only proceed at elevated temperatures and in the presence of carbon monoxide, the latter condition being required to prevent the more facile back reaction of deinsertion from occurring. The difference in the reactivity between rhodium and iridium alkyl complexes with respect to migratory insertion can probably be ascribed to the greater strength of both Ir–CH_3 and Ir–CO bonds, as suggested by our qualitative analysis of the electronic structure changes along the reaction co-ordinates. The large endothermic enthalpy change calculated for the iridium system is an indication that the heavier transition metal complex has a greater dependence on M–CO π bonding for its stability.

The potential influence of solvent on the migratory insertion reaction has been studied. MP2 SCRF calculations have shown that the static electrostatic solvent effect is insignificant in this system. A donating solvent molecule such as methanol can stabilize the five co-ordinate acyl product by co-ordinating in the vacant site but a low energy acceptor orbital which could be utilised to lower the activation barrier is not created until after the transition state has been passed. Attaching a proton to the forming acyl oxygen atom appears to lead to a significantly earlier transition state in the iridium system.

Migratory insertion in a neutral iridium tricarbonyl complex $[CH_3Ir(CO)_3I_2]$ is not predicted by theory to be a facile process. At the MP2 level, the reaction is found to have a large activation barrier of 100 kJ mol^{-1} and is endothermic by 27 kJ

mol^{-1}. This result is in contrast to the conclusions from previous experimental studies which have suggested that protic solvents such as methanol can promote migratory insertion in $[CH_3Ir(CO)_2I_3]^-$ by aiding the substitution of an iodide by a carbonyl ligand through hydrogen bonding interactions. The conflict between theory and experiment in this case, may point to the involvement of an additional factor which has not yet been considered.

Although the models used may be oversimplified, this theoretical investigation has yielded results which are in most cases consistent with the experimental observations and has provided a number of extra details which have been lacking in previous experimental studies. Given the importance of homogeneous transition metal catalysis, and the limited investigatory powers of experimental techniques to the study of highly reactive species central to catalysis, such efforts are clearly warranted.

Appendix A

Z-Matrices for Geometries of Key Rhodium Species

Parameters have been optimized at the RHF/LANL1DZ level.

A.1 $[Rh(CO)_2I_2]^-$

Z-MATRIX (ANGSTROMS AND DEGREES)

CD	Cent	Atom	N1	Length/X	N2	Alpha/Y	N3	Beta/Z	J
1	1	Rh							
2		X	1	1.000000(1)					
3		X	1	1.000000(2)	2	90.000(14)			
4		X	1	1.000000(3)	2	90.000(15)	3	180.000(26)	0
5	2	I	1	2.807300(4)	2	90.000(16)	3	-48.984(27)	0
6	3	I	1	2.807300(5)	2	90.000(17)	3	48.984(28)	0
7	4	C	1	1.882700(6)	2	90.000(18)	4	46.992(29)	0
8	5	C	1	1.882700(7)	2	90.000(19)	4	-46.992(30)	0
9		X	7	1.000000(8)	1	90.000(20)	2	0.000(31)	0
10		X	8	1.000000(9)	1	90.000(21)	2	0.000(32)	0
11		X	7	1.000000(10)	9	90.000(22)	1	180.000(33)	0
12		X	8	1.000000(11)	10	90.000(23)	1	180.000(34)	0
13	6	O	7	1.143400(12)	9	90.000(24)	11	-0.913(35)	0
14	7	O	8	1.143400(13)	10	90.000(25)	12	0.913(36)	0

A.2 Ion-dipole complex $[Rh(CO)_2I_2]^-\cdots CH_3I$

Z-MATRIX (ANGSTROMS AND DEGREES)

CD	Cent	Atom	N1	Length/X	N2	Alpha/Y	N3	Beta/Z	J
1	1	Rh							
2		X	1	1.000000(1)					
3		X	1	1.000000(2)	2	90.000(21)			
4		X	1	1.000000(3)	2	90.000(22)	3	180.000(40)	0
5	2	C	1	1.885104(4)	2	46.980(23)	3	-92.952(41)	0
6	3	C	1	1.885104(5)	2	46.980(24)	3	92.952(42)	0
7	4	I	1	2.809857(6)	2	130.975(25)	4	92.762(43)	0
8	5	I	1	2.809857(7)	2	130.975(26)	4	-92.762(44)	0
9		X	5	1.000000(8)	1	90.000(27)	2	0.000(45)	0
10		X	5	1.000000(9)	9	90.000(28)	1	180.000(46)	0
11	6	O	5	1.142544(10)	9	89.238(29)	10	-0.057(47)	0
12		X	6	1.000000(11)	1	90.000(30)	2	0.000(48)	0
13		X	6	1.000000(12)	12	90.000(31)	1	180.000(49)	0
14	7	O	6	1.142544(13)	12	89.238(32)	13	0.057(50)	0
15	8	C	1	5.481060(14)	3	90.000(33)	2	180.000(51)	0
16		X	15	1.000000(15)	1	90.000(34)	3	0.000(52)	0
17		X	15	1.000000(16)	16	90.000(35)	1	180.000(53)	0
18	9	H	15	1.072982(17)	17	101.161(36)	16	0.000(54)	0
19	10	H	15	1.072459(18)	17	109.630(37)	16	-118.194(55)	0
20	11	H	15	1.072459(19)	17	109.630(38)	16	118.194(56)	0
21	12	I	15	2.210527(20)	16	95.533(39)	1	180.000(57)	0

A.3 S_N2 inversion TS

Z-MATRIX (ANGSTROMS AND DEGREES)

CD	Cent	Atom	N1	Length/X	N2	Alpha/Y	N3	Beta/Z	J
1	1	Rh							
2		X	1	1.000000(1)					
3		X	1	1.000000(2)	2	90.000(21)			
4		X	1	1.000000(3)	2	90.000(22)	3	180.000(40)	0
5	2	C	1	1.933334(4)	2	93.191(23)	3	-48.516(41)	0
6	3	C	1	1.933334(5)	2	93.191(24)	3	48.516(42)	0
7	4	I	1	2.732619(6)	2	80.769(25)	4	48.620(43)	0
8	5	I	1	2.732619(7)	2	80.769(26)	4	-48.620(44)	0
9		X	5	1.000000(8)	1	90.000(27)	2	0.000(45)	0
10		X	5	1.000000(9)	9	90.000(28)	1	180.000(46)	0

11	6	O	5	1.132693(10)	9	88.723(29)	10	0.763(47)	0
12		X	6	1.000000(11)	1	90.000(30)	2	0.000(48)	0
13		X	6	1.000000(12)	12	90.000(31)	1	180.000(49)	0
14	7	O	6	1.132693(13)	12	88.723(32)	13	-0.763(50)	0
15	8	C	1	2.189489(14)	3	90.000(33)	2	180.000(51)	0
16		X	15	1.000000(15)	1	90.000(34)	3	0.000(52)	0
17		X	15	1.000000(16)	16	90.000(35)	1	180.000(53)	0
18	9	H	15	1.069172(17)	17	74.826(36)	16	0.000(54)	0
19	10	H	15	1.070718(18)	17	79.601(37)	16	-120.669(55)	0
20	11	H	15	1.070718(19)	17	79.601(38)	16	120.669(56)	0
21	12	I	15	3.202059(20)	16	82.275(39)	1	180.000(57)	0

A.4 Ion-dipole complex $[CH_3Rh(CO)_2I_2]\cdots I^-$

Z-MATRIX (ANGSTROMS AND DEGREES)

CD	Cent	Atom	N1	Length/X	N2	Alpha/Y	N3	Beta/Z	J
1	1	Rh							
2		X	1	1.000000(1)					
3		X	1	1.000000(2)	2	90.000(21)			
4		X	1	1.000000(3)	2	90.000(22)	3	180.000(40)	0
5	2	C	1	1.990627(4)	2	91.483(23)	3	-48.947(41)	0
6	3	C	1	1.990627(5)	2	91.483(24)	3	48.947(42)	0
7	4	I	1	2.729358(6)	2	81.858(25)	4	47.308(43)	0
8	5	I	1	2.729358(7)	2	81.858(26)	4	-47.308(44)	0
9		X	5	1.000000(8)	1	90.000(27)	2	0.000(45)	0
10		X	5	1.000000(9)	9	90.000(28)	1	180.000(46)	0
11	6	O	5	1.126720(10)	9	84.454(29)	10	-8.028(47)	0
12		X	6	1.000000(11)	1	90.000(30)	2	0.000(48)	0
13		X	6	1.000000(12)	12	90.000(31)	1	180.000(49)	0
14	7	O	6	1.126720(13)	12	84.454(32)	13	8.028(50)	0
15	8	C	1	2.013816(14)	3	90.000(33)	2	180.000(51)	0
16		X	15	1.000000(15)	1	90.000(34)	3	0.000(52)	0
17		X	15	1.000000(16)	16	90.000(35)	1	180.000(53)	0
18	9	H	15	1.077163(17)	17	70.675(36)	16	0.000(54)	0
19	10	H	15	1.076821(18)	17	74.416(37)	16	-121.080(55)	0
20	11	H	15	1.076821(19)	17	74.416(38)	16	121.080(56)	0
21	12	I	15	4.081727(20)	1	86.678(39)	16	0.000(57)	0

A.5 $[CH_3Rh(CO)_2I_2]$

Z-MATRIX (ANGSTROMS AND DEGREES)

CD	Cent	Atom	N1	Length/X	N2	Alpha/Y	N3	Beta/Z	J
1	1	Rh							
2		X	1	2.000000(1)					
3		X	1	1.000000(2)	2	90.000(22)			
4		X	1	1.000000(3)	2	90.000(23)	3	180.000(42)	0
5	2	I	1	2.688861(4)	2	95.027(24)	3	-47.716(43)	0
6	3	I	1	2.688861(5)	2	95.027(25)	3	47.716(44)	0
7	4	C	1	1.973568(6)	2	89.409(26)	4	311.326(45)	0
8	5	C	1	1.973568(7)	2	89.409(27)	4	-311.326(46)	0
9		X	7	1.000000(8)	1	90.000(28)	2	0.000(47)	0
10		X	8	1.000000(9)	1	90.000(29)	2	0.000(48)	0
11		X	7	1.000000(10)	9	90.000(30)	1	180.000(49)	0
12		X	8	1.000000(11)	10	90.000(31)	1	180.000(50)	0
13	6	O	7	1.128352(12)	9	89.240(32)	11	0.338(51)	0
14	7	O	8	1.128352(13)	10	89.240(33)	12	-0.338(52)	0
15		X	1	2.000000(14)	4	90.000(34)	2	180.000(53)	0
16		X	1	1.000000(15)	4	90.000(35)	2	180.000(54)	0
17	8	C	1	2.022412(16)	4	90.000(36)	15	180.000(55)	0
18		X	17	1.000000(17)	1	90.000(37)	3	0.000(56)	0
19		X	17	1.000000(18)	18	90.000(38)	1	180.000(57)	0
20	9	H	17	1.078411(19)	19	69.535(39)	18	241.474(58)	0
21	10	H	17	1.074680(20)	19	76.392(40)	18	0.000(59)	0
22	11	H	17	1.078411(21)	19	69.535(41)	18	-241.474(60)	0

A.6 *fac-cis*-$[CH_3Rh(CO)_2I_3]^-$

Z-MATRIX (ANGSTROMS AND DEGREES)

CD	Cent	Atom	N1	Length/X	N2	Alpha/Y	N3	Beta/Z	J
1	1	Rh							
2		X	1	2.000000(1)					
3		X	1	1.000000(2)	2	90.000(22)			
4		X	1	1.000000(3)	2	90.000(23)	3	180.000(42)	0
5	2	I	1	2.769545(4)	2	88.817(24)	3	-48.188(43)	0
6	3	I	1	2.769545(5)	2	88.817(25)	3	48.188(44)	0
7	4	C	1	1.936379(6)	2	89.882(26)	4	311.325(45)	0
8	5	C	1	1.936379(7)	2	89.882(27)	4	-311.325(46)	0
9		X	7	1.000000(8)	1	90.000(28)	2	0.000(47)	0

10		X	8	1.000000(9)	1	90.000(29)	2	0.000(48)	0
11		X	7	1.000000(10)	9	90.000(30)	1	180.000(49)	0
12		X	8	1.000000(11)	10	90.000(31)	1	180.000(50)	0
13	6	O	7	1.133124(12)	9	88.148(32)	11	0.775(51)	0
14	7	O	8	1.133124(13)	10	88.148(33)	12	-0.775(52)	0
15		X	1	2.000000(14)	4	90.000(34)	2	180.000(53)	0
16	8	I	1	2.941661(15)	4	79.255(35)	2	180.000(54)	0
17	9	C	1	2.050366(16)	4	90.000(36)	15	180.000(55)	0
18		X	17	1.000000(17)	1	90.000(37)	3	0.000(56)	0
19		X	17	1.000000(18)	18	90.000(38)	1	180.000(57)	0
20	10	H	17	1.083785(19)	19	68.568(39)	18	241.255(58)	0
21	11	H	17	1.076366(20)	19	74.258(40)	18	0.000(59)	0
22	12	H	17	1.083785(21)	19	68.568(41)	18	-241.255(60)	0

A.7 Migratory Insertion TS

Z-MATRIX (ANGSTROMS AND DEGREES)

CD	Cent	Atom	N1	Length/X	N2	Alpha/Y	N3	Beta/Z	J
1	1	Rh							
2		X	1	1.000000(1)					
3		X	1	1.000000(2)	2	90.000(23)			
4		X	1	1.000000(3)	3	90.000(24)	2	180.000(44)	0
5		X	1	1.000000(4)	2	90.000(25)	3	180.000(45)	0
6	2	I	1	2.745700(5)	2	86.332(26)	5	2.650(46)	0
7	3	I	1	2.914000(6)	2	87.269(27)	5	-95.517(47)	0
8	4	I	1	2.717800(7)	5	90.000(28)	2	181.573(48)	0
9	5	C	1	1.948200(8)	2	94.779(29)	5	86.390(49)	0
10		X	9	1.000000(9)	1	90.000(30)	2	0.000(50)	0
11		X	9	1.000000(10)	10	90.000(31)	1	180.000(51)	0
12	6	O	9	1.132900(11)	10	89.025(32)	11	0.566(52)	0
13	7	C	1	1.841500(12)	2	63.000(33)	3	0.000(53)	0
14		X	13	1.000000(13)	1	90.000(34)	2	0.000(54)	0
15		X	13	1.000000(14)	14	90.000(35)	1	180.000(55)	0
16	8	O	13	1.165900(15)	14	106.590(36)	15	-2.797(56)	0
17	9	C	1	2.325000(16)	3	79.000(37)	2	0.000(57)	0
18		X	17	1.000000(17)	1	90.000(38)	3	0.000(58)	0
19		X	17	1.000000(18)	18	90.000(39)	1	180.000(59)	0
20		X	17	1.000000(19)	19	90.000(40)	18	180.000(60)	0
21	10	H	17	1.077800(20)	19	98.992(41)	20	0.000(61)	0
22	11	H	17	1.080500(21)	18	75.041(42)	19	60.000(62)	0
23	12	H	17	1.080400(22)	18	74.786(43)	19	-60.000(63)	0

A.8 $[(COCH_3)Rh(CO)I_3]^-$

Z-MATRIX (ANGSTROMS AND DEGREES)

CD	Cent	Atom	N1	Length/X	N2	Alpha/Y	N3	Beta/Z	J
1	1	Rh							
2		X	1	1.000000(1)					
3		X	1	1.000000(2)	2	90.000(20)			
4		X	1	1.000000(3)	2	90.000(21)	3	180.000(38)	0
5	2	C	1	1.964692(4)	2	87.870(22)	3	0.000(39)	0
6		X	5	1.000000(5)	1	90.000(23)	2	0.000(40)	0
7	3	O	5	1.130990(6)	6	92.852(24)	1	180.000(41)	0
8	4	I	1	2.767881(7)	2	105.576(25)	4	0.000(42)	0
9	5	I	1	2.722185(8)	2	92.180(26)	4	-93.708(43)	0
10	6	I	1	2.722185(9)	2	92.180(27)	4	93.708(44)	0
11	7	C	1	1.930217(10)	3	90.000(28)	2	0.000(45)	0
12		X	11	1.000000(11)	1	90.000(29)	3	0.000(46)	0
13		X	11	1.000000(12)	12	90.000(30)	1	180.000(47)	0
14	8	O	11	1.216521(13)	12	30.242(31)	13	0.000(48)	0
15	9	C	11	1.515005(14)	13	62.478(32)	12	180.000(49)	0
16		X	15	1.000000(15)	11	90.000(33)	13	0.000(50)	0
17		X	15	1.000000(16)	16	90.000(34)	11	180.000(51)	0
18	10	H	15	1.083038(17)	17	71.992(35)	16	0.000(52)	0
19	11	H	15	1.079535(18)	17	69.971(36)	16	-120.721(53)	0
20	12	H	15	1.079535(19)	17	69.971(37)	16	120.721(54)	0

A.9 *trans*-$[(COCH_3)Rh(CO)_2I_3]^-$

Z-MATRIX (ANGSTROMS AND DEGREES)

CD	Cent	Atom	N1	Length/X	N2	Alpha/Y	N3	Beta/Z	J
1	1	Rh							
2		X	1	1.000000(1)					
3		X	1	1.000000(2)	2	90.000(23)			
4		X	1	1.000000(3)	2	90.000(24)	3	180.000(44)	0
5	2	C	1	1.986849(4)	2	88.987(25)	3	0.000(45)	0
6		X	5	1.000000(5)	1	90.000(26)	2	0.000(46)	0
7	3	O	5	1.128583(6)	6	91.871(27)	1	180.000(47)	0
8	4	I	1	2.895018(7)	3	87.962(28)	2	180.000(48)	0
9	5	I	1	2.734989(8)	2	86.137(29)	4	-88.858(49)	0
10	6	I	1	2.734989(9)	2	86.137(30)	4	88.858(50)	0
11	7	C	1	1.998907(10)	3	90.000(31)	2	0.000(51)	0

12		X	11	1.000000(11)	1	90.000(32)	3	0.000(52)	0
13		X	11	1.000000(12)	12	90.000(33)	1	180.000(53)	0
14	8	O	11	1.224339(13)	12	29.279(34)	13	0.000(54)	0
15	9	C	11	1.520523(14)	13	59.077(35)	12	180.000(55)	0
16		X	15	1.000000(15)	11	90.000(36)	13	0.000(56)	0
17		X	15	1.000000(16)	16	90.000(37)	11	180.000(57)	0
18	10	H	15	1.082391(17)	17	70.840(38)	16	0.000(58)	0
19	11	H	15	1.083046(18)	17	69.985(39)	16	-119.942(59)	0
20	12	H	15	1.083046(19)	17	69.985(40)	16	119.942(60)	0
21	13	C	1	1.967965(20)	2	96.216(41)	4	0.000(61)	0
22		X	21	1.000000(21)	1	90.000(42)	2	0.000(62)	0
23	14	O	21	1.130974(22)	22	91.049(43)	1	180.000(63)	0

Bibliography

[1] W. Keim; *Advances in Catalysis Design*, World Scientific (1991).

[2] J. A. Osborn, F. H. Jardine, J. F. Young and G. Wilkinson; *J. Chem. Soc. A*, 1711 (1966).

[3] T. G. Appleton, H. C. Clark and L. E. Manzer; *Coord. Chem. Rev.*, **10**, 335 (1973).

[4] F. Basolo and R. G. Pearson; *Prog. Inorg. Chem.*, 4, 381 (1962).

[5] J. M. Jenkins and B. L. Shaw; *J. Chem. Soc.*, 6789 (1965).

[6] A. J. Deeming and B. L. Shaw; *J. Chem. Soc.*, 1128 (1968).

[7] J. Chatt, R. S. Coffey and B. L. Shaw; *J. Chem. Soc.*, 7391 (1965).

[8] R. C. Taylor, J. F. Young and G. Wilkinson; *Inorg. Chem.*, **5**, 20 (1966).

[9] M. J. S. Dewar; *Bull. Soc. Chim. Fr.*, **71**, C18 (1951).

[10] J. Chatt and L. A. Duncanson; *J. Chem. Soc.*, 2939 (1953).

[11] J. P. Collman, L. S. Hegedus, J. R. Norton and R. G. Finke *Principles and Applications of Organotransition Metal Chemistry*; University Science Books: Mill Valley, CA (1987).

[12] L. Vaska and J. W. Luzio; *J. Am. Chem. Soc.*, **83**, 2784 (1961).

[13] J. P. Collman; *Acc. Chem. Res.*, **1**, 136 (1968).

[14] S. Henderson and R. A. Henderson; *Adv. Phys. Org. Chem.*, **23**, 1 (1987).

[15] A. Haynes, B. E. Mann, G. E. Morris and P. M. Maitlis; *J. Am. Chem. Soc.*, **115**, 4093 (1993).

[16] P. J. Stang, M. D. Schlavell, H. K. Cenault and J. L. Breidagam ; *Organometalics*, **3**, 1133 (1984).

[17] J. A. Labinger, R. J. Braus, D. Dolphin and J. A. Osborn; *J. Chem. Soc., Chem. Commun.*, 612 (1970).

[18] P. R. Ellis, J. M. Pearson, A. Haynes, H. Adams, N. A. Bailey and P. M. Maitlis; *Organometalics*, **13**, 3215 (1994).

[19] P. K. Byers, A. J. Canty, M. Crespo, R. J. Puddephatt and J. D. Scott; *Organometalics*, **7**, 1363 (1988).

[20] R. G. Pearson and W. R. Muir; *J. Am. Chem. Soc.*, **92**, 5519 (1970).

[21] R. G. Pearson; *Acc. Chem. Res.*, 4, 152 (1971).

[22] M. Kubota, G. W. Kiefer, R. M. Ishikawa and K. E. Bencala; *Inorg. Chim. Acta.*, **7**, 195 (1973).

[23] M. R. Wilson, H. Liu, A. Prock and W. P. Giering; *Organometalics*, **12**, 2044 (1993).

[24] J. Halpern; *Acc. Chem. Res.*, **3**, 386 (1970).

[25] T. C. Flood, J. E. Jensen and J. A. Stalter; *J. Am. Chem. Soc.*, **103**, 4410 (1981).

[26] H. Berke and R. Hoffmann; *J. Am. Chem. Soc.*, **100**, 7224 (1981).

[27] T. Ziegler, L. Versluis and V. Tschinke; *J. Am. Chem. Soc.*, **108**, 612 (1986).

[28] F. U. Axe and D. S. Marynick; *Organometalics*, **6**, 572 (1987).

[29] R. W. Glyde and R. J. Mawby *Inorg. Chim. Acta.*; 4, 331 (1970).

[30] R. J. Mawby, F. Basolo and R. G. Pearson; *J. Am. Chem. Soc.*, **86**, 3994 (1964).

[31] M. Bassestti, G. L. Sunley, F. P. Fanizzi and P. M. Maitlis; *J. Chem. Soc., Dalton Trans.*, 179 (1990).

[32] M. J. Howard, M. D. Jones, M. S. Roberts and S. A. Taylor; *Catalysis Today*, **18**, 325 (1993).

[33] J. R. Zoeller, V. H. Agreda, S. L. Cook, N. L. Lafferty, S. W. Polichnowski and D. M. Pond; *Catalysis Today*, **13**, 73 (1992).

[34] N. V. Kutepow, W. Himmele and H. Hohenschutz; *Chem. Ing. Tech.*, **37**, 383 (1965).

[35] H. Hohenschutz, N. V. Kutepow and W. Himmele; *Hydrocarbon Process*, **45**, 141 (1966).

[36] F. E. Paulik and J. F. Roth; *J. Chem. Soc., Chem. Commun.*, 1578, (1968).

[37] D. Forster; *Inorg. Chem.*, 8, 2556 (1969).

[38] B. R. James and G. L. Rempel; *J. Chem. Soc., Chem. Commun.*, 158 (1967).

[39] T. W. Dekleva and D. Forster; *Adv. in Catal.*, **34**, 81 (1986).

[40] D. Forster; *Adv. Organomet. Chem.*, **17**, 255 (1979).

[41] D. Forster and T. C. Singleton; *J. Mol. Catal.*, **17**, 299 (1982).

[42] M. A. Murphy, B. L. Smith, G. P. Torrance and A. Aguilo; *Inorg. Chim. Acta.*, **101**, 147 (1985).

[43] M. A. Murphy, B. L. Smith, G. P. Torrance and A. Aguilo; *J. Organomet. Chem.*, **303**, 257 (1986).

[44] M. Schrod and G. Luft; *Ind. Eng. Chem. Prod. Res. Dev.*, **20**, 649 (1981).

[45] M. Schrod, G. Luft and J. Grobe; *J. Mol. Catal.*, **22**, 169 (1983).

[46] G. Luft and M. Schrod; *J. Mol. Catal.*, **20**, 175 (1983).

[47] J. Hjortkjaer and J. C. A. Jorgensen; *J. Mol. Catal.*, **4**, 199 (1978).

[48] D. Forster; *J. Am. Chem. Soc.*, **98**, 846 (1976).

[49] J. J. Daly, F. Sanz and D. Forster; *J. Am. Chem. Soc.*, **97**, 2551 (1975).

[50] D. Forster; *Inorg. Chem.*, **11**, 1686 (1972).

[51] D. Forster; *J. Am. Chem. Soc.*, **97**, 951 (1975).

[52] A. J. Hart-Davis and W. A. Graham; *Inorg. Chem.*, **9**, 2658 (1970).

[53] P. B. Chock and J. Halpern; *J. Am. Chem. Soc.*, **88**, 3511 (1966).

[54] A. Fulford, C. E. Hickey and P. M. Maitlis; *J. Organomet. Chem.*, **398**, 311 (1990).

[55] P. M. Maitlis, A. Haynes, G. J. Sunley and M. J. Howard; *J. Chem. Soc., Dalton Trans.*, **11**, 2187 (1996).

[56] A. Haynes, P. Vickers and H. Adams; *Unpublished Results.*

[57] I. S. Butler, F. Basolo and R. G. Pearson; *Inorg. Chem.*, **6**, 2077 (1967).

[58] G. W. Adamson, J. J. Daly and D. Forster; *J. Organomet. Chem.*, **77**, C17 (1974).

[59] C. H. Cheng, D. E. Hendrickson and R. Eisenberg; *J. Am. Chem. Soc.*, **99**, 2791 (1977).

[60] J. F. Roth, J. H. Craddock, A. Hershman and F. E. Paulik; *Chem. Technol.*, 600 (1971).

[61] B. L. Smith, G. P. Torrance, M. A. Murphy and A. Aguilo; *J. Mol. Catal.*, **39**, 115 (1987).

[62] C. E. Hickey and P. M. Maitlis; *J. Chem. Soc., Chem. Commun.*, 1611 (1984).

[63] D. Brodski, B. Densise and G. Pannetier; *J. Mol. Catal.*, 2, 149 (1977).

[64] T. Matsumoto, T. Mizoroki and A. Ozaki; *J. Catal.*, 51, 96 (1978).

[65] T. Mizoroki, T. Matsumoto and A. Ozaki; *Bull. Chem. Soc. Jpn.*, 430, 111 (1979).

[66] D. Forster; *J. Chem. Soc., Dalton Trans.*, 1639 (1979).

[67] J. M. Pearson; *Ph.D. Thesis*, University of Sheffield (1994).

[68] J. M. Pearson, A. Haynes, G. E. Morris, G. J. Sunley and P. M. Maitlis; *J. Chem. Soc., Chem. Commun.*, 1045 (1995).

[69] *Theoretical Aspects of Homogeneous Catalysis*, eds. P. W. N. M. Van Leeuwen, K. Morokuma and J. H. Van Lenthe; Kluwer Academic Publishers: Dordrecht, The Netherlands (1995).

[70] E. Schrödinger; *Ann. Physik*, 79, 361 (1926).

[71] R. McWeeny; *Nature*, 243, 196 (1973).

[72] M. Born and J. R. Oppenheimer; *Ann. Physik*, 84, 457 (1927).

[73] W. Pauli; *Z. Physik*, 31, 765 (1925).

[74] J. C. Slater; *Phys. Rev.*, 34, 1293 (1929).

[75] J. C. Slater; *Phys. Rev.*, 35, 509 (1930).

[76] P. A. M. Dirac; *The Principles of Quantum Mechanics*; Clarendon Press: Oxford (1st Ed.) (1930).

[77] D. R. Hartree; *Proc. Cambridge Philos. Soc.*, 24, 328 (1928).

[78] V. A. Fock; *Z. Physik*, 61, 126 (1930).

[79] T. A. Koopmans; *Physica*, 1, 104 (1933).

[80] A. Szabo and N. S. Ostlund; *Modern Quantum Chemistry*; McGraw-Hill: New York (1982).

[81] C. C. J. Roothaan; *Rev. Mod. Phys.*, 23, 69 (1951).

[82] G. G. Hall; *Proc. Roy. Soc. (London)*, A205, 541 (1951).

[83] I. Shavitt; *Methods of Electronic Structure*; eds H. F. Schaefer III; Plenum: New York (1977).

[84] L. Brillouin; *Actualities Sci. Ind.*, 71, 159 (1934).

[85] R. Shephard; *Adv. Chem. Phys.*, 69, 63 (1987).

[86] S. R. Langhoff and E. R. Davidson; *Int. J. Quant. Chem.*, 8, 61 (1974).

[87] W. Kutzelnigg; *Methods of Electronic Structure*; ed. H. F. Schaefer III; Plenum: New York (1977).

[88] R. Ahlrichs and P. Scharf; *Adv. Chem. Phys.*, 67, 501 (1987).

[89] C. Møller and M. S. Plesset; *Phys. Rev.*, 46, 618 (1934).

[90] I. N. Levine; *Quantum Chemistry*; Allyn and Bacon: Boston (1983).

[91] L. H. Thomas; *Proc. Cambridge Philos. Soc.*, 23, 542 (1927).

[92] E. Fermi; *Z. Physik*, 48, 73 (1928).

[93] E. Fermi; *Rend. Accad., Lincei*, 6, 602 (1927).

[94] P. A. M. Dirac; *Proc. Cambridge Philos. Soc.*, 26, 376 (1930).

[95] E. P. Wigner; *Phys. Rev.*, 46, 1002 (1934).

[96] T. Ziegler; *Chem. Rev.*, 91, 651 (().1991)

[97] D. R. Salahub, R. Fournier, P. Mlynarski, I. Papai and A. St. Amant; *Density Functional Methods in Chemistry*; Eds J. Labanowski and J. Andzelm; Springer: New York (1991).

[98] J. Andzelm and E. Wimmer; *J. Chem. Phys.*, 96, 1280 (1992).

[99] B. G. Johnsom, P. M. W. Gill and J. A. Pople; *J. Chem. Phys.*, 98, 5612 (1993).

[100] P. Hohenberg and W. Kohn; *Phys. Rev.* A, 136, 864 (1964).

[101] W. Kohn and L. J. Sham; *Phys. Rev.* A, 140, 1133 (1965).

[102] R. G. Parr and W. Yang; *J. Am. Chem. Soc.*, 106, 4049 (1984).

[103] R. G. Parr and W. Yang; *Density Functional Theory of Atoms and Molecules*; Oxford University Press: New York (1989).

[104] D. M. Ceperly and B. J. Alder; *Phys. Rev. Lett.*, 45, 566 (1990).

[105] S. J. Vosko, L. Wilk and M. Nusair; *Can. J. Phys.*, 58, 1200 (1980).

[106] J. C. Slater; *Phys. Rev.*, 81, 385 (1951).

[107] B. Y. Tong and L. J. Sham; *Phys. Rev.*, 144, 1 (1966).

[108] K. Schwarz; *Chem. Phys. Lett.*, 57, 605 (1978).

[109] H. B. Shore, J. H. Rose and E. Zaremba; *Phys. Rev.* B, 15, 2858 (1977).

[110] J. Harris and R. O. Jones; *J. Chem. Phys.*, 68, 3316 (1978).

[111] F. Sim, A. St-Amant, I. Papai and D. R. Salahub; *J. Am. Chem. Soc.*, 114, 4391 (1992).

[112] S. Kristyan and P. Pulay; *Chem. Phys. Lett.*, 229, 175 (1994).

[113] E. Ruiz, D. R. Salahub and A. Vela; *J. Am. Chem. Soc.*, 117, 1141 (1995).

[114] E. I. Proynov, E. Ruiz, A. Vela and D. R. Salahub; *Int. J. Quant. Chem. Symp.*, 29, 61 (1995).

[115] R. van Leeuwen and E. J. Baerends; *Phys. Rev.* A, 49, 2421 (().1994)

[116] J.P. Perdew and A. Zunger; *Phys. Rev.* B, 23, 5048 (1981).

[117] M.R. Pederson and C.C. Lin; *J. Chem. Phys.*, 88, 1807 (1988).

[118] E.S. Fois, J.I.Penman and P.A.Madden; *J. Chem. Phys.*, 98, 6352 (1993).

[119] F. Herman, J. P. Van Dyke and I. B. Ortenburger; *Phys. Rev. Lett.*, 22, 807 (1969).

[120] F. Herman, J. P. Van Dyke and I. B. Ortenburger; *Int. J. Quant. Chem. Symp.*, 3, 827 (1970).

[121] J. P. Perdew and Y. Wang; *Phys. Rev.* B, 33, 8800 (1986).

[122] J. P. Perdew; *Phys. Rev.* B, 33, 8822 (1986).

[123] A. D. Becke; *J. Chem. Phys.*, 84, 4524 (1986).

[124] A. D. Becke; *Phys. Rev.* A, 38, 3098 (1988).

[125] C. Lee, W. Yang and R. Parr; *Phys. Rev.* B, 37, 785 (1988).

[126] E. Clementi and S. J. Chackravorty; *J. Chem. Phys.*, 93, 2591 (1990).

[127] A. D. Becke; *J. Chem. Phys.*, 98, 1372 (1993).

[128] R. M. Dreizler and E. K. U. Gross; *Density Functional Theory. An approach to the Quantum Many-Body Problem*; Springer-Verlag: Berlin (1990).

[129] A. D. Becke; *J. Chem. Phys.*, 98, 5648 (1993).

[130] K. Kim and K. D. Jordan; *J. Phys. Chem.*, 98, 10089 (1994).

[131] J. Korringa; *Physica*, 13, 392 (1947).

[132] K. H. Johnson; *J. Chem. Phys.*, 45, 3085 (1966).

[133] J. A. Pople, P. M. W. Gill and B. G. Johnson; *Chem. Phys. Lett.*, 199, 557 (1992).

[134] Gaussian 92/DFT; Revision G.2; M. J. Frisch, G. W. Trucks, H. B. Schlegel, P. M. W. Gill, B. G. Johnson, M. W. Wong, J. B. Foresman, M. A. Robb, M. Head-Gordon, E. S. Replogle, R. Gomperts, J. L. Andres, K. Raghavachari, J. S. Binkley, C. Gonzalez, R. L. Martin, D. J. Fox, D. J. Defrees, J. Baker, J. J. P. Stewart, and J. A. Pople; Gaussian Inc.: Pittsburgh PA (1993).

[135] H. Hellmann; *J. Chem. Phys.*, **3**, 61 (1935).

[136] H. Hellmann and W. Kassatotschkin; *J. Chem. Phys.*, 4, 325 (1936).

[137] P. Gombas; *Z. Physik*, 94, 473 (1935).

[138] J. C. Phillips and L. Kleinman; *Phys. Rev.*, **116**, 287 (1959).

[139] J. P. Desclaux and P. Pyykko; *Chem. Phys. Lett.*, **29**, 534 (1974).

[140] P. Pyykko and J. P. Desclaux; *Acc. Chem. Res.*, **12**, 276 (1979).

[141] J. D. Weeks, A. Hazi and S. A. Rice; *Adv. Chem. Phys.*, **16**, 283 (1969).

[142] L. R. Kahn, P. Baybutt and D. G. Truhlar; *J. Chem. Phys.*, **65**, 3826 (1976).

[143] L. R. Kahn, P. J. Hay and R. D. Cowan; *J. Chem. Phys.*, **68**, 2386 (1978).

[144] P. J. Hay and W. R. Wadt; *J. Chem. Phys.*, **82**, 270 (1984).

[145] P. J. Hay and W. R. Wadt; *J. Chem. Phys.*, **82**, 284 (1984).

[146] P. J. Hay and W. R. Wadt; *J. Chem. Phys.*, **82**, 299 (1984).

[147] A. Redondo, W. A. Goddard and T. C. McGill; *Phys. Rev.* B, **15**, 5038 (1977).

[148] P. A. Christiansen, Y. S. Lee and K. S. Pitzer; *J. Chem. Phys.*, **71**, 4445 (1979).

[149] R. W. Cowan and D. C. Griffin; *J. Opt. Soc. Am.*, 66, 1010 (1976).

[150] D. B. Cook; *Ab initio Valence Calculations in Chemistry*; Wiley: New York (1974).

[151] R. McWeeny and B. T. Sutcliffe; *Methods of Molecular Quantum Mechanics* 2nd ed; Academic Press: New York (1976).

[152] B. J. Deppmeier, A. J. Driessen, W. J. Hehre, H. C. Johnson, J. M. Leonard, J. Yu and L. Lou; *SPARTAN SGI version 4.0*; Wavefunction Inc: California, CA (1995).

[153] S. Huzinaga and B. Miguel; *Chem. Phys. Lett.*, **175**, 289 (1990).

[154] S. Huzinaga, J. Andzelm, M. Klobukowski, E. Radzio-andzelm, Y. Sakai and H. Tatewaki; *Gaussian Basis Sets for Molecular Calculations*; Physical Sciences Data 16; Elsevier: Amsterdam (1984).

[155] T. H. Dunning and P. J. Hay; *Methods of Electronic Structure*; ed. H. F. Schaefer III; Plenum: New York (1977).

[156] E. A. Salter, A. Wierzbicki, J. M. Seminario, N. W.Hoffman, M. L. Easterling and J. D. Madura; *J. Phys. Chem.*, **98**, 12945 (1994).

[157] D. J. Fox; *Personal Communication.*

[158] R. V. Stanton and K. M. Merz Jr.; *J. Chem. Phys.*, **100**, 434 (1994).

[159] B. G. Johnson, P. M. W. Gill, and J. A. Pople; *J. Chem. Phys.*, **97**, 7846 (1992).

[160] L. Fan and T. Ziegler; *J. Chem. Phys.*, **92**, 3645 (1990).

[161] L. Fan and T. Ziegler; *J. Am. Chem. Soc.*, **114**, 10890 (1992).

[162] H. Chen, M. Krasowski and G. Fitzgerald; *J. Chem. Phys.*, **98**, 8710 (1993).

[163] H. B. Schlegel; *J. Comp. Chem.*, **3**, 214 (1982).

[164] C. Gonzalez and H. B. Schlegel; *J. Phys. Chem.*, **90**, 2154 (1989).

[165] M. W. Wong, M. J. Frisch and K. B. Wiberg; *J. Am. Chem. Soc.*, **113**, 4776 (1991).

[166] M. W. Wong, K. B. Wiberg and M. J. Frisch; *J. Am. Chem. Soc.*, **114**, 523 (1992).

[167] M. W. Wong, K. B. Wiberg and M. J. Frisch; *J. Am. Chem. Soc.*, **114**, 1645 (1992).

[168] M. W. Wong, K. B. Wiberg and M. J. Frisch; *J. Chem. Phys.*, **95**, 8990 (1991).

[169] L. Onsager; *J. Am. Chem. Soc.*, **58**, 1486 (1934).

[170] T. A. Keith, M. J. Frisch and K. B. Wiberg; *Unpublished Results.*

[171] P. Kitts, B. T. Pickup and A. Grant; *Unpublished Results.*

[172] R. S. Mulliken; *J. Chem. Phys.*, **23**, 1833 (1955).

[173] J. Bigeleisen and M. Goeppert-Mayer; *J. Chem. Phys.*, **16**, 261 (1947).

[174] J. Bigeleisen; *J. Chem. Phys.*, **17**, 675 (1949).

[175] D. A. McQuarrie; *Statistical Mechanics*; Harper and Row: New York (1976).

[176] O. Redlich; *Z. Physik Chem.*, **B28**, 371 (1935).

[177] S. Wolfe and C. K. Kim; *J. Am. Chem. Soc.*, **113**, 8056 (1991).

[178] S. S. Shaik, H. B. Schlegel and S. Wolfe; *J. Chem. Soc. Commun.*, 1322 (1988).

[179] R. A. Poirieri, Y. Wang and K. C. Westaway; *J. Am. Chem. Soc.*, **116**, 2526 (1994).

[180] W. J. Hehre, L. Radom, P. Schleyer and J. A. Pople; *Ab initio Molecular Orbital Theory*; Wiley; New York (1986).

[181] P. D. Mallinson; *J. Mol. Spec.*, **55**, 94 (1975).

[182] R. C. Weast; *CRC Handbook of Chemistry and Physics*: CRC Press Inc.; Florida (1980).

[183] A. Veillard; *Chem. Rev.*, **91**, 743 (1991).

[184] A. W. Ehlers and G. Frenking; *J. Am. Chem. Soc.*, **116**. 1514 (1994).

[185] D. Dahm and D. Forster; *Inorg. Nucl. Chem. Lett.*, **6** 15 (1970).

[186] E. Cetinkaya, A. W. Johnson, M. F. Lappert, G. M. McLaughlin and K. W. Muir; *J. Chem. Soc., Dalton Trans.*, 1236 (1974).

[187] A. L. Rheingold and S. J. Geib; *Acta Cryst.*, **C43** 784 (1987).

[188] S. S. Basson, J. G. Leipoldt and A. Roodt; *Acta Cryst.*. **C46**, 142 (1990).

[189] K. A. Bernard, M. R. Churchill, T. S. Janik and J. D. Atwood; *Organometalics*, **9**, 12 (1990).

[190] W. M. Rees, M. R. Churchill, J. C. Fettinger and J. D. Atwood; *Organometalics*, **4**, 2179 (1985).

[191] M. R. Churchill, J. C. Fettinger, L. A. Buttrey, M. D. Barkan and J. S. Thompson; *J. Organomet. Chem.*, **340**, 252 (1988).

[192] F. Calderazzo; *J. Organomet. Chem.*, **400**, 303 (1990).

[193] J. P. Collman, P. A. Christian, S. Current, P. Denisevich. T. R. Halbert, E. R. Schmittou and K. O. Hodgson; *Inorg. Chem.*, **15**, 223 (1976).

[194] P. G. H. Troughton and A. C. Skapski; *J. Chem. Soc., Chem. Commun.*, 575 (1968).

[195] P. J. Brothers, A. K. Burrell, G. R. Clark, C. E. F. Rickard and W. R. Roper; *J. Organomet. Chem.*, **394**, 615 (1990).

[196] L. E. Sutton; *Interatomic Distances*; The Chemical Society: London (1958).

[197] H. Adams, N. A. Bailey, B. E. Mann and C. P. Manuel: *Inorg. Chim. Acta*, **200**, 111 (1992).

[198] K. G. Moloy and J. L. Peterson; *Organometalics*, **14**, 2931 (1995).

[199] H. Adams, N. A. Bailey, B. E. Mann, C. P. Manuel, C. M. Spencer and A. G. Kent; *J. Chem. Soc., Dalton Trans.*, 489 (1988).

[200] C. S. Collins and N. S. Bowman; *Isotope Effects in Chemical Reactions*; Van Nostrand-Reinhold: New York (1970).

[201] H. Maskill; *The Physical Basis of Organic Chemistry*. Oxford University Press: Oxford (1985).

[202] P. J. Stang, M. Hanack, and L. R. Subramanian; *Synthesis*, 85 (1982).

[203] T. R. Griffin, D. B. Cook, A. Haynes, J. M. Pearson, D. Monati and G. E. Morris; *J. Am. Chem. Soc.*, **118**, 3029 (1996).

[204] J. E. Huheey; *Inorganic Chemistry*; Harper and Row: New York (1983).

[205] P. Pyykko; *Chem. Rev.*, 88, 563 (1988).

[206] P. R. Ellis; *Ph.D. Thesis*, University of Sheffield (1993).

[207] N. Koga and K. Morokuma; *Chem. Rev.*, **91**, 823 (1991).

[208] P.J. Hay; *Transition Metal Hydrides*; VCH Publishers: New York (1992).

[209] P. E. M. Siegbahn; *Theoretical Aspects of Homogeneous Catalysis*, eds. P. W. N. M. Van Leeuwen, K. Morokuma and J. H. Van Lenthe; Kluwer Academic Publishers: Dordrecht, The Netherlands (1995).

[210] J. O. Noell and P. J. Hay; *J. Am. Chem. Soc.*, **104**, 4578 (1982).

[211] M. R. A Blomberg and P. E. M. Siegbahn; *J. Chem. Phys.*, **78**, 986 (1983).

[212] S. Obara, K. Kitaura and K. Morokuma; *J. Am. Chem. Soc.*, **106**, 7482 (1984).

[213] J. J. Low and W. A. Goddard; *J. Am. Chem. Soc.*, 108. 6115 (1986).

[214] C. Daniel, N. Koga, J. Han, X. Y. Fu and K. Morokuma; *J. Am. Chem. Soc.*, **110**, 3773 (1988).

[215] A. L. Sargent, M. B. Hall and M. F. Guest; *J. Am. Chem. Soc.*, **114**, 517 (1992).

[216] F. Abu-Hasanayn, K. Krogh-Jespersen and A. S. Goldman; *Inorg. Chem.*, **32**, 495 (1993).

[217] J. Song and M. B. Hall; *Organometalics*, **12**, 3118 (1993).

[218] T. R. Cundari; *J. Am. Chem. Soc.*, **116**, 341 (1994).

[219] D. G. Musaev and K. Morokuma; *J. Am. Chem. Soc.*, **117**, 799 (1995).

[220] N. Koga and K. Morokuma; *J. Phys. Chem.*, **94**, 5454 (1990).

[221] N. Koga and K. Morokuma; *J. Am. Chem. Soc.*, **115**, 6883 (1993).

[222] D. G. Musaev and K. Morokuma; *J. Am. Chem. Soc.*, **117**, 799 (1995).

[223] T. Ziegler, V. Tschinke, L. Fan and A. D. Becke; *J. Am. Chem. Soc.*, **111**, 9177 (1989).

[224] P. O. Stoutland, R. G. Bergman, S. P. Nolan and C. D. Hoff; *Polyhedron*, **7**, 1429 (1988).

[225] W. D .Jones and F. J. Feher; *J. Am. Chem. Soc.*, **104**, 4240 (1982).

[226] R. H. Crabtree; *Chem. Rev.*, **85**, 245 (1985).

[227] R. Jiménez-Catano and M. B. Hall; *Organometalics*, **15**, 1889 (1996).

[228] M. R. A. Blomberg, P. E. M. Siegbahn and M. Svensson; *J. Am. Chem. Soc.*, **114**, 6095 (1992).

[229] M. R. A. Blomberg, P. E. M. Siegbahn and M. Svensson; *J. Phys. Chem.*, **98**, 2062 (1994).

[230] P. E. M. Siegbahn, M. R. A. Blomberg and M. Svensson; *J. Am. Chem. Soc.*, **115**, 4191 (1993).

[231] P. E. M. Siegbahn and M. R. A. Blomberg; *Organometalics*, **13**, 354 (1994).

[232] P. E. M. Siegbahn; *J. Organomet. Chem.*, **491**, 231 (1995).

[233] P. E. M. Siegbahn; *Organometalics*, **13**, 2833 (1994).

[234] F. M. Bickelhaupt, T. Ziegler and P. von Rague Schleyer; *Organometalics*, **14**, 2288 (1995).

[235] S. Shaik, A. Ioffe, A. C. Reddy, A. Pross; *J. Am. Chem. Soc.*, **116**, 262 (1994).

[236] T. H. Dunning and P. J. Hay; *Modern Theoretical Chemistry*, ed. H. F. Schaefer III; Plenum: New York (1977).

[237] H. F. Schaefer III, R. A. Klemm and F. E. Harris; *J. Chem. Phys.*, **51**, 4643 (1969).

[238] J. Almlöf and P. R. Taylor; *J. Chem. Phys.*, **86**, 4070 (1987).

[239] R. Vetter and L. Zülicke; *J. Am. Chem. Soc.*, **112**, 5136 (1990).

[240] S. Wolfe; *Personal Communication.*

[241] L. Q. Deng, V. Branchadell and T. Ziegler; *J. Am. Chem. Soc.*, **116**, 10645 (1994).

[242] A. Haynes; *Personal Communication.*

[243] G. Yoneda and H. D. M. Blake; *Inorg. Chem.*, **20**, 67 (1981).

[244] S. Seltzer and A. A. Zavitsas; *Can. J. Chem.*, **45**, 2023 (1967).

[245] C. M. Rohlfing, P. J. Hay and R. L. Martin; *J. Chem. Phys.*, **85**, 1447 (1986).

[246] M. Born; *Z. Physik*, **1**, 45 (1920).

[247] T. Ziegler, V. Tschinke, A. Becke; *J. Am. Chem. Soc.*, **109**, 1987 (1351).

[248] T. Ziegler, W. Cheng, E. J. Baerends and W. Raveneck; *Inorg. Chem.*, **27**, 3458 (1988).

[249] T. Ziegler, V. Tschinke, L. Fan and A. Becke; *J. Am. Chem. Soc.*, **111**, 9177 (1989).

[250] J. March; *Advanced Organic Chemistry*; mcGraw-Hill: Kogakus ha (1977).

[251] D. P. Schlusser, W. R. Robinson and W. F. Edgell; *Inorg. Chem.*, **13**, 153 (1974).

[252] K. Noack and F. Calderazzo; *J. Organomet. Chem.*, **10**, 101 (1967).

[253] T. C. Flood and K. D. Campbell; *J. Am. Chem. Soc.*, **106**, 2853 (1984).

[254] C. F. J. Barnard, J. A. Daniels and R. J. Mawby; *J. Chem. Soc., Dalton Trans.*, 1331 (1979).

[255] R. W. Glyde and R. J. Mawby; *Inorg. Chim. Acta.*, **5**, 317 (1971).

[256] F. J. G. Alonso, A. Llamazeras, V. Riera, M. Vivanco, S. G. Granda and M. R. Diaz; *Organometalics*, **11**, 2826 (1992).

[257] M. Bassetti, D. Monti, A. Haynes, J. M. Pearson, I. A. Stanbridge and P. M. Maitlis; *Gazz. Chim. Ital.*, **122**, 391 (1992).

[258] S. B. Butts, T. Richmond and D. F. Shriver; *Inorg. Chem.*, **20**, 278 (1981).

[259] J. P. Collman, J. N. Cawse and J. I. Brauman; *J. Am. Chem. Soc.*, **94**, 5905 (1972).

[260] S. B. Butts, E. M. Holt, S. H. Strauss, N. W. Alcock, R. E. Stimson and D. F. Shriver; *J. Am. Chem. Soc.*, **10**, 5864 (1979).

[261] N. Koga and K. Morokuma; *Theoretical Aspects of Homogeneous Catalysis*, eds. P. W. N. M. Van Leeuwen, K. Morokuma and J. H. Van Lenthe; Kluwer Academic Publishers: Dordrecht, The Netherlands (1995).

[262] S. Sakaki, K. Kitaura, K. Morokuma and K. Ohkubo; *J. Am. Chem. Soc.*, **105**, 2280 (1983).

[263] N. Koga and K. Morokuma; *J. Am. Chem. Soc.*, **108**, 6136 (1986).

[264] J. O. Noell and P. J. Hay; *J. Chem. Phys.*, **21**, 14 (1982).

[265] S. Nakamura and A. Dedieu; *Chem. Phys. Lett.*, **111**, 243 (1984).

[266] L. Versluis, T. Ziegler, E. J. Baerends and W. Ravenek; *J. Am. Chem. Soc.*, **111**, 2018 (1989).

[267] P. Margl, T. Ziegler and P. E. Blöchl; *J. Am. Chem. Soc.*, **118**, 5412 (1996).

[268] H. P. Lüthi, P. E. M. Siegbahn and J. Almlöf; *J. Phys. Chem.*, **89**, 2156 (1985).

Addendum

1. page 19, chapter 1:
In 1996 British Petroleum commercialised a new iridium-based catalytic carbonylation process – "Cativa".

2. page 22, chapter 1; pages 212-255, chapter 6:
Haynes has recently observed $[CH_3Ir(CO)_3I_2]$ by infra-red spectroscopy. This new experimental information supports the results of theoretical calculations reported in this thesis that the neutral iridium tricarbonyl, originally thought to be an unstable species, is in fact relatively stable.

3. page 203, chapter 5:
The hydride complex, $[Rh(CO)_2H_2]^-$, is an unknown species.

4. page 251, chapter 6:
The arguments regarding the relative rates of migratory insertion in $[CH_3Ir(CO)_2I_3]^-$ and $[CH_3Ir(CO)_3I_2]$ do not take into account that the reaction:

$$[CH_3Ir(CO)_2I_3]^- + CO \rightarrow [CH_3Ir(CO)_3I_2] + I^-$$

is predicted to be exothermic by 80 - 100 kJ mol^{-1} (page 247). If migratory insertion in $[CH_3Ir(CO)_2I_3]^-$ proceeds via loss of an iodide ligand, then the effective activation barrier would be expected to be significantly lower than migratory insertion occurring directly in the anion due to the preceding exothermic substitution of iodide by CO.